IntechOpen

Compendium of New Techniques in Harmonic Analysis

Edited by Moulay Tahar Lamchich

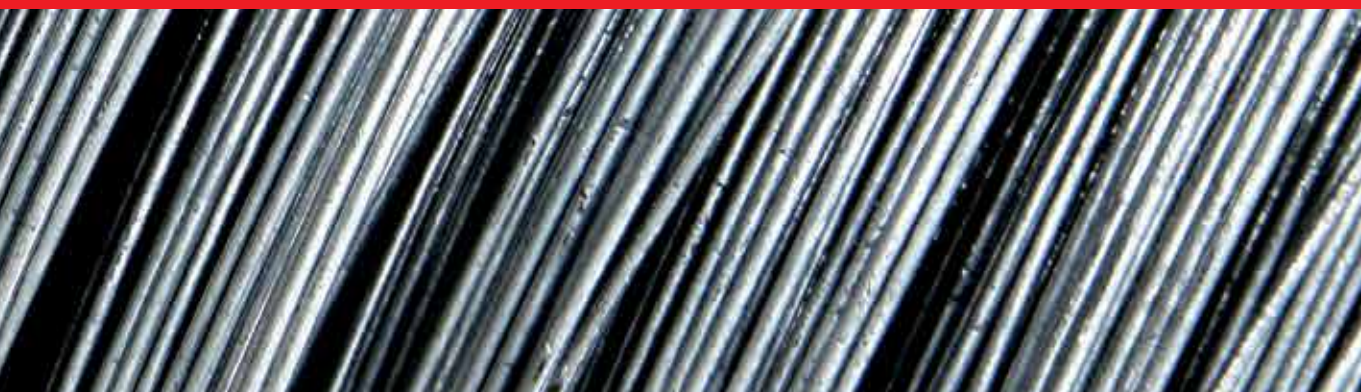

COMPENDIUM OF NEW TECHNIQUES IN HARMONIC ANALYSIS

Edited by **Moulay Tahar Lamchich**

Compendium of New Techniques in Harmonic Analysis
http://dx.doi.org/10.5772/intechopen.68400
Edited by Moulay Tahar Lamchich

Contributors

Ertugrul Aksoy, Yasin Yavuz, Mert Karahan, Hui Hwang Goh, Chin Wan Ling, Kai Chen Goh, Qing Shi Chua, Sy Yi Sim, Mohd Ariff Mohd Aifaa, Abdullahi Lanre Amoo, Usman O. Aliyu, Ganiyu Ayinde Bakare, Emmanuel Hernández, Miguel Angel Hernandez, Hugo Jorge Cortina Marrero, Reynaldo Iracheta Cortez, Ragini Meshram, Sushama Wagh, Monika Madhusoodan, Norio Tagawa, Takuya Horaoka, Iwaki Akiyama, Dragos Daniel Taralunga, G. Mihaela Ungureanu, Harish Kumar Sahoo, Umamani Subudhi

Notice

First published in London, United Kingdom, 2018 by IntechOpen
eBook (PDF) Published by IntechOpen, 2019
IntechOpen is the global imprint of INTECHOPEN LIMITED, registered in England and Wales, registration number: 11086078, The Shard, 25th floor, 32 London Bridge Street
London, SE19SG – United Kingdom
Printed in Croatia

British Library Cataloguing-in-Publication Data
A catalogue record for this book is available from the British Library

Additional hard and PDF copies can be obtained from orders@intechopen.com

Compendium of New Techniques in Harmonic Analysis
Edited by Moulay Tahar Lamchich

p. cm.

Print ISBN 978-1-78923-636-1

Online ISBN 978-1-78923-637-8

eBook (PDF) ISBN 978-1-83881-317-8

Meet the editor

Lamchich Moulay Tahar is presently a professor at the Faculty of Sciences Semlalia, Cadi Ayyad University at Marrakech (Morocco). He submitted his thesis in electrotechnics in September 1991 and received his third cycle degree. He received his PhD from the same university in July 2001. Dr. Lamchich main research is based on short-circuit mechanical effects in substation structures, control of different types of machine drives, static converters, and active power filters. In the last decade, his research interests have included renewable energies, particularly the control and supervision of hybrid and multiple source systems for decentralized energy production and intelligent management of energy. He has published more than fifty technical papers in journals and international conferences. With Intech open, Dr.Lamchich has published two chapters and was editor of the book "Torque control." He is the director of the laboratory "Intelligent management of energy and information's systems." Dr. Lamchich is a promotor of several doctoral and professional training programs and director of more than 10 thesis projects.

Contents

Preface

Harmonic analysis is a diverse field including such branches as signal processing, medical imaging, power electrical systems, wireless telecommunications, etc. This book was written with the objective of providing recent developments and new techniques in harmonic analysis. In the recent years, a number of methods of quality control of signals under different perturbations, and especially the harmonics, have emerged. Some of these techniques are described in this book.

In the field of power electrical systems, due to the increased use of nonlinear electrical loads, harmonics currents are generated and returned to the grid causing voltage distortion, which will be absorbed by sensitive loads and cause losses in the lines. In addition, the development of power generation-based renewable energies is subject of many problems with harmonics. On the other hand, harmonic noise in electrical machines is due to many factors such as harmonics in control systems, switching harmonics, and harmonic voltages supplied by the power inverter. These harmonics cause many undesired phenomena such as electromagnetic interference and torque ripples, which diminish the performance of the drive-in demanding applications. Recently, many research efforts have been carried out on the reduction of the harmonics essentially due to inverter switching by using an inverter output passive filter topology but with certain limitations and, in other cases, active filter design to reduce or compensate harmonics on the supply side by injecting harmonics into the line current. Other investigations were studied to suppress the harmonic contents.

This book is the result of contributions from many researchers and is a collection of eight research works, which are focused on the harmonic analysis theme but with different applications. This book comprises two sections. The topics covered concern the areas of medical imaging, biopotential systems, renewable energy conversion systems, wireless telecommunications, power converters, as well as the different techniques for estimating, analyzing, reducing, and eliminating harmonics.

In the first section, composed of chapters 1 to 4, we present a variety of harmonic analysis applications for various fields.

Chapter 1 “Compensation of Frequency-Dependent Attenuation for Tissue Harmonic Pulse Compression Imaging” concerns a crucial problem in medical tissue imaging, which is the frequency-independent attenuation and its influence on harmonics. The authors proposed a novel and simple method for frequency-dependent attenuation to realize fine tissue harmonic imaging, which can also compensate transducer characteristics. The technique proposed is based on FM chirp pulse compression to realize high SNR.

In Chapter 2, "Cancelling Harmonic Power Line Interference in Biopotentials," the authors present a review of the existing methods for the elimination of power line inference harmonics from biopotential signals and analyze the distortion introduced by some of the most basic approaches for the cancellation of PLI and determine how this distortion affects the diagnostic performance in biopotential investigations. Also, and mainly for the purpose of removing PLI and its harmonics without loss of diagnostic information, four types of traditional fixed frequency band stop filters and a time-varying pole radius multiple notch IIR filter are implemented in MATLAB and tested on a real ElectroCardioGram database. It's concluded that the TVNM filter presents better performances and provides almost no distortion.

In Chapter 3, "Harmonic Analysis of the Wind Energy Conversion System Connected with Electrical Network," a harmonic analysis for a wind energy conversion system based on a doubly-fed induction generator is developed. This study focused on the components of the wind turbine system, namely induction generator, frequency converter, and electric network, with steady state and dynamic state models.

Chapter 4 "Optimization Approaches in Sideband Calculations and a Non-Iterative Harmonic Suppression Strategy in 4D Arrays" concerns wireless communication technologies. The authors examine methods using optimization techniques for the suppression of harmonic radiations. Common excitation strategies, calculation of the total power of SRs, and techniques used in harmonic calculations are also presented. This research work is, above all, focused on a noniterative harmonic suppression algorithm, illustrated by a simple example of 10-element linear control, in the object of harmonic suppression with lateral control.

Section 2, composed of four chapters, is related to different computational tools, methods, and techniques for the identification, analysis, reduction, and elimination of harmonics. So:

In Chapter 5, "Compendium of Computational Tools for Power Systems Harmonic Analysis," the authors explore artificial neural networks for fast evaluation of harmonic distortion in distribution infrastructures. They show, through this study, that it may be possible to achieve fast resolution of harmonic problems with the application of a neural network, expert systems, and other computational intelligence tools. These tools have the potential of minimizing the cost of multiple on-site harmonic monitoring and field recording and the rigorous harmonic modelling of the system in its entirety.

In Chapter 6, "Power System Harmonic Estimation Using Adaptive Filters," the authors present a synthesis of different adaptive filtering models used to estimate harmonic amplitudes and phases in distorted power systems. The focus is especially on least mean square (LMS) and recursive least square (RLS)-based adaptive estimation models, which can estimate and track the harmonic amplitudes and phases in practical power system applications. In this chapter, the simulation results, using MATLAB, show the performances of Volterra series–based adaptive filters. It's concluded that VLMS/F filters provide a better harmonic estimation accuracy and stable convergence of estimation error compared to LMS, VLMS, and LMS/F. Also, Volterra RLS-based harmonic estimation model provides faster and more stable convergence with minimum estimation error.

Chapter 7, "Harmonic Reduction of a Single-Phase Multilevel Inverter Using Genetic Algorithm and Particle Swarm Optimization," is mainly focalized on three aspects: the first part concerns the choice of cascade H-bridge topology multilevel inverter based on a sinusoidal PWM technique, which produces better quality output both in total harmonic distortion and

in fundamental component voltage boosting capability. The second part proceeds with the optimized harmonic stepped waveform technique, the basic concept of which applies to selective harmonic elimination PWM and quarter-wave symmetric to eliminate low order harmonics and therefore reduce harmonic distortion. In addition, the selective harmonic elimination calculation is adapted with a genetic algorithm and particle swarm optimization, which give a better output quality in terms of selected harmonic elimination. Optimization algorithms are compared, for equal and unequal sources, in terms of total harmonic distortion and selected harmonic elimination.

Chapter 8, "Harmonic Mitigation for VSI Using DP-Based PI Controller," addresses the design of a conventional PI controller, based on the dynamic phasor modelling technique, which eliminates selected current harmonics. Two systems are considered and corresponding respectively to a single-phase voltage source inverter and grid-connected single-phase PV inverter. Also, a comparison with the repetitive control technique, which allows full compensation of selected frequencies, is also detailed.

Finally, this book intends to provide the reader with recent developments and new technologies in the field of harmonic analysis, and in my capacity as the editor of this book, I would like to thank the authors for their contributions and for ensuring the best quality of their submitted works.

I hope all will enjoy the book.

Pr. Moulay Tahar Lamchich
Department of Physics
Research Group "Intelligent management of energy and information systems"
Faculty of Sciences Semlalia – University Cadi Ayyad
Marrakech, Morocco

Section 1

Harmonic Analysis in Systems of Imaging, Wireless Communication, Biopotential and Renewable Energy

Chapter 1

Compensation of Frequency-Dependent Attenuation for Tissue Harmonic Pulse Compression Imaging

Norio Tagawa, Takuya Hiraoka and Iwaki Akiyama

Additional information is available at the end of the chapter

http://dx.doi.org/10.5772/intechopen.74577

Abstract

Tissue harmonic imaging (THI) is highly effective for correct diagnosis. On the other hand, pulse compression is often used in a radar system and an ultrasound imaging system to perform high SNR measurement. Therefore, the performance of pulse compression of tissue harmonic imaging is required to be improved. The frequency-dependent attenuation (FDA) is a crucial problem in medical tissue imaging. In the pulse compression imaging, the deterioration of echoes by the FDA lowers the performance of a matched filtering using an ideal transmitted pulse as a template signal. Since, especially in the harmonic imaging, higher-frequency components are used for imaging than the fundamental imaging, the compensation of the FDA is strongly important for high-definition imaging. In this study, we examine a method to reduce the influence of the FDA on harmonics.

Keywords: FDA, pulse compression, tissue harmonic imaging, FM chirp, compensation for FDA

1. Introduction

The ultimate goal of our study is to perform high-resolution and high signal-to-noise ratio (SNR) ultrasound imaging required for high-quality diagnosis. Such imaging is strongly demanded particularly in the deep part of a living body. On the other hand, we are developing a puncture ultrasound microscope [1–3], in which echo is very weak and cell-level resolution is required, so high-definite imaging technique is absolutely important. A pulse compression technique (PCT) is effective for improving SNR while maintaining safety to the living body [4–6].

In PCTs, broadband modulation is necessary to improve the range resolution. The bandwidth that is used efficiently for transmission and reception is limited by the resonance characteristics of the transducer that utilizes thickness resonance vibration. In order to widen the bandwidth of the transducer, a layered-type transducer has been developed in which two piezoelectric oscillators having different thicknesses are longitudinally bonded and one of a pair of electrodes is inserted between two oscillators [7]. In addition, we are proposing the concept of a new transducer based on a PMUT structure with a thicker diaphragm than conventional PMUT and by which the bandwidth can be greatly widened [8]. In general, the wide bandwidth of the transmitted pulses is a prerequisite for sharp pulses. Therefore, broadband transmission in PCTs improves range resolution. On the other hand, in order to improve the SNR by PCTs, it is necessary to increase energy inflow into the body by transmitting a signal with a wide pulse width. Namely, a PCT using pulses having a wideband and a wide pulse width is suitable for our objective.

Due to its high resolution, tissue harmonic imaging (THI) is useful, and many studies have been done [9, 10]. THI uses harmonic components generated as nonlinear distortion caused by ultrasonic propagation in living tissue for imaging. In a commercial implement, the second harmonic component is generally used since its amplitude is drastically greater than the amplitude of the higher-order harmonic components. The advantages of THI can be summarized as follows: (i) THI has high-resolution characteristics along the range direction compared to fundamental imaging due to the broadband characteristics of the harmonic components, (ii) THI has high-resolution characteristics along the azimuth direction since the nonlinear effect strongly occurs at the center of the transmitted beam with high sound pressure, and (iii) there are almost no artifacts such as multiple reflection and side lobes in THI since the sound pressure of the echo reflected from the scatterer is low and hence the sound pressure of the multiple reflected echo is further low, and the amplitude of the side lobes of harmonics is 60–80 dB smaller than that of the main lobe. On the other hand, in THI the amplitude of the harmonic components is significantly smaller than the amplitude of the fundamental component. In order to solve this problem, we proposed a method based on the Bayesian estimation using the prior information of the second harmonic echoes introduced from fundamental echoes [11].

Applying a PCT to THI is expected to improve the SNR while maintaining high-resolution characteristics, but frequency-dependent attenuation (FDA) must be strongly aware. FDA causes severe distortion of echo signals, when the broadband pulse propagates through the soft tissue in the living body. Since the high-frequency component attenuates more than the low-frequency component, particularly large distortion occurs in harmonic components. **Figure 1** shows the FDA in the time domain and **Figure 2** shows it in the frequency domain. The distortion of the echo caused by FDA makes exact pulse compression impossible, and, hence, image blurring occurs [10]. In order to prevent the SNR degradation and of the range resolution degradation due to the echo distortion caused by FDA, we have proposed an FDA compensation method [12–14]. In the methods, an amplitude-modulated FM chirp pulse is transmitted, the echo for which is distorted by FDA and, as a result, is received as an ideal waveform. The proper amplitude modification (AM) of the transmission is determined using the FDA characteristic measured by transmitting a reference pulse toward a region of interest (ROI) and receiving the corresponding echo. Since the methods proposed [12, 13] have been constructed for fundamental imaging, this study aims to extend them for THI imaging. The method [13] was constructed for

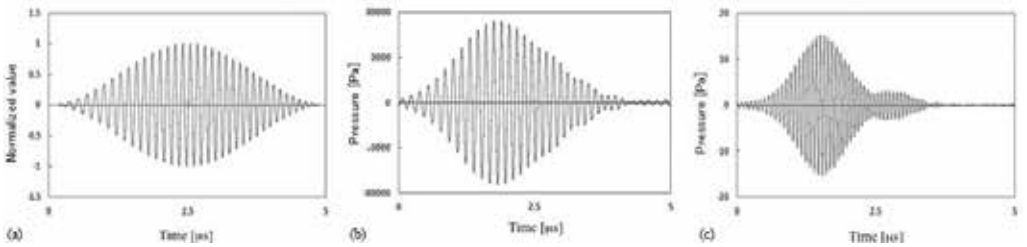

Figure 1. Temporal distortion caused by FDA: (a) transmitted signal, (b) fundamental echo, and (c) second harmonic echo.

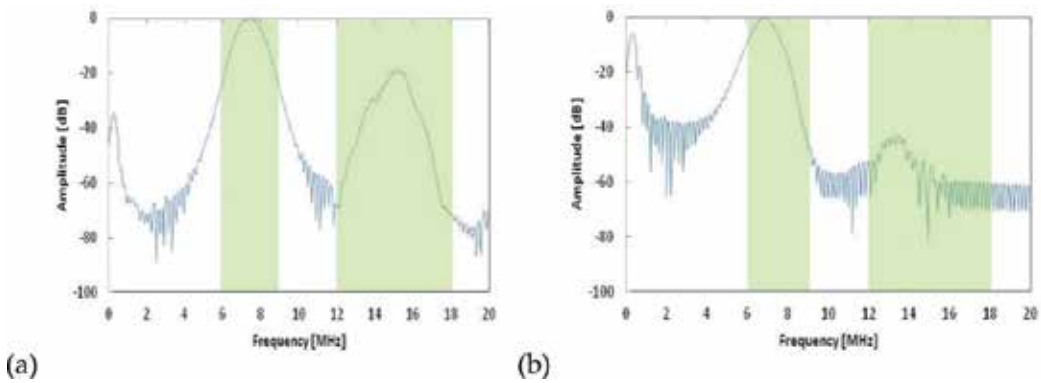

Figure 2. FDA represented in frequency domain: (a) without FDA and (b) after FDA distortion. Green boxes indicate fundamental band and second harmonic band.

harmonic imaging, but the compensation of the transducer characteristics was insufficient, which will be solved in this study to propose an FDA compensation method with high completeness. Typical purposes of AM of an FM chirp signal are side-lobe suppression and compensation of the resonance characteristics of a transducer [15]. The techniques for these purposes can be also integrated into our method. The effectiveness of our method on the harmonic FDA compensation is confirmed through numerical simulations by finite element method (FEM) and simple experiments.

2. Method

2.1. Transducer characteristic compensation

2.1.1. Compensation for fundamental band

Before considering FDA compensation, it is necessary to correct the frequency characteristic of the transducer, which must be done only once for each transducer. For fundamental imaging, the transmission and reception characteristics of the transducer are simply compensated for

both amplitude and phase. To evaluate the characteristic, any arbitrary FM chirp signal $f(t)$ covering the entire frequency band used for imaging is applied as a voltage to the transducer, and the corresponding echo $g(t)$ is received. Their frequency representations are denoted as $F(\omega)$ and $G(\omega)$, respectively. The complex distortion function $R(\omega)$ is defined as follows:

$$R(w) = \frac{H(w)}{G(w)}. \tag{1}$$

In this equation, $H(\omega)$ is the frequency representation of the ideal FM chirp signal and should have spectrum amplitude with a window function suitable for reducing side lobes.

$S(\omega)$ defined by the following equation can be adopted as a transmission pulse for compensating transducer characteristics and observing an appropriate FM chirp echo:

$$S(w) = R(w)F(w). \tag{2}$$

The simulation confirmed that beam focusing has little effect on measuring transducer characteristics.

2.1.2. Compensation for fundamental transmission and harmonic reception

For tissue harmonic imaging, the transmission characteristic in the fundamental frequency band and the reception characteristic in the harmonic frequency band must be corrected at the same time. That is, the harmonic echo is distorted due to the fundamental transmission characteristic and the harmonic reception characteristic. Hereafter, attention is focused only on the second harmonic component. The fundamental transmission characteristic can be evaluated by experimentally measuring the transmitted pressure by a hydrophone. We represent an arbitral FM chirp transmission signal $f_F(t)$ and the corresponding pressure $g_F(t)$ measured in the propagation medium and define the fundamental transmission distortion as $R_F(\omega) = H_F(\omega)/G_F(\omega)$, where $H_F(\omega)$ is a frequency representation of an ideal fundamental FM chirp signal. The harmonic reception distortion is defined as $R_H(\omega) = H_H(\omega)/G_H(\omega)$, where $H_H(\omega)$ is a frequency representation of an ideal second harmonic FM chirp signal. The harmonic reception characteristic can be evaluated by measuring the transmitted pressure $f_H(t)$ and the received echo voltage $g_H(t)$ in the transmission/reception experiment using the frequency band corresponding to the second harmonic frequency under the condition that FDA can be neglected. Furthermore, the mapping from the fundamental component $C_F(\omega)$ to the second harmonic component $C_H(\omega)$ in the frequency domain is defined as follows:

$$C_H(w) = M_{conv}(C_F(w)). \tag{3}$$

In addition, the inverse mapping is also defined as follows:

$$C_F(w) = M_{inv}(C_H(w)). \tag{4}$$

http://dx.doi.org/10.5772/intechopen.74577

These mapping functions can simply be determined by scaling and shifting the corresponding components on the frequency axis. The scale factor between $C_F(\omega)$ and $C_H(\omega)$ is not important, as it is only intended to reduce the distortion of the spectral shape.

Using these definition and the harmonic pressure $f_H(t)$ generated in the tissue and returned to the transducer, the transmission signal that compensates for the transducer characteristic signal $S_H(\omega)$ can be generated as follows:

$$S_H(w) = R_F(w)M_{inv}(R_H(w)F_H(w)). \tag{5}$$

As the transmitted fundamental pulse propagates toward the ROI, harmonics are gradually generated, and such a detailed process is ignored in the derivation of the above equation. To generate the time signal $s_H(t)$ corresponding to $S_H(\omega)$, it is necessary to perform somewhat complicated experiments. Instead of the experiments, it is realistic to calculate transducer characteristics by simulating exactly the material and structure of the transducer. In this study, we determine the distortion functions $R_F(\omega)$ and $R_H(\omega)$ by simulations. Details of the simulation procedure are described in Section 3. **Figure 3** shows the results of the transducer

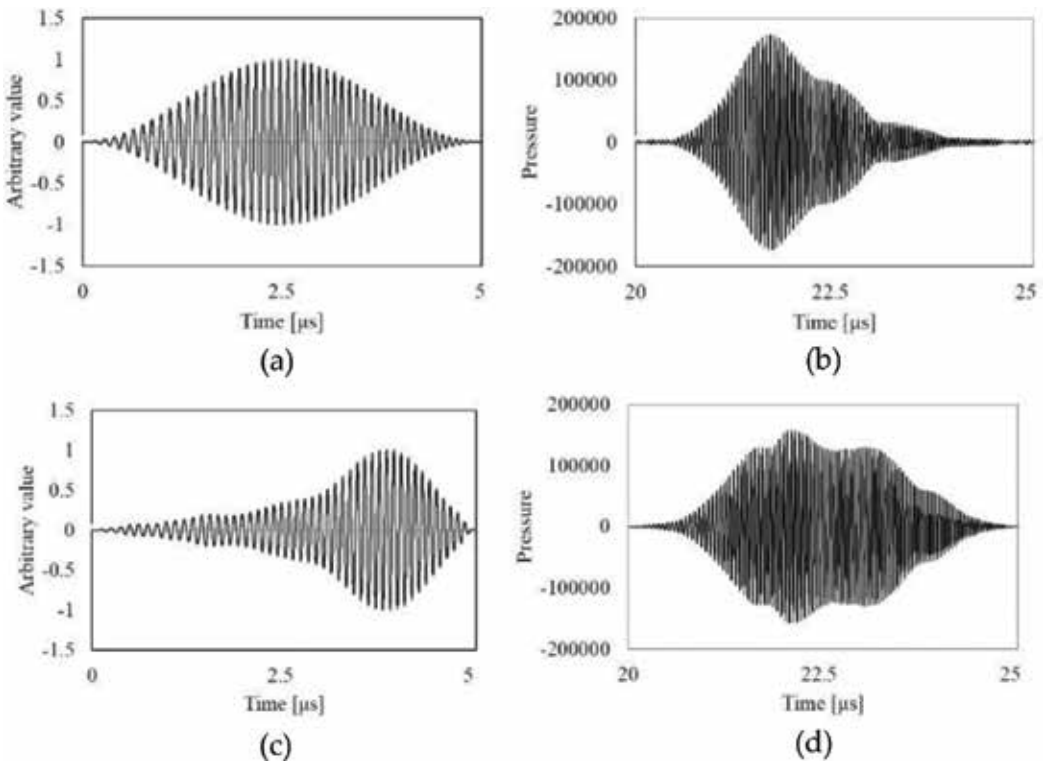

Figure 3. Simulation results of transducer characteristic compensation. Ideal FM chirp signal shown in (a) is applied to transducer, and second harmonic echo in (b) is received without attenuation in water. Signal that compensates for transducer characteristic which is determined by Eq. (5) is shown in (c), and corresponding second harmonic echo is shown in (d).

characteristic compensation. By comparing **Figure 3(b)** and **(d)**, it can be confirmed that the transducer characteristics are almost corrected.

2.2. FDA compensation

2.2.1. Method for fundamental component

FDA compensation can be performed basically in the same way as compensating the characteristics of the transducer. However, it is noted that the FDA compensation should be carried out for each region of interest (ROI) that is required to be finely imaged. To estimate the distortion characteristics caused by FDA in the propagation medium, as a reference transmission for investigation, we transmit $s_F(t)$ defined by Eq. (2) representing a frequency representation, which already compensates for the characteristics of the transducer in the fundamental band, with focusing on the ROI, and we receive the echo signal $e_F(t)$ as voltage. In this study, we assume that the FDA affects the amplitude of the echo signal and that the phase is unaffected. Therefore, the fundamental distortion function of the FDA for the fundamental component $R_{FFDA}(\omega)$ is defined as.

$$R_{FFDA}(w) = \frac{H_F(w)}{E_F(w)}. \tag{6}$$

By using this, the transmission signal $S_{Fcmp}(\omega)$ suitable for compensating the FDA in the fundamental band can be determined as follows:

$$S_{Fcmp}(w) = |R_{FFDA}|S_F(w). \tag{7}$$

The definition of $R_{FFDA}(\omega)$ in Eq. (6) is an ideal formation, and its actual estimate is described in Section 3.4. Therefore, in our previous study [12], the generation of $S_{Fcmp}(\omega)$ is iteratively done, but we confirmed that the FDA can be compensated almost at once [13]. In the following simulations and experiments, the compensation is done with only one reference transmission/reception.

2.2.2. Method for harmonic component

We transmit $s_H(t)$ corresponding to Eq. (5) and receive the corresponding second harmonic echo $e_H(t)$; the second harmonic distortion function of FDA is defined in the same way as in Eq. (6):

$$R_{HFDA}(w) = \frac{H_H(w)}{E_H(w)}. \tag{8}$$

Therefore, the transmission signal $S_{Hcmp}(\omega)$ that compensates for the FDA in the second harmonic band can be determined as follows:

$$S_{Hcmp}(w) = |R_{FFDA}(w)|M_{inv}(|R_{HFDA}(w)|M_{conv}(S_H(w))). \tag{9}$$

It should be noted that the FDA within the fundamental band only occurs in the outbound path from the transducer to the reflective target. However, since the scale factor as a constant

independent of the frequency does not affect the distortion of the waveform, $|R_{FFDA}(\omega)$ can be used in Eq. (10) without reducing it to half.

The amplitude-modulated FM chirp pulse $s_{Hcmp}(t)$ corresponding to $s_{Hcmp}(\omega)$ is transmitted, and then its echo that is expected to have no FDA distortion is used for imaging. Instead of the proposed modification of the transmission pulse, you can amplify the echo and easily reduce the FDA distortion. However, in this case, the SNR is drastically lowered particularly at the high-frequency portion, and the imaging quality is lowered.

3. Simulations

3.1. Simulation condition for transducer characteristic compensation

The simulations in this study were performed using PZFlex (Weidlinger Associates, Inc.), which is a standard finite element method (FEM) simulator for ultrasound propagation and piezoelectric analysis. A two-dimensional simulation model for determining a transmission signal that compensates transducer characteristics is shown in **Figure 4**. A linear array transducer having 64 oscillating elements of PZT was assumed, and an iron plate was used as a reflector. Parameters of the transmission signal is shown in **Table 1**. To evaluate the characteristics of the transducer purely, FDA should not occur, so the attenuation coefficient of water is set to 0 dB/cm/MHz. The transmission pulse is focused on the front face of the iron plate. The characteristics of the transducer and the signal compensating for it can be confirmed from the simulation results already shown in **Figure 3** in Section 2.1.2.

3.2. Definition of FDA model

In the PZFlex, the definition of FDA is represented as

$$\text{FDA} = d\left(f_c/f_d\right)^n \left[\frac{\text{dB}}{\text{cm}}\right], \tag{10}$$

where d is the in vivo attenuation coefficient, f_c is the center frequency, f_d is the measurement frequency, and n is the exponent of FDA. Through the simulations assuming tissue with FDA modeled by logarithmic linear characteristic, namely, n = 1, we confirmed that this model is effective [12]. However, a living body generally has logarithmic nonlinear characteristics. Therefore, we experimentally measured the value of n for a phantom mimicking living tissue, and as a result, n = 1.6 was obtained, and this value is used in the following simulations.

3.3. Simulation condition for FDA compensation

It is necessary to confirm the effectiveness of our method under medical usage condition assuming a living body. Since it is difficult to verify such effectiveness from the beginning through experiments, two-dimensional FEM simulations were performed using a model shown in **Figure 5** in which the propagation medium imitates the liver and the object corresponds to a tumor. Transmission pulses are formed in the same way as the simulations in

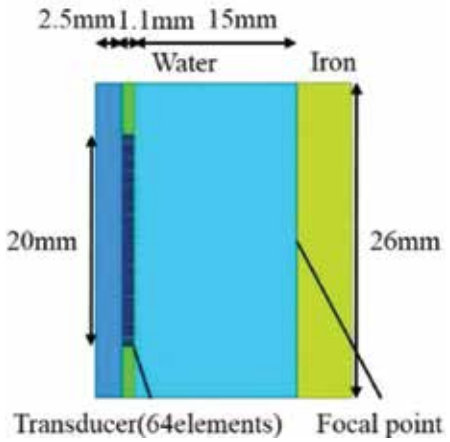

Figure 4. Simulation model for compensating transducer characteristics.

Type of transmission signal	FM chirp with Hanning window
Center frequency [MHz]	10
Frequency bandwidth [MHz]	4
Pulse duration [μm]	5
Focus of transducer [mm]	15
Sampling frequency [MHz]	500
Transmission voltage [V]	40
Number of oscillator elements	64

Table 1. Measurement condition in simulations.

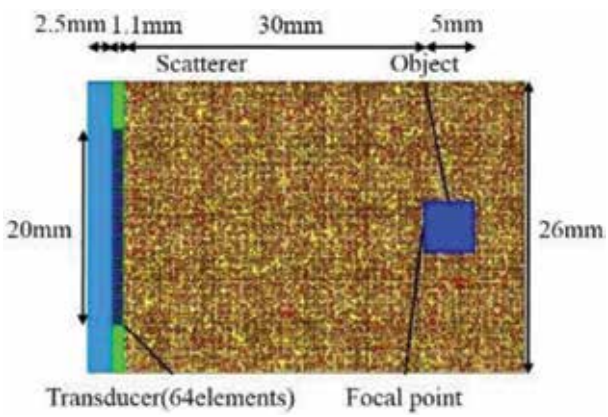

Figure 5. Simulation model for FDA compensation.

Section 3.1 and are focused on 30 mm away from the transducer, i.e., on the front of the target object. Parameters of the transmission signal are also the same as in **Table 1** in Section 3.1. The medium in **Figure 5** consists of scatterers that can mimic the speckle patterns of the liver. Sound speed, density, and attenuation coefficient of each scatterer are randomly defined within the range of **Table 2**. The blue object shown in **Figure 5** mimics the tumor, and its properties are also shown in **Table 2**. We simulate the echoes reflected from the front of the object and analyze them.

3.4. Results of harmonic FDA compensation

The absolute values of R_{FFDA} in Eq. (6) and R_{HFDA} in Eq. (8) must be estimated from the reference echo received by transmitting the FM chirp pulse in Eq. (5) that compensates for the transducer characteristics in order to generate the transmission signal $s_{Hcmp}(t)$ corresponding to Eq. (6), which can compensate for the FDA in the second harmonic band. The dashed line in **Figure 6** is an example of the logarithm of $|R_{FFDA}|$ that was measured by the simulation. From the figure we can know that $|R_{FFDA}|$ is distorted at the high-frequency part and there are several small ripple patterns, which may not be FDA characteristics and may indicate the characteristics of the reflection process and the propagation medium. Therefore, in the actual procedure, the observed $|R_{FFDA}|$ should be approximated by function fitting as a smooth function $|R_{FFDA}|^*$. **Figure 6(a)** shows a linear approximation by line fitting of the log of $|R_{FFDA}|$, and **Figure 6(b)** shows a nonlinear approximation by fifth-order polynomial curve fitting. In actual use, the optimal order of the polynomial function should be determined using appropriate criteria, but in the following

Medium	Sound speed [m/s]	Density [kg/m^3]	Attenuation coefficient [dB/cm/MHz]	Nonlinear parameter [B/A]
Liver	1560–1590	1050–1070	0.75–0.95	6.75
Tumor	1900	2500	0.6	7.00

Table 2. Various parameters in simulation model mimicking the liver and tumor.

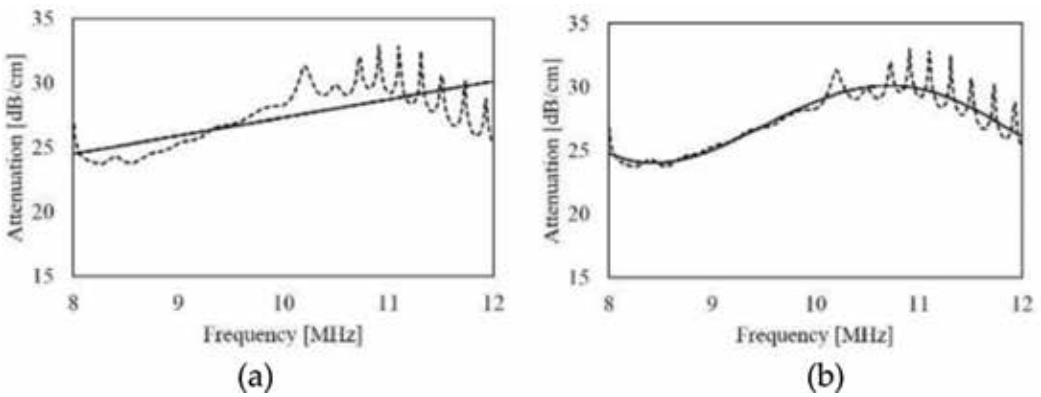

Figure 6. Logarithm of $|R_{FFDA}|$ measured by simulations (dashed line) and its approximations $|R_{FFDA}|^*$ with (a) line fitting and with (b) fifth-order polynomial function fitting (solid line).

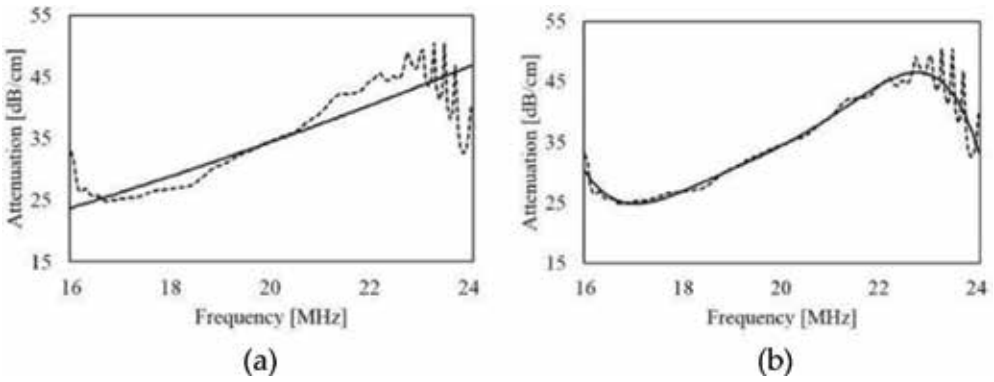

Figure 7. Logarithm of $|R_{HFDA}|$ measured by simulations (dashed line) and its approximations $|R_{HFDA}|^*$ with (a) line fitting and with (b) fifth-order polynomial function fitting (solid line).

simulations and experiments, we compare the performance of line fitting and fifth-order polynomial function fitting. Similarly, the results of R_{HFDA} are shown in **Figure 7**. Comparing **Figures 6** and **7**, it is obvious that the frequency dependence of FDA is larger in the second harmonic band than in the fundamental band, which means that the distortion of the pulse compression echo is large in the second harmonic band, and hence the influence of FDA is very serious for harmonic imaging compared to fundamental imaging.

Figure 8(a) shows the second harmonic component of the echo from the object in **Figure 5** without FDA compensation, i.e., the echo corresponds to $s_H(t)$ which compensates only the transducer characteristics. The spectrum amplitude corresponding to **Figure 8(a)** is shown by the solid line in **Figure 8(b)**. It can be seen that the high-frequency band is greatly attenuated. **Figure 9(a)** is a harmonic echo obtained by transmitting $s_{Hcmp}(t)$ corresponding to Eq. (9) using $|R_{FFDA}|^*$ and $|R_{HFDA}|^*$ approximated by line fitting. The spectrum amplitude is shown in **Figure 9(b)**. **Figure 10** shows the results corresponding to the approximation by fifth-order polynomial function fitting of $|R_{FFDA}|^*$ and $|R_{HFDA}|^*$. From **Figures 9** and **10**, it is confirmed

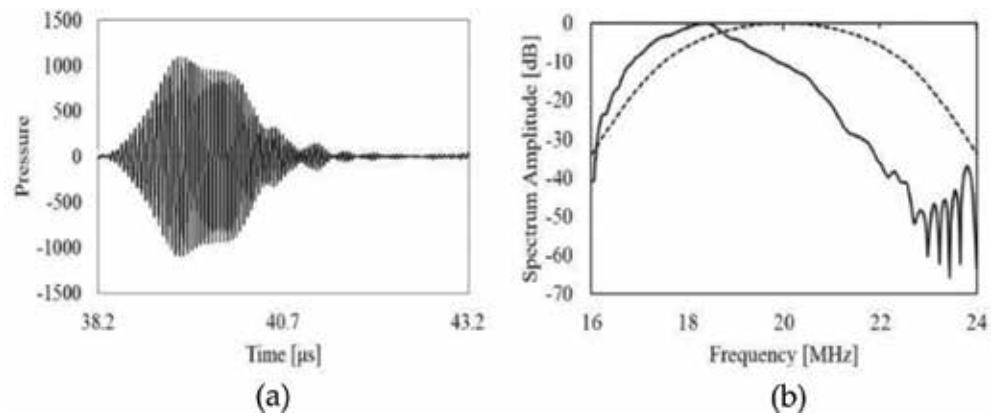

Figure 8. Second harmonic echo obtained by simulation without FDA compensation is shown in (a), and its spectrum amplitude is shown in (b) as solid line with ideal amplitude as dashed line.

that our compensation method based on amplitude-modulated transmission can effectively avoid FDA especially for high-frequency parts. **Figure 11** shows the normalized envelope signals of compressed second harmonic echoes corresponding to **Figures 9(a)** and **10(a)**

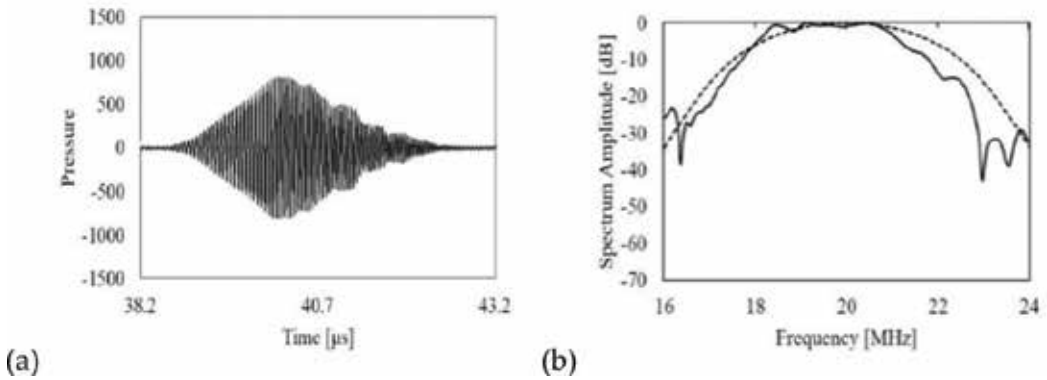

Figure 9. Second harmonic echo obtained by simulation with linear FDA approximation is shown in (a), and its spectrum amplitude is shown in (b) as solid line with ideal amplitude as dashed line.

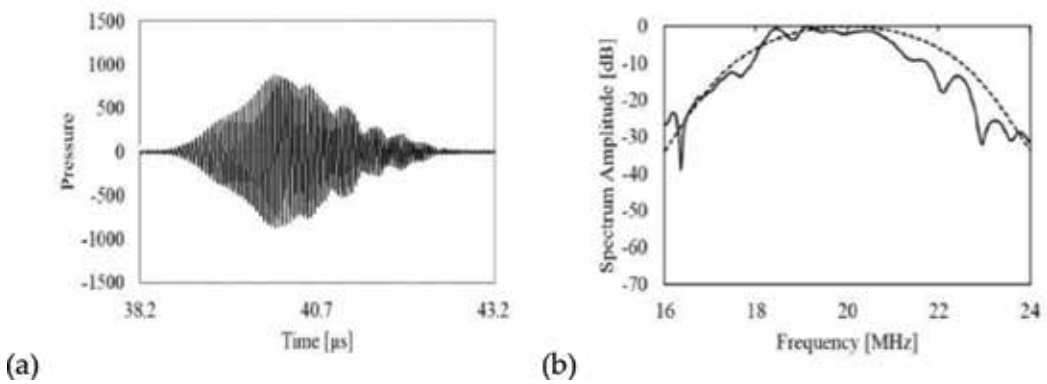

Figure 10. Second harmonic echo obtained by simulation with nonlinear FDA approximation is shown in (a), and its spectrum amplitude is shown in (b) as solid line with ideal amplitude as dashed line.

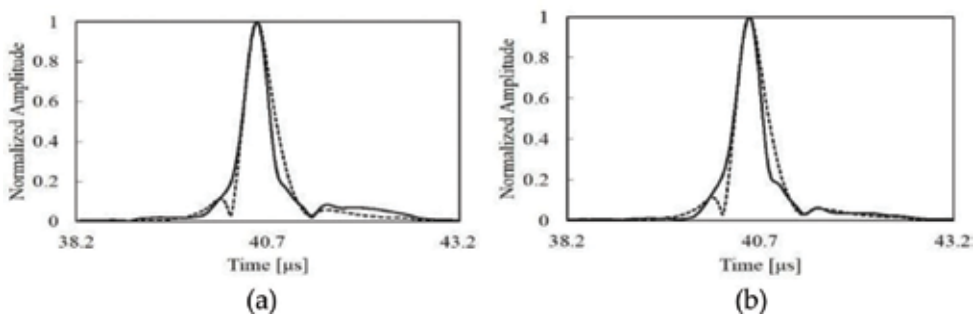

Figure 11. Normalized envelope signal of compressed second harmonic echo obtained by simulation before FDA compensation (dashed line) and after FDA compensation (solid line): (a) with linear FDA approximation and (b) with nonlinear FDA approximation.

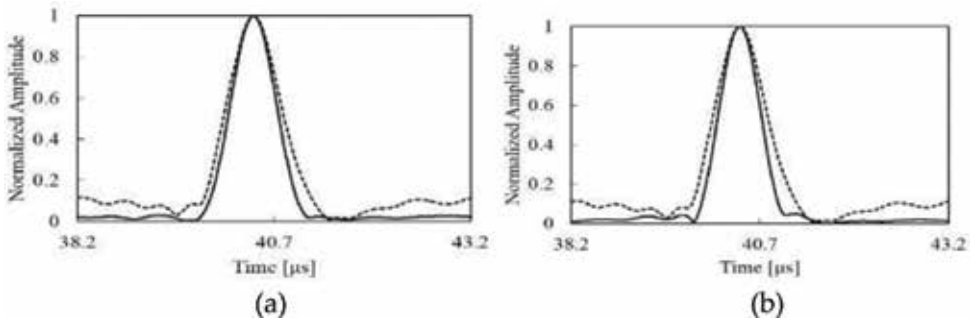

Figure 12. Normalized envelope signal of compressed fundamental echo obtained by simulation before FDA compensation (dashed line) and after FDA compensation (solid line): (a) with linear FDA approximation and (b) with nonlinear FDA approximation.

respectively. The −3 dB pulse width before FDA compensation is 0.442 μs and the −3 dB pulse width after FDA compensation is 0.378 μs with linear approximation and 0.374 μs with nonlinear approximation. The envelope signals of the fundamental echo corresponding to the same transmission of $s_{Hcmp}(t)$ are shown in **Figure 12**. The optimal transmission for compensating FDA in the fundamental band is $s_{Fcmp}(t)$ defined in Eq. (7), but $s_{Hcmp}(t)$ is sufficiently effective against the fundamental FDA compensation.

4. Experiments

4.1. Experimental setup

In order to confirm the actual effectiveness of our FDA compensation, we conducted simple experiments using the experimental system shown in **Figure 13(a)**. The transducer used in the experiments shown in **Figure 13(b)** is SONIX ISI506R having a center frequency of 5 MHz. The amplifier is Amplifier Research 50A15, the function generator is Tektronix APG3102, and the oscilloscope is IWATSU DS-5552. A linear FM chirp signal was transmitted toward the iron

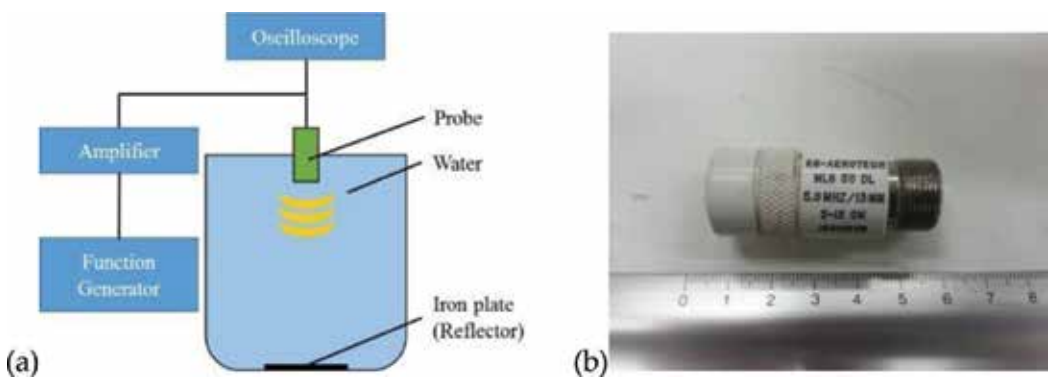

Figure 13. Experimental system is constructed as (a), and (b) indicates probe used in this system.

Type of transmission signal	FM chirp with Hanning window
Center frequency [MHz]	7.5
Frequency bandwidth [MHz]	3
Pulse duration [μm]	10
Focus of transducer [mm]	15
Sampling frequency [MHz]	500
Transmission voltage [V]	40

Table 3. Measurement condition in experiments.

plate placed 15 cm away from the transducer, and the echo reflected from the iron plate was observed. The measurement conditions are shown in **Table 3**. Experimental verification of the characteristics of the transducer can be realized by measurement of transmitted sound pressure in water by a hydrophone. In this issue, we focused on confirming the effect of FDA compensation and conducted experiments using frequency bands with relatively flat transducer characteristics. Hence, in the experiments, the characteristics of the transducer were not taken into account, and only the FDA of water was compensated. That is, instead of $S_H(\omega)$ in Eq. (10), an ideal FM chirp was used to generate a signal to be transmitted.

4.2. Experimental results

In this section, the experimental results of our method for compensating FDA in the second harmonic band caused by water corresponding to a sufficient propagating distance are shown. **Figure 14(a)** shows the experimentally measured echo reflected from the iron plate without FDA compensation. **Figure 14(b)** shows the second harmonic echo extracted from the whole echo of **Figure 14(a)**, and its spectrum amplitude is shown in **Figure 14(c)**. In the high-frequency part in **Figure 14(c)**, the FDA of the second harmonic component is seen. By transmitting a reference signal and estimating $|R_{FFDA}|^*$ and $|R_{HFDA}|^*$ using nonlinear polynomial function fitting, the FDA in the second harmonic band can be compensated. **Figure 15(a)** shows the entire echo with FDA compensation, and the harmonic component and its spectrum amplitude are shown in **Figure 15(b)** and **(c)**, respectively. By comparing **Figures 14(c)** and **15(c)**, the FDA compensation at the high-frequency part can be confirmed, although the FDA is not so large in this experiment. The reason why the FDA is smaller in the experiment than in the simulation

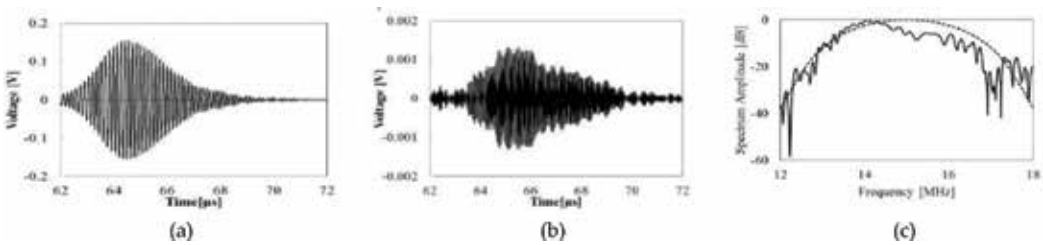

Figure 14. Experimentally received echo without FDA compensation: (a) whole echo, (b) harmonic echo extracted from (a), and (c) spectrum amplitude shown as solid line (ideal amplitude is indicated as dashed line).

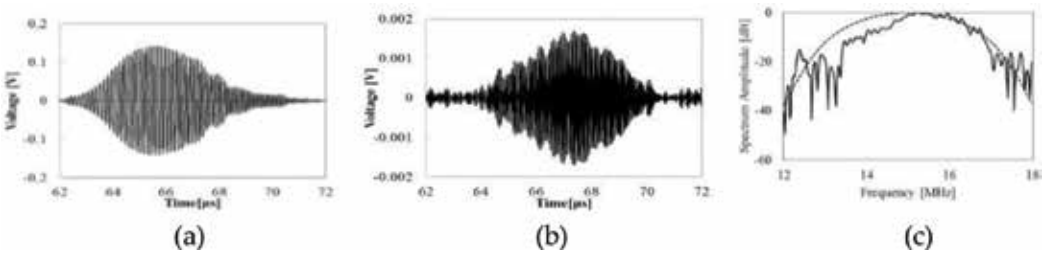

Figure 15. Experimentally received echo with FDA compensation using nonlinear approximation: (a) whole echo, (b) harmonic echo extracted from (a), and (c) spectrum amplitude shown as solid line (ideal amplitude is indicated as dashed line).

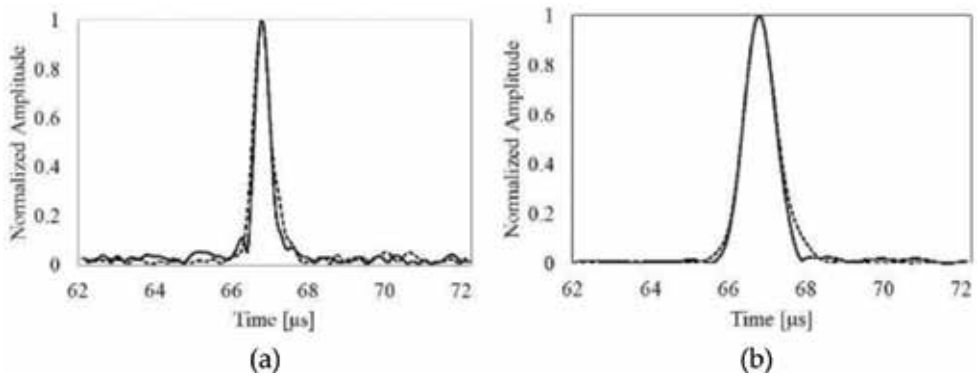

Figure 16. Experimentally obtained envelope signal of compressed echo before FDA compensation (dashed line) and after FDA compensation (solid line): (a) second harmonic one and (b) fundamental one.

is that the water attenuation is considered to be smaller than that in the living body. Therefore, in the future study, we need to use a more attenuated propagation medium that imitates living tissue for experiments. **Figure 16** shows the normalized envelopes of the compressed echo signals before and after FDA compensation. In addition to the second harmonic component in **Figure 16(a)**, the fundamental one is also shown in **Figure 16(b)**. For both the second harmonic component and the fundamental component, the FDA compensation is actually effective.

5. Conclusions

In this study, we proposed a novel and simple method for FDA compensation to realize the fine THI, which can also compensate transducer characteristics. Its effectiveness was confirmed by two-dimensional simulations using a model imitating liver and tumor and by simple experiments. Our method is based on FM chirp pulse compression to realize high SNR, and we expect that fine imaging is effectively performed in a local manner by setting a ROI determined by preimaging by conventional B-mode imaging. In this study, investigation of FDA characteristics is assumed to be performed locally by transmitting a reference signal

and receiving its echo position to be finely imaged. However, it can be considered that such FDA characteristics are invariant in the tissue region having uniform characteristics. This indicates that it is possible to reduce the number of transmission and reception for reference and it becomes easy to obtain the whole high-definition imaging. In the future, we will examine such an extended method and conduct the experiments using a phantom that imitates a living body and also the experiments on living tissue.

In the research field of ultrasound harmonic imaging, mainly the method of extracting the harmonic component appropriately from the echo [16] and the technique to increase the noise resistance of the harmonic component [11] are extensively examined. As sound pressure is higher, large harmonic components are generated, so sharp transmission pulses are generally used in many studies in general. In our study, from the viewpoint of using more energy, we aim to improve the SNR of the harmonic components by using FM chirp pulses, and FDA compensation is important for PCT in order to avoid deterioration of the waveform after compression processing. We are studying a method to enable super resolution by multiple transmission and reception with different carrier frequencies [17], and FDA compensation is also important for applying this method to harmonic components.

Acknowledgements

A part of this work was supported by JSPS KAKENHI Grant Number 25350569.

Author details

Norio Tagawa[1]*, Takuya Hiraoka[1] and Iwaki Akiyama[2]

*Address all correspondence to: tagawa@tmu.ac.jp

1 Faculty of Systems Design, Tokyo Metropolitan University, Tokyo, Japan

2 Doshisha University, Kyoto, Japan

References

[1] Irie T, Hasegawa T, Sato M, Tagawa N, Tanabe M, Yoshizawa M, Iijima T, Moriya T, Itoh K. Transmission of 100-MHz-range ultrasound through a fused quartz fiber. In: Proceeding of IEEE Int. Ultrasonics Symp. 2012. pp. 358-361

[2] Irie T, Hasegawa T, Itoh K, Hirota N, Tagawa N, Yoshizawa M, Moriya T, Iijima T. Tissue imaging using the transmission of 100-Mhz-range ultrasound through a fused quartz fiber. In: Proceeding of IEEE Int. Ultrasonics Symp. 2013. pp. 2010-2013

[3] Irie T, Tagawa N, Yoshizawa M, Moriya T. A study for B-mode imaging using 100-MHz-range ultrasound through a fused quartz fiber. In: Proceeding of IEEE Int. Ultrasonics Symp., CD. 2015

[4] Chiao RY, Hao X. Coded excitation for diagnostic ultrasound: A system developer's perspective. IEEE Transactions on Ultrasonics, Ferroelectrics, and Frequency Control. 2005;**52**:160-170

[5] Hu Z, Moriya T, Tanahashi Y. Imaging system for intravascular ultrasonography using pulse compression technique. Japanese Journal of Applied Physics. 2001;**40**:3896-3899

[6] Misaridis T, Jensen JA. Use of modulated excitation signals in medical ultrasound. IEEE Transactions on Ultrasonics, Ferroelectrics, and Frequency Control. 2005;**52**:177-192

[7] Akiyama I, Yoshizumi N, Saito S, Wada Y, Koyama D, Nakamura K. Development of multiple-frequency ultrasonic imaging system using multiple resonance piezoelectric transducer. Japanese Journal of Applied Physics. 2012;**51**:07GF02-1-07GF02-9

[8] Ishiguro Y, Zhu J, Okubo T, Tagawa N, Okubo K. Piezoelectric characteristic analysis of diaphragm type PZT oscillator. In: Proceeding of IEEE Int. Ultrasonics Symp. CD. 2016

[9] Frijlink ME, Goertz DE, van Damme CA, Krams R, van der Steen AFW. Intravascular ultrasound tissue harmonic imaging in vivo. IEEE Transactions on Ultrasonics, Ferroelectrics, and Frequency Control. 2006;**53**:1844-1852

[10] Szabo TL. Diagnostic Ultrasound Imaging: Inside Out, Chap. 4. Elsevier; 2004

[11] Yamamura T, Tanabe M, Okubo K, Tagawa N. A method for improving signal-to-noise ratio of tissue harmonic imaging based on Bayesian inference using information of fundamental echoes. Japanese Journal of Applied Physics. 2012;**51**:07GF01-1-07GF01-12

[12] Koumoto K, Tagawa N, Okubo K, Akiyama I. Wide band pulse compression imaging with transmission compensation for frequency dependent attenuation In: Proceeding of IEEE Int. Ultrasonics Symp 2012. pp. 1658-1661

[13] Hiraoka T, Tagawa N, Okubo K, Akiyama I. Recursive reduction of frequency dependent attenuation for wide-band ultrasound imaging in a living body. In: Proceeding of IEEE Int. Ultrasonics Symp. 2013. pp. 914-917

[14] Hiraoka T, Tagawa N, Okubo K, Akiyama I. Compensation method of frequency dependent attenuation for tissue harmonic imaging. In: Proceeding of IEEE Int. Ultrasonics Symp., CD. 2014

[15] Levanon N, Mozeson E. Radar Signals. Wiley Inter-science; 2004

[16] Hasegawa H, Tanaka H, Takezaki T, Machida S. Amplitude modulated pulse inversion technique for high SNR of tissue harmonic imaging using CMUT. In: Proceeding of IEEE Int. Ultrasonics Symp. CD. 2017

[17] Wada T, Ho Y, Okubo K, Tagawa N, Hirose Y. High frame rate super resolution imaging based on ultrasound synthetic aperture scheme. Physics Procedia. 2015;**70**:1216-1220

Chapter 2

Cancelling Harmonic Power Line Interference in Biopotentials

Țarălungă Dragoș Daniel and
Mihaela Neagu (Ungureanu)

Additional information is available at the end of the chapter

http://dx.doi.org/10.5772/intechopen.74579

Abstract

Biopotential signals, like the electrocardiogram (ECG), electroencephalogram (EEG), electromyogram (EMG), and so on, contain vital information about the health state of human body. The morphology and time/frequency parameters of the biopotentials are of interest when diagnostic information is extracted and analyzed. The powerline interference (PLI), with the fundamental PLI component of 50 Hz/60 Hz and its harmonics, is one of the most disturbing noise sources in biopotential recordings that hampers the analysis of the electrical signals generated by the human body. The aim of this chapter is to review the existing methods to eliminate harmonics PLI from biopotential signals and to analyze the distortion introduced by some of the most basic approaches for PLI cancelation and whether this distortion affects the diagnostic performance in biopotentials investigations.

Keywords: biopotentials, power line interference, harmonics, diagnostic

1. Introduction

At the cellular level, the movement of ions like K^+, Na^+, Ca^{2+} and Cl^- determines the presence of biopotentials at the level of the cellular membrane. When a stimulus arrives on the membrane, an action potential is generated and is transmitted to the neighboring cells, spreading within the entire tissue or just within some parts of the tissue, depending on the presence of inhibitory channels. At the macroscopic level, the sums of all the action potentials generate a biopotential. By placing electrodes on the human body, in specific configurations, a projection of the investigated biopotentials on the measurement direction may be recorded. Basically,

every human body tissue has associated an electromagnetic field, which can be theoretically measured. However, usually the biopotentials have a very low power (amplitude of μV), thus just a few can be recorded: the electrical activity generated by the cardiac tissue, the electrocardiogram (ECG), by the brain, the electroencephalogram (EEG), by the skeletal muscles, the electromyogram (EMG), by the uterus, electrohysterogram (EHG), by the retina, the electroretinogram (ERG), by the stomach muscles, the electrogastrogram (EGG), by the fetal cardiac tissue, the fetal electrocardiogram (fECG), and so on. All these signals contain diagnostic information about the health status of the source tissue, which can be extracted by applying different signal processing methods.

Nevertheless, the raw signals recorded after the measurement cannot be used directly to evaluate the health status of the source tissue because it contains also noise, which in most of the cases hampers the extraction of diagnostic information. The disturbing biopotentials (e.g., when the fECG analysis is of interest, the mECG, which is also recorded, represents a noise source and has to be eliminated) or other noise sources like electronic noise (thermal noise, shot noise, flicker noise) and power line interference have to be canceled/diminished. The latter is one of the most common types of noise in biopotential recordings, and its efficient cancelation is still an open question in biomedical signal processing. Therefore, the optimal elimination of the noise sources is critical since any residual or disturbance introduced by the cancelation method can impair the diagnostic information and could lead to a wrong diagnostic.

Thus, in this chapter, a review of the principal methods for removing PLI from biopotentials is introduced. Also, a case study reveals the influence on the diagnostic parameters of the most common PLI cancelation methods applied in ECG analysis. The chapter has the following sections:

- Sources of the PLI and its harmonics—this section presents the most common sources of the PLI and the ways it usually interferes with biopotential measurements.
- Methods for canceling PLI and its harmonics—this section includes a review of the recent methods for PLI removal from biopotentials.
- The influence of bandstop filters on the diagnostic parameters of the ECG signals—this section describes the morphological parameters of the ECG signal which are used to make a diagnostic, the filters used, the data considered and the results obtained.

2. Sources of the PLI and its harmonics

The PLI is generated by the alternative 50/60 Hz sinusoidal current from the power grid. However, the PLI has also hamonics due to the fact that the PLI is in most of the cases non-sinusoidal. This is caused usually by the so-called "non-linear" loads connected to the power grid.

A load which draws a proportional current with the applied voltage is considered to be linear (e.g., loads that are purely resistive or that are simple combinations of pure resistance, inductance or capacitance). They do not change the shape of the waveform current but may change the phase between the current and the applied voltage.

On the other hand, nonlinear loads draw non-sinusoidal current even when sinusoidal voltage is applied (**Figure 1**). Thus, nonlinear loads change the shape of the current waveform from a sine wave to some other form and create harmonic currents in addition to the original (fundamental frequency) AC current. In turn, these harmonic currents will cause harmonic voltages to be generated. According to the IEEE 519-2014, the harmonic is a sinusoidal component of a periodic wave or quantity having a frequency that is an integral multiple of the fundamental frequency or a component of order greater than one of the Fourier series of a periodic quantity [1].

The main nonlinear loads consist of the static power converters (rectifiers, **Figure 2**) that are used in switch-mode power supplies, uninterruptable power supplies, and so on. Thus, fluorescent lamps, medical devices, personal computers, induction motors, and so on represent nonlinear loads connected to the power grid and sources of harmonics [2, 3].

Moreover, it seems that some harmonics have a greater impact than others. For example, the third harmonic is probably the most challenging one in terms of neutral conductor loading within a three-phase system (the most common method used by electric power distribution grids worldwide to distribute power). However, other harmonics currents cancel each other out in the neutral point (like normal 50 Hz load current), third harmonics are in phase with each other, and the summing in the neutral conductor significantly increases the current [4].

There are different ways in which the PLI interferes with the biopotential recordings [5]:

- *Magnetic induction*: the cables used for biopotential recordings can form a loop, and if a variable magnetic field is present, then a potential will be induced in the leads which is proportional with the area and orientation of the loop, and the magnitude of the magnetic field.
- *Displacement current into recording leads*: by capacitive coupling between the AC power line and the leads, a current is induced in the recording leads, which is called displacement current. The latter disturbs the recording just if the impedances of the electrode-skin interfaces are different, because in this case, the "potential divider effect" appears, that is, common mode interference is converted into differential mode interference voltage which

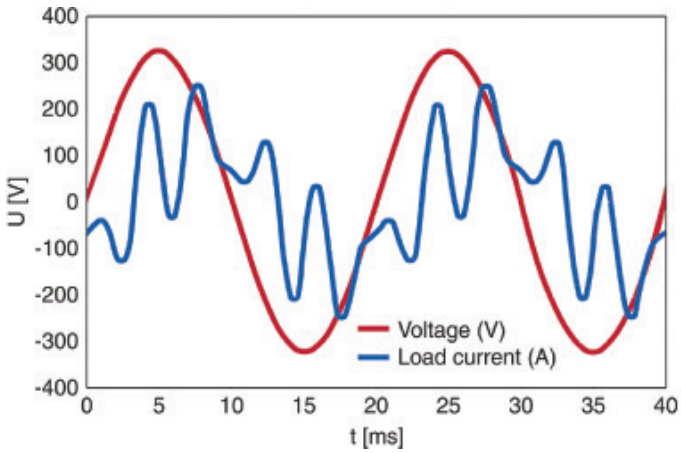

Figure 1. The sinusoidal voltage and the current generated by a nonlinear load.

is amplified. In this case, not even an instrumentation amplifier with infinitely high common mode rejection ratio (CMRR) will make any difference.

- *Displacement current into the body*: because of parasitic capacities, the body is capacitive coupled with the AC power lines. The displacement current travels through the body to the ground and because the body has impedance, a voltage drop will appear. Hence at different locations on the body, the induced potential is at slightly different values which in turn are amplified by the instrumentation amplifier.

In **Figure 3**, a schematic representation of the way the displacement currents are induced in the measurement setup is illustrated.

Empirical solutions can be applied in order to reduce the amount of PLI and its harmonics present in the biopotential measurements: twisting the recording leads will reduce the area between them, and thus the induced current from the variable magnetic field is much smaller; the preparation of the skin before attaching the electrode is going to reduce and balance the electrode-skin impedance so that the difference between the two impedances is as small as possible; movement of the ground electrode, and so on.

However, in spite of all the precautions taken before measuring, the PLI is still going to interfere with the recorded biopotentials. Nevertheless, because most of the biopotentials have low power, any PLI disturbance, even if much attenuated by different approaches, will impair the analysis of the diagnostic information.

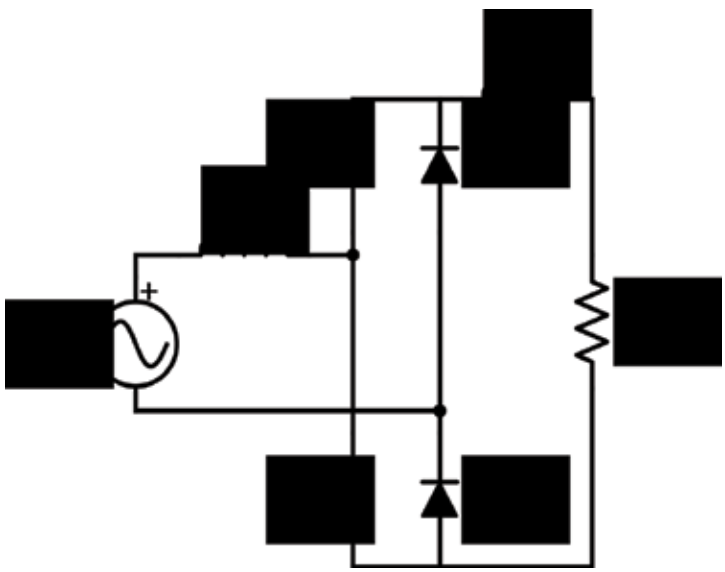

Figure 2. A load containing an inductance (L_{dc}) and a resistance (R_{dc}) is supplied from a single-phase full wave diode bridge rectifier.

http://dx.doi.org/10.5772/intechopen.74579

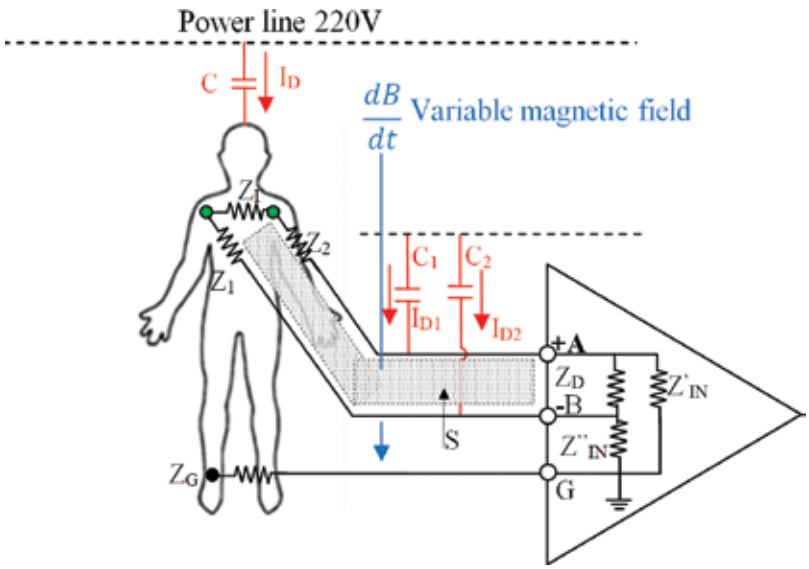

Figure 3. Capacitive coupling between the power line and the measurement leads and the human body: I_D—the displacement current in the human body; C—coupling capacity between the power line and the human body; I_{D1}, I_{D2}—the displacement current in the measurement leads; Z_I—the impedance of the human body between the two electrodes; Z_1, Z_2—the impedance of the electrodes; Z_G—the impedance of the ground electrode; Z_D—the differential input impedance of the instrumentation amplifier; Z_{IN}—the input impedance of the instrumentation amplifier; C_1, C_2—the coupling capacities between the power line and the measurement leads; S—the area described by the measurement leads.

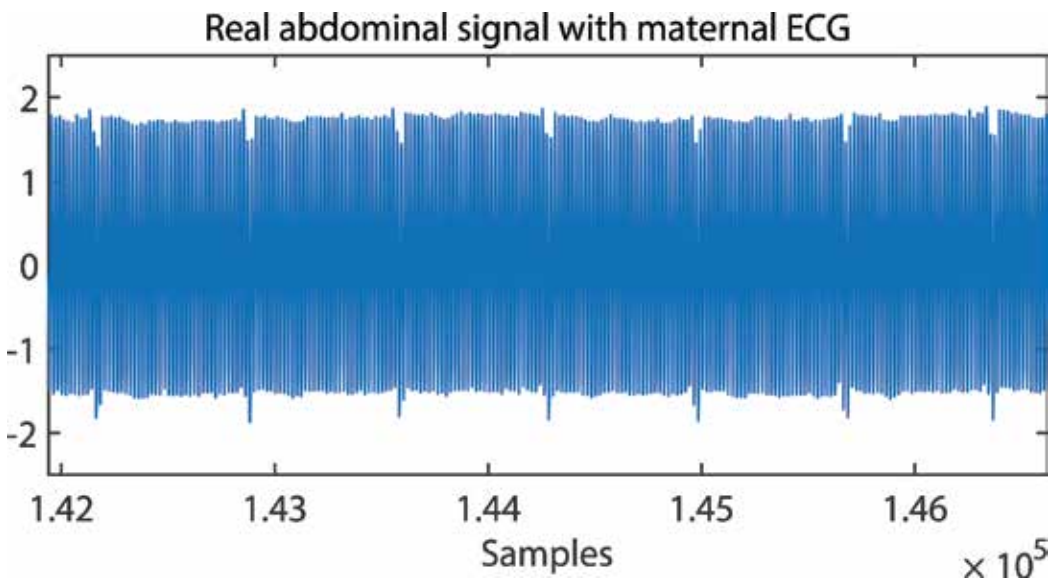

Figure 4. Abdominal recorded signal with strong PLI contamination.

In **Figure 4**, a real measurement of biopotentials recorded on the abdomen of a pregnant woman is depicted. By visual inspection, it can be observed that only the PLI and its harmonics are visible.

3. PLI and harmonic cancelation methods

The main problem when considering removing the PLI is that the frequency bandwidths of the biopotentials include the 50/60 Hz fundamental frequency and also the third harmonic (**Figure 5**). Thus, the method for PLI cancelation should ideally not remove useful information too.

There are many approaches for removing PLI and harmonics from biopotential measurements. The most common hardware solutions mainly consist of implementing hardware notch filters [6]. Another common hardware approach is the right leg driven (DLR) circuit [7], which is used to reduce the common mode interferences. A recent paper proposes a new version of the classical DLR circuit, reporting an improvement of 30 dB in reducing the PLI [8]. However, recent studies suggest that this approach can increase actually, in some situations, the interference [9].

In this chapter, we focus on software methods for PLI and harmonics removal. The main software methods for PLI cancelation are: (1) band stop digital filters; (2) fixed—frequency notch filters; (3) neural networks; (4) adaptive filters; (5) blind source separation; (6) Kalman filters; (7) time-frequency processing of nonstationary signals (wavelet transform); (8) subtraction methods; (9) spectral Hampel filter; (10) time-frequency nonlinear analysis of nonstationary signals (empirical mode decomposition—EMD, Hilbert Huang Transform—HHT) [10].

In **Table 1**, a selection of recent contributions in PLI removing from biopotentials is introduced.

Loss of information can appear when the methods for PLI cancelation are applied. Thus, methods for information retrieval are also implemented. In [11], the authors apply the EMD

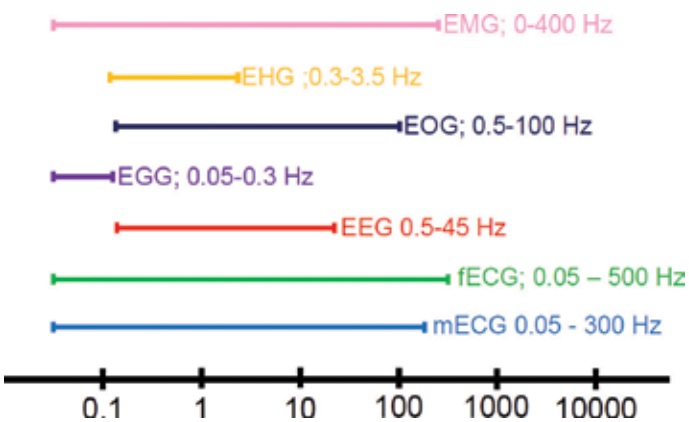

Figure 5. Frequency domain of different biopotentials.

Time-varying pole radius multiple notch filters			
Authors	**Year**	**Biopotentials**	**Observations**
Piskorowski [12]	2012	ECG	A time-varying pole radius multiple notch infinite impulse response (IIR) filter is introduced. The performance is evaluated on ECG signals and compared with traditional time-invariant notch filters. A significant reduction in transient time is reported in comparison with the traditional notch filters. The filter is evaluated also in [6] on removing the PLI from abdominal signals in order to extract the fECG showing a good performance: root mean square deviation (RMSD) of 2.11% and signal-to-noise ratio (SNR) improvement of 76 dB
Piskorowski [13]	2013	EMG	A modified version of the algorithm introduced in [14] is proposed by finding optimal nonzero initial conditions (based on vector projection algorithm) for reduction of transient time of IIR digital notch filters. The modification consists of choosing the length of the initial segment to cover the PLI fundamental frequency. The filter is applied on canceling the PLI from the EMG signals with good results
Rana et al. [15]	2017	ECG	Introduces a time varying pole-radius filter based on a hyperbolic tangent sigmoid function in order to achieve high-quality factor and short transient duration. The performance is assessed on PLI cancelation from ECG signal in the LabVIEW-based simulation reporting better results than similar approaches
a. Adaptive filters			
Wang et al. [16]	2017	–	Proposes an adaptive filter based on least mean square (LMS). In the first step, simplified all-pass filter is introduced to construct an IIR non-adaptive notch and then an adaptive LMS filter is applied. The performance is evaluated in different scenarios, also including up to three harmonics and it is compared with cascaded notch filters in multiple narrow bands interference suppression. This filter is not evaluated on biopotentials
Razzaq et al. [17]	2016	ECG	An adaptive filter for PLI and its harmonics suppression with no reference signal is proposed. It is based on recursive state space model and is evaluated on ECG signals. While good performance is reported, high computational complexity still remains an issue
Lin et al. [18]	2016	EEG	Introduces an adaptive framework for PLI removal from EEG signals when both the reference and the signal are contaminated with spike noise. M-estimation function is used for robustness of the adaptive filter to the influence of impulse components. Based on this approach, LMS and normalized LMS (NLMS) are extended to least mean M-estimate (LMM) and NLMM. The method is evaluated on the MIT-BIH Polysomnographic Database
Tomasini et al. [19]	2016	ECG, EMG	A wearable platform is described for biopotential acquisition with no PLI noise. The hardware platform is evaluated using digital notch filters, subtraction approach, sinusoidal modeling approach and adaptive filters [20]. The performance of PLI removal in real time. The lowest computational cost is achieved by the adaptive filter which requires only 36 μs at each sample
b. Wavelet transform			
Gallianno Merino et al. [21]	2013	EMG	Proposes a method which isolates the 50-Hz fundamental component and its harmonics using a shift invariant transform. Then the PLI is reconstructed using the Discrete Stationary Wavelet Packet Transform (DSWPT). The method is evaluated on both synthetic and real EMG signals and then it outperforms traditional band stop filters and adaptive filters. In a recent review [10], this PLI cancelation scheme was applied for removing PLI from abdominal signals in order to extract the fECG. It obtained the best results in two testing scenarios (PLI with fixed 50-Hz fundamental frequency, and with harmonics,

Time-varying pole radius multiple notch filters			
Authors	**Year**	**Biopotentials**	**Observations**
			respectively). However, it is not working when the PLI has time varying fundamental frequency [10]
c. EMD			
Pal et al. [11]	2012	ECG	The PLI is extracted from ECG recordings based on the fact that high-frequency components are isolated in the first obtained Intrinsec Mode Functions (IMF). Cumulative mean and the power of the IMFs are used to decide which IMFs component contains PLI. However, when the PLI has similar power as the signal of interest, the robustness of the method decreases.
d. Hybrid methods			
Suchetha et al. [22]	2013	ECG	Proposes an adaptive filter and subtraction scheme both based on EMD. The performance is evaluated on synthetic ECG signals and various noise levels (from 5 to 30%). The direct subtraction method based on EMD shows the best results
Taralunga et al. [23]	2015	fECG	An adaptive filter based on HHT is proposed. The internal generated PLI reference is obtained using the Hilbert Transform to identify the IMFs, obtained with EMD, which contains the PLI and its harmonics. This internal generated PLI reference is further used in the LMS adaptive filter. The method is evaluated on fECG signals contaminated with different PLI levels. It is also considered the scenario when the fundamental frequency is not fixed. High performance is reported in all scenario considered, preserving the morphology of the fECG
Jenkal et al. [24]	2016	ECG	The algorithm consists of three steps: first the signal is the decomposition with the Discrete Wavelet Transform (DWT); next an adaptive dual threshold filter (ADTF) is applied and finally a peak correction is applied for the ECG signal in order to compensate for possible information loss during the PLI removal. The performance is evaluated on a real ECG signal, which is contaminated with synthetic PLI
Warmerdam et al. [25]	2016	ECG	A fixed-lag Kalman smoother with adaptive noise estimation is proposed. The performance of the algorithm is analyzed on simulated and real signals and compared with the performance obtained by a fixed-bandwidth notch filter and some adaptive filters. A better SNR and transient time are reported
Mateo et al. [26]	2015	ECG, EEG	The authors introduce a radial basis function Wiener hybrid filter for removing the PLI from ECG and EEG recordings. Real signal is used, recorded from 100 subjects (adults and children). The PLI signal was simulated with a 50 Hz sinusoidal with the fundamental frequency varying from 48.5 Hz to 51.5 Hz. The proposed method outperforms the classical Wiener filter

Table 1. Contributions in the field of PLI removing from biopotentials in the last 5 years.

in order to decompose the ECG signal into intrinsic mode functions (IMFs). Then the IMFs that contain the PLI signal are discarded, and the signal is reconstructed. However, the ECG information is not isolated in one IMF and its high-frequency components, that is, the QRS complex can be present in the discarded IMFs. An approach to recover some lost information consists of identifying the IMFs that contain QRS complexes and the QRS complexes boundaries. Next, a Tukey window centered on the R peaks is applied which offers a flat gain for the R wave. Thus, the information of the QRS complex is preserved.

4. Case study: the influence of fixed-bandwidth notch filters on the diagnostic information in ECG signals

In this section, the most basic, simplest and common approaches for PLI and its harmonics removal from ECG recordings is evaluated. Mainly, the loss of diagnostic information in the process of PLI removal is analyzed. In order to achieve this objective, four types of traditional fixed frequency band stop filters and a time-varying pole radius multiple notch IIR filter [12] are implemented in MATLAB and tested on a real ECG database.

4.1. Diagnostic information in ECG signals

The ECG signal is generated by the electrical activity of the cardiac tissue. It reflects differences in transmembrane voltages in myocardial cells that occur during depolarization and repolarization within each cardiac cycle [26]. By placing a specific electrode configuration on the human body, a projection of this electrical activity on the measurement lead can be recorded. The electrode configuration can be both bipolar (the three bipolar Einthoven derivations) and unipolar (the three augmented derivations and the six precordial ones).

The ECG signal is depicted in **Figure 6** and mainly consists of five waves: P wave, Q wave, R wave, S wave and T wave and U wave. The P wave corresponds to the electrical depolarization of the atrial cardiac tissue. The ventricular contraction generates the QRS and the electrical repolarization of the ventricular tissue generates the T wave. The U wave most likely represents an electric-mechanical phenomenon that occurs after repolarization is completed [27]. In

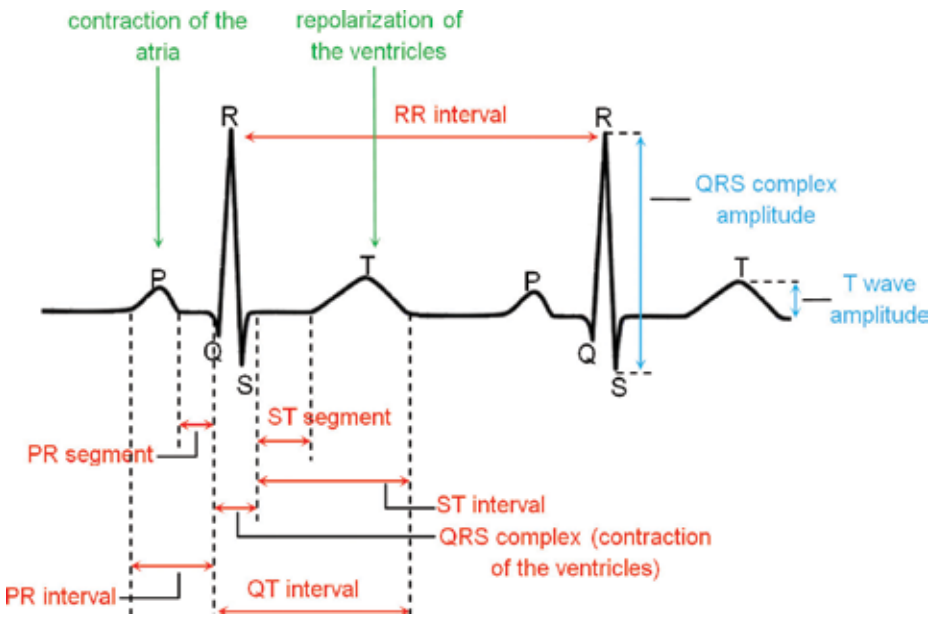

Figure 6. The waveforms, interval and segments of the ECG signal.

Figure 6, also the parameters of the ECG signal can be observed: the intervals (PR, QT, ST) and the segments (PR, ST).

The amplitude and the morphology of the ECG waves, segments and intervals represent the basic diagnostic information. Based on the analysis of these parameters, the health status of the heart can be investigated.

In **Table 2**, a small selection of abnormal electrical behavior of the heart and the influence of the ECG parameters is presented.

Thus, width, duration and amplitude measurements of the ECG waves are used to define abnormal electrical conduction in the heart, to detect cardiac tissue damage, and to classify patients at risk of cardiac arrhythmias.

4.2. Data used in the case study

The data used in this study are available from the Physionet QT interval database [28]. It contains a wide variety of QRS and ST-T morphologies and includes 105 ECG records taken from the following ECG databases: MIT-BIH Arrhythmia Database [29], the European Society of Cardiology ST-T Database [30], MIT-BIH Supraventricular Arrhythmia Database [27], The MIT-BIH Long-Term Database [31], MIT-BIH Normal Sinus Rhythm Database [32], Sudden Cardiac Death Holter Database [33] and MIT-BIH ST Change Database [34].

The data are sampled at 250 Hz and have annotations for the beginning and the end of P wave, QRS complex and T wave (**Figure 7**). For this study, 17 ECG recordings are used: sel51,

Some electrical abnormalities of the heart	ECG parameters characteristics
1. Sino-atrial (SA) block—type2	• PR segment is constant • For one, two, or three cycles, the P wave is missing (no firing of the SA node)
2. Atrio-ventricular (AV) block—1st degree	• PR segment is longer than normal, PR segment >300 ms • The P waves are superimposed on the T waves
3. AV block—2nd degree, Mobitz I	• The PR segments increases its length progressively culminating in an absence of QRS waves • The PR is the longest immediately before the dropped of the QRS waves • The PR is the shortest immediately after the dropped QRS waves
4. AV block—3rd degree (complete heart block)	• There is no relation between the frequency of the atrias contraction and the one of the ventricles contraction. Thus, the PR segment and interval have random lengths in each cardiac cycle
5. Atrial fibrillation	• Absence of P wave • Irregular RR interval • Random oscillations in the place of the P wave
6. Atrial flutter	
7. Intracranial hemorrhage	• Giant T-wave inversion [23]

Table 2. A few abnormal electrical behaviors of the heart and the influence on the ECG parameters.

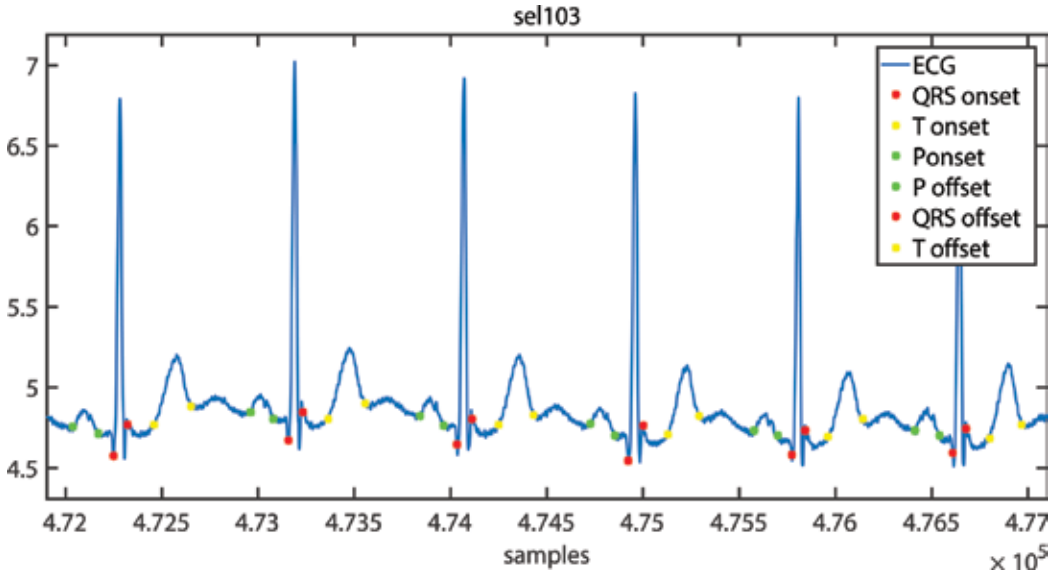

Figure 7. An ECG example with marked onset and offset for P, QRS and T waves.

sel103, sel302, sel306, sel307, sel808, sel872, sel16483, sel16786, sel17453, sele0121, sele0122, sele0170, sele0303, sele0509, sele0606, sele0607.

The real ECG signals are contaminated with synthetic PLI generated using 50 Hz and 150 Hz sine waves and having SNR = −2 dB:

$$PLI(t) = A_1 \cdot \sin\left(2\pi f_1 t\right) + A_3 \cdot \sin\left(2\pi f_3 \cdot t\right), f_1 = 50\ Hz,\ \ f_3 = 150\ Hz, A_3 = kA_1 \tag{1}$$

4.3. Digital filters

Four types of traditional IIR band stops filters are considered: Butterworth, Chebyshev I, Chebyshev II and elliptic. Cascaded filters from each type are implemented with the following stop bands: 49.5–50.5 Hz and 149.5–150.5 Hz. Their performance is compared against the time-varying pole radius multiple notch IIR filter [12] defined by the following equations:

$$H(z) = \prod_{i=1}^{K} \frac{1 - 2\cos\left(\Omega_{\mathrm{Ni}}\right)\mathrm{z}^{-1} + \mathrm{z}^{-2}}{1 - 2rcos(\Omega_{\mathrm{Ni}})\mathrm{z}^{-1} + \mathrm{r}^2\mathrm{z}^{-2}} = \frac{B(z)}{B(r^{-1}z)},\ \ B(z) = \sum_{i=0}^{2K} b_i \mathrm{z}^{-\mathrm{i}} \tag{2}$$

where K is the number of notches, Ω_{Ni} is the central frequency of the notch, N is the order of the harmonics, $B(z)$ is a symmetrical polynomial and r is the pole radius. In (3), the difference equation of the IIR multiple notch filter with a time-varying parameter r is presented:

$$\begin{aligned} y(n) = {} & b_0 x(n) + b_1 x(n-1) + \cdots + b_{2K} x(n-2K) \\ & - r(n) b_1 y(n-1) - \cdots - r^{2K}(n) b_{2K} y(n-2K) \end{aligned} \tag{3}$$

where the variation of $r(n)$ is:

$$r(n) = \bar{r}\left(1 + (d_r - 1)e^{-\frac{n}{vf_s}}\right), n \geq 0, \tag{4}$$

with variation range $d_r = r(0)/\bar{r}$ and $\bar{r} = \lim_{n\to\infty} r(n)$; v includes the exponential variation of $r(n)$ in (3), and f_s is the sampling frequency [7].

4.4. Performance measurements

The performance analysis is focused on the ST segment. Thus, 19,715 ST segments are included in the case study from the 20 ECG recordings. Three performance indices are considered:

- Mean square error (MSE):

$$MSE_j = \frac{1}{N}\sum_{i=1}^{N}\left(ST_{orig\_j}(i) - ST_{est\_j}(i)\right)^2 \tag{5}$$

  where N is the number of samples of a ST segment, $j = \overline{1 \ldots M}$, M is the total number of ST segments ($M = 19,715$), ST_{orig} is the ST segment from the clean ECG recording, before PLI contamination and ST_{est} is the ST segment obtained after the filters are applied for PLI and its harmonic cancelation;

- Normalized root mean square error (NRMSE):

$$NRMSE_j = \sqrt{\frac{\sum_{i=1}^{N}\left(ST_{orig\_j}(i) - ST_{est\_j}(i)\right)^2}{\sum_{i=1}^{N}\left(ST_{orig\_j}(i) - \overline{ST_{orig\_j}}\right)^2}} \tag{6}$$

- Noise retention expressed in percentage

$$NR_j = \frac{P_{STorig\_j} - P_{STest\_j}}{P_{STorig\_j}} \times 100 \tag{7}$$

  where $P_{STorig} = 10\log_{10}\sum_{i=1}^{N}\left(ST_{orig}(i)\right)^2$

4.5. Results

In **Figure 8**, a segment from the ECG sel103 record is displayed before and after the contamination with synthetic PLI.

Figure 9 depicts a detail from the ECG sel16773 after the digital filters are applied for PLI and its harmonic cancelation, and in **Figure 10**, a zoom of the ST segment from the ECG cycle presented in **Figure 9** is displayed.

http://dx.doi.org/10.5772/intechopen.74579

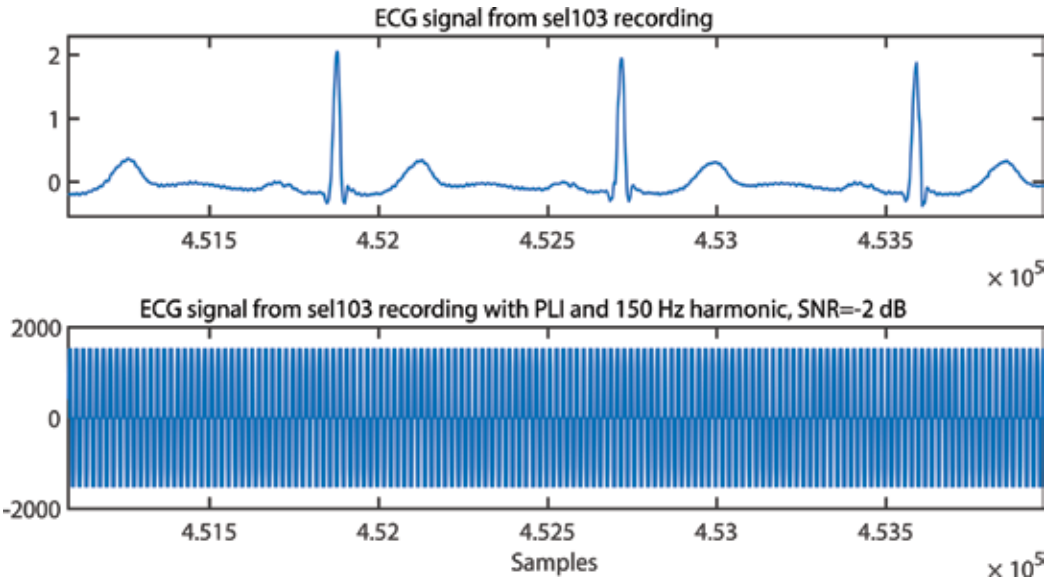

Figure 8. Upper subplot: clean ECG signal; lower subplot: ECG signal with PLI and its harmonics (SNR = −2 dB).

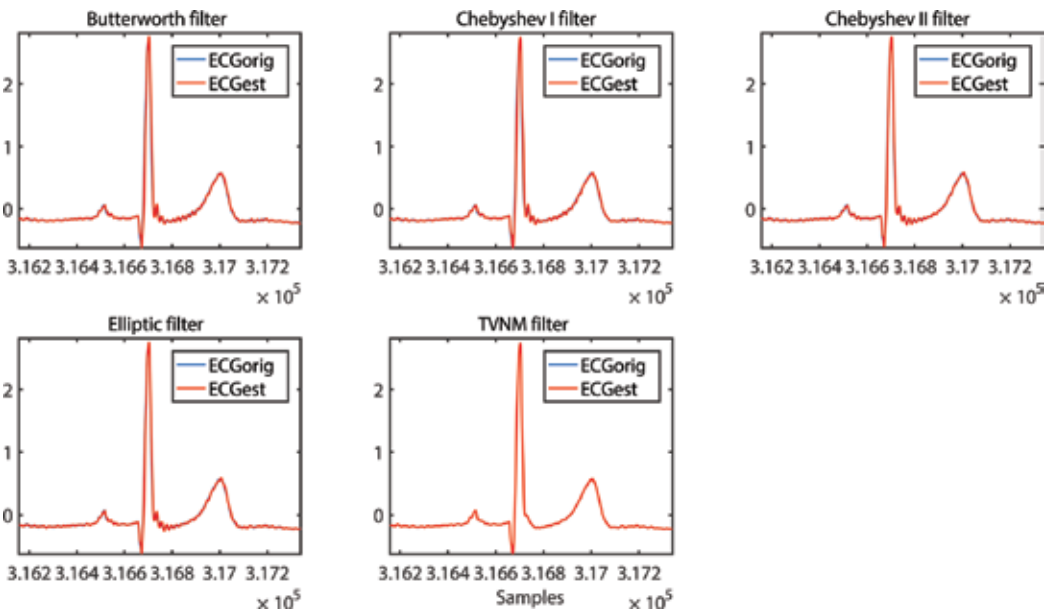

Figure 9. ECG sel16773 after the digital filters is applied. The estimated ECG signal is depicted with red.

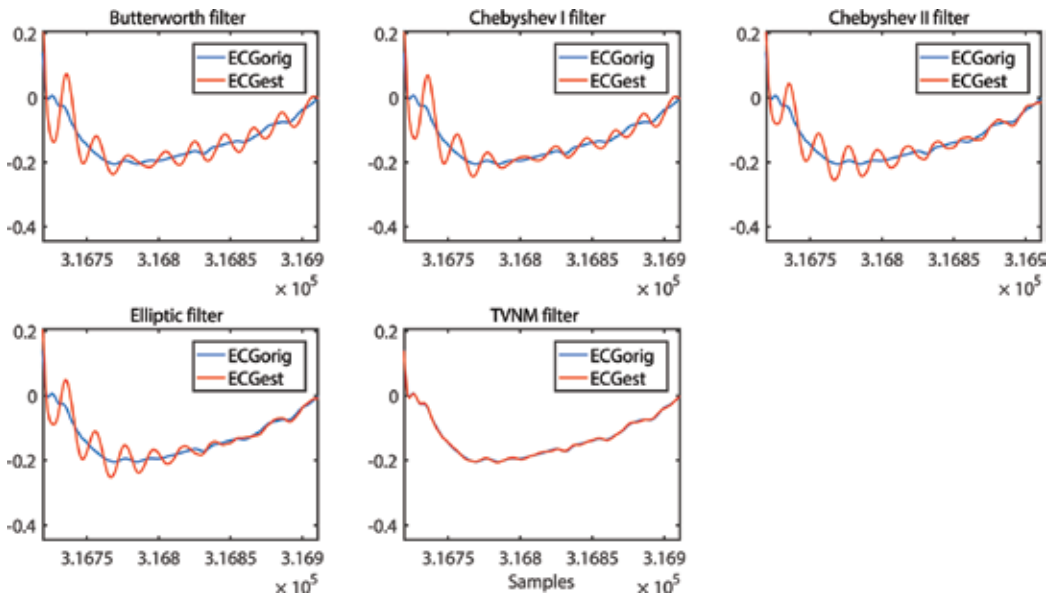

Figure 10. Detail on a ST segment. The estimated ECG signal is depicted with red.

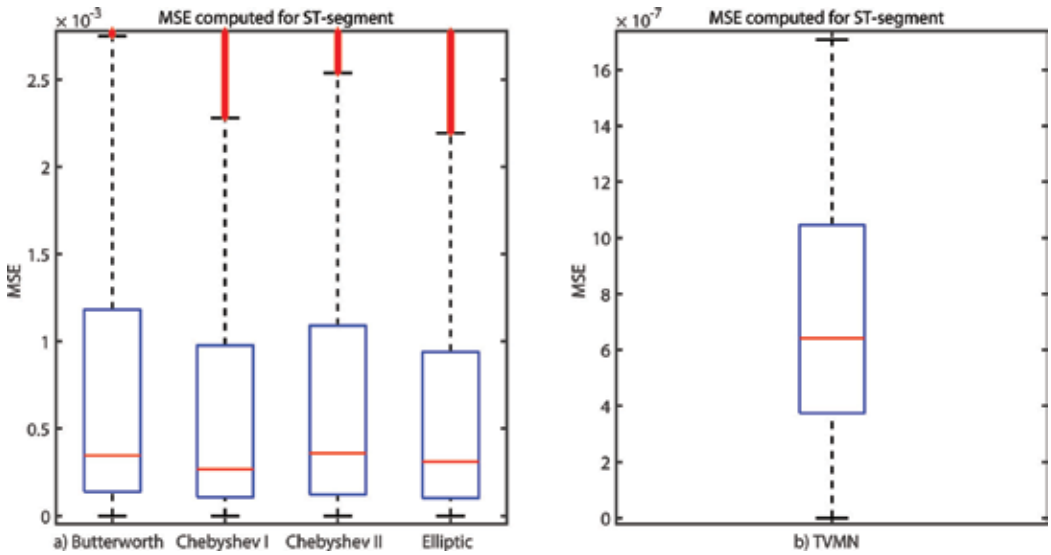

Figure 11. MSE determined for all 19,715 ST segments: (a) after the digital traditional band stop filters are applied; (b) after the TVMN is applied.

Figures 11–13 illustrate boxplots for the MSE, NRMSE and NR respectively, across all 19,715 ST segments. The results for TVNM are depicted in separated subplots because the indices computed in this case have very different values (much smaller).

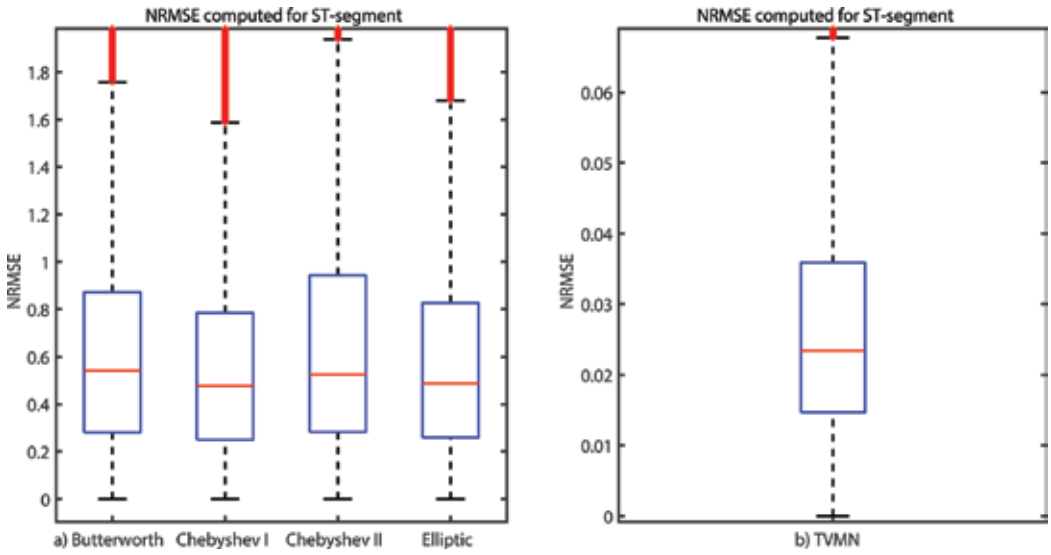

Figure 12. NRMSE determined for all 19,715 ST segments: (a) after the digital traditional band stop filters are applied; (b) after the TVMN is applied.

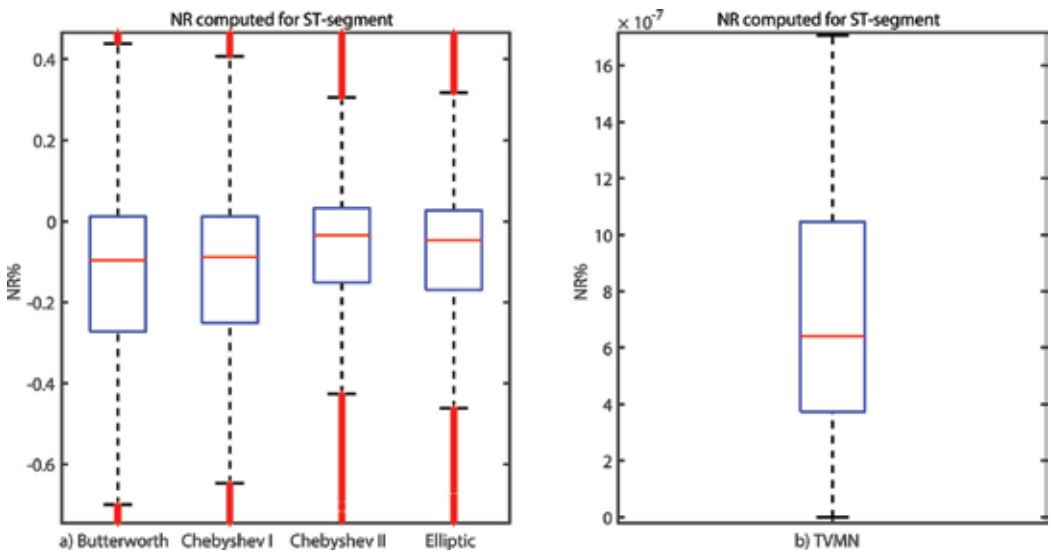

Figure 13. NR determined for all 19,715 ST segments: (a) after the digital traditional band stop filters are applied; (b) after the TVMN is applied.

4.6. Conclusions

The digital traditional band stop filters introduce a ringing effect, especially after the QRS complex, which show the highest ECG frequency components. This can be observed in **Figures 9** and **10**. Also, the performance indices computed for 19,715 ST segments confirm

the presence of the distortion introduced by the filters. All four traditional filters have similar performance. In contrast, the TVNM filter has far better performance with indices having the values 10–100 times smaller. TVNM introduces almost no distortion (**Figures 9** and **10**). The ringing effect introduced by the traditional filters can impair the ST segment identification, and so the physician diagnostic. Moreover, the impact is not only when discussing the health status of the adult heart but also when considering the fetal heart diagnosis. fECG is an important clinical tool to evaluate the wellbeing of the fetus during pregnancy. In particular, the ST segment from the fECG has strong diagnostic power. Changes in fetal ST segment can indicate fetal hypoxia, myocardial dystrophy, cardiac malformations, and so on. Thus, the residuals of the traditional filters will have a greater impact on the fECG parameters because this signal has much smaller power than the adult ECG. Hence, traditional band stop filters should be avoided if the parameters of the ECG are to be extracted.

On the other hand, the TVNM shows no ringing effect and the resulted ECG signal after the PLI and its harmonic removal is almost identical with the original ECG. Hence, the risk of misreading the ECG parameters is almost nonexistent. In addition, in comparison with the traditional filters, it has a very short transient time.

Author details

Ţarălungă Dragoş Daniel* and Mihaela Neagu (Ungureanu)

*Address all correspondence to: dragos.taralunga@upb.ro

Department of Applied Electronics and Information Engineering, Politehnica University, Faculty of Electronics, Telecommunications and Information Technology, Bucharest, Romania

References

[1] IEEE Recommended Practice and Requirements for Harmonic Control in Electric Power Systems. IEEE Std 519-2014 (Revision of IEEE Std 519-1992). 2014;1-29. DOI: 10.1109/IEEESTD.2014.6826459

[2] Umeh KC, Mohamed A, Mohamed R. Comparing the harmonic characteristics of typical single-phase nonlinear loads. In: Proceedings. National Power Engineering Conference; 2003. pp. 383-387. DOI: 10.1109/PECON.2003.1437479

[3] Saraiva F d O, Bernardes WMS, Asada EN. A framework for classification of non-linear loads in smart grids using artificial neural networks and multi-agent systems. Neurocomputing. 2015;**170**:328-338. DOI: 10.1016/j.neucom.2015.02.090

[4] Arthur R, Shanahan RA. Neutral currents in three phase wye systems. Power Systems Engineering Data. 1996:0104ED9501R8/96

[5] Widrow B, Glover JR Jr, McCool JM. Adaptive noise cancelling: Principles and applications. Proceedings of the IEEE. 1975;**63**(12):1692-1716

[6] Li H, Zhang J, Wang L. A fully integrated continuous-time 50-Hz notch filter with center frequency tunability. In: Annual International Conference of the IEEE Engineering in Medicine and Biology Society; Boston. 2011. pp. 3558-3562. DOI: 10.1109/IEMBS.2011.6090593

[7] Huhta JC, Webster JG. 60-Hz interference in electrocardiography. IEEE Transactions on Biomedical Engineering. 1973;BME-**20**(2). DOI: 10.1109/TBME.1973.324169

[8] Guermandi M, Scarselli EF, Guerrieri R. A driving right leg circuit (DgRL) for improved common mode rejection in bio-potential acquisition systems. IEEE Transactions on Biomedical Circuits and Systems. 2016;**10**(2):507-517. DOI: 10.1109/TBCAS.2015.2446753

[9] Gomez-Clapers J, Serrano-Finetti E, Casanella R Pallas-Areny R. Can driven-right-leg circuits increase interference in ECG amplifiers. In: Annual International Conference of the IEEE Engineering in Medicine and Biology Society; Boston. 2011. pp. 4780-4783. DOI: 10.1109/IEMBS.2011.6091184

[10] Ţarălungă D-D, Ungureanu G-M, Gussi I, Strungaru R, Wolf W. Fetal ECG extraction from abdominal signals: A review on suppression of fundamental power line interference component and its harmonics. Computational and Mathematical Methods in Medicine. 2014;**2014**:Article ID 239060. DOI: 10.1155/2014/239060

[11] Pal S, Mitra M. Empirical mode decomposition based ECG enhancement and QRS detection. Computers in Biology and Medicine. 2012;**42**(1):83-92. DOI: 10.1016/j.compbiomed.2011.10.012

[12] Piskorowski J. Suppressing harmonic powerline interference using multiple-notch filtering methods with improved transient behavior. Measurement. 2012;**45**(6):1350-1361. DOI: 10.1016/j.measurement.2012.03.004

[13] Piskorowski J. Time-efficient removal of power-line noise from EMG signals using IIR notch filters with non-zero initial conditions. Biocybernetics and Biomedical Engineering. 2013;**33**(3):171-178. DOI: 10.1016/j.bbe.2013.07.006

[14] Pei S-C, Tseng C-C. Elimination of AC interference in electrocardiogram using IIR notch filter with transient suppression. IEEE Transactions on Biomedical Engineering. 1995; **42**(11):1128-1132. DOI: 10.1109/10.469385

[15] Rana KPS, Kumar V, Gupta A. A pole-radius-varying IIR notch filter with enhanced post-transient performance. Biomedical Signal Processing and Control. 2017;**33**:379-391. DOI: 10.1016/j.bspc.2016.12.015

[16] Wang Q, Gu X, Lin J. Adaptive notch filter design under multiple identical bandwidths. AEU—International Journal of Electronics and Communications. 2017;**82**:202-210. DOI: 10.1016/j.aeue.2017.08.054

[17] Razzaq N, Sheikh SAA, Salman M, Zaidi T. An intelligent adaptive filter for elimination of power line interference from high resolution electrocardiogram. IEEE Access. 2016;**4**: 1676-1688

[18] Lin J, Sun X, Wu J, Chan SC, Xu W. Removal of power line interference in EEG signals with spike noise based on robust adaptive filter. In: IEEE Region 10 Conference, TENCON; Singapore. 2016. p. 2707-2710

[19] Tomasini M, Benatti S, Milosevic B, Farella E, Benini L. Power line interference removal for high-quality continuous biosignal monitoring with low-power wearable devices. IEEE Sensors Journal. 2016;**16**(10):3887-3895

[20] Keshtkaran MR, Yang Z. A robust adaptive power line interference canceler VLSI architecture and ASIC for multichannel biopotential recording applications. IEEE Transactions on Circuits and Systems II: Express Briefs. 2014;**61**(10):788-792. DOI: 10.1109/TCSII.2014.2345302

[21] Galiana-Merino JJ, Ruiz-Fernandez D, Martinez-Espla JJ. Power line interference filtering on surface electromyography based on the stationary wavelet packet transform. Computer Methods and Programs in Biomedicine. 2013;**111**(2):338-346

[22] Suchetha M, Kumaravel N. Empirical mode decomposition based filtering techniques for power line interference reduction in electrocardiogram using various adaptive structures and subtraction methods. Biomedical Signal Processing and Control. 2013;**8**(6):575-585. DOI: 10.1016/j.bspc.2013.05.001

[23] Taralunga DD, Gussi I, Strungaru R. Fetal ECG enhancement: Adaptive power line interference cancellation based on Hilbert Huang transform. Biomedical Signal Processing and Control. 2015;**19**:77-84. DOI: 10.1016/j.bspc.2015.03.009

[24] Jenkal W, Latif R, AhmedToumanari AD, El B'charri O, Maoulainine FMR. An efficient algorithm of ECG signal denoising using the adaptive dual threshold filter and the discrete wavelet transform. Biocybernetics and Biomedical Engineering. 2016;**36**(3):499-508. DOI: 10.1016/j.bbe.2016.04.001

[25] Warmerdam GJJ, Vullings R, Schmitt L, Van Laar JOEH, Bergmans JWM. A fixed-lag Kalman smoother to filter power line interference in electrocardiogram recordings. IEEE Transactions on Biomedical Engineering. 2017;**64**(8):1852-1861. DOI: 10.1109/TBME.2016.2626519

[26] Mateo J, Sánchez-Morla EM, Santosd JL. A new method for removal of powerline interference in ECG and EEG recordings. Computers & Electrical Engineering. 2015;**45**:235-248. DOI: 10.1016/j.compeleceng.2014.12.006

[27] Kligfield P, Gettes LS, Bailey JJ, Childers R, Deal BJ, William Hancock E, van Herpen G, Kors JA, Macfarlane P, Mirvis DM, Pahlm O, Rautaharju P, Wagner GS. Recommendations for the standardization and interpretation of the electrocardiogram. Circulation. 2007;**115**:1306-1324. DOI: 10.1161/CIRCULATIONAHA.106.180200

[28] Rautaharju PM, Surawicz B, Gettes LS. AHA/ACCF/HRS recommendations for the standardization and interpretation of the electrocardiogram. Part IV: The ST segment, T and U waves, and the QT interval. Circulation. 2009;**119**:e241-e250

[29] Goldberger AL, Amaral LAN, Glass L, Hausdorff JM, Ivanov PC, Mark RG, Mietus JE, Moody GB, Peng C-K, Stanley HE. PhysioBank, PhysioToolkit, and PhysioNet: Components

of a new research resource for complex physiologic signals. Circulation. 2000;**101**(23): e215-e220

[30] Moody GB, Mark RG. The MIT-BIH Arrhythmia Database on CD-ROM and software for use with it. In: Proceedings Computers in Cardiology; Chicago, IL. 1990. pp. 185-188. DOI: 10.1109/CIC.1990.144205

[31] Taddei A, Biagini A, et al. The European ST-T database: Development, distribution and use. In: Proceedings Computers in Cardiology; Chicago, IL. 1990. pp. 177-180

[32] Greenwald SD, Patil RS, Mark RG. Improved detection and classification of arrhythmias in noise-corrupted electrocardiograms using contextual information. In: Proceedings Computers in Cardiology; Chicago, IL. 1990. pp. 461-464. DOI: 10.1109/CIC.1990.144257

[33] Greenwald SD. The development and analysis of a ventricular fibrillation detector [dissertation]. Massachusetts Institute of Technology. Department of Electrical Engineering and Computer Science: Massachusetts Institute of Technology; 1986. Available from: http://hdl.handle.net/1721.1/92988

[34] Albrecht P. ST segment characterization for long term automated ECG analysis [dissertation]. Massachusetts Institute of Technology, Department of Electrical Engineering and Computer Science: Massachusetts Institute of Technology; 1983. 378 p

Chapter 3

Harmonic Analysis of the Wind Energy Conversion System Connected with Electrical Network

Emmanuel Hernández Mayoral,
Miguel Ángel Hernández López,
Hugo Jorge Cortina Marrero and
Reynaldo Iracheta Cortez

Additional information is available at the end of the chapter

http://dx.doi.org/10.5772/intechopen.74584

Abstract

A harmonic analysis for a wind energy conversion system (WECS) based in a doubly fed induction generator (DFIG) is presented. A *back-to-back* frequency converter as voltage source for excite to rotor winding is used whereas than the electrical network excites to stator winding. The analysis is based on the induction machine model and the steady-state frequency converter model. Additionally, dynamic-state and steady-state models are developed and compared validating the results of the simulations obtaining a harmonic model, in steady-state, clear, and precise of the wind energy conversion system.

Keywords: harmonic analysis, doubly fed induction generator, *back-to-back* frequency converter, electrical network, harmonic and inter-harmonics

1. Introduction

Energy demand is increasing day by day around the world and renewable energy has proven to be an excellent choice of competition against conventional energy sources, which produce environmental pollution and contribute to climate change and global warming. An effective and proven type of renewable energy is wind energy, which achieved an increase of 63 GW in Mexico, reaching 433 GW in total capacity worldwide. This energy has been used by the human civilization for millennia to navigate and pump water for agricultural activities. Nowadays, the wind energy is used to produce electricity that leads the world of technology. This energy is used to impulse, mechanically, the generators that produce electrical energy. The

device that allows this conversion is called wind turbine. There are different concepts regarding the coupling of the generator with the wind turbine being the most well-known fixed velocity and variable velocity wind turbines. The squirrel-cage induction generator was the first fixed velocity concept developed during the early years of wind turbines. This configuration is shown in **Figure 1**. The generator is directly connected to the electrical network but has the disadvantage of operating at low efficiency producing poor power quality. On the other hand, the double-fed induction generator (DFIG) is the technology that has the largest presence in the wind industry today as it has the advantage of have a higher energy efficiency compared to the squirrel-cage induction generator, a reduction in mechanical loads, a simple system of pitch control, and greater control of active and reactive power (see **Figure 2**). Due to the unpredictable nature of wind, wind energy still presents several challenges such as fluctuations in voltage generated and complications to achieve efficient couplings with the electrical network.

These problems have led to develop strategies to solve these mishaps. However, the devices used by these strategies produce certain alterations in the energy signal required by the generator to function properly. This implies variations in the energy delivered by the generator, which leads to a further challenge in the area of wind energy: **the power quality**. This concept describes how close the energy is to the appropriate standards to operate and allow the proper use of equipment that employ this energy. Variations in voltage can result in malfunction of sensitive components of system, a reduction in generator efficiency and in general, degradation of power quality, while harmonics, which are current and/or voltages signals occurring in electrical systems with multiple frequencies of the fundamental, can cause severe problems such as generator induction effects and torque oscillations reducing the life of generator. Therefore, it is very important to obtain a clear harmonic analysis of the wind energy conversion system (WECS) when they are excited by non-sinusoidal voltage sources since the wind industry currently lacks models for harmonic propagation studies; this is done using the Fourier transform tool described later in the chapter.

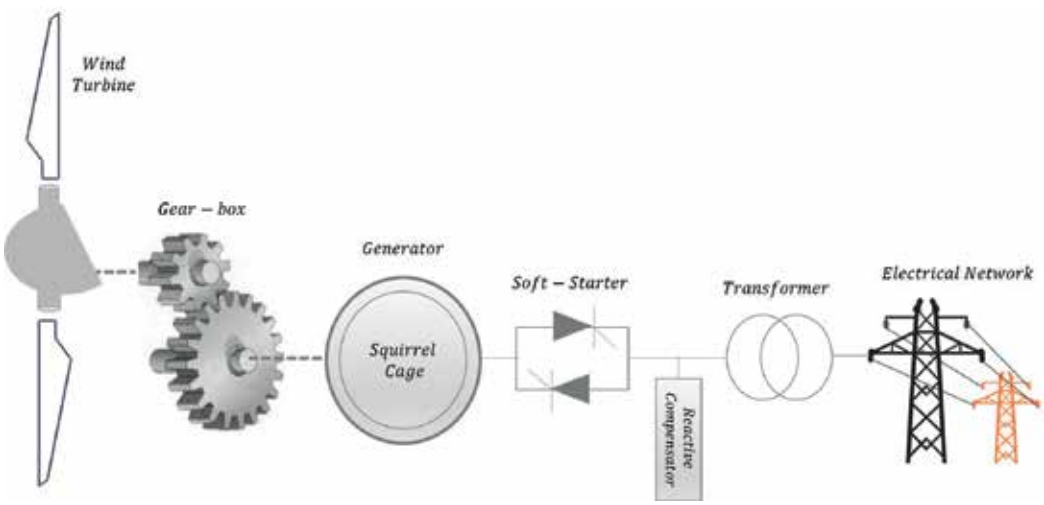

Figure 1. Configuration of squirrel-cage induction generator.

http://dx.doi.org/10.5772/intechopen.74584

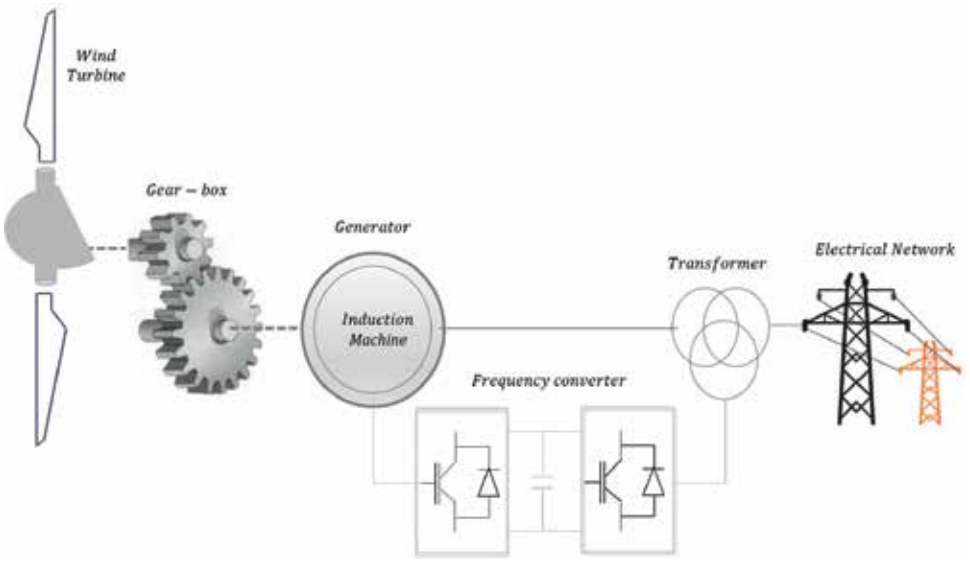

Figure 2. WECS based in doubly fed induction generator connected to the electrical network.

2. Harmonic analysis

In the beginning, Fourier series emerged as a method for the explanation of physics phenomena, at a time when there was no knowledge of electronics or telecommunications, but they are also very useful in our times applied in computer science and communication. This is possible since electrical phenomena are also physical phenomena and their behaviors explained through periodic functions or periodic wave movements, where a Fourier transform allows obtaining discontinuous waves. In addition, the harmonic analysis is the process of calculating the magnitudes and phases of the fundamental frequency and all the higher order of a periodic waveform. The resulting series is known as the Fourier series [1], which for the periodic function $X(t)$ has the expression:

$$X(t) = a_0 + \sum_{n=1}^{\infty} \left[a_n \cos\left(\frac{2\pi n t}{T}\right) + b_n \sin\left(\frac{2\pi n t}{T}\right) \right] \tag{1}$$

This constitutes a representation in the time-domain of the periodic function. In this expression, a_0 is the average value and T is the period of the function $X(t)$, whereas a_n and b_n are the coefficients of the series for the *n-th* harmonic. These signals can be visualized in a 3-D system in which their magnitude, frequency location, and over time are represented (see **Figure 3**).

The constant term of the Fourier series is given by:

$$a_0 = \frac{1}{T} \int_{-T/2}^{T/2} X(t)dt \tag{2}$$

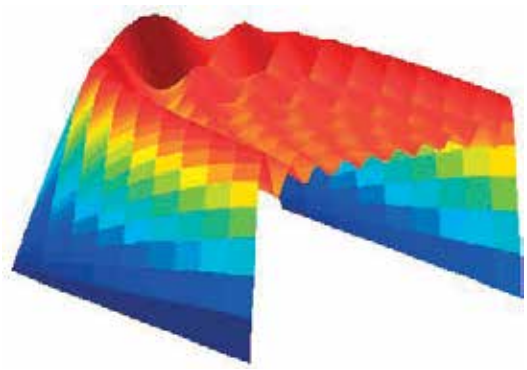

Figure 3. Harmonics signals in 3-D.

which represents the area under the curve of $X(t)$ from $-T/2$ to $+T/2$, divided by the period of the waveform T, that is the average value of the function. While a_n and b_n are given respectively by:

$$a_n = \frac{2}{T}\int_{-T/2}^{T/2} X(t)\cos\left(\frac{2\pi nt}{T}\right)dt \qquad for\ n = 1 \to \infty$$
$$b_n = \frac{2}{T}\int_{-T/2}^{T/2} X(t)\sin\left(\frac{2\pi nt}{T}\right)dt \qquad for\ n = 1 \to \infty \tag{3}$$

The above equations are simplified when the waveform has symmetry. If the waveform has odd symmetry, this is $X(t) = -X(-t)$, then a_n is zero for all values of n, and b_n is given by:

$$b_n = \frac{4}{T}\int_{0}^{T/2} X(t)\sin\left(\frac{2\pi nt}{T}\right)dt \tag{4}$$

The Fourier series for an odd function will have only sine terms. If the waveform has even symmetry, this is $X(t) = X(-t)$, then b_n is zero for all values of n, and a_n is given by:

$$a_n = \frac{4}{T}\int_{0}^{T/2} X(t)\cos\left(\frac{2\pi nt}{T}\right)dt \tag{5}$$

2.1. Transform Fourier

Formerly the process to find the Fourier transform was a bit expensive, due to the calculations that had to be done manually, nowadays with the help of technology and computers, different algorithms have been developed to simplify and make this process easier, besides of the discrete Fourier transform (DFT) and the fast Fourier transform (FFT). The main idea of the Fourier transform is to transform a signal from the time domain or space to the frequency-domain. In addition, through inverse Fourier transform, you can pass functions from the frequency-domain to the time-domain. The Fourier series therefore represents the special case of the Fourier transform applied to a periodic signal. In practice, the data are

frequently available in the form of a time-sampled function, represented by a time series of amplitudes separated by fixed time intervals of limited duration. When Fourier analysis is applied to a periodic continuous signal in the time-domain produces a series of discrete frequency components in the frequency-domain [2]. The following equations form the pair of the Fourier transform:

$$X(f) = \int_{-\infty}^{\infty} x(t)e^{-j2\pi ft}dt$$
$$x(f) = \int_{-\infty}^{\infty} X(t)e^{j2\pi ft}dt \tag{6}$$

where t is time, f is the frequency, $x(t)$ is the test signal, $e^{-j2\pi ft}$ is probing phasor and $X(f)$ is spectrum as a function of frequency f. Eq. (7) is called the 'forward transformation' and Eq. (8) is the 'reverse transform'. Generally, $X(f)$ is complex and can be written as:

$$X(f) = ReX(f) + jImX(f) \tag{7}$$

The real part of $X(f)$ is obtained:

$$ReX(f) = \frac{1}{2}[X(f) + X(-f)] = \int_{-\infty}^{\infty} x(t)\cos 2\pi ft\, dt \tag{8}$$

In analogous form, the imaginary part of $X(f)$ is obtained from:

$$ImX(f) = \frac{1}{2}j[X(f) - X(-f)] = \int_{-\infty}^{\infty} x(t)\sin 2\pi ft\, dt \tag{9}$$

The amplitude spectrum of the frequency signal is obtained from:

$$|x(t)| = [(ReX(f))^2 + (ImX(f))^2]^{1/2} \tag{10}$$

In addition, the phase spectrum is:

$$\phi(f) = \tan^{-1}\left[\frac{Im\,X(f)}{Re\,X(f)}\right] \tag{11}$$

2.2. Fourier discrete transform

When frequency-domain spectrum is a sampled function, as well as the time-domain function, a Fourier transform pair of discrete components is obtained [3]:

$$X(f) = \frac{1}{n}\sum_{n=0}^{N-1} x(t)e^{-j2\pi kn/N}$$
$$x(t) = \sum_{n=0}^{n-1} X(f)e^{-j\pi kn/N} \tag{12}$$

Equation (14) can be written in condensed form as:

$$[X(f)] = \frac{1}{n}[W^{kn}][x(t)] \tag{13}$$

In Eq. (15), $[X(f_k)]$ is a vector representing the N components of the function in the frequency-domain, while $[x(t)]$ is a vector representing the N samples of the function in the time-domain. The calculation of the N frequency components of N time samples requires a total of N^2 complex multiplications to solve Eq. (16).

2.3. Fourier fast transform

The implementation of Eq. (14) involves a number of complex additions and multiplications that is proportional to N^2. The term $-j2\pi kn/N$ can be calculated at one time and summarized in a table for subsequent applications; for this reason, the multiplication of k by n in this term is not normally counted as part of the implementation. The fast Fourier transform is an algorithm that allows calculating the discrete Fourier transform of a harmonic signal with a substantial saving of calculations. For the case, a number of samples equal to 2^k, where k is integer, only $(N/2)log_2(N)$ multiplications [4] are required. The saving in calculations increases as the number of samples increases with the ratio:

$$\frac{N^2}{(N/2)log_2(N)} = \frac{\ln(4)N}{\ln(N)} \tag{14}$$

Thus for 2^{10} samples, the work is reduced to analyzing only 10^3 samples, which reduces the number of operations 205 times. The algorithm that is proposed is based on the method called 'successive folding'. Knowing that $N = 2M$ where M is a positive number, so

$$F(k) = \frac{1}{2M}\sum_{n=0}^{2M-1} f(x)W_{2M}^{nk} = \frac{1}{2}\left\{\frac{1}{M}\sum_{n=0}^{M-1} f(x)\,W_{2M}^{(2x)} + \frac{1}{M}\sum_{n=0}^{M-1} f(2x+1)W_{2M}^{(2x+1)}\right\} \tag{15}$$

which can be expressed as

$$F(k) = \frac{1}{2}\left\{\frac{1}{M}\sum_{x=0}^{M-1} f(2x)W_M^{kn} + \frac{1}{M}\sum_{x=0}^{M-1} f(2x+1)W_M^{nk}W_{2M}^{k}\right\} \tag{16}$$

If it is defined as

$$F_{even}(k) = \frac{1}{M}\sum_{x=0}^{M-1} f(2x)\,W_M^{nk} \tag{17}$$

For $k = 0,1,\ldots,M-1$ and

$$F_{odd}(k) = \frac{1}{M}\sum_{x=0}^{M-1} f(2x+1)\,W_M^{nk} \tag{18}$$

For $k = 0,1,\ldots,M-1$, then we have

$$F_{(k)} = \frac{1}{2}\{F_{even}(k) + F_{odd}(k)W_{2M}^{k}\} \tag{19}$$

Also, given that $W_M^{k+M} = W_M^k$ and $W_{2M}^{k+M} = -W_{2M}^k$,

$$F(k+M) = \frac{1}{2}\left[F_{even}(k) - F_{odd}(k)W_{2M}^k\right] \tag{20}$$

A careful analysis of the last equations shows some interesting properties of these expressions. Note that an N-point transform can be calculated by dividing the original expression into two parts, as indicated in the last two equations. The calculation of the first half of $F(k)$ requires the evaluation of the two transforms of N/2 points according to the last equations. The resulting values of $F_{odd}(k)$ and $F_{even}(k)$ are replaced in $F_{(k)}$ for $k = 0,1,2,\ldots,(N/2-1)$. The other half is obtained by equation $F(k+M)$ without requiring additional evaluations of the transform. Considering a number of samples equal to 2^n, with n positive integer, it can be shown that the number of complex operations (multiplications and additions) is given by:

$$m(n) = 2m(n-1) + 2^{n-1} \quad n \geq 1$$

$$a(n) = 2a(n-1) + 2^n \quad n \geq 1$$

These expressions indicate the number of multiplications $(m(n))$ and sums $(a(n))$ for which $m(0)$ and $a(0)$ are equal to zero, since the transformation of a point does not require any operation. It is possible to conclude, by induction, that the number of operations, sums and complex multiplications, which is required to implement an algorithm for FFT, is given by:

$$m(n) = \frac{1}{2}2^n log_2 2^n = \frac{1}{2}Nlog_2 N = \frac{1}{2}Nn \qquad n \geq 1$$

And

$$a(n) = 2^n log_2\, 2^n = Nlog_2\, N = Nn \qquad n \geq 1$$

The application of this mathematical tool are varied, for electrical engineering, electronics, telecommunications and other fields of information sciences. All these sciences can to demonstrate that the sinusoidal signals can represent the sending of data by electrical transmission networks. In the following sections, a model of the doubly fed induction generator for harmonic analysis based on the Fourier transform is presented. Initially, the mathematical model of DFIG is presented at the fundamental frequency. Then, the model is performed at harmonic frequencies to obtain the harmonics components generated in the electrical variables of the generator. Finally, the results are compared and summarized in tables.

3. Wind turbines technologies

The connection of wind farms to an existing transmission or distribution network can affect the behavior of the same depending on two main variables:

1. Installed wind power.
2. 'Strength' to network to which its connects (expressed as PCC/P_{wind}).

This analysis must be done both from the point of view of static and dynamic behavior of the system. Unlike other types of generation technologies, it is not usual for wind generation to cause problems in terms of the harmonic, inter-harmonic and sub-harmonic distortion. This is due both to the fact that most of the machines used are of the asynchronous type, that is, the technology type of wind energy conversion system used in wind farms determines the harmonic distortion intensity. For example, the fixed velocity wind turbines based in squirrel-cage induction generator, the element that causes current distortion is the soft-starter, formed by a thyristor bridge, which not in all operations of the turbine is in operation. On the other hand, variable-velocity wind turbines today have in common the use of power electronic converters to be able to vary the velocity and to maintain the power factor within the desired limits. However, these devices produce harmonic signals in the generator and the harmonic distortion magnitude depends mainly on the type of inverter or converter and its control because these use the IGBT thyristors (isolated gates bipolar transistors). The switching frequency in these inverters is limited to the range of 2–3 kHz. The frequency converters affect waveform quality and can negatively affect other consumers connected to the electrical network.

3.1. WECS using DFIG with conventional *back-to-back* frequency converter

Considering the different types of WECS configuration, a wind turbine based on a doubly fed induction generator (DFIG) connected directly to the electrical network via a frequency converter is analysed. Among electronic power converters there are three types widely used in the wind power market: *back-to-back* converter, multilevel converter and the matrix converter [5]. In this section, the revision is made around the network-connected WECS-based DFIG and a *back-to-back* converter attached at a point common coupling (PCC). A rotor-side converter (RSC), a network-side converter (NSC) and a decoupling capacitor between the two converters constitute this converter. Notice that the harmonic distortion is a phenomenon that causes problems for both the users and the entity responsible for the provision of the electric power service [6], so it is considered necessary an appropriate understanding of the techniques currently used to mitigate this phenomenon. In this sense, the literatures that define the harmonic sources in WECS are classified as follow: Harmonic distortion from the network and harmonic distortion form the WECS:

1. The harmonic distortion from the electrical network: Since the WECS is connected to the electrical network; it becomes sensitive to any harmonic distortion coming from it. Distorted voltages in the stator generate harmonic currents in the WECS, which in turn can generate ripples voltage, torque pulsations, overheating, and increased losses in stator windings, under power factor, among others [7]. In some cases, these affections can have destructive effects on the WECS [8]. The solutions found in the literature involve the use of custom power devices as well as various control strategies implemented in the frequency converters.
2. The harmonic distortion from the WECS: The harmonics coming from the WECS is another of the harmonic distortion scenario, which the injection of harmonic components of voltage or current into the electrical network can cause problems such as excessive heating of transformers and conductors [9]. The main causes of harmonics from the WECS are: harmonics produced by nonlinear loads inherent to the generation system and harmonics produced by the WECS itself that is to say, associated to the operation of the components (generator, electronic power converter).

http://dx.doi.org/10.5772/intechopen.74584

3.1.1. Operating principle of doubly fed induction generator

As in traditional three-phase induction generator, the doubly fed induction generators have a magnetic field formed by the stator phases rotating at synchronous velocity (ω_{es}), which is determined by the network frequency and the number of poles of the generator [10, 11], which is determined as $\omega_{es} = 2\pi f_{es}$ or $n_s = 120 \times f_{es}/p$ where f_{es} is the voltage frequency of network in Hertz, p is the poles number of generator, ω_{es} is the synchronous velocity in rad/s and n_s is the synchronous velocity in rev/min. Unlike the first generators, the frequency of the rotor currents in the doubly fed induction generator can be controlled, thanks to the operation of the converter located on the generator-side. The control of the rotational currents governs the velocity and torque characteristic curve, which allows optimizing and regulating the power generated by the DFIG [12]. In the same way that the velocity stator fields are obtained, the velocity of the rotor fields formed by the rotor currents is defined by $\omega_{er} = 2\pi f_r$ where f_r is the frequency of rotor voltage in Hertz, and ω_r is the angular velocity of rotor fields in rad/s. Then, slip s is defined as the relative velocity of the stator fields with respect to the rotor velocity ω_r, measured in per unit:

$$s = \frac{\omega_{es} - \omega_r}{\omega_{es}} \tag{21}$$

The concept 'slip' is very important because it describes the machine operation. Now, with the above equation, we can establish in $f_{er} = sf_{es}$ where f_{es} is the frequency of stator current. From this, it is possible to characterize the modes of operation of the machine, which in general in wind systems present velocity variations around 30% [13]. In order to produce a non-zero torque necessary for generator operation, the magnetic fields caused by the stator and rotor currents must rotate at the same velocity with respect to a point coupling common [14], $\omega_{es} = \omega_r + \omega_{er}$. Now, the mechanical velocity of the rotor is obtained and can be controlled according to previous equations by controlling the frequency of the rotor currents affected by the rotor-side converter. When the slip is positive, it has ω_{es} to be greater ω_r and therefore ω_{er} to be positive and the rotating magnetic fields generated by the stator and rotor coils rotate in the same direction. In this case:

$$\omega_m = \frac{2\pi(f_{es} - f_{er})}{(p/2)} \tag{22}$$

where ω_m is the rotation velocity of rotor measure with respect to stator in radians geometrics. When the slip is negative, it has ω_{es} to be minor to ω_r and therefore ω_{er} to be positive and the rotating magnetic fields generated by the stator and rotor coils rotate in the opposite direction. This means that the rotor is fed with the inverse stator sequence. Under these conditions:

$$\omega_m = \frac{2\pi(f_{es} + f_{er})}{(p/2)} \tag{23}$$

As can be seen in the equations just described, the velocity at which the rotor rotates depends exclusively on the network and rotor frequencies, and not on the torque imposed by the turbine, as is the case with other types of generators.

3.1.2. Steady-state model of DFIG at harmonic frequencies

The general scheme of doubly fed induction generator (DFIG) in the stationary reference-frame uses a wound rotor with slip rings to transmit current between the stator and rotor voltage sources is shown in **Figure 4**. The voltage equation that describes the equivalent circuit is given by

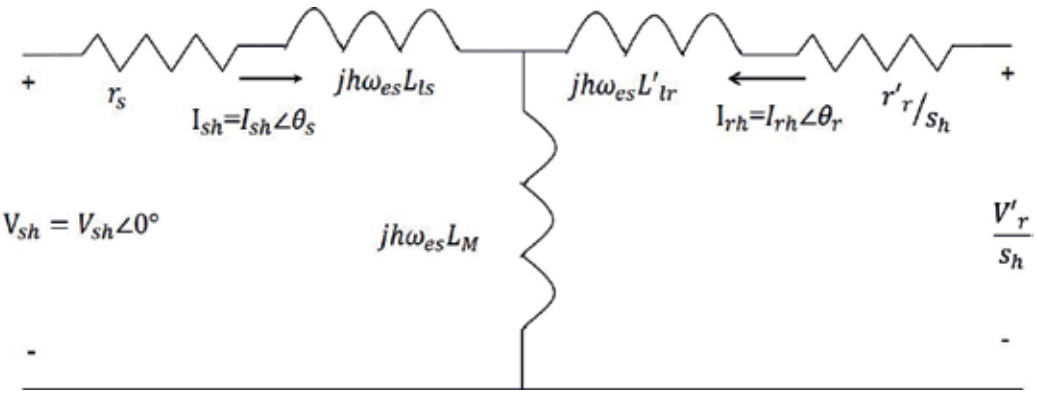

Figure 4. Steady-state equivalent circuit of the induction machine.

$$V_{sh}\angle 0° = -r_s I_{sh} - jh\omega_{es}L_{ls}I_{sh} - jh\omega_{es}L_M I_{sh} - jh\omega_{es}L_M I_{rh}$$
$$\frac{V_r}{s_h} = \frac{r_r}{s_h} I_{rh} - jh\omega_{es}L_{lr}I_{rh} - jh\omega_{es}L_M I_{rh} - jh\omega_{es}L_M I_{sh} \tag{24}$$

where V_{sh} and V'_{rh} are stator and rotor harmonic voltages, I_{sh} and I'_{rh} are the stator and rotor harmonic currents, respectively, and L_M is the magnetizing inductance given by $L_M\,3/2\;L_{ms}$, and s_h is the harmonic slip. To calculate the slip, s_h, corresponding to the harmonic h, it is necessary to determine if the harmonic is a positive, negative or zero sequence. All multiples of three in a three-phase system are zero sequence, that is, corresponding to the harmonics $h = 3k$, and since they do not produce a rotating magnetic field, they do not contribute to the production of electric torque. The rest of the odd harmonics produce positive or negative electric torques depending on the sequence of the harmonic system generated by the rotating magnetic field, that is, the harmonics with behavior $h = 3k + 1$ and $h = 3k - 1$. Thus, the harmonic slip is defined by [15]:

$$s_h = \frac{\pm h\omega_{es} - \omega_r}{+h\omega_{es}} \tag{25}$$

The sign (+) and (−) is used for positive and negative sequence, respectively. In order for a harmonic of order h in a three-phase system to be in sequence positive, the following relation must be fulfilled:

$$\frac{2\pi}{3}h = \frac{2\pi}{3} + 2\pi n \;\rightarrow h = (2n-1) = 1 + 3h \;\rightarrow n = 1 + \frac{3h}{2} \tag{26}$$

Since h must be an odd number, n must belong to natural numbers; this implies that k must be a multiple of 2

$$k = 2m; \quad \forall m \in N \rightarrow n = 1 + 3m \rightarrow h = 6m + 1; \quad \forall m \in N \tag{27}$$

In order for a harmonic of order h in a three-phase system to be in sequence negative, the following relation must be fulfilled

http://dx.doi.org/10.5772/intechopen.74584

$$\frac{2\pi}{3}h = \frac{4\pi}{3} + 2\pi n \rightarrow h = (2n-1) = 2 + 3h \rightarrow n = 1 + \frac{3(h+1)}{2} \tag{28}$$

Since h must be an odd number, n must belong to natural numbers; this implies that k+1 must be a multiple of 2,

$$k+1 = 2m; \qquad \forall\, m \in N \rightarrow n = 3m \rightarrow \mathrm{h} = 6m - 1; \qquad \forall\, m \in N, \qquad m \neq 0$$

In summary:

a. Harmonics of positive sequence: $h = 6m + 1,\ \ m = 0,1,2, \ldots$

b. Harmonics of negative sequence: $h = 6m - 1,\ \ m = 0,1,2, \ldots$

The stator and rotor phasors currents are obtained from the above equation:

$$\begin{aligned} \mathrm{I}_{sh} &= \frac{-V_{sh}(r_r + r_r + jhs_h\omega_{es}L_{lr}) + V_{rh}(jh\omega_{es}L_M)}{(r_s r_r - s_h\omega_{es}L_{ls}\omega_{es}L_{lr} + s_h\omega_{es}L_M) + jh(r_r\omega_{es}L_{ls} + s_h r_s\omega_{es}L_{lr})} \\ \mathrm{I}_{rh} &= \frac{V_{sh}(js_h\omega_{es}L_M) - V_{rh}(r_s + jh\omega_{es}L_{ls})}{(r_s r_r - s_h\omega_{es}L_{ls}\omega_{es}L_{lr} + s_h\omega_{es}L_M) + jh(r_r\omega_{es}L_{ls} + s_h r_s\omega_{es}L_{lr})} \end{aligned} \tag{29}$$

Then, $V_{sh} = V_{sh}\angle 0°$ and $V_{rh} = V_{rh}\angle\varphi$; can be written as:

$$\begin{aligned} \mathrm{I}_{sh} &= \frac{1}{A^2 + B^2}[-(Br_r + As_h\omega_{es}L_{lr})V_{sh} + A\omega_{es}L_M V_{rh}\cos\varphi - B\omega_{es}L_M V_{rh}\sin\varphi] \\ &+ jh\frac{1}{A^2 + B^2}[(Ar_r - Bs_h\omega_{es}L_M)V_{sh} + B\omega_{es}L_M V_{rh}\cos\varphi + A\,\omega_{es}L_M V_{rh}\sin\varphi] \\ \mathrm{I}_{rh} &= \frac{1}{A^2 + B^2}[As_h\omega_{es}L_M V_{sh} - (Br_s + A\omega_{es}L_{ls})V_{rh}\cos\varphi - (Ar_s - B\omega_{es}L_{ls})V_{rh}\sin\varphi] \\ &jh\frac{1}{A^2 + B^2}[Bs_h\omega_{es}L_M V_{sh} - (Ar_s + B\omega_{es}L_{ls})V_{rh}\cos\varphi - (Br_s - A\omega_{es}L_{ls})V_{rh}\sin\varphi] \end{aligned} \tag{30}$$

where $A = s_h r_s\omega_{es}L_{lr} + r_r\omega_{es}L_{ls}$ and $B = r_r r_s + s_h(\omega_{es}{L_M}^2 - \omega_{es}L_{lr}\omega_{es}L_{ls})$.

3.1.3. Analysis of back-to-back converter at harmonic frequencies

One of the most used equipment in the industry for the control of doubly fed induction generators (DFIG) is the AC-AC three-phase converter. In such equipment, the voltage generated in the DC link (V_{dc}) is provided by a three-phase rectifier, either from the network voltage, or from the power generated in the rotor. This will depend on the velocity of rotation of the generator.

The controlled rectifiers allow a bidirectional flow of power and through appropriate control and modulation; techniques generate virtually sinusoidal input currents. The power factor of this type of rectifiers can be adjusted at will. It should be mentioned that in these devices, the harmonics present in the current are the same as those present in the voltage. Therefore, the ripple that appears on the voltage, just like in the current, is rippled from high frequency due to the switching function. To determine the voltage that is obtained from the inverter, first obtain the voltage in the capacitor according to the following expression:

$$C_{dc}\frac{dv0_{dc}}{dt}=\left\{\sum_{h=n}^{\infty}\left(I_{inv\_h}+I_{rect\_h}\right)\cos\left[\omega_{inv}+\left(\theta_{rect}\right)\right]-\sum_{h=n}^{\infty}\left(I_{inv\_h}+I_{rect\_h}\right)\cos\left[h\omega_{inv}t+\left(\theta_{inv}\right)\right]\right\} \tag{31}$$

Solving, in steady state, with $v_{inv}(0) = V_{inv}$, where V_{inv} represents the average value voltage in the inverter, we have the following expression:

$$v_{inv}=V_{inv}+\sum_{h=n}^{\infty}{}'\frac{I_{inv\_h}}{\omega_{inv}(h\quad 1)}sin\left|\omega_{inv}t(h-1)+(\theta_{inv}-\theta_{inv})\right|-\sum_{h=n}^{\infty}{}'\frac{I_{inv\_h}}{\omega_{inv}(h\quad 1)}sin\left|\omega_{inv}t(h-1)+(\theta_{inv}-\theta_{inv})\right| \tag{32}$$

To obtain the value of the inverter current, it is necessary to know the capacitor current (I_{DC}) and according to the differential equation governing the behavior of the DC bus in the frequency converter, it is known that this capacitor current is given by:

$$C_{dc}\frac{dv_{dc}}{dt}=\frac{1}{2}\left|\left(m_{inv}^{a}I_{inv}^{a}+m_{rect}^{a}I_{rect}^{a}\right)+\left(m_{inv}^{b}I_{inv}^{b}+m_{rect}^{b}I_{rect}^{b}\right)+\left(m_{inv}^{c}I_{inv}^{c}+m_{rect}^{c}I_{rect}^{c}\right)\right| \tag{33}$$

where the switching function $m \in \{-1, 0, 1\}$ is a discrete variable of the modulation SPWM, which is defined as

$$m_1^a=2S_{11}-1,\quad m_1^b=2S_{12}-1\quad and\quad m_1^c=2S_{15}-1 \tag{34}$$

whose mathematical representation can be obtained by decomposition in Fourier series by

$$m_{inv,rect}^{a}=M_{inv,rect}^{a}\,sin\left(\omega_{inv,rect}t+\theta_{inv,rect}\right)+\sum_{h=n}^{\infty}M_{inv,rect}^{a}sin\left(h\omega_{inv,rect}t+\theta_{inv,rect}\right) \tag{35}$$

where ω represents the network frequency; $M_{inv,rect}^{a}$ and $\theta_{inv,rect}$ is the magnitude and phase angle of the fundamental component of the modulation signal, respectively, whereas $M_{inv,rect\_h}^{a}$ and $\theta_{inv,rect\_h}$ represent the magnitude and phase of the harmonic component of the modulation signal. The first term of the summation provides the fundamental component and the second determines the harmonic components. On the other hand, the representation of the line current is given by

$$I_{inv,rect}^{a}=\frac{P_{r,a\,(inv,rect)}}{3V_{inv,rect}}\,sin\left(\omega_{inv,rect}t+\theta_{inv,rect}\right) \tag{36}$$

where P represents the power in inverter and $\theta_{inv,rect}$ the angle of the power factor of $V_{inv,rect}$ which is the phase-neutral effective voltage of the electrical network. Then, the current I_{inv}^{a} a is given by

$$I_{inv}^{a}=I_{inv}^{a}\,sin\left(\omega_{inv}t+\theta_{inv}\right)+\sum_{h=n}^{\infty}M_{inv\_h}^{a}I_{inv}^{a}\,sin\left(h\omega_{inv}t+\theta_{inv}\right)sin\left(h\omega_{inv}t+\theta_{inv}\right) \tag{37}$$

By analyzing only, the harmonic components, previous expression is reduced to

$$I_{inv}^{a}=\sum_{h=n}^{\infty}{}'M_{inv\_h}^{a}I_{inv}^{a}\,sin\left(h\omega_{inv}t+\theta_{inv}\right)sin\left(h\omega_{inv}t+\theta_{inv}\right) \tag{38}$$

In addition, for *b* and *c* phases, the independent products can be calculated by

$$I_{inv}^{a} = \sum_{h=n}^{\infty} M_{inv\,h}^{b} I_{inv}^{b} \sin\left(h\omega_{inv}t + \theta_{inv} - \frac{2\pi}{3}\right) \sin\left(h\omega_{inv}t + \theta_{inv} - \frac{2\pi}{3}\right)$$
$$I_{inv}^{c} = \sum_{h=n}^{\infty} M_{inv\,h}^{c} I_{inv}^{c} \sin\left(h\omega_{inv}t + \theta_{inv} + \frac{2\pi}{3}\right) \sin\left(h\omega_{inv}t + \theta_{inv} + \frac{2\pi}{3}\right) \quad (39)$$

Using the trigonometric identity:

$$\sin A \sin B = \frac{1}{2}[\cos(A-B) - \cos(A+B)]$$

Finally, the sum defined by the above equations is represented by

$$I_{inv} = \frac{1}{2} I_{inv}^{a} \left\{ \sum_{h=n}^{\infty} M_{inv\,h}^{a} \cos[\omega_{inv} t(h \quad 1) + (\theta_{inv} + \theta_{inv})] \quad \sum_{h=n}^{\infty} M_{inv\,h}^{a} \cos[\omega_{inv} t(h+1) + (\theta_{inv} + \theta_{inv})] \right\} +$$
$$\frac{1}{2} I_{inv}^{b} \left\{ \sum_{h=n}^{\infty} M_{inv\,h}^{b} \cos\left[\omega_{inv} t(h-1) - \frac{2\pi}{3}(h-1) + (\theta_{inv} - \theta_{inv})\right] - \sum_{h=n}^{\infty} M_{inv\,h}^{b} \cos\left[s_{inv}\omega_{inv} t(h+1) - \frac{2\pi}{3}(\theta_{inv} + \theta_{inv})\right] \right\} +$$
$$\frac{1}{2} I_{inv}^{c} \left\{ \sum_{h=n}^{\infty} M_{inv\,h}^{c} \cos\left[\omega_{inv} t(h-1) + \frac{2\pi}{3}(h-1) + (\theta_{inv} - \theta_{inv})\right] - \sum_{h=n}^{\infty} M_{inv\,h}^{c} \cos\left[s_{inv}\omega_{inv} t(h+1) + \frac{2\pi}{3}(\theta_{inv} + \theta_{inv})\right] \right\}$$

The same procedure is performed for the network-side converter. The DC link parameter is shown in **Table 1**. **Figures 5** and **6** show the voltage generated and harmonic frequency of the rotor side converter.

Parameters	Value
DC link capacitor	32.5 F
DC link voltage	180 V
Base voltage	176.5 V
Base current	33 A
Base power	22.5 kVA

Table 1. DC link parameters.

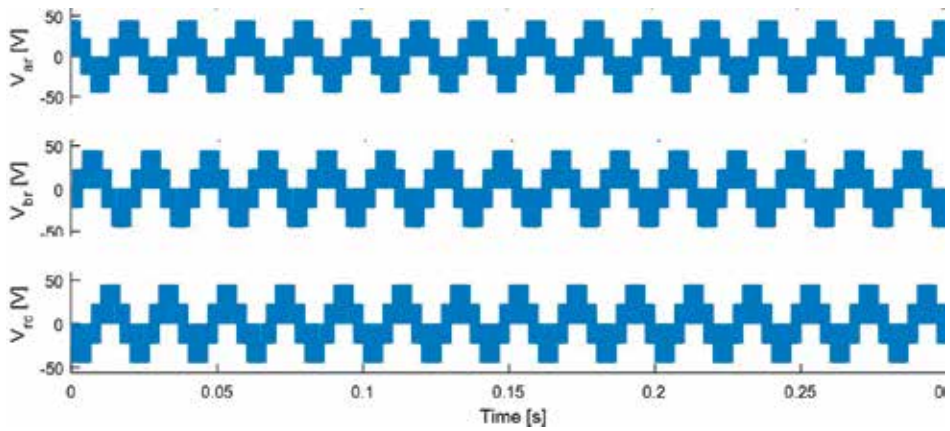

Figure 5. Voltage generated for rotor-side converter.

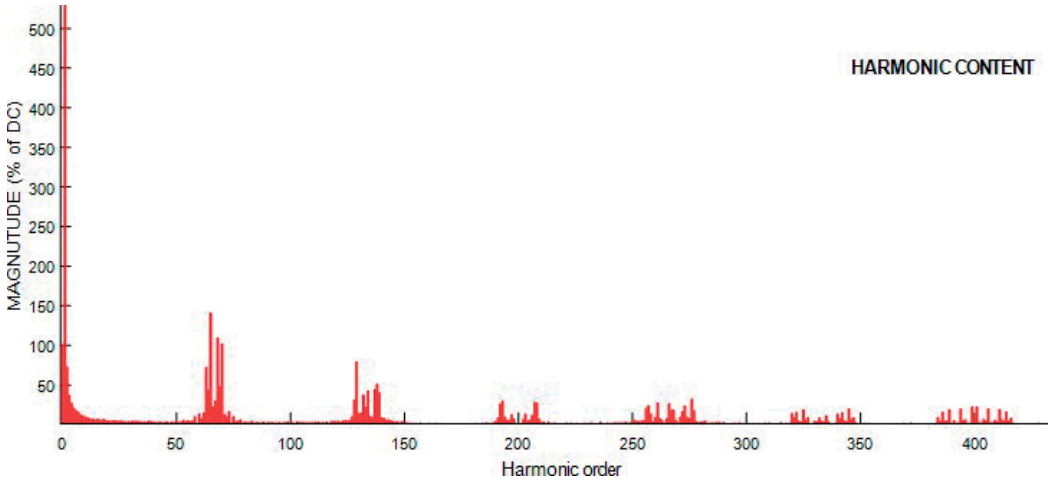

Figure 6. Harmonic frequencies of rotor-side converter.

Figures 7 and **8** show the voltage generated and the harmonic order of the network-side converter. The voltage generated by the converter and shown in **Figure 5** will be the excitation source of the rotor winding. The harmonic slip of rotor-side converter is shown in **Table 2**.

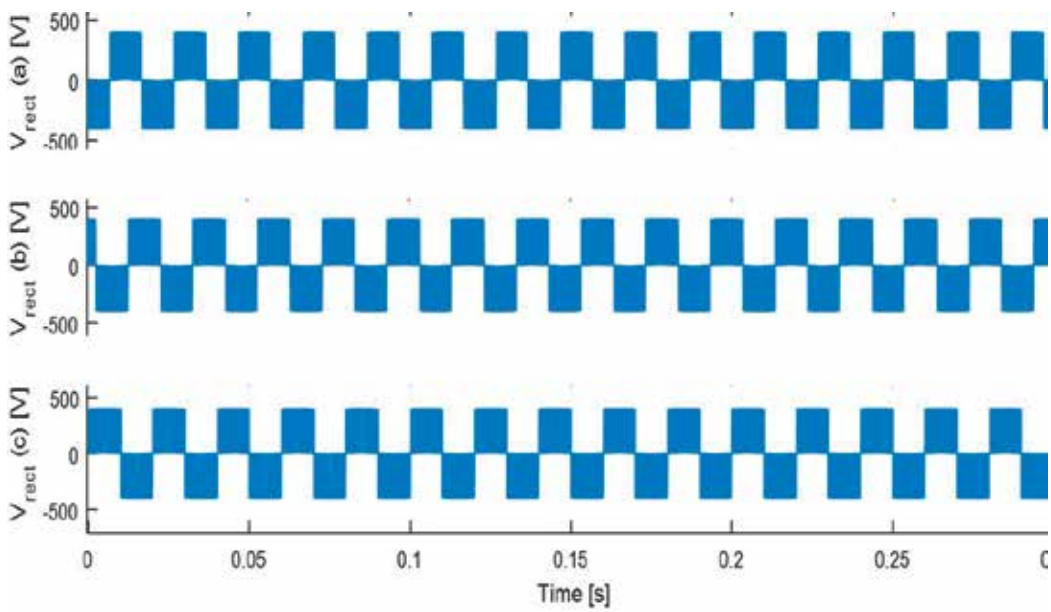

Figure 7. Voltage generated for network-side converter.

http://dx.doi.org/10.5772/intechopen.74584

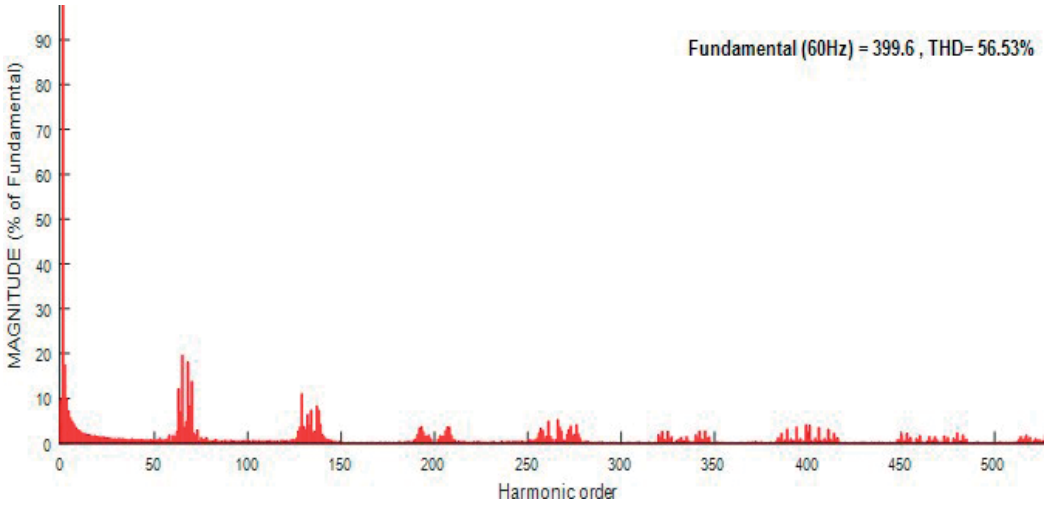

Figure 8. Harmonic order of network-side converter.

Harmonic	**5**	**7**	**11**	**13**	**17**	**76**	**80**	**158**	**159**
Sequence	—	+	—	+	—	+	—	+	—
Harmonic slip	1.21	0.96	1.32	0.97	1.25	0.98	1.01	0.993	1.07

Table 2. Harmonic slip of rotor side converter.

4. Model validation

To validate the proposed model a three-phase generator of 37.5 kW, 460 V, and 46.8 A is used. The induction generator parameters are shown in **Table 3**. Noted that the results obtained from the proposed model (steady-state) are compared with those obtained from the simulated complete model (dynamic) ones the steady-state has been reached. For this case study, a $T_m = 198\ N \cdot m$ in the induction generator was used.

4.1. Case study 1: DFIG excited with conventional *back-to-back* converter

For this case, the generator is excited in the stator windings with a sinusoidal three-phase balanced voltage source of 460 V at 60 Hz shown in **Figure 9**. Rotor windings are excited with a quasi-sine voltage source of 50 V at 45 Hz. The voltage waveforms of rotor winding are shown in **Figure 5**. The stator and rotor current waveforms obtained from dynamic-state are shown in **Figures 10** and **11**, respectively. An expansion of these currents is made once they have reached their steady-state. The electromagnetic torque and the nominal velocity reached by the generator are shown in the **Figures 12** and **13**, respectively.

Parameters	50 HP/37.5 kW
Wind speed	10 m/s
Number of poles	4
Rotor speed	1705 rpm
Inertia	1.662 kg·m^2
Nominal line current	46.8 Amps
Nominal line-to-line voltage	460 Vrms
Nominal torque	198 N.m
Nominal frequency	60 Hz
Stator resistance, r_s	0.087 Ω
Stator inductance, L_{ls}	0.0008010 H
Rotor resistance, r_r	0.228 Ω
Rotor inductance, L_{lr}	0.0008010 H
Magnetizing inductance, $L_{mr} = L_{ms}$	0.347 H

Table 3. Parameters of a 50 HP induction generator.

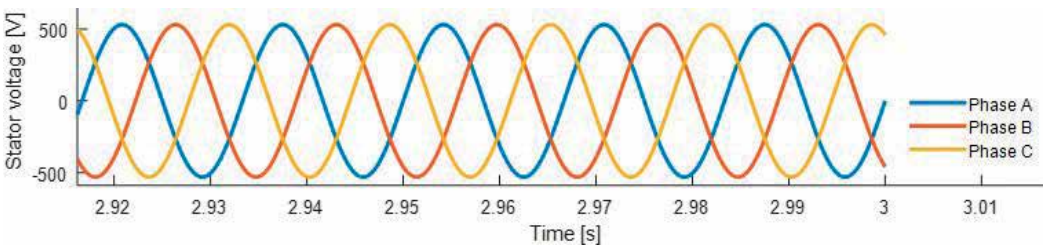

Figure 9. Stator voltage.

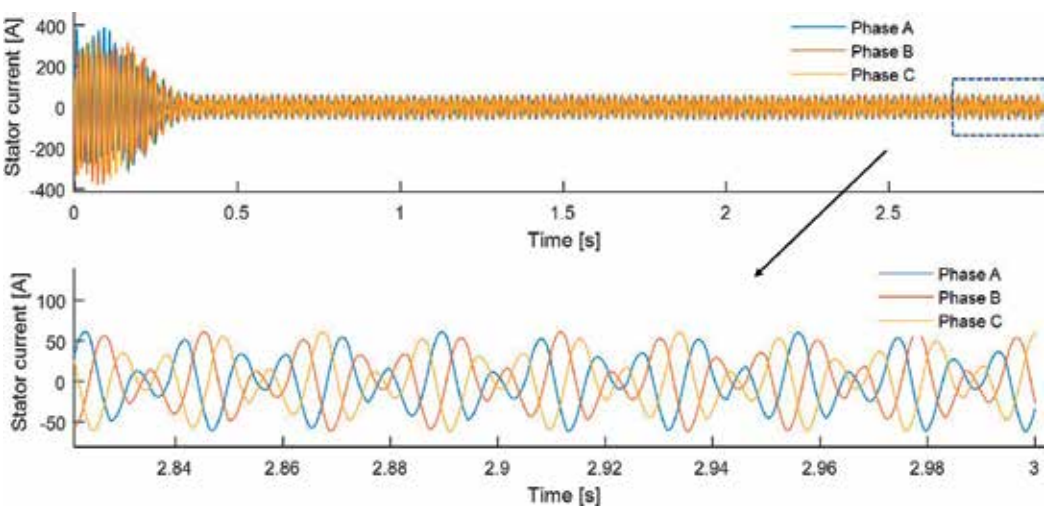

Figure 10. Three-phase stator current in dynamic-state.

http://dx.doi.org/10.5772/intechopen.74584

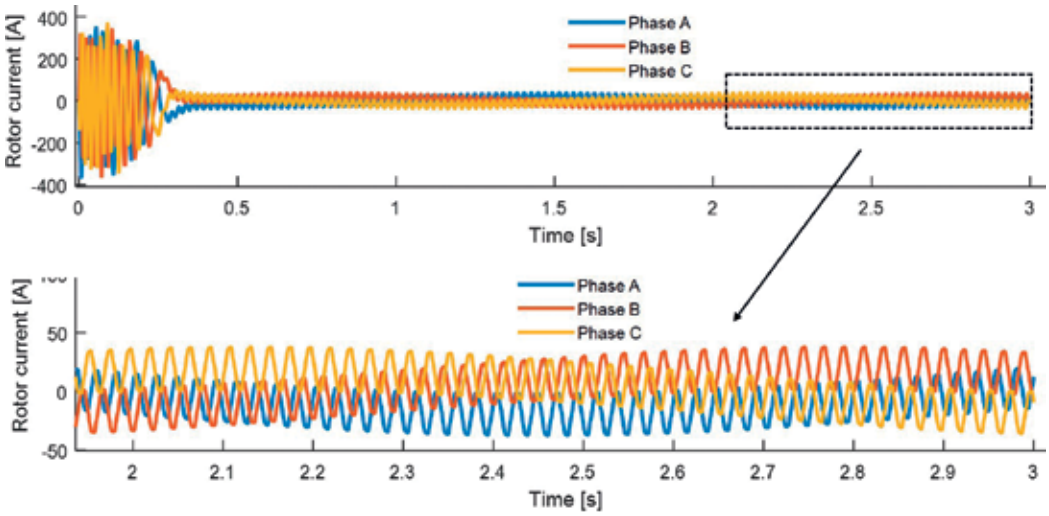

Figure 11. Three-phase rotor current in dynamic-state.

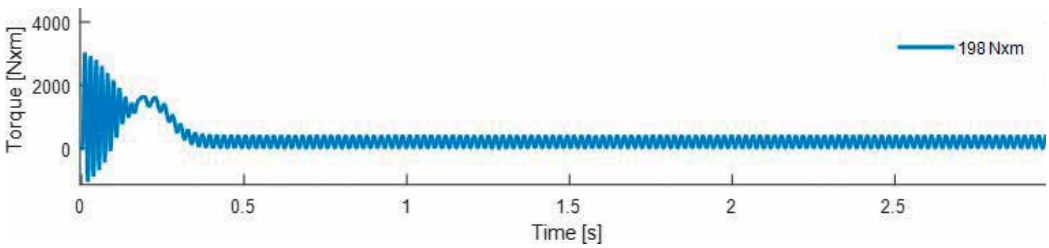

Figure 12. Electromagnetic torque.

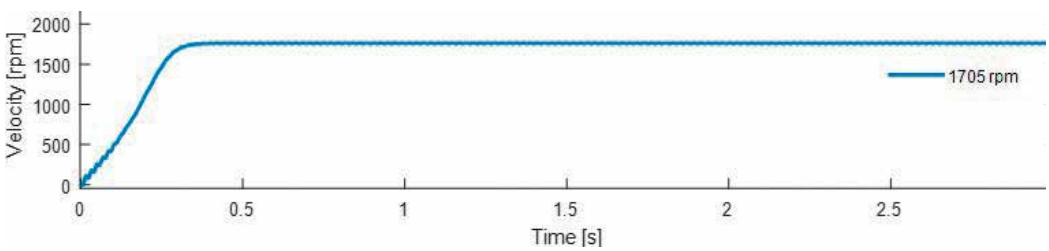

Figure 13. Nominal velocity.

The current waveforms of stator and rotor are obtained from steady-state model and shown in **Figures 14** and **15**, respectively. In addition, an expansion of these currents is made and shown in **Figures 16** and **17**.

Finally, a comparison is made of the forms obtained in both models, both in magnitude and in phase angle, concluding that both models coincide in these aspects. The graphic result of this is shown in **Figures 18** and **19**, respectively.

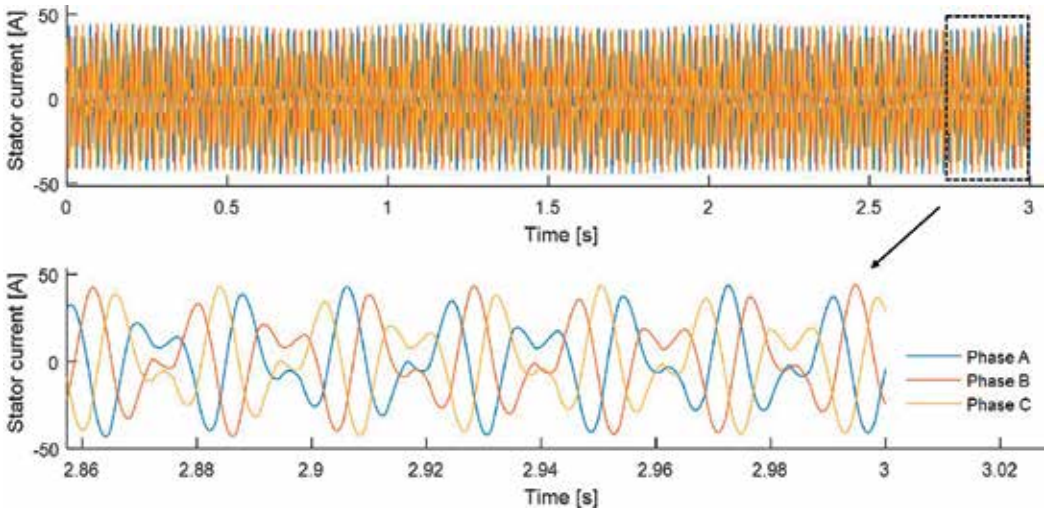

Figure 14. Three-phase stator current in steady-state.

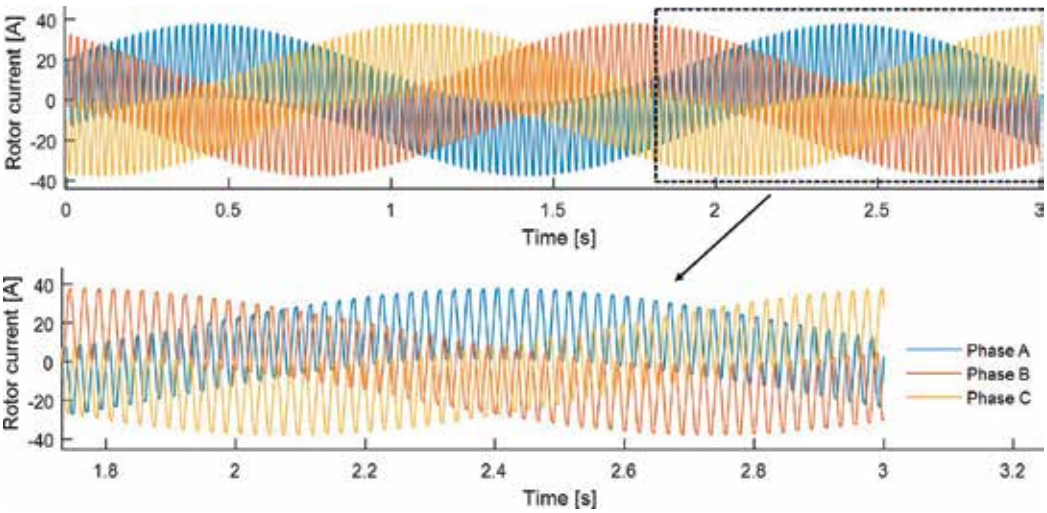

Figure 15. Three-phase rotor current in steady-state.

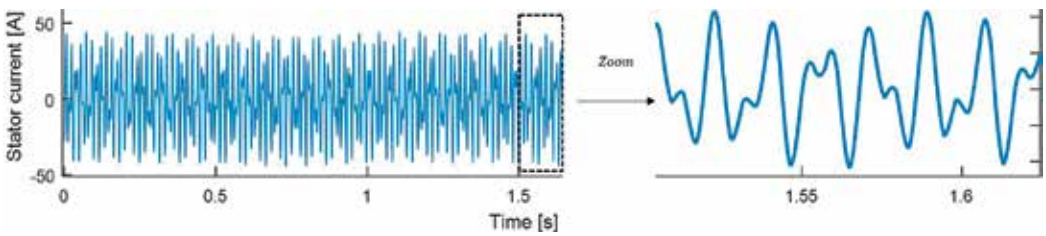

Figure 16. Expansion of the stator current in steady-state.

http://dx.doi.org/10.5772/intechopen.74584

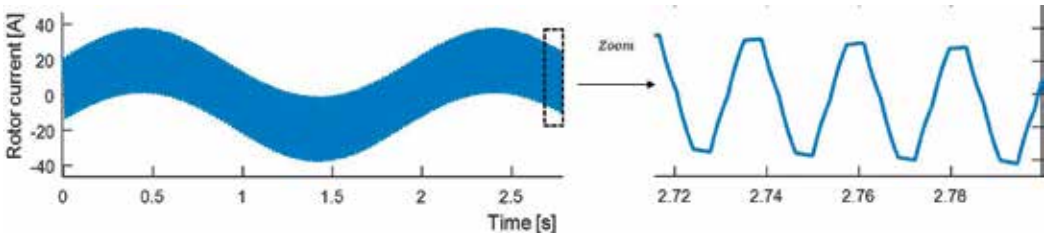

Figure 17. Expansion of the rotor current in steady-state.

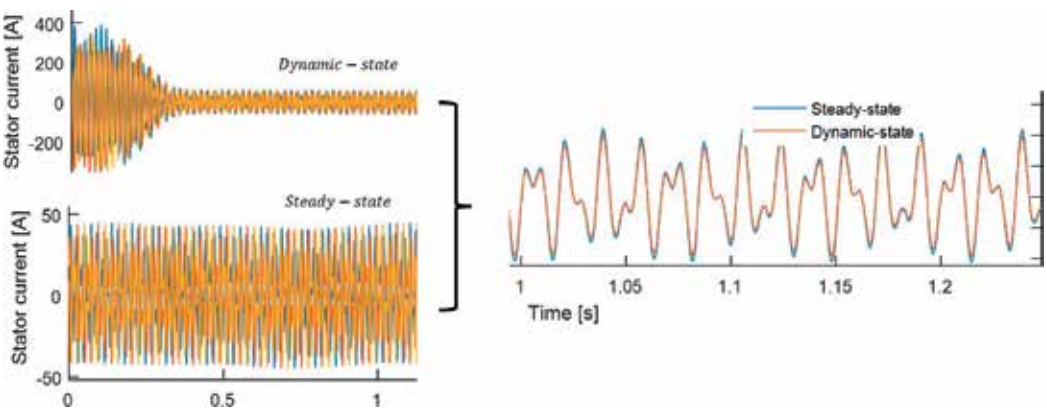

Figure 18. Results comparison of both models: steady-state and dynamic-state, respectively.

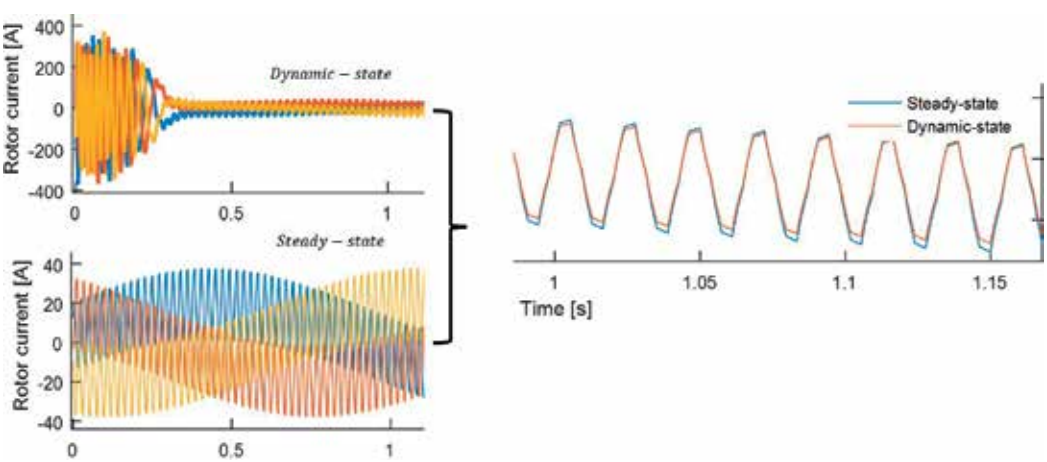

Figure 19. Results comparison of both models: steady-state and dynamic-state, respectively.

5. Incorporation to the electrical network

The integration of wind farms into the network is not an easy problem to solve. Numerous studies have been carried out related to the impact of wind penetration on electric power systems, including those related to stability studies, response of electrical protections and harmonic effects in the electrical network. In some power systems, the penetration of wind energy is rapidly increasing and begins to influence the overall behavior of the system and its stability. In **Figure 20**, it is possible to observe the equivalent diagram of the system to be simulated, which corresponds to the simplification of an induction generator, a frequency converter and typical distribution system. It is presented a three-phase circuit that feeds an industrial load, consisting of a doubly fed induction generator (DFIG), controlled by a back-to-back converter (which injects the harmonic current components).

The presence of harmonics in an electrical power distribution system can bring serious problems, both for the same equipment or system that produces them as for other equipment connected in the same network. The generated harmonic currents interact with the system impedance and cause the voltage distortion, increase the losses and produce effects of overloads connected to the electrical network. Furthermore, they reduce the power factor, given its reactive nature. The presence of harmonic distortion will be more appreciable in some points than in others. However, we can establish that, in general, the effects of harmonics depend on:

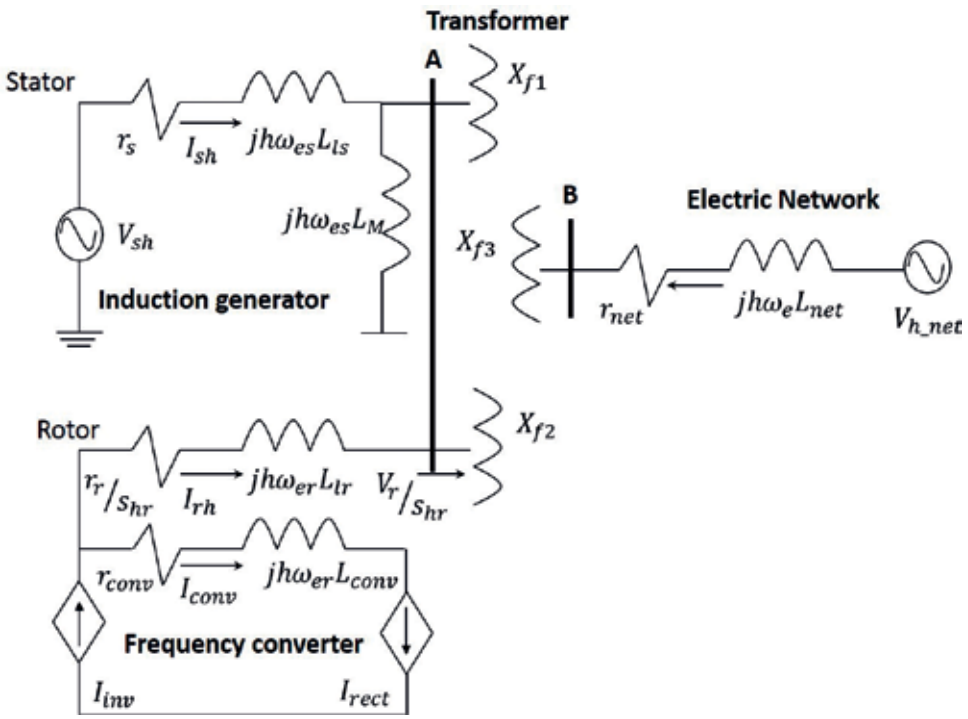

Figure 20. Complete equivalent diagram of WECS connected to the electrical network.

- the elements that generate harmonics, their diversity within the system, the spectral content they inject and their operating regime in time-domain
- the quantity, configuration and values of the elements in the electrical network, both in the time-domain and frequency-domain;
- the sensitivity of the equipment to the presence of harmonic currents or voltages;
- the degree of interest shown by electricity companies and commercial and industrial companies for the harmonic problems that may arise;
- the establishment of norms to set individual total harmonic distortion limits and their compliance on the part of the sectors involved; and
- the effectiveness of standards over time, depending on the technological cases registered in the manufacture of new equipment.

In the study of the effects of harmonics in the distribution systems, it is important to know the propagation paths of the harmonic currents, whose important effect in the system consists in the distortion of the voltage in the different nodes, transferring the harmonic presence to other subsystems. The presence of harmonic voltages results in currents with those harmonic frequencies, which cause additional losses. The induction generator operating with non-sinusoidal voltages cause additional losses due to harmonics. The harmonic losses that occur are losses in stator copper, losses in the core, mechanical losses and losses in the rotor. The largest losses occur on rotor bars (for squirrel cage generator). In addition, harmonic losses are independent of the generator load, but may be much greater than losses due to a pure sine wave, depending on the harmonic content of the applied voltage waveform. These factors raise the temperature of all generator components reducing the efficiency and the useful life. This elevation in temperature may result in excessive heating and may not meet the demands of the load coupled to its axis, or resulting in the destruction of the generator. Harmonic currents cause increased losses in copper for to the skin effect due to their high frequencies, cause insulation stresses, Eddy current losses in the conductive parts and possible resonance at a harmonic frequency between the inductive reactance of the transformer and the capacitance of the line or capacitors for power factor improvement.

The effect of the losses, then, is an increase in the heating of the transformer, which may be significant. Due to behavior of triple harmonic currents in three-phase systems, the three currents of line are in phase, and when they reach the center of a wye connection, they will return through the neutral or ground. This fact, although the three-phase system is perfectly balanced, can cause the heating of cables and connectors when its ampacity is exceeded.

5.1. Power-quality problems of WECS connected to the electrical network

The term 'power quality' refers to voltage and frequency stability, and the absence of various forms of electrical noise (e.g., flicker or harmonic distortion) in the electrical network. Generally, electric companies (and their customers) prefer an AC with a sinusoidal waveform, free of interruptions or disturbances. The consequences of large-scale supply incidents are well

documented. A recent study in the United States has shown that digital industrial and commercial firms are losing $ 45.7 billion per year because of power network disruptions. In all commercial sectors, it is estimated that between 104,000 and 164,000 million dollars are lost due to interruptions and another 15,000–24,000 million dollars because of other power quality problems in the network. Many problems in the supply originate in the electric network that with its thousands of miles of transmission is subject to climatic conditions such as hurricanes, storms with snow, ice and floods, along with equipment failures, traffic accidents and major operations of connection.

The power quality study and ways to control it is a topic of interest for electricity suppliers, large industrial companies, businesses and even residential users. The study has intensified as teams have become increasingly sensitive to even minimal changes in voltage, current and frequency in the supply. The Institute of Electrical and Electronics Engineers (IEEE) has developed a standard that includes definitions of energy disturbances. The standard (Standard 1159–1995 of the IEEE, IEEE Recommended Practice for Monitoring Electric Power Quality) describes many problems of the power quality. Regarding the wind sector, there are regulations that regulate the limits for this type of problems, as indicated by the IEC 61400-21 standard. The IEC–61400-21 standard provides recommendations for preparing the measurements and assessment of power-quality characteristics of wind turbines. The measurement procedures described in the IEC61400-21 standard are valid to test the power-quality characteristic parameters for the full operational range of a wind turbine, connected to a MV or HV network with fixed frequency within ±1 Hz, sufficient active and reactive power regulation capabilities and sufficient load to absorb the wind power production.

5.1.1. Start and stop of the wind turbine

Most of the electronic wind turbine power controllers are programmed so that the turbine runs in no-load at low wind speeds (if it were connected to the network at low wind speeds, in fact it would work as an engine). Once the wind becomes strong enough to rotate the rotor and generator at its rated speed, it is important that the turbine generator be connected to the power network at the appropriate time. If this is not the case, only the mechanical strength of the multiplier and the generator will be present to prevent the rotor from accelerating, and eventually it will be packed (there are various safety devices, including fail-safe brakes, in the case that the of correct start fail).

5.1.2. Soft-started with thyristors

If a high-power wind turbine is connected to the electrical network by means of a normal switch, a partial dimming would be observed (due to the current required to magnetize the generator), followed by a power peak, due to the generator current overloading. Another unpleasant side effect when using 'hard' switches would be to apply extra wear to the multiplier, since the generator connection would act as if the mechanical brake of the turbine were suddenly activated. To avoid this situation, modern wind turbines have a soft-start; they are connected and disconnected from the electrical network gradually by means of thyristors, a type of semiconductor continuous switch that can be controlled electronically. Thyristors lose

about 1–2% of the energy that passes through them. Thus, modern wind turbines are usually equipped with a switch called 'drift', that is, a mechanical switch that is activated after the turbine has made the soft start. In this way, the amount of energy lost is minimized.

5.1.3. Weak electrical network

If a turbine is connected to a weak electrical network (i.e., it is very far in a remote corner of an electrical network with a low-power transport capacity), there may be some problems of partial obscuration and/or power overvoltage. In these cases, it may be necessary to reinforce the electrical network to transport the AC from the wind turbine. The local power company is experienced in dealing with these voltage problems, as they are the exact reflection of what happens when a large user (e.g., a factory with large electric motors) is connected to the electrical network.

5.1.4. Islanding

'Islanding' is a situation that can occur if a section of the electrical network is disconnected from the main electrical network, as would happen by accidental or intentional tripping of a large circuit breaker in the network (e.g., due to stoppages in the network electrical supply or short-circuits in the network). If the wind turbines continue to operate in the part of the network that has been isolated, it is very likely that the two separate networks are not in phase after a short interval of time. The restoration of the connection to the main power network can cause huge overcurrent's in the wind turbine network and generator. This would also cause a great release of energy in the mechanical transmission (i.e., in the axes, the multiplier and the rotor), as would a 'hard connection' from the generator of the turbine to the electrical network. Thus, the electronic controller will have to constantly monitor the voltage and frequency of the AC of the network. In the event that the voltage or frequency of the local network are within certain limits for a fraction of a second, the turbine will automatically disconnect from the network, and immediately afterwards it will stop (normally activating the aerodynamic brakes).

The distributed generation (generation of electricity through of solar panels, wind farms, etc.), is increasingly having a greater presence in the world, in the case of the sector of self-consumption and injection of surplus energy into the network. This factor causes that the energy systems supplier has more advanced control means to verify the variations of loads that cause important fluctuations in the parameters of the voltage, injection of harmonics, change in the power factor, greater technical losses, among others. Therefore, it is advisable to make a power-quality study in an industry, commerce or home. This analysis must be done with high-resolution RMS equipment in order to detect and accurately measure the different parameters mentioned.

5.2. Case study 2. DFIG excited with three-phase *back-to-back* converter SPWM to improve the power quality

For this case, the generator is excited in the stator windings with a sinusoidal three-phase balanced voltage source of 460 V at 60 Hz shown in **Figure 9** and rotor winding is excited with a quasi-sine voltage source of 50 V at 45 Hz to which the SPWM switching technique was

applied. The stator and rotor current waveforms obtained from dynamic-state are shown in **Figures 21** and **22**, respectively. An expansion of these currents is made once they have reached their steady-state.

The current waveforms of stator and rotor are obtained from steady-state model and shown in **Figures 23** and **24**, respectively. In addition, an expansion of these currents is made and shown in **Figures 25** and **26**.

Finally, a comparison is made of the forms obtained in both models, both in magnitude and in phase angle, concluding that both models coincide in these aspects. The graphic result of this is shown in **Figures 27** and **28**, respectively.

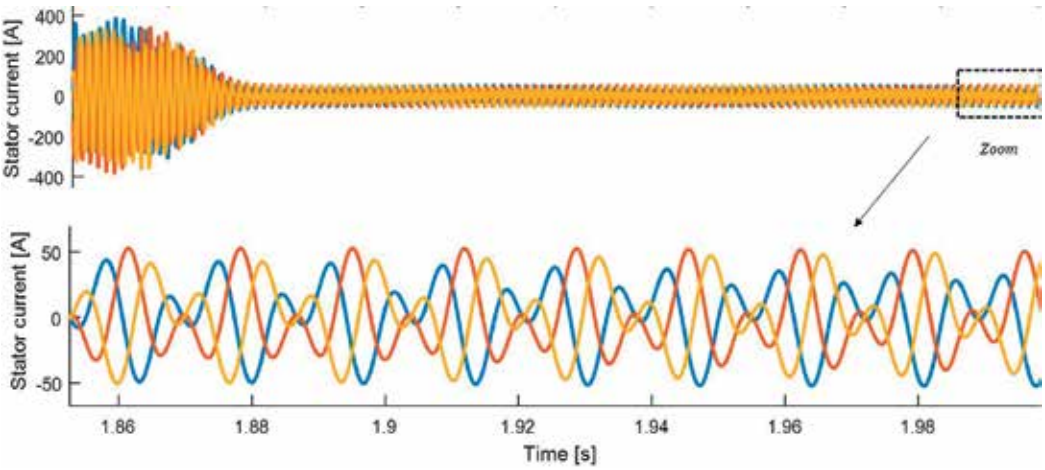

Figure 21. Three-phase stator current in dynamic-state.

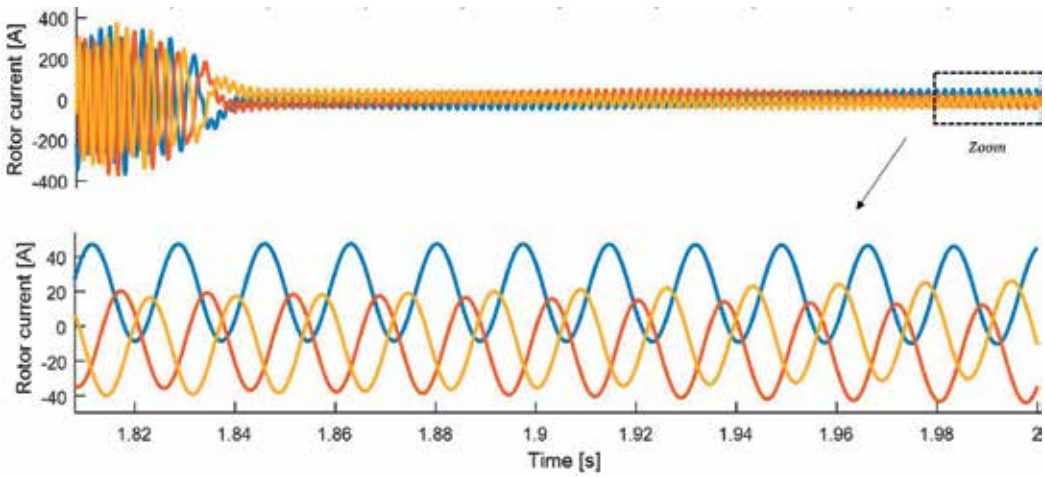

Figure 22. Three-phase rotor current in dynamic-state.

http://dx.doi.org/10.5772/intechopen.74584

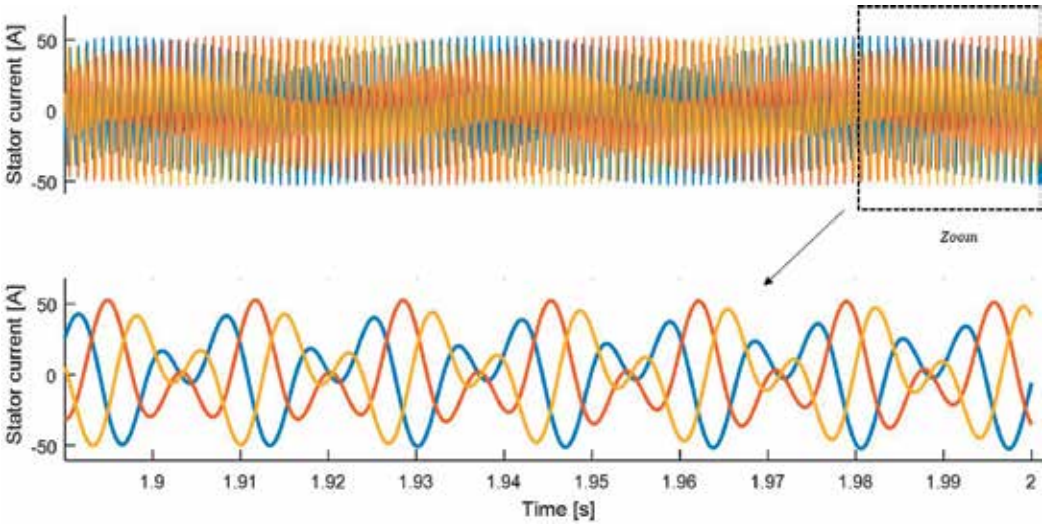

Figure 23. Three-phase stator current in steady state.

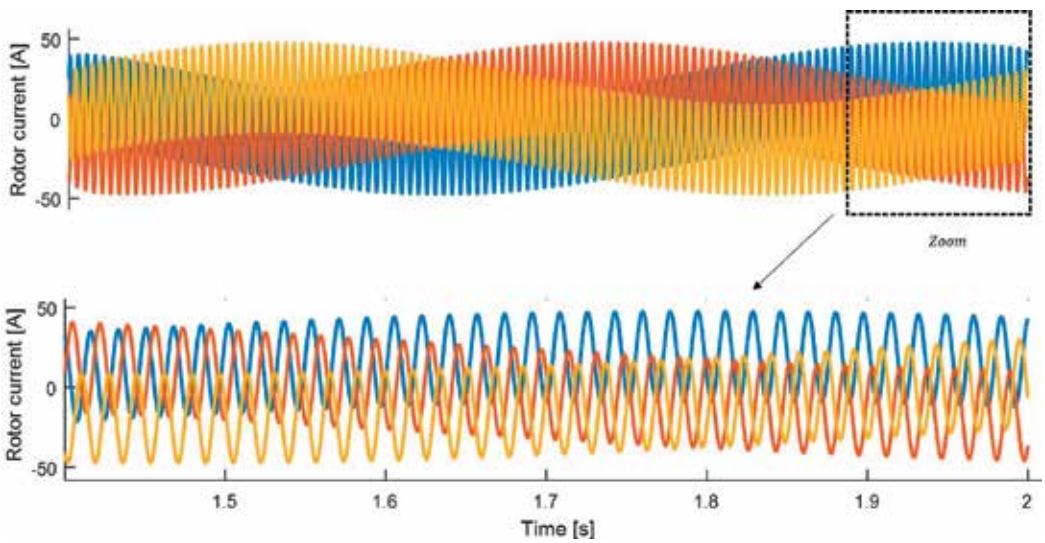

Figure 24. Three-phase rotor current in steady state.

5.3. Analysis of simulation results

The doubly fed induction generator (DFIG) interconnected to the electric network is simulated based on a steady-state model. This proposed model consists of the integration of induction generator, frequency converter and the electric network. Each of those sections is then analysed.

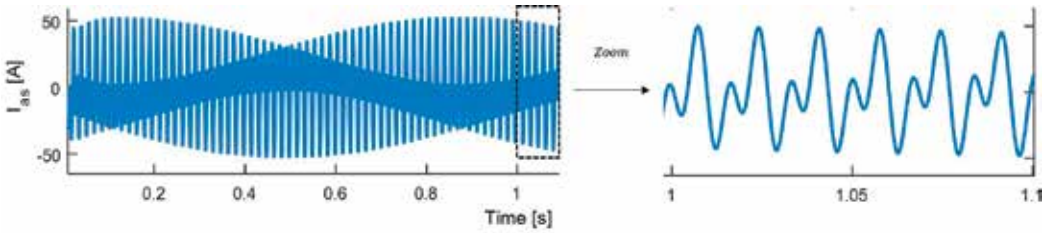

Figure 25. Zoom of **Figure 23**.

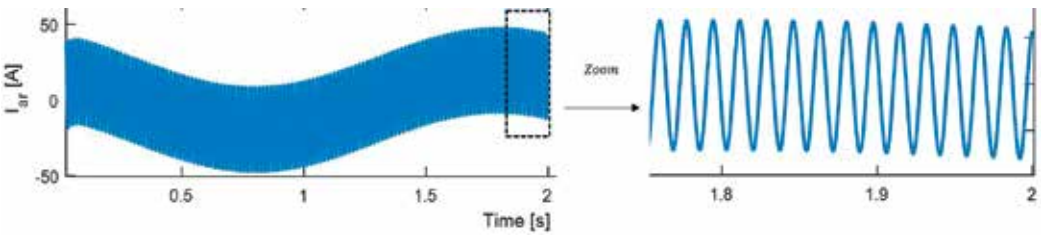

Figure 26. Zoom of **Figure 25**.

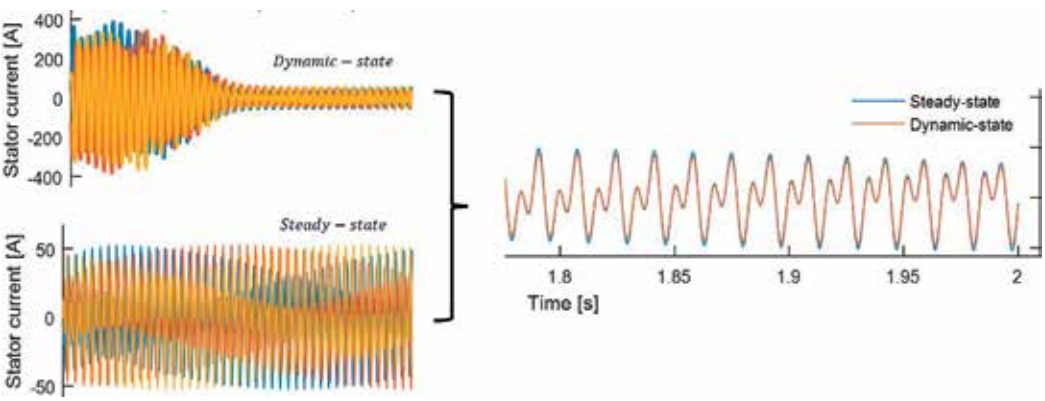

Figure 27. Results comparison of both models: steady-state and dynamic state, respectively.

5.3.1. Rotor-side non-sinusoidal voltage source

Once the harmonic slip for each harmonic signal is determined, the frequencies generated in the rotor-side non-sinusoidal voltage source are obtained as shown in **Table 2**. **Figure 29** shows the frequency spectrum of rotor side non-sinusoidal voltage source. There are harmonics of the order $(6h \pm 1)$ where the signs + and − express the positive and negative sequences (−5, 7, −11…); these components generate rotating magnetic fields with the identical or opposite direction of the fundamental field. The rotor voltage during commutation is equal to half of the sum of two-phase voltages that are under commutation with the rotor-line voltage being zero in this period.

http://dx.doi.org/10.5772/intechopen.74584

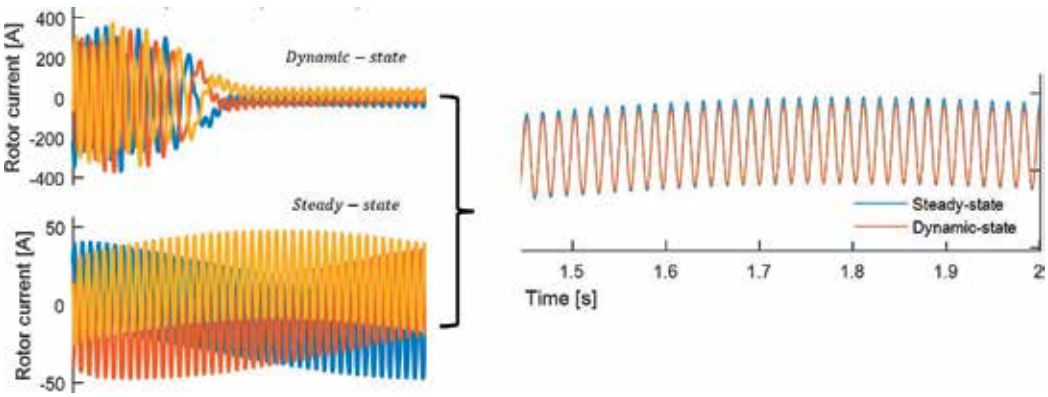

Figure 28. Results comparison of both models: steady-state and dynamic state, respectively.

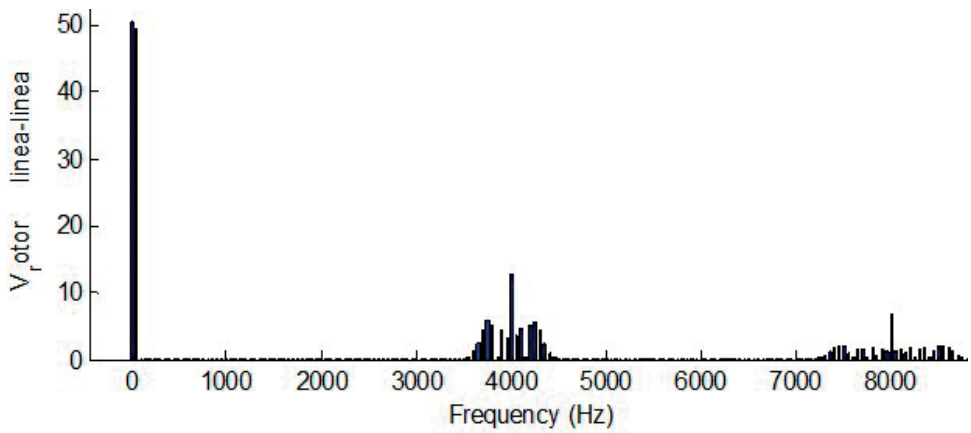

Figure 29. Frequency spectrum of rotor side non-sinusoidal voltage source.

$$f_{hr} = |1 \pm 6h|s_{hr}f_f = |1 - 6(5)| \times 1.21 \times 8.24 = 289.14\ Hz$$

$$f_{hr} = |1 \pm 6h|s_{hr}f_f = |1 + 6(7)| \times 0.96 \times 8.24 = 340.14\ Hz$$

$$f_{hr} = |1 \pm 6h|s_{hr}f_f = |1 - 6(11)| \times 1.32 \times 8.24 = 706.992\ Hz$$

$$f_{hr} = |1 \pm 6h|s_{hr}f_f = |1 + 6(13)| \times 0.97 \times 8.24 = 631.43\ Hz$$

$$f_{hr} = |1 \pm 6h|s_{hr}f_f = |1 + 6(76)| \times 0.9811 \times 8.24 = 3683.29\ Hz$$

$$f_{hr} = |1 \pm 6h|s_{hr}f_f = |1 - 6(80)| \times 1.0198 \times 8.24 = 4022.34\ Hz$$

$$f_{hr} = |1 \pm 6h|s_{hr}f_f = |1 + 6(158)| \times 0.993 \times 8.24 = 7787.390\ Hz$$

$$f_{hr} = |1 \pm 6h|s_{hr}f_f = |1 - 6(159)| \times 1.0173 \times 8.24 = 8002.05\ Hz$$

5.3.2. Electrical network analysis

The network voltage could only be influenced by non-ideal voltage modulation, if the power of the modulated source is in the same class as the network. However, the harmonic current flow over the network generating always-harmonic voltage, which shows undesired effects in the network, independent from the power of the harmonic current source. This means, that harmonic currents are always of high interest for the resulting power quality of the electrical network. For this case, a harmonic voltage and harmonic current of the network is considered. **Figures 30** and **31** present the network current and the network voltage, respectively.

5.3.3. Stator and rotor current analysis

The stator current waveform is shown in **Figure 23** where it is observed that it contains considerable harmonic components. The interaction between the rotor flux harmonics and the fundamental flux in the air-gap induces currents in the stator which are not integer multiple of the supply frequency. These are commonly called inter-harmonic with stator current fluctuation. The harmonic in the rotor are induced in the stator due to the dominant rotor harmonics (harmonic numbers are fifth and seventh).

The behavior of the rotor current in steady-state is shown in **Figure 25**. The ripples on the rotor current and its large rate of variation result in pulsed voltage waveforms. The rotor harmonic current establishes rotating magnetic fields in the air-gap, inducing currents of corresponding frequencies to the stator winding. It is known that the $6h + 1$ harmonics of the rotor current set

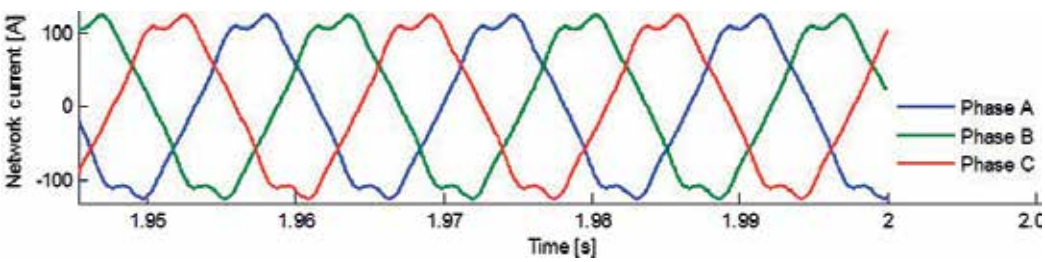

Figure 30. Electrical network current.

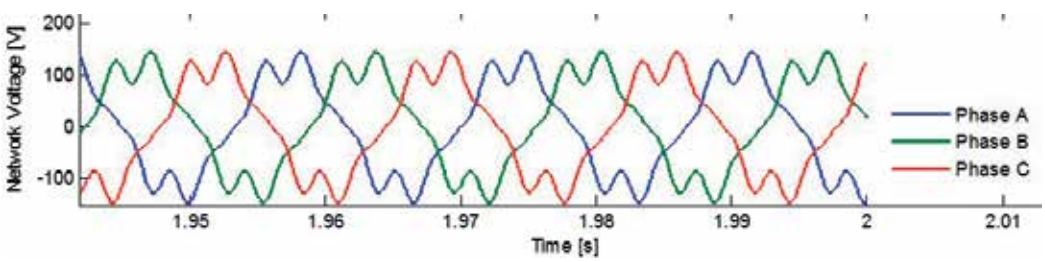

Figure 31. Electrical network voltage.

up positive sequence magnetomotive force (MMF) waves, rotating in the same direction as the fundamental rotor MMF, whereas the $6h-1$ harmonics establish negative sequence MMFs. Since the fundamental rotor MMF rotates in the same direction as the rotor for s > 0 (motoring mode) and in the opposite for $s < 0$ (regenerative mode), the angular velocity of the rotating MMFs relative to the rotor is always $(1 \pm 6h)sf_{es}$. Adding the rotor velocity, $(1 - s)f_{es}$, yields the velocity of the rotating MMF waves relative to the stator and, therefore, the frequency of the induced harmonic currents is obtained with: $f_{es\_h} = |1 \pm 6hs|f_{es}, h = 0,1,2,3\ldots$. Similarly, the rotor side-band frequencies due to the rotor-side converter harmonics also set up MMF waves, rotating at $[(1 \pm 6h)s \pm 6m]\, f_{es}$, with respect to the rotor. The frequency of the induced harmonic currents to the stator is then: $|1 \pm 6hs \pm 6_m|f_{es}$, h, $m = 0,1,2,3\ldots$. Since the slip s is non-integer, the harmonic content of stator current consists mainly of sub- and inter-harmonics, which create undesirable effects on the supply system. For instance, low-frequency sub-harmonics appear as unidirectional components superimposed on the phase currents, while sub- and inter-harmonics neighbouring to the supply frequency may create a beat effect on the stator current magnitude. The rotor harmonic current due to the switching of the transistor appear at frequencies $f_{er\_h} = (6h \pm 1)|s|f_{es}$, $h = 0,1,2,3\ldots$, that is, at the 5th, 7th, 11th, 13th … of the fundamental rotor frequency $|s|f_{es}$ $h = 0$ for the fundamental.

The DC current distortion introduced by the network-side converter (at the frequencies f_{dc_h}) is also reflected on the rotor currents, however, resulting in the appearance of additional harmonics. More specifically, each rotor-side converter-related harmonic frequency f_{dc_h} of the DC current is superposed on the harmonics f_{er_h} of the rotor current, resulting in the appearance of two 'side-bands' at frequencies $|f_{er\_h} \pm f_{dc\_h}|$. Hence, the full harmonic content of the rotor current is given by: $f_{es\_h} = |(6h \pm 1)s \pm 6m|f_{es}$, $h,m, = 0,1,2,3\ldots$.

It explains only the harmonic frequencies at 20 Hz (fundamental rotor frequency), 100, 140, 220, 260, 340 and 380 Hz, corresponding to h = 1, 5, 7, 11, 13, 17 and 19. For instance, the spectral lines at 280 and 320 Hz result from the interaction of the 20 Hz fundamental rotor frequency with the basic inverter DC harmonic at 300 Hz $[20 \pm 300]$Hz, for $h = 0$ and $m = 1$]. **Table 4** resumes the harmonic currents in the induction generator for this research. Note that the waveform of current presented in **Figures 23** and **25** has been attained from the current shown in **Table 4**.

5.4. Case study 3. High-power DFIG excited with *back-to-back* converter

Finally, a last case study of the doubly fed induction generator is presented. To validate the proposed model, a three-phase generator of 372.8 kW, 2300 V and 93.8 A at 60 Hz is used. The rotor windings are excited with a quasi-sine voltage source of 500 V at 45 Hz. The induction generator parameters are shown in **Table 4**.

For this case study, a $T_m = 1980\ N$ in the induction generator was used. The stator and rotor current waveforms obtained from dynamic-state are shown in **Figures 32** and **33**, respectively.

The electromagnetic torque and the nominal velocity reached by the generator are shown in the **Figures 34** and **35**, respectively. The current waveforms of stator and rotor are obtained

Case study	Stator current				Rotor current			
	Sequence (+, –, 0)	Magnitude (%)	Angle (°)	Frequency (Hz)	Sequence (+, –, 0)	Magnitude (%)	Angle (Degrees)	Frequency (Hz)
Case I	+	100	−64.3	60	+	100	160.2	19.8
		31.2	176.2	180	–	16	205.1	100
	–	19.7	172.4	300	+	14	197.7	140
	+	14.3	186.4	420	–	12	128.1	220
	+	3.6	52.9	72.6	+	11	201.7	260
	–	2.1	−3.5	151.2	–	2.3	188.7	340
	+	1.1	−6.8	210.7	+	2	192.8	380
	–	0.74	7.2	330.1	–	1.7	195	460
	+	0.56	186.1	408.2	+	1	175	500
	–	0.23	192.1	533.8	–	0.9	178.2	580
	+	0.21	200	596.6	+	0.8	195	620
	–	0.08	202	722.2	–	9.6	209.8	1540
	+	0.07	203.7	750	+	8.2	209.5	1640
	–	0.02	206.2	910.6	–	4.9	236.4	3140
	+	0.01	212.8	973.4	–	4.2	237.9	3160

Table 4. Summary of the harmonic current for the case study.

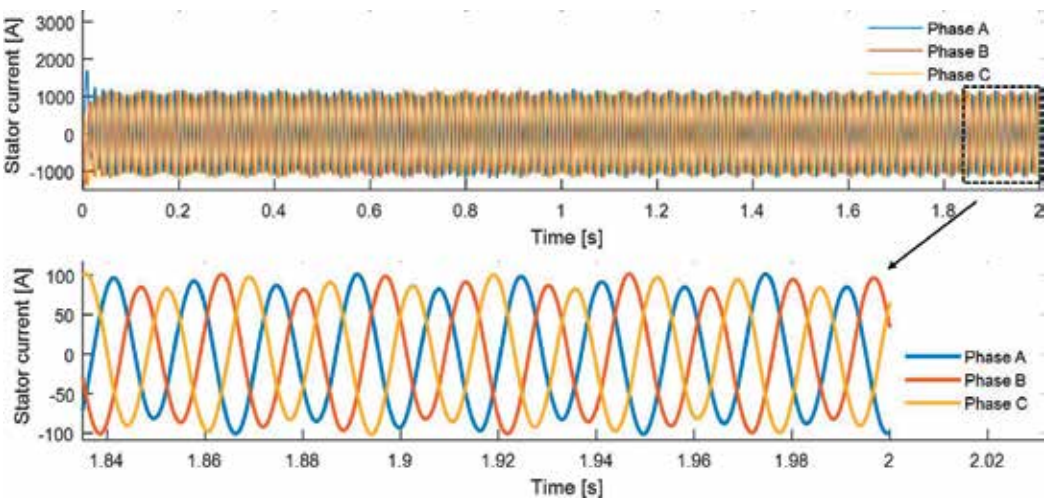

Figure 32. Three-phase stator current in dynamic-state.

http://dx.doi.org/10.5772/intechopen.74584

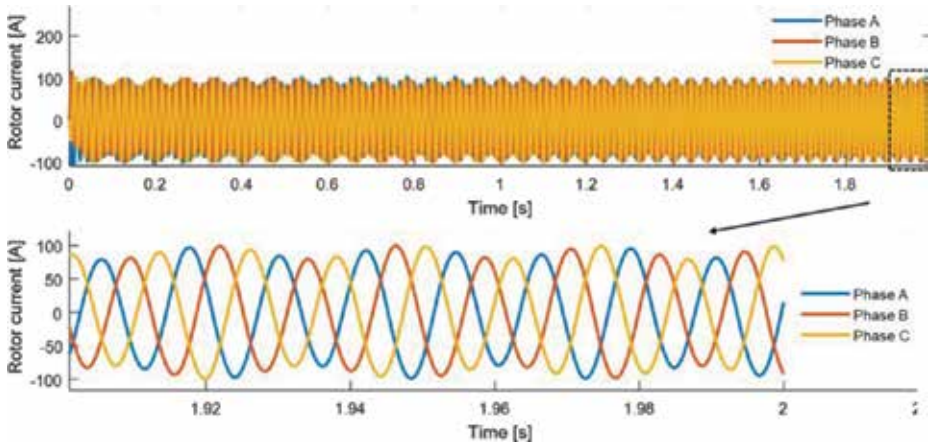

Figure 33. Three-phase rotor current in dynamic-state.

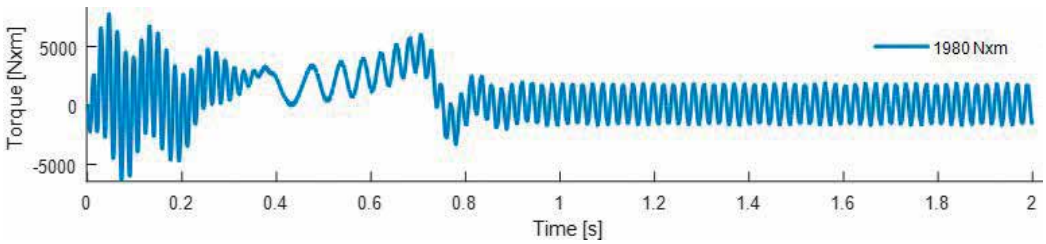

Figure 34. Electromagnetic torque.

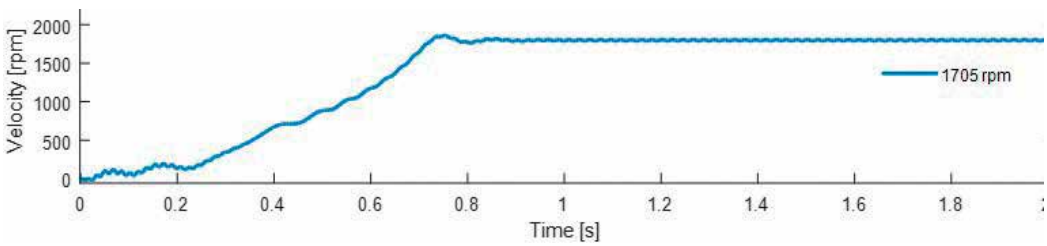

Figure 35. Nominal velocity.

from steady-state model and shown in **Figures 36** and **37**, respectively. Also, an expansion of these currents is made and shown in **Figures 38** and **39**.

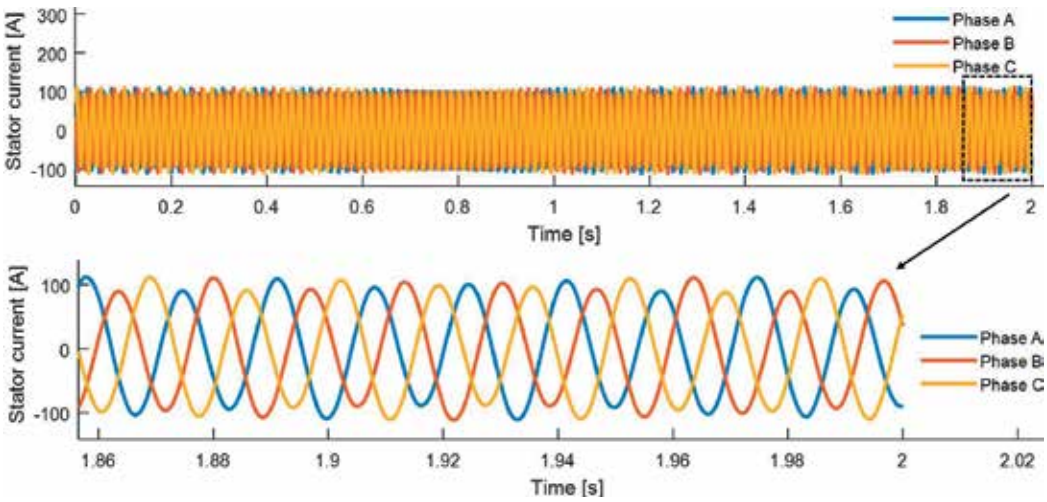

Figure 36. Three-phase stator current in steady-state.

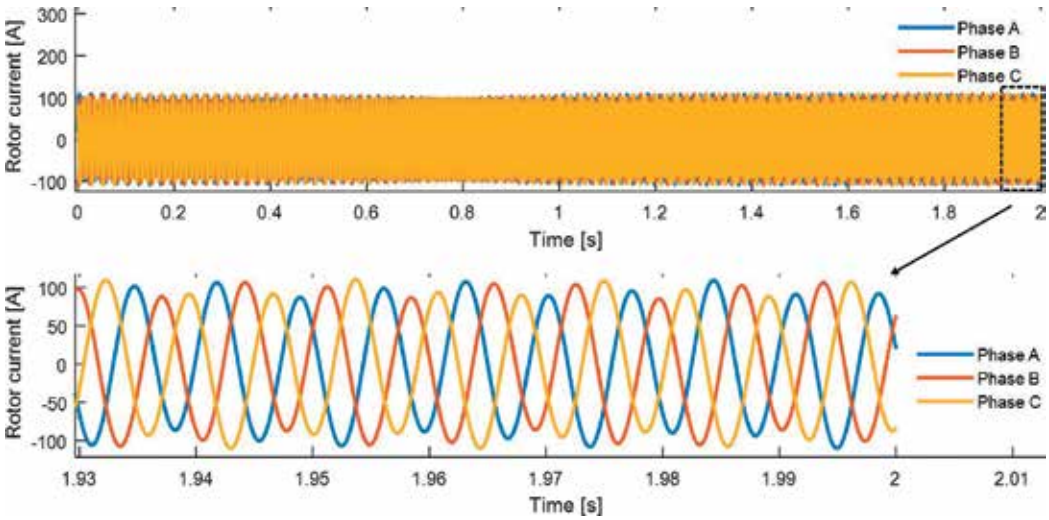

Figure 37. Three-phase rotor current in steady-state.

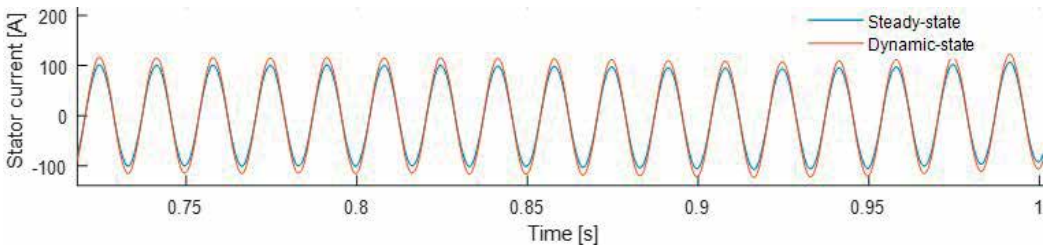

Figure 38. Results comparison of both models: steady-state and dynamic state, respectively.

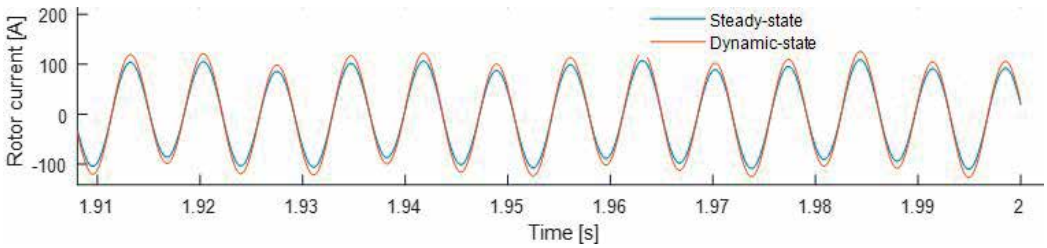

Figure 39. Results comparison of both models: steady-state and dynamic state, respectively.

Parameters	**500 HP/372.8 kW**
Wind speed	10 m/s
Number of poles	4
Rotor speed	1773 rpm
Inertia	11.06 kg·m^2
Nominal line current	93.6 Amps
Nominal line-to-line voltage	2300 Vrms
Nominal torque	1980 N.m
Nominal frequency	60 Hz
Stator resistance, r_s	0.262 Ω
Stator inductance, L_{ls}	0.0032 H
Rotor resistance, r_r	0.187 Ω
Rotor inductance, L_{lr}	0.0032 H
Magnetizing inductance, $L_{mr} = L_{ms}$	0.1432 H

Table 5. Parameters of a 500 HP induction generator.

Noted that the results obtained from the proposed model (steady-state) are compared with those obtained from the simulated complete model (dynamic) ones the steady-state has been reached (**Table 5**).

6. Conclusion

Based on the results of this research, we propose a wind turbine model based on a double-fed induction generator for harmonics propagation studies. This model consists of three stages: analysis of the induction generator, analysis of the frequency converter and analysis of the electric network. It should be mentioned that the models were developed in steady-state and dynamic-state. Finally, the three stages are integrated for the development of a single model for

the harmonic analysis of the double-fed induction generator interconnected to the electrical network. The results indicate harmonic and non-harmonic currents can exist in both generator windings depending on the slip and the fundamental frequency in both voltage sources. The results of the steady-state simulation were compared with the results in dynamic-state model obtaining great similarity in the waveforms of the currents in the stator and rotor, in both magnitude and phase angle resulting in a proper model for harmonic and non-harmonic analysis of the doubly fed induction generator (DFIG) which can be used for 'harmonic' analysis in electrical power systems.

Author details

Emmanuel Hernández Mayoral*, Miguel Ángel Hernández López,
Hugo Jorge Cortina Marrero and Reynaldo Iracheta Cortez

*Address all correspondence to: emanuel.mayoral7@gmail.com

Universidad del Istmo, Av. Universitaria s/n Bo. Santa Cruz Tagolaba, Tehuantepec, Oaxaca, Mexico

References

[1] Arrillaga D, Bradley A, Bodger PS. Power System Harmonics. 2nd ed. California: John Wiley & Sons; 1989. p. 500

[2] Randall RB. Application of B and K Equipment to Frequency Analysis. 1st ed. USA: Bruel and Kjaer; 2003. p. 485

[3] Kreyzig E. Advanced Enginnering Mathematics. 6th ed. USA: John Wiley & Sons; 2010. p. 806

[4] Bergland GD. A Fast Fourier Transform Algorithm for Real Valued Series. Communications of the ACM. 1st ed. England; 1986. p. 710

[5] Carrasco JM, Franquelo LG, Bialasiewicz JT, Member S, Galván E, Guisado RCP, Member S, Ángeles M, Prats M, León JI, Moreno-Alfonso N. Power-electronic systems for the grid integration of renewable energy sources: A survey. IEEE Transactions on Industrial Electronics. 2006;**53**(4):1002-1016

[6] Arcega FJ, Pardina A. Study of harmonics thermal effect in conductors produced by skin effect. IEEE Latin American Transaction. 2014;**26**(1):1488-1495

[7] Hu J, Nian H, Xu H, He Y. Dynamic modeling and improved control of DFIG under distorted grid voltage conditions. IEEE Transaction Energy Conversion. 2011;**26**(1):163-175

[8] Amini J. Novel control method of grid connected converter of doubly fed induction generator to achieve disturbances rejection. In: International Conference on Environment and Electrical Engineering. Washington, DC; 2011. pp. 1-5

[9] Mora-Barajas M, Bañuelos-Sánchez P. Contaminación armónica producida por cargas no lineales de baja potencia: modelo matemático y casos prácticos [dissertation]. Madrid: 2010. p. 111

[10] Comech MP. Análisis y Ensayo de Sistemas Eólicos ante Huecos de Tensión [thesis]. Zaragoza: Universidad de Zaragoza; 2007. p. 100

[11] Boldea. Synchronous Generators. 1st ed. USA: Taylor & Francis Group; 2006. p. 256

[12] Cuevas M. Control Vectorial de un Motor de Inducción Doble Alimentado [thesis]. Mexico: CENIDET; 2003. p. 113

[13] Gamarra. Control de un Generador Doblemente Alimentado para Turbinas Eólicas [thesis]. Universidad Politécnica de Cataluña: Ingeniería Técnica Industrial; 2009. p. 110

[14] Sierra E. Análisis del diseño y control de un generador trifásico doblemente alimentado [thesis]. Chile: Ingeniería Civil Electricista; 2012. p. 152

[15] Hernandez E, Madrigal M. A step forward in the modelling of the doubly fed induction machine for harmonic analysis. IEEE Transaction Energy Conversion. 2014;**29**(3):149-157

Chapter 4

Optimization Approaches in Sideband Calculations and a Non-Iterative Harmonic Suppression Strategy in 4D Arrays

Ertugrul Aksoy, Yasin Yavuz and Mert Karahan

Additional information is available at the end of the chapter

http://dx.doi.org/10.5772/intechopen.74586

Abstract

In this chapter, the harmonic calculations and suppression methods in 4D arrays are explored. First, the fundamentals of the 4D arrays including the switching strategies and metaheuristic approach to suppression of sidebands are provided, and further, the harmonic reduction strategies using optimizers are discussed. Finally, a novel noniterative algorithmic way to suppress the harmonic radiations is introduced and exemplified by an illustrative example.

Keywords: harmonic radiations, harmonic reduction, time-modulated arrays, 4D arrays, optimization

1. Introduction

Channel capacity is one of the most critical constraints in wireless communication technology that both academic and industrial foundations are trying to efficiently use and/or to increase the capacity with the help of various multiplexing, duplexing and coding algorithms. Although software-based algorithms allow channel capacity to be efficiently used, when it is compared with the hardware modifications of antenna elements (e.g. adaptive smart antenna, MIMO, switched arrays, etc.), the gain stays at minor levels; however, it does not mean that either one of them is strictly selected. Instead, hardware- and software-based modifications should be mixed in order to obtain the best results [1, 2].

In the late 1950s, Shanks and Bickmore introduced a new concept of antenna array design which is based on switching of individual array elements periodically [3]. The concept so-called time

modulation enables time variable, t, as an antenna design parameter alongside of complex excitations and placement of the elements. While having a new design parameter, due to the nature of periodic excitations, infinite number of sideband radiations occurs at the multiplying frequencies of switching frequency. In a short while after the introduction of the time modulation concept, Kummer et al. analyzed the time-modulated arrays (i.e., TMAs) in terms of sideband radiations (i.e., SR) [4]. However, time modulation concept has not attracted much attention in scientific community, until the publication of a study on SR suppression with adjusting the sidelobe level using differential evolution algorithm by Yang et al. in 2002 [5]. Furthermore, with the emerging technology in computers and mobile communication infrastructures, TMAs gained popularity, and many studies have been conducted using different metaheuristic algorithms to suppress the harmonics [6–12] and using different excitation schemes so as to have more control parameters on array design such as shifting/splitting pulses and using different pulse amplitudes [6, 13–17]. Additionally, interference suppression and adaptive beamforming using TMAs have been studied in the literature [18–21]. Moreover, TMAs having different geometries such as planar and conformal are analyzed for harmonic suppression [22–24], and closed form finite calculations have been done expressed in order to calculate total radiated power in SRs for different excitation schemes and geometries [25–32].

Although there are many studies that are trying to suppress the all SRs since harmonic radiations consume main radiation power, the emerging concepts such as direction finding, spatial diversity and adaptive beamforming require harmonic radiations to be used in communication. In the literature, TMAs have been used for direction finding and direction of arrival estimation applications [33–37], harmonic beam steering, adaptive beamforming and communication over sidebands [38–40]. Furthermore, an overview about TMAs and additional enhancements for TMA concept have been published by Maneiro-Catoria *et al.* in 2017 [41–42].

In this chapter, harmonic radiation suppression methods using metaheuristic algorithms will be examined in detail, total power calculations for SRs will be presented and novel non-iterative algorithmic method for harmonic suppression will be introduced.

2. Theoretical background of switched arrays

Antenna arrays having identical elements are examined independently of directional characteristics of the radiating elements (e.g., dipole, horn, etc.) since total electric field is calculated by multiplication of array factor with electric field of single element at reference point according to pattern multiplication. The time-modulation concept introduces a periodic switching for array elements and array factor, naturally, becomes dependent to excitation function unlike conventional arrays. Although it is shown that signal radiation in switched arrays (i.e., time-modulated arrays, TMAs) may be approximated to an unmodulated array under the condition of switching frequency being much smaller than carrier frequency by Bregains *et al*. [25], relation between conventional arrays' and switched arrays' radiation power density should be derived in order to obtain limitations and constraints of calculations [12, 25, 43].

http://dx.doi.org/10.5772/intechopen.74586

In order to derive an average power density for TMAs, it is convenient to start the derivation from the Poynting vector, and the instantaneous power density is defined as

$$\boldsymbol{\mathcal{W}} = \boldsymbol{\mathcal{E}} \times \boldsymbol{\mathcal{H}} \tag{1}$$

where $\boldsymbol{\mathcal{E}}$ and $\boldsymbol{\mathcal{H}}$ represent the time-dependent electric and magnetic field vectors, and once the time modulation is considered, electric and magnetic fields may be expressed by

$$\boldsymbol{\mathcal{E}} = \mathrm{Re}\left\{\boldsymbol{E}e^{i\left(\omega_0+q\omega_p\right)t}\right\} = \frac{1}{2}\left[\boldsymbol{E}e^{i\left(\omega_0+q\omega_p\right)t} + \boldsymbol{E}^{*}e^{i\left(\omega_0+q\omega_p\right)t}\right] \tag{2}$$

and

$$\boldsymbol{\mathcal{H}} = \mathrm{Re}\left\{\boldsymbol{H}e^{i\left(\omega_0+q\omega_p\right)t}\right\} = \frac{1}{2}\left[\boldsymbol{H}e^{i\left(\omega_0+q\omega_p\right)t} + \boldsymbol{H}^{*}e^{i\left(\omega_0+q\omega_p\right)t}\right]. \tag{3}$$

Here, $\mathrm{Re}\{z\}$ and $q \in (-\infty, \infty)$ stand for real part of $z \in \mathbb{C}$ and harmonic level, respectively. Furthermore, $\omega_0 = 2\pi f_0$ and $\omega_p = 2\pi f_p$ represent angular carrier frequency and angular switching frequency, respectively. If Eqs. (2) and (3) are substituted into Eq. (1) and after some basic mathematical operations, Eq. (1) may be rewritten as

$$\boldsymbol{\mathcal{W}} = \frac{1}{2}\mathrm{Re}\{\boldsymbol{E} \times \boldsymbol{H}^{*}\} + \frac{1}{2}\mathrm{Re}\left\{\boldsymbol{E} \times \boldsymbol{H}e^{i2\left(\omega_0+q\omega_p\right)t}\right\}. \tag{4}$$

In order to obtain time average radiation power density, Poynting vector can be integrated over one period (i.e., T_p), and the time average Poynting vector may be expressed as

$$\boldsymbol{W}_{\langle av\rangle} = \frac{1}{2T_p}\int_{T_p}\mathrm{Re}\{\boldsymbol{E} \times \boldsymbol{H}^{*}\}dt + \frac{1}{2T_p}\int_{T_p}\mathrm{Re}\left\{\boldsymbol{E} \times \boldsymbol{H}e^{i2\left(\omega_0+q\omega_p\right)t}\right\}dt = \frac{1}{2}Q_1 + \frac{1}{2}Q_2. \tag{5}$$

If Q_1 is integrated, it may be written as

$$Q_1 = \frac{1}{T_p}\,\mathrm{Re}\{\boldsymbol{E} \times \boldsymbol{H}^{*}\}\int_{T_p} dt = \mathrm{Re}\{\boldsymbol{E} \times \boldsymbol{H}^{*}\}. \tag{6}$$

Once the Q_2 is examined, as the term $\boldsymbol{E} \times \boldsymbol{H}$ is time-independent complex constant (i.e., $\boldsymbol{E} \times \boldsymbol{H} = \mathrm{g}$, $\mathrm{g} \in \mathbb{C}$), it becomes

$$Q_2 = \frac{1}{T_p}\,\mathrm{Re}\{\boldsymbol{E} \times \boldsymbol{H}\}\int_{T_p}\cos\left(2\left(\omega_0 + q\omega_p\right)t\right)dt - \frac{1}{T_p}\,\mathrm{Im}\{\boldsymbol{E} \times \boldsymbol{H}\}\int_{T_p}\sin\left(2\left(\omega_0 + q\omega_p\right)t\right) = \Gamma_1 - \Gamma_2 \tag{7}$$

where $\mathrm{Im}\{z\}$ denotes imaginer part of $z \in \mathbb{C}$. If Γ_1 and Γ_2 are solved, Eqs. (6) and (7) may be rewritten as

$$\Gamma_1 = \mathrm{Re}\{\boldsymbol{E} \times \boldsymbol{H}\}\frac{\sin\left(2\left(\omega_0 + q\omega_p\right)t\right)}{2T_p\omega_p\left(\frac{\omega_0}{\omega_p} + q\right)} \tag{8}$$

and

$$\Gamma_2 = \mathrm{Im}\{\boldsymbol{E} \times \boldsymbol{H}\} \left[\frac{\cos\left(2(\omega_0 + q\omega_p)t\right) - 1}{2T_p\omega_p\left(\frac{\omega_0}{\omega_p} + q\right)} \right] \tag{9}$$

where $T_p\omega_p = 2\pi$. Looking closely to Eq. (8), Γ_1 tends to zero as $\kappa = \omega_0/\omega_p$ ratio tends to infinity. The same situation holds true for also Eq. (9). Since Γ_2 oscillates in range $[1/2\pi(\kappa + m) : 0]$ as κ tends to infinity, Γ_2 also vanishes. Hence, it can be said that both Γ_1 and Γ_2 vanish when $\omega_0 \gg \omega_p$ so that under $\kappa \gg 1$ approximation Eq. (7) reduces to

$$Q_2 = \Gamma_1 - \Gamma_2 \approx 0 \tag{10}$$

Since, Q_2 vanishes, the time average Poynting vector may be written as

$$\boldsymbol{W}_{\langle av \rangle} \approx \frac{1}{2}\mathrm{Re}\{\boldsymbol{E} \times \boldsymbol{H}^*\}. \tag{11}$$

It must be noted that Eq. (11) is only valid under the condition of $\kappa = \omega_0/\omega_p \gg 1$, and it clearly defines that the time average power density of switched arrays may be approximated to conventional arrays' under defined conditions. In the light of this information, the array factor in time domain of an N element time-modulated array with periodic switching function of $g_n(t)$ may be written as

$$\mu(\theta, \phi, t) = e^{i\omega_0 t}\sum\nolimits_n W_n g_n(t) e^{ik\left(\widehat{a}_{pn} \cdot \widehat{a}_r\right)} \tag{12}$$

where W_n, $\widehat{a}_{pn}$ and $\widehat{a}_r$ represent the complex excitations, the position vector and the radial unit vector in Cartesian coordinates, respectively. Since $g_n(t)$ is periodic in time, it can be decomposed into Fourier series, hence, if G_{nq} is being the Fourier coefficients, the array factor becomes

$$\mu(\theta, \phi, t) = e^{i\omega_0 t}\sum\nolimits_n W_n \sum_{q=-\infty}^{\infty} G_{nq} e^{iq\omega_p t} e^{ik\left(\widehat{a}_{pn} \cdot \widehat{a}_r\right)}. \tag{13}$$

Hence, in the light of the result obtained in Eq. (11), this array factor may be written in phasor form for a specific harmonic number q as

$$\mu_q(\theta, \phi) = \sum\nolimits_n W_n G_{nq} e^{ik\left(\widehat{a}_{pn} \cdot \widehat{a}_r\right)} \tag{14}$$

As shown in Eq. (14), in switched arrays, the excitation strategies directly affect both the main and sideband radiations. Every periodic function is eligible to be used for switching the array elements; however, once the constraint number that shapes the radiation patterns increases, excitation strategies are needed to be evolved in order to meet the requirements. Time modulation concept firstly introduced by binary switching scheme, which switches the elements

http://dx.doi.org/10.5772/intechopen.74586

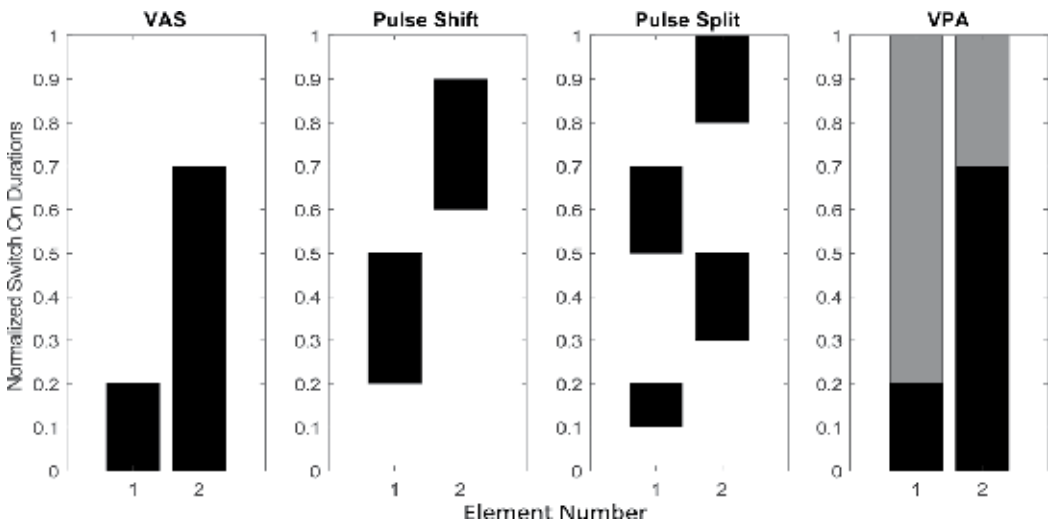

Figure 1. Common excitation schemes - darker bars represent a higher amplitude level.

between on ('1') and off ('0') (i.e., variable aperture size (VAS) time scheme), then, the ideas shifting (i.e., pulse shift (PS)) and splitting pulses (i.e., pulse split (PSp) time scheme) are raised in order to get more control on antenna array characteristics. Additionally, another scheme so-called variable pulse amplitude (VPA) has been recently introduced, but the definition of this scheme is left to the further sections. An illustrative representation of these schemes is depicted in **Figure 1**.

3. Harmonic suppression via metaheuristics

3.1. A general overview on metaheuristic optimization

Metaheuristics may be defined as the nature-inspired algorithms which mimics a natural phenomenon in order to achieve a certain goal. To be specific, the main purpose of this kind of approach is to find a close-optimal parameter set over a specifically constructed mathematical space so-called a search space with some limiting constraints for the problem at hand. Most of the metaheuristic algorithms operate on a point-based search mechanism in order to keep the dimension space unchanged. In other words, these kinds of algorithms operate on a search space sampling strategy which forms a parallel optimal point search mechanism over the search space. These search space samples form a potential solution set called, usually, the population. If there is no pre information about search space behavior, usually, these optimizers start their search from a uniformly distributed search space sample set so-called the initial population.

Here, the search space mentioned above is a user-defined mathematical function space, usually called as cost function, fitness function, and so on, which varies depending on the problem

construction. Definition of the search space is one of the key issues for these kinds of algorithms since it directly defines the problem. A poorly defined search space may lead inappropriate results even the algorithm works properly. A search space may be constructed in several ways but constructing it on an error function such as mean square or absolute error is a popular approach since the optimal point in an error function is predictable or known. However, using an error-based function is not a necessity, and some other well-defined functions may be used as the function that is to be optimized. If an error-based cost function is formed for a problem at hand, typically the problem becomes a minimization process, and the algorithm tries to find the possible solutions close to a desired one with a minimal error. A typical error-based cost function may be defined as

$$\begin{aligned} &\underset{\overline{x}}{\text{minimize}} \quad f(\overline{x}) \\ &\text{subjectto}: \quad \overline{y} \end{aligned} \tag{15}$$

where $\overline{x}$ stands for the parameter vector to be optimized, $\overline{y}$ is the constraint set and $f(\overline{x})$ is the cost function may be defined by $f(\overline{x}) = \left[\sum_i \left(g_i^d(\overline{x}) - g_i^a(\overline{x})\right)^2\right]^{1/2}$. Here, in the cost function, g, d and a represent the specification that is to be optimized, the desired level and the actual level, respectively.

After constructing and sampling the search space, that is, defining the cost function and constructing the initial population, all point-based metaheuristics move these initial samples to different points by their predefined operators. Actually, at this point, it should be noted that mainly the algorithms differ from each other by their relocation processes. Each algorithm uses a different method to relocate the initial samples, and usually this relocation process gives the algorithms name. By the relocation of the initial samples, a newly generated sample points are created which stands for new solutions. Comparing these new solutions with old ones and keeping the suitable ones and discarding the others cause an overall improvement in the solution set. In other words, after creating new points by relocation process, comparing them with already known possible solutions and keeping the better ones provide an overall convergence to the optimal point. This comparing and selecting process may be conducted in several ways such as using a roulette wheel or a binomial selection. In any way, the basic idea behind this process is comparing the solutions and keeping the better ones in order to improve the solution quality at hand. The relocation and selection process continues until a satisfied convergence rate is achieved or an iteration limit is reached. By this way a close optimal point may be found after the overall process in an iterative manner.

The basic idea behind the metaheuristics may be defined in main four steps as

Step 1: Constructing a search space

Step 2: Forming a randomly generated initial sample set

Step 3: Moving the samples in search space and create new solutions

Step 4: Comparing the new set with old one and keeping the suitable ones

http://dx.doi.org/10.5772/intechopen.74586

As stated above, *Step 3* and *Step 4* are repeated in an iterative manner to achieve a satisfactory result. Here it should be noted that, because of their randomized nature, none of the metaheuristics guarantees to find an optimal solution. But it can be said that elitist methods (the methods that always keeping the current best solution in the solution set) with enough randomization of the solution set (this process is usually necessary to avoid local optimal points) guarantees to find a close optimal solution with enough convergence rate as the time tends to infinity.

3.2. Application to the harmonic suppression problem

As all metaheuristic approaches, definition of the problem is the key issue in sideband suppression problems. In TMA design which the sidebands are not to be used on specific purpose, the sideband radiation levels are preferred to be as low as possible in order to concentrate the total power in main radiation, lowering the total signal interference and unwanted signal radiations. However, suppressing sideband radiations is not the only problem while designing a switched antenna array. The most important problem needs to be solved is shaping main radiation beam with required side lobe level which may be a 'must' of design procedure since it affects communication quality directly. Then, other parameters which affect the performance such as harmonic-level suppression, harmonic beamforming and spatial filtering (i.e., adaptive beamforming to use the power effectively and null-steering to reduce interference) need to be handled to have the best fit design for application. Thus, if all the constraints are taken into consideration at the same time, different optimization algorithms become practical once today's computers' calculation speed, performance and technology are getting better day by day.

As mentioned earlier, designing a switching array via a metaheuristic algorithm starts with the definition of the problem at hand which will directly appears as the cost function that the algorithm uses. After the problem definition, the switching strategy should be decided which directly affects the parameter vector construction. These two steps should be taken into account carefully. First, a possible mistake in problem definition causes a defected mathematical search space, actually the search space will not be mathematically defected, but wrong statements will lead completely different search space that does not related to the actual problem. The algorithm will produce some results but completely unrelated to the problem actually at hand. Second, an improper selection of the excitation strategy may lead the problem unsolvable. As a simple example to this situation, for a problem involving only the suppression of specific harmonic levels, the selection of a VAS or PS switching scheme makes the problem unsolvable, since the harmonic levels are bounded to each other in these schemes. Hence, the independent suppression of different harmonics is mathematically impossible for this problem using the mentioned time schemes. At this point, it is beneficial to decide which conventional array design parameters such as element orientation or excitation phase to use in addition to the 'time' parameter. Since many problems may be solved via only correct switching strategy, this selection is not crucial and the traditional parameters may be excluded from the problem. However, adding some extra degrees of freedom will relax the solution of the problem and in some specific cases such as main beam steering, inclusion of the excitation

phase to the parameter vector is inevitable. From this point on, the rest of the procedure is the application of the optimizer to the problem. The key points in the TMA design may be summarized as

- Defining the problem correctly,
- Selecting the switching strategy correctly,
- Deciding whether the conventional parameters are necessary.

The first study dealing with harmonic suppression via an optimizer has been appeared by Yang *et al.* in 2002 [5]. In Yang's study, the switch-on durations of a VAS schemed linear array has been tried to be optimized. Unlike conventional array design, in designing a switched array, the harmonic radiations should be taken into account and the question of 'how?' is an issue that needs to be considered. At early researches, the calculation of the sidebands was conducted as a sidelobe-like algorithmic procedure, and the result of the procedure is used in metaheuristic algorithms as in Yang's study [6, 7]. In these researches, the pattern of the sidebands has been sampled in a certain precision, and the maximum of these sample set has been taken as the maximum sideband level (SBL) which has been used as the parameter to be minimized. The basic idea behind this approach is to lower the maximum level of the infinite harmonics below a certain level usually a certain communication threshold. However, her the main problem is: there exist infinite harmonics in number and the question is how many of them should be considered? For this issue, usually the first M harmonics are taken into account in practice and M depends on the problem at hand. However, there also exists a common opinion that conducting operation only on the first harmonic is enough to extract the maximum harmonic level since the Fourier coefficients should follow an envelope of a 'sinc' function. This idea is not entirely true since there exist situations that the first harmonic is not the highest especially in forced cases (e.g., the situation in [23]). SBL suppression is a generally applicable generic way to gather information about sidebands; however, calculating sidebands from array factor definition with a certain accuracy is a time- and system resource-consuming process even conducting operation in the first harmonic. If first M harmonics are considered, the time consumption is M fold for SBL extraction. Over and above, in azimuthal asymmetric cases such as planar and volumetric situations, the calculation time is enormously increasing exponentially in proportion to the azimuth resolution. Hence, there exists a solution time-accuracy trade-off in this technique, which always needed to be considered. An illustrative block diagram of this technique may be found in [31].

In the cost function of an optimizer, this SBL information may be directly added. As an example, for a linear array and a problem involving only sideband suppression, the cost function of the metaheuristic algorithm may be written as

$$f = H(\Lambda)\max_{\overline{x}}\left[\mu_{\overline{m}}(\overline{x},\theta)\right] \tag{16}$$

where $H(\cdot)$ represents the standard Heaviside step function. Here, $\Lambda = \left(\max_{\overline{x}}\left[\mu_{\overline{m}}(\overline{x},\theta)\right] - \Xi_d\right)$, $\mu(\cdot)$ is the array factor, Ξ_d is the desired sideband level and $\overline{m}$ represents the harmonic number vector where$\forall m \in \mathbb{Z}^+$, $m \leq M$ and M represents the harmonic number taken into account.

http://dx.doi.org/10.5772/intechopen.74586

Additionally, it should be kept in mind that in switched array design, the parameter vector $\overline{x}$ should contain the switching parameters. For this kind cost function, the expected value of the cost of the solution is zero. In other words, the optimizer should stop when the cost value reaches zero and the parameter vector $\overline{x}$ that satisfies $f = 0$ regarded as a solution to the problem.

Extracting harmonic information to use in an optimizer from harmonic pattern samples is a generic way, but it is not the only way to gather information about sidebands. Calculating the power in sidebands and forming a bound function may also be used in sideband suppression problems. These two methods will be discussed in separate sections.

4. Total harmonic power radiation calculation

4.1. Harmonic power calculations in literature

In 2008, Bregains *et al.* published a paper that contains a closed form equation which defines an asymptotic approximation of the total power in infinite harmonic radiations for a VAS schemed linear array [25]. The main idea behind this approach is the total power of the radiated field, which may be expressed as the integral of the absolute squared array pattern over elevation under far field and $\kappa \gg 1$ approximations. Since the infinite series of absolute squared complex Fourier coefficients is convergent which appears in the raw equation, the infinite summation reduces to a specific function involving switch-on durations. After taking the integration over elevation, the result becomes an elegant closed form equation which gives an asymptotic approximation of the total power in infinite harmonics. After this first paper, Poli *et al.* published a paper that extends this equation to a rectangular grid planar array [26], and Aksoy and Afacan rewrite the equation for arbitrarily distributed planar case [27]. The main idea behind these papers is the integration of the array factor in planar case, which may be expressed as ordinary Bessel functions. After this conversion, the rest of the way to writing the equation is similar to the original Bregains' paper. One handicap of this equation is that it only holds for the VAS scheme. For a shifted case (i.e., PS scheme), the results of the equation have been considered as inappropriate, since the equation does not contain information about starting instants. In 2012, this situation is added and combined with original equation by Aksoy and Afacan [28]. The idea behind this attempt is writing the infinite summation of the absolute squared complex Fourier coefficients as the Riemann's zeta function. From this moment on, the equation has been valid for VAS and PS switched linear and planar arrays. But the equation still did not include volumetric cases, and in 2015, Aksoy published a paper to close this gap [29]. The key point in volumetric calculations is solving a definite integral over elevation involving an ordinary Bessel function times a complex exponential function. Writing this multiplication using spherical Bessel and Legendre functions makes this integral easily solvable, and the result reduces to a zeroth order spherical Bessel function which is equal to a 'sinc' function with argument of Euclidean distances as in linear and planar cases. Hence, by the publication of [29], the equation has been taken its final and more general form for VAS and PS switched arrays. Here, it must be noted that the studies mentioned so far have been conducted using ideal pulses (i.e., rectangular pulses with no transition regions). In addition to the studies given above, a pulse model having transition region

has been studied by Bekele *et al.* and may be a reference to practical pulse models [32]. The summary of the derivation of the general form of power equation (from this point on, it will be referred as SR equation) is given in the next subsection, and for more information, references given above may be followed.

4.2. Derivation of generalized total harmonic power calculation

In this section, the general form of the harmonic power equation will be briefly derived. Before beginning derivation, some remarks should be noted. First of all, the equation derived here is an asymptotic approximation which the far field and $\kappa \gg 1$ approximations are assumed. Since the wave front of a spherically propagating wave may be assumed as planar in Fraunhofer region, this assumption helps to write the array factor in a simple summation consisting of planar wave front oriented phase shifts. Hence, in the region where the maximum phase error is below a certain tolerable level, the wave may be assumed as planar wave. Second, as stated earlier, the Poynting vector of a switched array may be written as in ordinary cases under $\kappa \gg 1$ approximation which makes the power density calculations as in conventional arrays.

Under these approximations, assume that N isotropic radiators are randomly oriented in a three-dimensional space. In this general case, the time average power at harmonics may be represented as

$$\mathcal{P}_H = \frac{1}{2}\int_0^{2\pi}\int_0^{\pi}\sum_{\substack{q=-\infty \\ q\neq 0}}^{\infty}\left|\mu_q(\theta,\phi)\right|^2 \sin\theta d\,\theta d\phi. \tag{17}$$

Here, $\mu_q(\theta,\phi)$ is being the array factor of isotropic sources and can be written for volumetric arrays as

$$\mu_q(\theta,\phi) = \sum_{n=0}^{N-1} W_n G_{nq} e^{ikx_n \sin\theta\cos\phi} e^{iky_n \sin\theta\sin\phi} e^{ikz_n\cos\theta} \tag{18}$$

where W_n and G_{nq} represent the complex excitations and complex Fourier coefficients, respectively. x_n, y_n and z_n stand for the coordinates of the array element in three orthogonal axis in standard Cartesian coordinates, $k = 2\pi/\lambda_o$ is being the wavenumber and $i = \sqrt{-1}$. In Eq. (18), the absolute squared array factor may be written as $\left|\mu_q(\theta,\phi)\right|^2 = \mu_q(\theta,\phi)\mu_q^*(\theta,\phi)$, and after simple manipulations, $\mathcal{P}_H$ turns out to be.

$$\begin{aligned}\mathcal{P}_H = {} & \frac{1}{2}\sum_n |W_n|^2 \int_0^{2\pi}\int_0^{\pi}\sin\theta d\theta d\phi \sum_{\substack{q=-\infty \\ q\neq 0}}^{\infty}\left|G_{nq}\right|^2 \\ & + \frac{1}{2}\sum_{\substack{m,\,n=0 \\ m\neq n}}^{N-1} W_m W_n^* \int_0^{2\pi}\int_0^{\pi} e^{ikx_n\sin\theta\cos\phi} e^{iky_n\sin\theta\sin\phi} e^{ikz_n\cos\theta}\sin\theta d\theta d\phi \sum_{\substack{q=-\infty \\ q\neq 0}}^{\infty} G_{mq}G_{nq}^*.\end{aligned} \tag{19}$$

Here, the Fourier coefficients depend on the switching strategy. If an ideal PS time scheme consisting of rectangular pulses is considered, the switching function may be modeled as

$$g_n(t) = \begin{cases} 1, & 0 \le t_n^1 < t < t_n^2 \le T_p \\ 0, & otherwise \end{cases} \tag{20}$$

where t_n^1 and t_n^2 represent the starting and finishing instants of the corresponding pulse. For this time scheme, the Fourier coefficients may be written as

$$G_{nq} = \frac{i}{2\pi q}\left[e^{-iq2\pi t_n^2} - e^{-iq2\pi t_n^1}\right] \tag{21}$$

where q stands for the harmonic number and the infinite summation of $G_{mq}G_{nq}^*$ product may be examined for $m = n$ and $m \neq n$ cases.

For $m = n$, this product may be written as

$$G_{nq}G_{nq}^* = \frac{1}{2\pi^2 q^2}\left[1 - \cos\left(2\pi q\left(t_n^2 - t_n^1\right)\right)\right]. \tag{22}$$

Hence, the infinite summation of this product turns out to be

$$\sum_{\substack{q=-\infty \\ q\neq 0}}^{\infty} G_{nq}G_{nq}^* = \sum_{q=1}^{\infty}\frac{1}{\pi^2 q^2} - \sum_{q=1}^{\infty}\frac{1}{\pi^2 q^2}\cos\left(2\pi q\tau_n\right) \tag{23}$$

where $\tau_n = \left(t_n^2 - t_n^1\right)/T_p$ represents the normalized on-time duration of nth element. Since, this series is convergent, using the Riemann's zeta function where $\sum_{x=1}^{\infty} 1/x^n = \zeta(n)$, the infinite series of coefficient product reduces to

$$\sum_{\substack{q=-\infty \\ q\neq 0}}^{\infty} G_{nq}G_{nq}^* = \frac{1}{\pi^2}\frac{\pi^2}{6} - \frac{1}{\pi^2}\left\{\frac{\pi^2}{6} - \frac{\pi}{2}2\pi\tau_n + \frac{\left(2\pi\tau_n\right)^2}{4}\right\} = \tau_n(1-\tau_n). \tag{24}$$

For $m \neq n$ by using the fact that cosine is an even function and sine is odd, this infinite series turns out to be

$$\begin{aligned}\sum_{\substack{q=-\infty \\ q\neq 0}}^{\infty} G_{nq}G_{mq}^* = {} & \frac{1}{2(\pi q)^2}\sum_{q=1}^{\infty}\left\{\cos\left[2\pi q\left(t_n^1 - t_m^1\right)\right] - \cos\left[2\pi q\left(t_n^1 - t_m^2\right)\right]\right\} \\ & + \frac{1}{2(\pi q)^2}\sum_{q=1}^{\infty}\left\{\cos\left[2\pi q\left(t_n^2 - t_m^2\right)\right] - \cos\left[2\pi q\left(t_n^2 - t_m^1\right)\right]\right\}.\end{aligned} \tag{25}$$

By using relation for summable series, see [25, Appendix], Eq. (25) reduces to

$$\sum_{\substack{q=-\infty \\ q\neq 0}}^{\infty} G_{nq}G_{mq}^{*} = \frac{1}{2}\left(-\left|t_n^1 - t_m^1\right| + \left|t_n^1 - t_m^2\right| - \left|t_n^2 - t_m^2\right| + \left|t_n^2 - t_m^1\right| - 2\tau_n\tau_m\right). \tag{26}$$

For above equation, there exist 53 different situations in terms of equality and inequality conditions of switching instants. However, considering the fact that $t_n^2 > t_n^1$ and $t_m^2 > t_m^1$ should be satisfied always, these possibilities reduce to six. If these six equality and inequality possibility of starting and finishing instants of the pulses are considered, these six conditions may be written in one form given by

$$\sum_{\substack{q=-\infty \\ q\neq 0}}^{\infty} G_{nq}G_{mq}^{*} = \overline{\tau_{mn}} - \tau_n\tau_m. \tag{27}$$

In this expression, the bar represents the duration of the intersection between n^{th} and m^{th} element's pulses. For more detailed calculations, [28] may be followed. By substituting this result into Eq. (19), it becomes

$$\mathcal{P}_H = 2\pi\sum_n |W_n|^2[\tau_n(1-\tau_n)] + \frac{1}{2}\sum_{\substack{m,\,n=0 \\ m\neq n}}^{N-1} W_m W_n^{*}(\overline{\tau_{mn}} - \tau_m\tau_n)\Omega(\theta,\phi) \tag{28}$$

where $\Omega(\theta,\phi)$ is being

$$\Omega(\theta,\phi) = \int_0^{2\pi}\int_0^{\pi} e^{ikx_n\sin\theta\cos\phi}e^{iky_n\sin\theta\sin\phi}e^{ikz_n\cos\theta}\sin\theta d\theta d\phi \tag{29}$$

and it should be solved. Solving this integral is not an easy task, and some manipulations should be conducted. It can be started from to write some exponential terms in terms of Bessel functions. To do that, the following fact may be used

$$a\cos x + b\sin x\sqrt{a^2+b^2}\cos\left(x - \tan^{-1}\left[\frac{b}{a}\right]\right). \tag{30}$$

By using this conversion and integral definition of ordinary Bessel functions with $a = k(x_m - x_n)\sin\theta$ and $b = k(y_m - y_n)\sin\theta$, the $\Omega(\theta,\phi)$ can be written as

$$\Omega(\theta,\phi) = 2\pi\int_0^{\pi} J_0\left(\sqrt{a^2+b^2}\right)e^{ik(z_m - z_n)\cos\theta}\sin\theta d\theta. \tag{31}$$

Here, $J_0(\cdot)$ represents the ordinary Bessel function of order zero. By letting $c_1 = k\sqrt{(x_m - x_n)^2 + (y_m - y_n)^2}$ and $c_2 = k\sqrt{(z_m - z_n)^2}$ with $\Omega(\theta,\phi) = 2\pi\Omega'(\theta,\phi)$, Eq. (31) becomes

$$\Omega'(\theta,\phi) = \int_0^{\pi} J_0(c_1 \sin\theta) e^{ic_2 \cos\theta} \sin\theta d\theta. \tag{32}$$

Here, c_1 and c_2 are orthogonal to each other and can be represented as $c_1 = Rcos\,\psi$ and $c_2 = Rsin\,\psi$ where $R = kR'$ and $\psi = \cos^{-1}\widehat{a}_z \cdot (\mathbf{r}_m - \mathbf{r}_n)$. Here, R' represents the Euclidean distance between corresponding elements (i.e., nth and mth elements under process) and $\mathbf{r}_m(x_m, y_m, z_m)$ and $\mathbf{r}_n(x_n, y_n, z_n)$ stand for the position vectors mth and nth elements. By using this conversion, Eq. (32) can be written as

$$\Omega'(\theta,\phi) = \int_0^{\pi} J_0(R \sin\theta \sin\psi) e^{iR \cos\theta \cos\psi} \sin\theta d\theta. \tag{33}$$

Once the $\Omega'(\theta,\phi)$ is written as in Eq. (33), the following relation may be used instead

$$J_0(R \sin\theta \sin\psi) e^{iR \cos\theta \cos\psi} = 2 \sum_{n=0}^{\infty} i^n \left(n + \frac{1}{2}\right) j_n(R) P_n(\cos\theta) P_n(\cos\psi). \tag{34}$$

Here, $j_n(\cdot)$ and $P_n(\cdot)$ represent the nth order spherical Bessel and Legendre functions, respectively. Multiplying both sides of Eq. (34) by $P_l(\cos\theta)\sin\theta$ and integrate over $[0, \pi]$ results in the following relation

$$\begin{aligned} &\int_0^{\pi} J_0(R \sin\theta \sin\psi) e^{iR \cos\theta \cos\psi} P_l(\cos\theta) \sin\theta d\theta \\ &= \sum_{n=0}^{\infty} i^n (2n+1) j_n(R) P_n(\cos\psi) \int_0^{\pi} P_n(\cos\theta) P_l(\cos\theta) \sin\theta d\theta \end{aligned} \tag{35}$$

where

$$\int_0^{\pi} P_n(\cos\theta) P_l(\cos\theta) \sin\theta d\theta = \frac{2}{2n+1} \delta_{n,l}. \tag{36}$$

In this expression, $\delta_{n,l}$ represents the Kronecker delta function defined by

$$\delta_{n,l} = \begin{cases} 1, & n = l \\ 0, & n \neq l \end{cases}. \tag{37}$$

Hence, for $l = 0$, the equation Eq. (35) becomes

$$\int_0^{\pi} J_0(R \sin\theta \sin\psi) e^{iR \cos\theta \cos\psi} \sin\theta d\theta = 2 j_0(R) \tag{38}$$

and $\Omega(\theta,\phi)$ can be written as

$$\Omega(\theta,\phi) = 2\pi\Omega'(\theta,\phi) = 4\pi j_0(R) = 4\pi \frac{\sin(R)}{R}. \tag{39}$$

If this result is substituted to Eq. (19) with Eq. (24) and Eq. (27), total power approximation may be finally written as

$$\mathcal{P}_H = 2\pi \sum_n |W_n|^2 [\tau_n(1-\tau_n)] + 2\pi \sum_{\substack{m,n=0 \\ m \neq n}}^{N-1} W_m W_n^* (\overline{\tau_{mn}} - \tau_m \tau_n) \frac{\sin(R)}{R}. \tag{40}$$

Once more, in Eq. (40), $R = \sqrt{(x_m - x_n)^2 + (y_m - y_n)^2 + (z_m - z_n)^2}$ represents the Euclidean distance between corresponding elements, I represents the complex excitations and τ represents the normalized switch-on durations for an N element volumetric array. For a more detailed proof, [29] may be followed, and for linear and planar case, see [25] and [27], respectively.

4.3. Using total power in suppression problems

The first usage of total power in harmonic suppression problems was conducted by Poli *et al.* in 2010 [10]. The main idea behind this technique is based on the idea of the total power reduction in harmonics will concentrate the power to main radiation, hence the harmonics become suppressed. Since the result of the equation does not meet the actual power in harmonics, the ratio of the harmonic power to the actual power is more meaningful in practice. Hence, usually the direct result of the Eq. (40) is not preferred to be used in an optimizer. Instead of using the direct result, the ratio of the harmonic power to the actual power is more meaningful which may be written by

$$\mathcal{P}_H' = \frac{\mathcal{P}_H}{\mathcal{P}_H + \mathcal{P}_0} \tag{41}$$

where $\mathcal{P}_0$ represents the power in main radiation given by

$$\mathcal{P}_0 = \frac{1}{2} \int_0^{2\pi} \int_0^{\pi} \left| \mu_q(\theta, \phi) \Big|_{q=0} \right|^2 \sin\theta d\,\theta d\phi \tag{42}$$

Without loss of generality for a problem concerning only harmonic reduction, the usage of Eq. (41) in a cost function may be written as

$$f = H(\varpi) \mathcal{P}_H'(\overline{I}, \overline{\tau}, \overline{R}) \tag{43}$$

where $\varpi = \left(\mathcal{P}_H'(\overline{I}, \overline{\tau}, \overline{R}) - \Theta_d \right)$ while Θ_d is being the desired harmonic to main power ratio.

5. Harmonic level bound (HLB)

5.1. HLB concept

As shown in [30] that neither harmonic level reduction nor power reduction ensures the total suppression in terms of both power and communication level. Hence, a combined way may be

http://dx.doi.org/10.5772/intechopen.74586

a more suitable approach if the both level and power reduction is necessary. At this point, the question of 'is there any simple method exist for the level calculation in order to avoid time consuming processes?' may be emerged in mind, and it can be said that such studies exist in the literature as an answer to this question.

As mentioned earlier, the SBL method extracts the harmonic level information in an algorithmic way similar to sidelobe calculations. Since there exists no analytical solution to find a maximum point in an unknown sidelobe region, the sidelobe calculations are being conducted such an operation involving sampling the pattern in sidelobe region and finding its maximum. In contrast, the sideband calculations are being conducted in whole visible region, which makes a difference in both SLL and SBL calculations. In other words, since the SBL calculations are being operated over a complete elevation and azimuth space, in some cases, the maximum of a pattern may be extracted analytically. Since the maximum points of all individual harmonic patterns can be calculated, they form a maximum sideband level set, and the maximum point of this set bounds the whole harmonic maxima. Hence, this maximum appears as a bound function covering all individual maximum harmonic levels which are infinite in number. By this way, lowering the total bound ensures that all harmonic levels are below this level.

First attempt to calculate a bound is conducted by Aksoy for linear arrays with a VAS time scheme [23]. In this attempt, the Poynting vector of a TMA has been considered, and the pattern equations are written as the normalized time average power densities. After this first attempt, Aksoy and Afacan published a proof including the planar case using the same idea [24]. By this way, an overall harmonic bound for a VAS switched time modulated linear and planar arrays has been written as

$$\Psi = \left(\frac{\sum_{n=0}^{N-1} I_n \sin(\pi \tau_n)}{\pi \sum_{n=0}^{N-1} \xi_n} \right)^2 \tag{44}$$

where Ψ stands for the normalized upper sideband bound, I_n and τ_n represent the excitation amplitude and the normalized on-time durations of the n^{th} element, respectively. Also, ξ_n is the dynamic excitation defined by $\xi_n = I_n \tau_n$ and N represents the total element number in the array. Here it must be noted that, to clear possible misunderstandings, the excitation vector represents only the amplitude of the complex excitations and defined in region $\forall I \in \mathbb{R}^+, 0 < I \leq 1$. Similarly, the normalized switch-on durations are also defined in region $\forall \tau \in \mathbb{R}^+$, where $0 < \tau \leq 1$. Since this equation is a closed form expression, the total computation time for harmonic information is tremendously short as compared to the SBL method. Since it is in a shorter form, the computation time is slightly better compared to SR equality. A detailed comparison may be found in [31].

Like all switched array calculations, this technique also uses an asymptotic approach and valid only under far-field and $\kappa \gg 1$ approximations and has its own advantages and disadvantages. The major advantage of this technique is that it ensures the harmonic level suppression among infinite sidebands in a very short time. However, currently, it is only applicable to linear and planar arrays with VAS time scheme, which may be considered as a handicap of this technique.

5.2. HLB applications

If the harmonic levels are wanted to be suppressed via the bound function in a metaheuristic approach, the result produced by the bound function may be used directly in the cost function of the optimizer. The aim of the optimization is to find a switch-on duration sequence to satisfy a desired level. Hence, the parameter vector should contain at least switch-on durations $\overline{\tau}$. For a uniform array, the excitation $\overline{I}$may be taken as a vector whose elements are set to unity. Without loss of generality for a linear case with only sideband level, reduction is necessary for such a cost function that may be written as

$$f = H(\lambda)\Psi\left(\overline{I}, \overline{\tau}\right) \tag{45}$$

where $H(\cdot)$ stands for the standard Heaviside step function and $\lambda = \left(\Psi\left(\overline{I}, \overline{\tau}\right) - \Xi_d\right)$ while Ξ_d is being the predefined desired harmonic level. Here, the $\left\{\overline{\tau}, \overline{I}\right\}$ set stands for a solution for $f = 0$.

Moreover, the equality has been derived for the VAS scheme, but it can be used for any switching strategy involving one pulse in one period. On the other hand, the efficiency of the bound function in shifted cases does not appear as good as in the VAS scheme, since the equality does not contain information about starting instants. In practice, the actual harmonic levels are usually less than, or at least equal to, the results produced by the bound function. In VAS scheme, the difference between actual and the bound is usually getting smaller as the iteration counts, but the same statement does not hold true for the PS scheme. Hence, using the bound function in shifted cases causes a random walk on starting instants, and this situation may lead to some impractical results.

6. A non-iterative algorithmic approach to suppress the harmonics using variable pulse amplitude

6.1. Variable pulse amplitude (VPA)

Instead of using "on–off" switching scheme, a novel approach is proposed by Aksoy in 2014 named as "Variable Pulse Amplitude (VPA)," which is based on switching each element between amplifiers [12]. The main purpose of the newly proposed method is preventing the array silencing, which means all the elements are switched to "off" position and no communication at that instant (e.g., see **Figure 1**). The binary "On – off" switching with modifications such as shifting and splitting allows the array to be silenced even for a very short time instant and the received or transmitted data may be missed at defined instants that all the elements are switched off in every period of switching. It may be seemed as minor possibility, but it results in additional optimization constraint to be checked whether there is an instant that all the elements are turned-off or not.

6.2. Harmonic suppression method

It is stated in previous sections that metaheuristic optimization algorithms do not guarantee to find the proper solution; however, they generally produce acceptable results. In addition,

optimization time may be longer than usual according to host computer performance, optimization constraints and iteration count. On the contrary, a noniterative approach offers a fast and reliable solution with respect to metaheuristic methods, and it is preferable if exists.

In this part of section, a novel approach in order to suppress the sideband levels using variable pulse amplitude excitation scheme will be presented with an explanatory example.

6.2.1. Mathematical expressions

The array factor of time-modulated array is given in Eq. (14), and it is easy to understand that complex Fourier coefficients (CFC), G_{nq}, affect the individual radiation patterns since excitation amplitude, excitation phase and placement of the elements are the same for main radiation and sideband radiations. In order to calculate G_{nq} values, VPA excitation strategy may be expressed as

$$g_n(t) = \begin{cases} K_n^1, & 0 < t < t_n \\ K_n^2, & t_n < t < T_p \end{cases} \tag{46}$$

where K_n^1 and K_n^2 are the adjacent pulse amplitudes and t_n represents amplitude reversal time. Hence, the $g_n(t)$ in Eq. (14) should be replaced with Eq. (46) whose CFCs are defined by

$$G_{nq} = \frac{1}{T_p}\int_{-\infty}^{\infty} g_n(t)e^{-iq\omega_p t}dt = \frac{1}{T_p}\int_{0}^{t_n} K_n^1 e^{-iq\omega_p t}dt + \frac{1}{T_p}\int_{t_n}^{T_p} K_n^2 e^{-iq\omega_p t}dt. \tag{47}$$

In this equation, while $q = 0$ represents main radiation, $|q| > 0$ defines sideband radiations, and they can be calculated individually. The CFCs for main radiation may be obtained as follows:

$$G_{n0} = \frac{1}{T_p}\int_{0}^{t_n} K_n^1 dt + \frac{1}{T_p}\int_{t_n}^{T_p} K_n^2 dt = \tau_n \Delta_n + K_n^2 \tag{48}$$

where $\tau_n = t_n/T_P$ and $\Delta_n = \left(K_n^1 - K_n^2\right)$. Here, τ_n and Δ_n represent normalized amplitude reversal time with respect to switching period and pulse amplitude difference of adjacent pulses, respectively. For the sideband radiations where $|q| > 0$, CFC values are defined by

$$G_{nq} = \frac{1}{T_p}\int_{0}^{t_n} K_n^1 e^{-iq\omega_p t}dt + \frac{1}{T_p}\int_{t_n}^{T_p} K_n^2 e^{-iq\omega_p t}dt = \frac{\Delta_n}{iq2\pi}\left[1 - e^{-iq\omega_p \tau_n}\right]. \tag{49}$$

To sum up, after some basic manipulations, CFCs for all radiation levels are expressed as

$$G_{nq} = \begin{cases} \Delta_n \tau_n + K_n^2 & , \quad q = 0 \\ \dfrac{\Delta_n}{q\pi}\sin(q\pi\tau_n)e^{-iq\pi\tau_n}, & |q| > 0 \end{cases} \tag{50}$$

Without loss of generality, since discrete windowing functions (e.g., Chebyshev or Taylor $\overline{n}$ distribution) are eligible to be used for controlling the sidelobe level of main radiation, CFC values may be selected equal to distribution coefficients for $q = 0$. In addition, for sideband radiations, $(\Delta_n/q\pi)\sin(q\pi\tau_n)$ expression appears as an amplitude term and may be used for suppressing the harmonic level.

In order to shape the main radiation pattern and to suppress the harmonic level, according to the abovementioned definitions, steps to be followed are given as:

Step 1: Use discrete window distribution coefficients, α_n, as main radiation CFCs (i.e., $\alpha_n = \Delta_n\tau_n + K_n^2$).

Step 2: Set a constant τ_n value where$\tau_n \in (0, 1)$.

Step 3: Select amplitude term of fundamental radiation, which is equal to α_n/γ in order to suppress the radiation level where γ is the suppression ratio and $\gamma \in \mathbb{R}^+$. (i.e., $\alpha_n/\gamma = (\Delta_n/\pi)\sin(\pi\tau_n)$).

Step 4: Calculate Δ_n values using step 3 (i.e., $\Delta_n = \frac{\pi\alpha_n}{\gamma\sin(\pi\tau_n)}$).

Step 5: Calculate $K_n^2 = \alpha_n - \Delta_n\tau_n$.

Step 6: Calculate $K_n^1 = \Delta_n + K_n^2$.

Step 7: Normalize Δ_n, K_n^1 and K_n^2 values individually with respect to $\rho = \max(\Delta_n, K_n^1, K_n^2)$ to obtain final design parameters.

Using this approach, main radiation sidelobe level is directly adjusted according to windowing function parameters, and fundamental harmonic radiation is suppressed with the ratio of γ. It is obvious that once the first harmonic radiation is suppressed, the other sideband radiations are self-suppressed for single pulsed schemes. In the next subsection, the method will be exemplified with an explanatory scenario.

6.2.2. A simple example

Let us assume a 10-element -30 dB Chebyshev array whose elements are located along z-axis with interelement spacing of $d = 0.5\lambda$. For simplicity, excitation amplitudes of each element are selected equal to unity (i.e., $I_n = 1$), and no progressive phase shift is applied to the elements (i.e., $\beta_n = 0$). Normalized pulse amplitude reversal time is selected as $\tau_n = 0.45$ for each element, but it does not have any effect on maximum harmonic level since normalized pulse difference values (i.e., Δ_n) are adjusted according to τ_n values.

Harmonic suppression ratio, γ, should be selected using $20\log_{10}(1/\gamma) = \delta$ where δ represents desired the maximum sideband radiation level in *dB*. It should be noted again that with the adjustment of γ, the maximum level of fundamental harmonic radiation is set to related *dB* value, thus, further sideband radiation levels are self-suppressed due to the nature of harmonic radiations.

http://dx.doi.org/10.5772/intechopen.74586

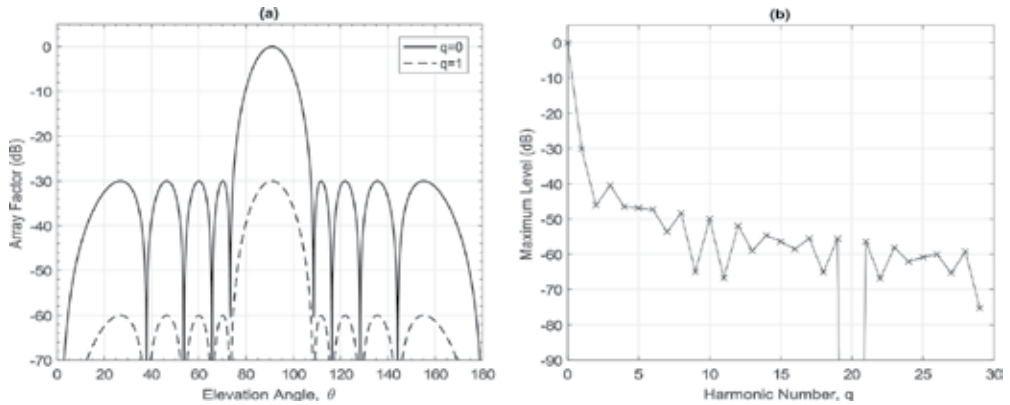

Figure 2. Results for $\gamma = 31.6$ (harmonic level= $-30dB$) (a) Radiation patterns of $q = 0$ and $q = 1$ (b) Maximum levels of first 30 harmonic radiations.

In this simple example, maximum harmonic levels are selected as $-30dB$ and$-40dB$ so that harmonic suppression ratios should be $\gamma = 31.6$ and $\gamma = 100$, respectively. Once $-30dB$ maximum level of sideband radiation is considered, main and first harmonic radiation patterns are given together in **Figure 2a**. Moreover, maximum levels of first 30 harmonic radiations are shown in **Figure 2b**. According to the calculation steps given in previous subsection, normalized pulse difference and adjacent pulse amplitude values that are used to obtain the results are given in **Table 1**.

If $-40dB$ of maximum harmonic level is taken into consideration (i.e., $\gamma = 100$), **Figure 3a** and **Figure 3b** display the radiation patterns for $q = 0$ together with $q = 1$ and maximum levels of first 30 harmonic radiations, respectively. Δ_n, K_n^1 and K_n^2 values are also shown in **Table 1**.

n		1	2	3	4	5	6	7	8	9	10
$\gamma = 31.6$	K_n^1	0.258	0.430	0.669	0.878	1.000	1.000	0.878	0.669	0.430	0.258
	K_n^2	0.233	0.389	0.605	0.794	0.905	0.905	0.794	0.605	0.389	0.233
	Δ_n	0.025	0.041	0.064	0.084	0.095	0.095	0.084	0.064	0.041	0.025
$\gamma = 100$	K_n^1	0.258	0.430	0.669	0.878	1.000	1.000	0.878	0.669	0.430	0.258
	K_n^2	0.249	0.417	0.648	0.851	0.969	0.969	0.851	0.648	0.417	0.249
	Δ_n	0.008	0.013	0.021	0.027	0.031	0.031	0.027	0.021	0.013	0.008

Table 1. Normalized pulse difference and adjacent pulse amplitude values for γ=31.6 and γ=100.

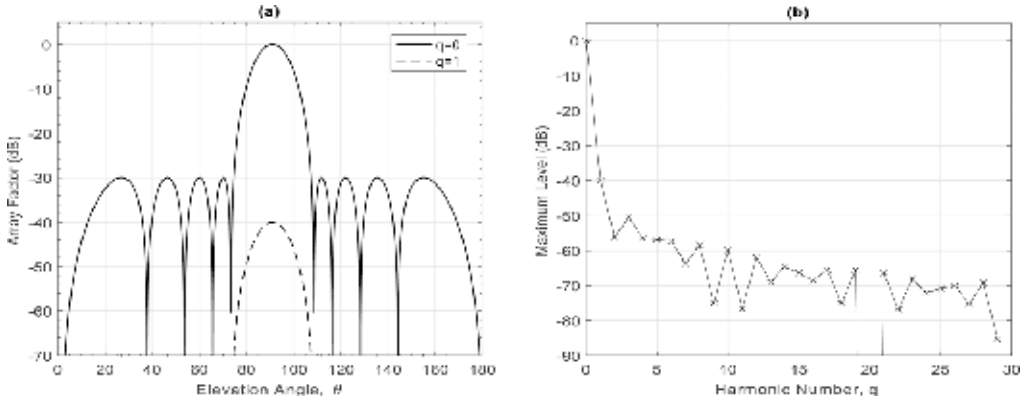

Figure 3. Results for $\gamma = 100$ (harmonic level $= -40dB$) (a) Radiation patterns of $q = 0$ and $q = 1$ (b) Maximum levels of first 30 harmonic radiations.

7. Conclusions

Nowadays, communication technology moving rapidly toward 5G, and frequency spectrum is one of the most important issues in terms of operational and capital expenses for industry. In order not to use redundant frequency bands and to make efficient use of channel capacity, it is preferred to suppress the unwanted harmonic radiations. In this study, a general overview on harmonic suppression in 4D arrays using optimization methods is given. A brief mathematical background for switched arrays and the optimization basics are explained. Furthermore, common excitation strategies and the techniques used in harmonic calculations are summarized. More importantly, a noniterative algorithmic suppression strategy is introduced and exemplified via a simple example of the harmonic suppression of a 10-element linear array with sidelobe control. The results of the introduced noniterative strategy seem quite satisfactory in terms of calculation complexity as compared to suppression via an optimizer.

Author details

Ertugrul Aksoy*, Yasin Yavuz and Mert Karahan

*Address all correspondence to: ertugrulaksoy@gazi.edu.tr

Department of Electrical and Electronics Engineering, Faculty of Engineering, Gazi University, Ankara, Turkey

References

[1] Méndez-Rial R, Rusu C, González-Prelcic N, Alkhateeb A, Heath RW. Hybrid MIMO architectures for millimeter wave communications: Phase shifters or switches? IEEE Access. 2016;**4**:247-167

[2] Renzo MD, Haas H, Ghrayeb A, Sugiura S, Hanzo L. Spatial modulation for generalized MIMO: Challenges, opportunities, and implementation. Proceedings of the IEEE. 2014; **102**(1):56-103

[3] Shanks H, Bickmore R. Four-dimensional electromagnetic radiators. Canadian Journal of Phsyics. 1959;**37**:263-275

[4] Kummer WH, Villeneuve AT, Fong T, Terrio F. Ultra-low sidelobes from time-modulated arrays. IEEE Transactions on Antennas and Propagation. 1963;**11**:633-639

[5] Yang S, Gan YB, Qing A. Sideband suppression in time-modulated linear arrays by the differential evolution algorithm. IEEE Antennas and Wireless Propagation Letters. 2002;**1**: 173-175

[6] Yang S, Gan YB, Qing A, Tan PK. Design of a uniform amplitude time modulated linear array with optimized time sequences. IEEE Transactions on Antennas and Propagation. 2005;**53**:2337-2339

[7] Fondevila J, Brégains JC, Ares F, Moreno E. Application of time modulation in the synthesis of sum and difference patterns by using linear arrays. Microwave and Optics Technology Letters. 2006;**48**:829-832

[8] Mandal SK, Ghatak R, Mahanti GK. Minimization of side lobe level and side band radiation of a uniformly excited time modulated linear antenna array by using artificial bee Colony algorithm. In: Proceedings of IEEE symposium on industrial electronics and applications (ISIEA'11). 25–28 September 2011; Malaysia. IEEE; 2011. pp. 247-250

[9] Aksoy E, Afacan E. Thinned non-uniform amplitude time-modulated linear arrays. IEEE Antennas and Wireless Propagation Letters. 2010;**9**:514-517

[10] Poli L, Rocca P, Manica L, Massa A. Handling sideband radiations in time-modulated arrays through particle swarm optimization. IEEE Transactions on Antennas and Propagation. 2010;**58**:1408-1411

[11] Li G, Yang S, Huang M, Nie Z. Sidelobe suppression in time modulated linear arrays with unequal element spacing. Journal of Electromagnetic Waves and Applications. 2010;**24**(5–6): 775-783

[12] Aksoy E. Time modulation through variable pulse amplitude in 4D arrays. In: 13th International Conference on Communications and Informatics(TELE-INFO'14). 2014. pp. 12-21

[13] Yang S, Gan YB, Tan PK. Comparative study of low sidelobe time modulated linear arrays with different time schemes. Journal of Electromagnetic Waves and Applications. 2004;**18**(11):1443-1458

[14] Poli L, Rocca P, Manica L, Massa A. Pattern synthesis in time-modulated linear arrays through pulse shifting. IET Microwaves, Antennas and Propagation. 2010;**4**:1157-1164

[15] Aksoy E, Afacan E. Sideband level suppression improvement via splitting pulses in time modulated arrays under static fundamental radiation. In: Proceedings of the Progress in Electromagnetics Research Symposium (PIERS '11). September 2011; China. pp. 364-367

[16] Zhu Q, Yang S, Zheng L, Nie Z. Design of a low sidelobe time modulated linear array with uniform amplitude and subsectional optimized time steps. IEEE Transactions on Antennas and Propagation. 2012;**60**(9):4436-4439

[17] Tong Y, Tennant A. Sideband level suppression in time-modulated linear arrays using modified switching sequences and fixed bandwidth elements. Electronics Letters. 2012; **48**(1):10-11

[18] Poli L, Rocca P, Oliveri G, Massa A. Adaptive nulling in time-modulated linear arrays with minimum power losses. IET Microwaves, Antennas and Propagation. 2011;**5**(2):157-166

[19] Aksoy E, Afacan E. Control of the sideband level and pattern null in time modulated linear arrays. In: Proceedings of the IEEE 19th Signal Processing and Communications Applications Conference (SIU '11). April 2011; Turkey. pp. 351-354

[20] Poli L, Rocca P, Oliveri G, Massa A. Adaptive nulling in time-varying scenarios through time-modulated linear arrays. IEEE Antennas and Wireless Propagation Letters. 2012;**11**: 101-104

[21] Tong Y, Tennant AA. Two-channel time modulated linear array with adaptive beamforming. IEEE Transactions on Antennas and Propagation. 2012;**60**(1):141-147

[22] Yang S, Nie Z, Yang F. Synthesis of low sidelobe planar antenna arrays with time modulation. In: Proceedings of the Asia-Pacific Microwave Conference. December 2005; China. pp. 1-3

[23] Aksoy E. An inequality for calculation of maximum sideband level in time–modulated linear arrays. In: Proceedings of 12th Mediterranean Microwave Symposium (MMS'12). 2012. pp. 2-6

[24] Aksoy E, Afacan E. An inequality for the calculation of relative maximum sideband level in time-modulated linear and planar arrays. IEEE Transactions on Antennas and Propagation. 2014;**62**:3392-3397

[25] Brégains JC, Fondevila J, Franceschetti G, Ares F. Signal radiation and power losses of time-modulated arrays. IEEE Transactions on Antennas and Propagation. 2008;**56**(6): 1799-1804

[26] Poli L, Rocca P, Manica L, Massa A. Time modulated planar arrays—Analysis and optimization of the sideband radiations. IET Microwaves, Antennas and Propagation. 2010;**4**(9):1165-1171

[27] Aksoy E, Afacan E. Generalized representation of sideband radiation power calculation in arbitrarily distributed time-modulated planar and linear arrays. In: Proceedings of the Progress in Electromagnetics Research Symposium (PIERS '11). September 2011; China. pp. 368-371

[28] Aksoy E, Afacan E. Calculation of sideband power radiation in time-modulated arrays with asymmetrically positioned pulses. IEEE Antennas and Wireless Propagation Letters. 2012;**11**:133-136

[29] Aksoy E. Calculation of sideband radiations in time-modulated volumetric arrays and generalization of the power equation. IEEE Transactions on Antennas and Propagation. 2014;**62**(9):4856-4860

[30] Aksoy E. Design of asymmetrically switched linear Chebyshev array with minimum harmonic power loss. In: Proceedings of the 9th International Conference on Electronics, Computer and Computation (ICECCO '12). November 2012; Turkey. pp. 112-115

[31] Aksoy E, Afacan E. A comparative study on sideband optimization in time-modulated arrays. International Journal of Antennas and Propagation. 2014;**2014**:1-14

[32] Bekele ET, Poli L, Rocca P, D'Urso M, Massa A. Pulse-shaping strategy for time modulated arrays—Analysis and design. IEEE Transactions on Antennas and Propagation. 2013;**61**(7):3525-3537

[33] Tennant A, Chambers B. A two-element time-modulated array with direction-finding properties. IEEE Transactions on Antennas and Propagation. 2007;**6**:64-65

[34] Tennant A. Experimental two-element time-modulated direction finding array. IEEE Transactions on Antennas and Propagation. 2010;**58**(3):986-988

[35] Li G, Yang S, Nie Z. Direction of arrival estimation in time modulated linear arrays with unidirectional phase center motion. IEEE Transactions on Antennas and Propagation. 2010;**58**(4):1105-1111

[36] Hong T, Song MZ, Liu Y. RF directional modulation technique using a switched antenna array for communication and direction-finding applications. Progress in Electromagnetics Research. 2011;**120**:195-213

[37] He C, Liang X, Liz Z, Geng J, Jin R. Direction finding by time-modulated array with harmonic characteristic analysis. IEEE Antennas and Wireless Propagation Letters. 2015; **14**:642-645

[38] Li G, Yang S, Chen Y, Nie Z. A novel electronic beam steering technique in time modulated antenna arrays. Progress in Electromagnetics Research. 2009;**97**:391-405

[39] Aksoy E. Harmonic beam steering in 4D linear arrays through pulse difference. In: Proceedings of 22th Telecommunications Forum Telfor (TELFOR'14). 2014. pp. 792-794

[40] Yavuz Y, Karahan M, Aksoy E. A dual channel AM receiver structure in 4D arrays. In: Proceedings of the 2015 IEEE International Symposium on Antennas and Propagation USNC/URSI National Radio Science Meeting. July 2015; Canada. pp. 804-805

[41] Maneiro-Catoria R, Bregains JC, Garcia-Naya JA, Castedo L. Time Modulated Arrays: From their Origin to Their Utilization in Wireless Communication Systems. 2017;**17**(3):590-604

[42] Maneiro-Catoria R, Bregains JC, Garcia-Naya JA, Castedo L. Enhanced time-modulated arrays for harmonic Beamforming. IEEE Journal of Selected Topics in Signal Processing. 2017;**11**(2):259-270

[43] Balanis CA. Antenna Theory - Analysis and Design. 3rd ed. New Jersey: Wiley; 2005. 1050 p

Section 2

Computational Tools, Methods and Techniques for Identification, Reduction and Elimination of Harmonics

Chapter 5

Compendium of Computational Tools for Power Systems Harmonic Analysis

Abdullahi Lanre Amoo, Usman O. Aliyu and
Ganiyu Ayinde Bakare

Additional information is available at the end of the chapter

http://dx.doi.org/10.5772/intechopen.77182

Abstract

Harmonic analysis comes into limelight at this contemporary world as a result of proliferation of non-linear loads producing waveform distortions in power systems. It has apparently outshined other important phrases such as power outage, power factor and so on which are known for their devastating impacts. The emergence of distorted waveform has adverse effects which could be slow or rapid damage of key apparatus and equipment, namely power transformers, electric motors and other sensitive computer as well as communication facilities. In fact, it is very easy to assess the menace of power outage or power factor since both the utility and consumers keep watchdog on their billings/operating costs in case of power factor or the economic losses when there is outage. Unfortunately, the detection of harmonics could only be analysed using high-tech power systems harmonic analysers and there is a need to provide stakeholders in the industry compendium of computational tools for fast harmonic analysis. Thus, the harmonic data acquired were used to train an artificial neural network (ANN) implemented on MATrix LABoratory (MATLAB 8) software platform to facilitate accurate prediction of harmonic distortions.

Keywords: artificial neural network, harmonic emulator

1. Introduction

In the present era of utility deregulation and competition, the impact of harmonics as well as interharmonics on equipment and system operations has been raising serious concerns. Nowadays, it is well known that harmonics have adverse effects on the whole power systems

such as misoperation of important control and protective equipment, overheating of transformers and overloading of other power apparatus [1–4]. On the other hand, interharmonics cause lighting flickers, erroneous firing of thyristor apparatus and display or monitor image fluctuation [5–7].

Power quality (PQ) problems are primarily due to voltage distortion in form of flat-topping. Harmonic currents create voltage distortion as they pass through the impedance of a power system. A high impedance system can create very high voltage distortion. However, when the voltage distortion becomes very severe, it can cause problems with connected equipment such as premature failure, reduced ride-through capability and other power quality problems. Harmonic distortion of voltages and currents can be generated either external or internal to an industrial or commercial facility, while at times, it can be exported to the utility network in an interconnected system. Power utility's consumers feel their effects and the end results of harmonics, therefore, are distorted waveforms in power outlets that supply very sensitive computer-based equipment. These devices have their useful lives reduced besides being unable to function correctly [8]. More so, power utility consumers cannot be exonerated. They are equally contributing negatively to the present menace of power waveform distortions due to use of non-linear loads, which inherently produce harmonics. By drawing currents in pulses rather than in pure sinusoidal forms, these devices, such as computer equipment, generate harmonic currents and the harmonic currents produced can then create overheating and power quality problems if left uncontrolled.

Generally, harmonics may be initiated in a power system from the following sources:

1. power electronic devices;
2. transformers, reactors, AC arc furnaces and fluorescent lamps; and
3. synchronous and induction motors.

Harmonic power distortion phenomenon was recognized by Utilities in the early 1920s and 1930s when distorted voltage and current waveforms were observed in transmission lines [9, 10]. Harmonics are high-frequency steady-state power involving multiple frequencies of 50/60 Hz flowing along with the fundamental frequency on a power network which may adversely affect the system performance. Over the past two decades in modern power systems, significant effort and advancement have been made to standardize the power system harmonic analysis, component models and simulation procedure for harmonic studies. The procedure for analyzing the harmonic problem could be classified into frequency domain [11, 12] and time-domain [13, 14], which are followed up with flexible control strategy adopted in recent time [12, 15]. Indeed, power system components such as overhead lines and underground cables, transformers, rotating machines and other non-linear loads on the system must be accurately modeled ever more than before, to determine their vulnerability to harmonic power flow. In harmonic power flow analysis, parameters of the system are specified in phasor domains and solutions are invoked by iterative methods. Time-domain methods, on the other hand, utilize time representation for the system components and other harmonic-producing devices to arrive at steady-state solutions.

http://dx.doi.org/10.5772/intechopen.77182

Power system harmonic analysis is a tool for assessing the impact of harmonic producing loads on a power system. Harmonic analysis has been widely used for system planning, system performance and evaluation, equipment design, troubleshooting and verification of standard compliance [16]. A rigid power system, comprising linear system impedance and harmonic source with constant and characteristics harmonic currents may be solved efficiently using the iterative harmonic power flow method. However, the presence of non-linear and time-varying elements in the system can significantly change the manner by which harmonic currents and voltages propagate through the network. As a consequence, the simplest system model using harmonic power flow by way of superposition of harmonic sources within the system may be invalidated thereby yielding inaccurate results. Therefore, researchers are now adopting new techniques to overcome the dynamic phenomena by invoking time-domain modeling and simulation or probabilistic modeling and simulation.

A general purpose time-domain simulation tool such as Electromagnetic Transient Programme (EMTP) and Simulation Program with Integrated Circuit Emphasis (SPICE) could be used to obtain steady-state solution of non-linear circuits by letting the simulation to run while starting from some initial conditions. This method is applicable to small-scale network but some practical cases of systems with low damping factor or widely far apart time constant (i.e. a stiff system) could prolong the simulation time or may even make the simulation not to converge at all [17]. Therefore, the time-domain method is still at its developmental stage and accordingly, the approach is only limited to simulation of simple networks.

In order to further reinforce the modeling techniques, harmonic distortion indices need to be accurately measured and detected early enough so as to proffer appropriate mitigation measures against its adverse effects. Also, any variation in the monitored waveforms that might be due to unpredictable activities within the substation network outlay should be recorded over long period of time. In Ref. [18], it was suggested that monitoring periods should be carried out at least 2 days or more. Thus, for adequate measurement of harmonics at distribution reticulations, it is prudent to monitor and record voltage and current harmonics at the customer's metering point using portable spectrum analysers that have facilities to acquire harmonic voltages and currents for the recommended periods. The data could be collected to help in the correlation of the load cycle patterns of non-linear loads with distortion indices such as THD_V, THD_I, the 3rd, 5th and 7th harmonic magnitudes. In this context, therefore, the chapter presents the measurement procedure for harmonic studies in distribution infrastructures.

Figure 1 summarizes the framework that could be adopted. It comprises three major harmonic studies, namely harmonic modeling, simulation and measurement techniques. The harmonic modeling includes harmonic current source models, non-linear voltage–current methods, power electronic converter models, high-frequency source models and rotating machine harmonic models. The simulation techniques entail the frequency scan method, harmonic current penetration method and harmonic power flow method. The measurement techniques consist of pre-measurements, measurement and post-measurement stages. Using **Figure 1** as a typical framework, the harmonic modeling stage could employ software such as PCFLO, PSCAD or MATLAB.

The measurement procedure may not be economically viable as it may involve several single-site dedicated data acquisition systems. In order to reduce cost, traditional heuristic approaches (HA) could be used to identify potential stations most vulnerable to harmonic problems using network historic harmonic data available at limited locations and durations and the artificial neural network (ANN) techniques applied to develop the harmonic power propagation patterns. However, detailed network loading analysis can ensure that power facilities are being utilized within safe limits and not be subjected to damage.

The distribution system is commonly broken down into three components: distribution substation, distribution primary and secondary feeders. At the substation level, the voltage is reduced and power is distributed in smaller amount to the customers from primary and secondary distribution networks. Consequently, one substation will supply many customers with power. Thus, the number of feeders in the distribution systems outnumbers that of the transmission systems. Furthermore, most customers are connected to only one of the three phases in the distribution network infrastructure. The power flow in each of the phases is different giving rise to an adverse effect referred to as 'unbalanced system'. This is undesirable and needs to be accounted for in harmonic power flow studies related to distribution networks.

With the increasing awareness for the use of comprehensive monitoring facilities, remote terminal units (RTUs) are introduced at distribution levels. This is intended to provide automation of power network resources so as to ensure that the network is being operated within the safe margin in terms of operating parameters such as load, duty and harmonic distortions.

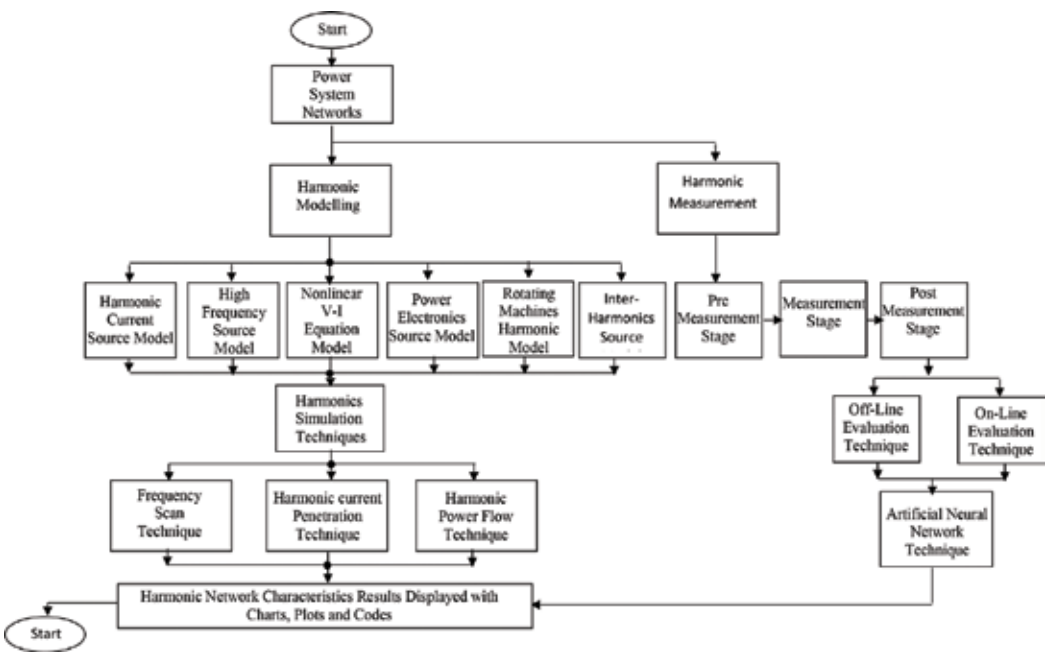

Figure 1. Framework of harmonic power flow studies.

Evaluation and simulation of planned operations using historic data will help to avoid damage to sensitive equipment due to these operations. From this standpoint, United Kingdom (UK) distribution network operators (DNO) have installed 60% of this RTU at their distribution reticulations to monitor the network conditions during different phases of operations [19] while the implementation of such automation by distribution company (DISCO) are envisaged for weak power systems.

2. Need for harmonic studies

The harmonic distortion needs to be accurately measured due to its adverse effects that include overheating, radio noise generation/interference, premature failure of sensitive equipment such as computers, hospital equipment and communication facilities. It is necessary to detect any variation in the monitored waveforms that might be due to unpredictable activities; such as system faults, customer non-linear loading, switching and so on, within the substation network outlay so as to keep the entire system safe and secure. On the other hand, the modern distribution networks are so diverse permitting the integration of New Energy Technologies (NETs), intertie AC/DC power transmission and domestic load-leveling devices as well as novel technical tools and monitoring equipment that may require new appraisal. There is a need to develop harmonic framework from the point of view of tripartite platform: modeling, simulation and prediction. This constitutes the motivation for the development of this monograph project to facilitate the documentation of pattern of harmonic distortion in some selected distribution reticulations and proffer appropriate remediation.

More importantly, the trends of harmonic studies have not satisfactorily determined whether harmonic-induced problems should be restricted to large industrial customers like rolling mills/process industries or should such harmonic monitoring framework be extended to commercial and domestic networks. This is simply accentuated due to the fact that such industries are equipped with direct current (DC) arc furnace known as major producers of harmonics. However, it may become apparent that the harmonic benchmarks set by existing standards such as IEEE519-1992, IEC 610000 need to be reviewed to capture emerging harmonic sources such as digital equipment, cell phone chargers, compact fluorescent lamps, PV inverters. This essentially represents contributions from commercial and domestic loads.

In pursuance of some specific objectives, the need for development of accurate computational engines that can replace the on-site harmonic survey and modeling of system is indispensable in modern emerging distribution systems. This is because the basic transmission network tools such as monitoring programme, contingency analysis and modern control systems aimed at improving system automation, reliability and integrity are still at developmental stages in distribution systems. More specifically, the field monitoring that is used to improve the knowledge of prevalent system operating conditions may not be cost effective at the distribution levels. It is also well known that the direct application of these techniques in the distribution systems is hampered by its unique nature, such as highly distributed and diverse loads, unbalanced phases and high R/X ratio. The high R/X ratio often requires the application of special distribution power flow solution. The unbalanced phases may need the solution

Harmonic order	Positive	Negative	Zero
1.	Yes	No	No
2.	No	Yes	No
3.	No	No	Yes
4.	No	Yes	No
5.	Yes	No	No
6.	No	Yes	No
7.	Yes	No	No
8.	No	Yes	No
9.	No	No	Yes
10.	No	Yes	No
11.	Yes	No	No

Table 1. Summary of harmonic phase sequence pattern.

of multiphase power flow and distributive loads may necessitate the deployment of several monitoring sites alongside the use of state estimation techniques on operating variables of the networks for realistic assessment of the networks. As a result, detailed distribution system analysis may not be reliably carried out especially in the development and evaluation of distribution system harmonic problems. On the other hand, it may be possible to achieve fast resolution of harmonic problems with the application of neural network, expert systems and other computational intelligence tools. These tools have the potential of minimizing the cost of multiple on-site harmonic monitoring and field recording and the rigorous harmonic modeling of the system in its entirety. **Table 1** summarizes the phase sequence pattern for harmonic orders up to 11th individual harmonic in power system.

3. Modeling of harmonic sources

It often requires serious research efforts to realistically qualify and model aggregate harmonic sources in a power system because some harmonics are non-characteristic, such as the even harmonics in transformer in-rush currents while others are non-deterministic, erratic and probabilistic in nature. Arc furnace load is one distribution load components can produce non-deterministic harmonic characteristics. Over the past two decades, significant efforts and meaningful progress have been made in the area of power system harmonic modeling. More so extensive specialized literatures are produced from time to time. In this context, the development of techniques for harmonic evaluation is often emphasized. However, according to a source [20], the tools for power system harmonic analysis are very few and as such the impact of harmonics on power quality degradation have not been fully explored.

Generally, there are four major approaches currently used for modeling of harmonics in power systems. They include:

http://dx.doi.org/10.5772/intechopen.77182

- frequency scan analysis;
- harmonic analysis using simple current source models;
- harmonic analysis considering fundamental frequency power flow results; and
- harmonic power flow.

Harmonic studies may also be undertaken to evaluate the effects of harmonic-producing devices predictably noticed in arc furnace, large adjustable speed drives, static VAR compensators, HVDC rectifiers, flexible AC transmission systems (FACTS) devices and other equipment in the system using power quality analyser such as Fluke 435 and Fluke VR1710. Herein, the two Fluke equipment shown in **Plates 1** and **2** were used as the major monitoring device to measure and analyse power quality events in real time as well as logging the harmonic data based on preset requirements of the findings. Then, post-processing tools that could be harnessed include the Fluke 435 inbuilt DFT, MATLAB and Excel software.

Plate 1. Voltage quality recorder (VR1710) logging data. (sources: (a) installation manual of fluke VR1710 (b) at a residential power outlet in Bauchi).

Plate 2. Monitoring equipment for PQ data collection at a substation with fluke 435.

4. Neural network as harmonic computational tool

The mathematical expression formulated with respect to **Figure 2** is given in Eq. (1) which is similar to that of Ref. [21].

$$y_i = f\left[\sum_{k=1}^{n}\left(f\left(\sum_{j=1}^{M}(x_i w_{ij})\right) v_{ik}\right)\right] \quad \mathrm{i} = 1, 2, \cdots \mathrm{m} \tag{1}$$

where $x_1, x_2 \ldots x_n$ and $y_1, y_2 \ldots y_m$ are input and output variables, respectively, and $w_{12}, w_{13} \ldots w_{ij}$ and $v_{12}, v_{13} \ldots v_{ik}$ are the synaptic weights for the inputs and output, respectively. Ideally, the set of input $x_1, x_2 \ldots x_n$ and the target $y_1, y_2 \ldots y_m$ are initially known through measurements or simulation. Then, the next task is to use those data to determine the optimum values of synaptic weights, $w_{12}, w_{13} \ldots w_{ij}$ and $v_{12}, v_{13} \ldots v_{ik}$ that will offer tolerable error margin. The rest of work is to reuse the trained network weights for a reliable determination of unfamiliar input patterns of similar processes.

The error values in **Figure 2** can be used to directly adjust the tap weights. If the system output is y, and the desired system output is known to be d, the error signal can be defined as in Eq. (2):

$$\mathrm{g(e)} = \mathrm{d} - \mathrm{y} \tag{2}$$

The error-correction learning algorithms attempt to minimize the error signal for all iterations. The most popular learning algorithm for use with error-correction learning is the gradient descent algorithm. The gradient descent algorithm is employed used to minimize an error function $g(e)$, through the manipulation of a weight vector $\overline{w}$. The cost function should be a linear combination of the weight vector and an input vector x. The algorithm is as follows:

http://dx.doi.org/10.5772/intechopen.77182

$$w_{ij}(n+1) = w_{ij}(n) + \eta g\left(w_{ij}(n)\right) \tag{3}$$

here, η is known as the step-size parameter and affects the rate of convergence of the algorithm. If the step size is too small, the algorithm will take a long time to converge. If the step size is too large, the algorithm might oscillate or diverge. The gradient function, g(.), in gradient descent algorithm, works by taking the gradient of the weight space to find the path of steepest descent as shown in **Figure 3**. By following the path of steepest descent and finding a minimum at each iterative step, the algorithm would not diverge especially if the weight space is infinitely decreasing. However, when a minimum is found, there is no guarantee that it is a global minimum. Hence, there is need for a more robust algorithm such as backpropagation technique to achieve global minimum. The backpropagation algorithm, in combination with a supervised error-correction learning rule (i.e. gradient descent algorithm), is one of the most popular and robust tools in the training of artificial neural networks. According to Ref. [22], backpropagation is used to find a local minimum in the error function. It passes the error signals backwards through the network during training to update the weights of the network. When talking about backpropagation, it is useful to define the term interlayer to be a layer of neurons, and the corresponding input tap weights to that layer. A superscript denotes a specific interlayer, and a subscript denotes the specific neuron from within that layer. These are expressed mathematically as in Eqs. (4) and (5).

$$\xi_j^{\,l} = \sum_{i-1}^{N^{l-1}} w_{ij}^{\,l}\, x_i^{\,l-1} \tag{4}$$

$$x_j^{\,l} = \sigma\left(\xi_j^{\,l}\right) \tag{5}$$

where $x_i^{\,l-1}$ are the outputs from the previous interlayer (the inputs to the current interlayer), $w_{ij}^{\,l}$ is the tap weight from the *i*-input from the previous interlayer to the *j* element of the current interlayer. N^{l-1} is the total number of neurons in the previous interlayer. $x_j^{\,l}$ is the output of the previous layer (l − 1) which is now an input to current layer (l).

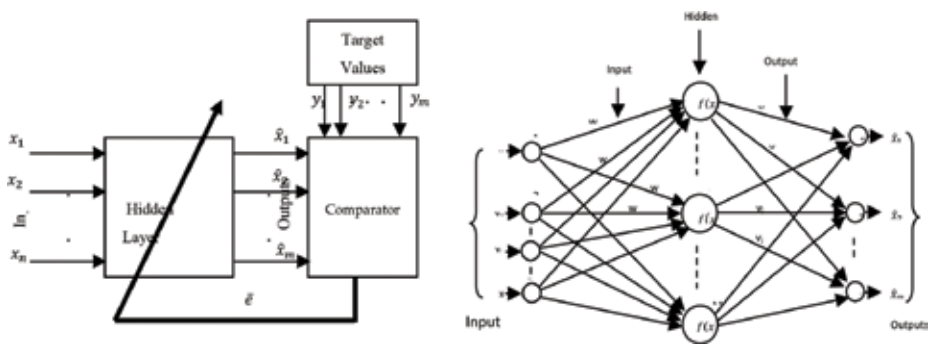

Figure 2. Input–output one hidden layer perceptron ANN.

The backpropagation algorithm specifies that the tap weights of the network are updated iteratively during training to approach the minimum of the error function. This is done via Eqs. (6) and (7):

$$w_{ij}^{\ l}(n) \ = \ w_{ij}(n-1) + \delta\left(w_{ij}^{\ l}(n)\right) \tag{6}$$

$$w_{ij}^{\ l-1}(n) \ = \ \eta\delta_j^{\ l}\, x_i^{l-1}(n) + \mu\Delta\, w_{ij}^{\ l}(n-1) \tag{7}$$

The relationship between this algorithm and the gradient descent algorithm should be immediately apparent. Here, η is known as the learning rate, not the step-size, because it affects the speed at which the system learns (converges). The parameter μ is known as the momentum parameter. The momentum parameter, μ, forces the search to take into account its movement from the previous iteration. By doing so, the system will tend to avoid local minima or saddle points, and tends to approach the global minimum. The parameter δ is what makes this algorithm a 'backpropagation' algorithm. This is given by Eq. (8):

$$\delta_j^{\ l} \ = \ \frac{dx_j^{\ l}}{dt}\sum_{k=1}^{r}\delta_k^{\ l+1}\, w_{kj}^{\ l+1} \tag{8}$$

The δ function for each layer depends on the δ from the previous layer. For the special case of the output layer (the highest layer), Eq. (9) can be used instead:

$$\delta_j^{\ l} \ = \ \frac{dx_j^{\ l}}{dt}\left(x_j^{\ l} - y_j\right) \tag{9}$$

In this way, the signals propagate backwards through the system from the output layer to the input layer. The next section presents the development of algorithmic framework for ANN harmonic predictor.

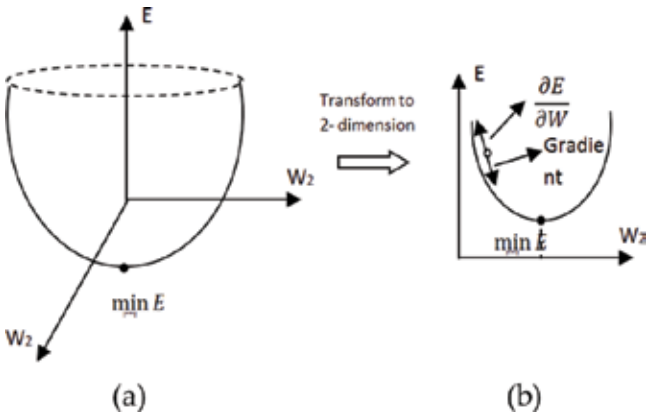

Figure 3. Iterative model for setting absolute error of ANN using gradient descent method. (a) 3-dimensional view of gradient descent. (b) 2-dimensional transform of gradient descent.

http://dx.doi.org/10.5772/intechopen.77182

5. Development of ANN harmonic predictor

Operators of an electric power system must be able to accurately quantify the level of harmonic distortion across the system. Harmonic distortion is a system-wide problem which cannot be modelled only with an integral part of the power system. It will therefore be difficult to determine which variables are best used for ANN models. According to Ref. [23], adaptive predictive techniques generally have some implementation problems. First, how to determine the number of input signal may pose some challenges, and second, the determination of convergence factor may be done subjectively. More specifically, the harmonic distortion problem is so complicated that conventional methods do not work so well for its prediction [24]. This is apparently due to non-linearity associated with harmonic components alongside with its random-like behaviour for very short terms and a periodicity for a fairly long term.

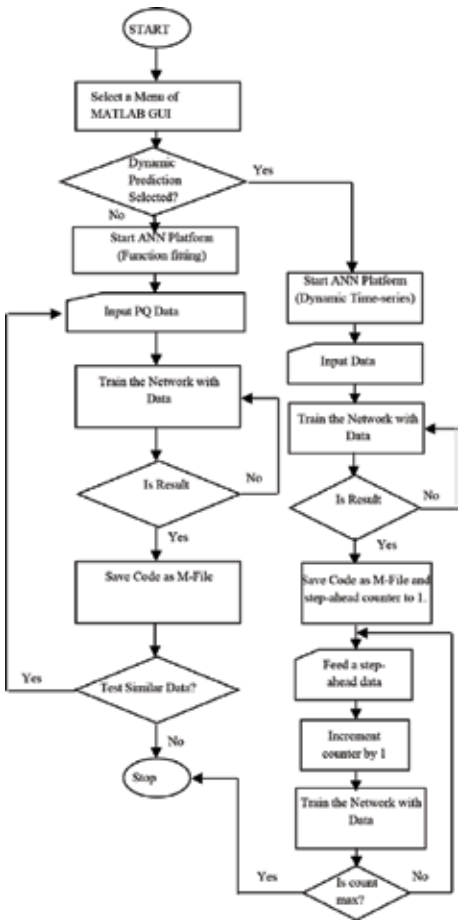

Figure 4. Flow chart for a MATLAB-based ANN function fitting and n-step-ahead prediction. (a) Training state of volt THD. (b) Performance of ANN THD_v tracking. (c) Tracking volt THD with ANN-Day1. (d) Tracking volt THD with ANN-Day3.

Three types of samples are presented to ANN, namely training, validation and testing samples. For the training data set, samples are presented to the network during this stage and the network is adjusted according to its error. In the validation regime, sample data are used to measure network generalization, and to halt training when generalization stops improving. Testing is used for generalization and has been said to have no effect on training performance but it is often used to provide an independent measure of network performance during and after training.

In the development of the ANN harmonics predictor, attempts were made to select the correct number of inputs for the network, optimum division of data into training, validation and testing regimes as well as their convergence indices according to acceptable best practices in the evaluation stage.

In this chapter, the ANN inputs are the RMS voltages, the RMS currents and frequency monitored in the two distribution reticulations. The outputs are the voltage or current THD and principal component indices like 3rd, 5th and 7th harmonic orders for short term comprising few seconds logged time of data up to 24 h, the long terms for daily data up to 1 week data. In the last scenario, a preconditioned non-linear harmonic network data under experimental set-up was also selected as input to ANN. The flow chart shown in **Figure 4** is proposed for the entire work in the application of neural network-based prediction technique.

The model predictor is used to train a neural network to track the harmonic data appropriately preprocessed outside the MATLAB environment with database software (POWERLOG and EXCEL). The POWERLOG is platform on which Fluke 435 power quality meter stored data into PC. However, MATLAB M-file works very well with EXCEL, serving as an interface hetween POWERLOG and ANN MATLAB programme. The ANN thus generates needful results presented in section 6. The predicted outputs of ANN are the responses/error output divided into three sub-model outputs; the training, validation and test errors. These errors are compared with the best practice error indices and fed to output evaluation unit.

6. Sample results of ANN emulator

The fitting functions established the THD for voltage and THD for current, being cumulative, using the set of input data based on selected daily harmonic data. The simulation results are as shown in **Figures 5** and **6** for harmonic estimation techniques using Malaysian university power quality (PQ) data while **Figures 7** and **8** for a Nigerian university PQ data. Each plot in these figures has three lines, because the seven inputs representing three-phase voltage and current RMS as well as nominal frequency and one target vector (output distortion index) are randomly divided into three sets as earlier stated. For all cases, 70% of the vectors were used to train the network and 15% of the matrices were used for validation whilst the remaining 15% used for testing. As a stopping criterion, the network is made to memorize the training pattern after six validations, otherwise the training is terminated. This technique has been adopted to avoid the problem of over fitting commonly experienced in the backpropagation type of optimization and learning algorithm using early stopping as observed in **Figures 5a**, **6a**, **7b**, **8b**. Finally, after the validation was accomplished, the last 15% of the data matrix provided an independent test of network generalization process. The family of plots in **Figures 5c–d**, **6c–d**, **7c–d**, **8c–d**, respectively, show sample results for snap-short emulators of volt and current THD in the two networks.

http://dx.doi.org/10.5772/intechopen.77182

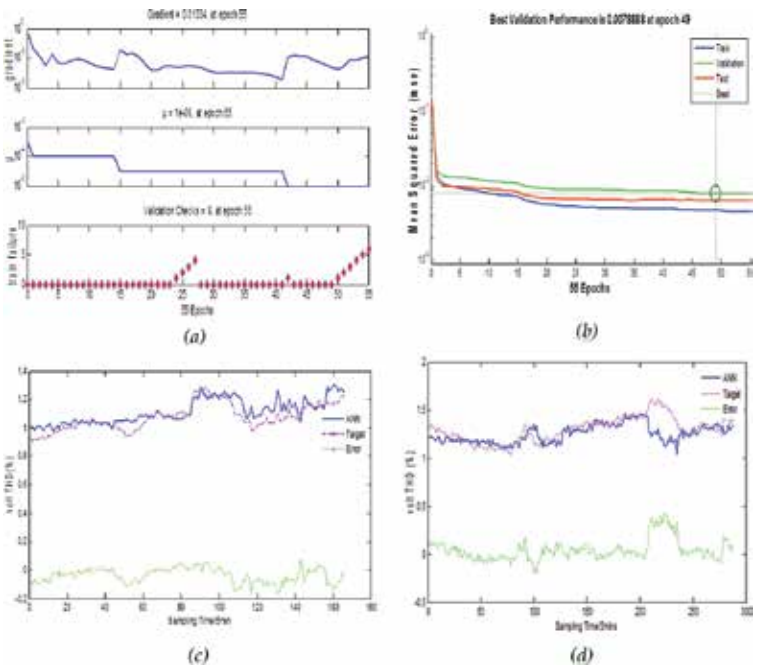

Figure 5. Field harmonic data and tracking of volt THD with ANN in Malaysia. (a) Training state of current THD. (b) Performance of ANN THD_I tracking. (c) Tracking THD_I with ANN-Day1. (d) Tracking THD_I with ANN-Day3.

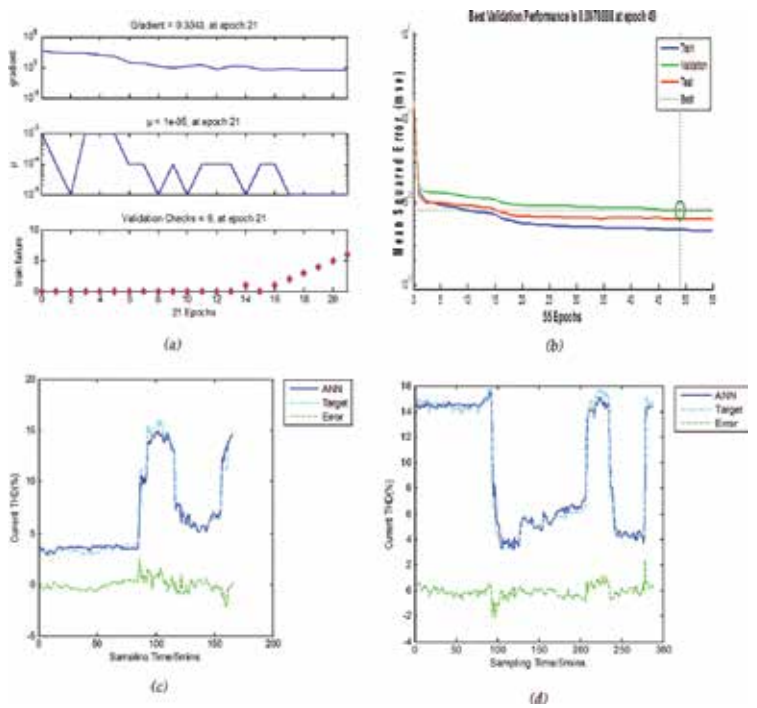

Figure 6. Field harmonic data and tracking of current THD with ANN in Malaysia. (a) Training state of volt THD. (b) Performance of ANN THD_I tracking. (c) Tracking THD_I with ANN-day 2 early morning (EM). (d) Tracking THD_I with ANN-Day2mid day (MD).

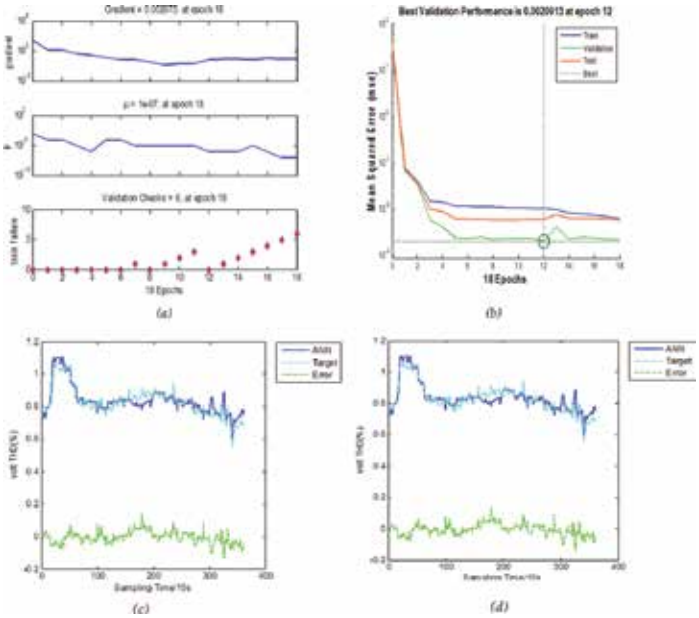

Figure 7. Field harmonic data and tracking of volt THD with ANN in Nigeria. (a) Training state of current THD. (b) Performance of ANN THD_I tracking. (c) Tracking THD_I with ANN-day 2 early morning (EM). (d) Tracking THD_I with ANN-Day2mid day (MD).

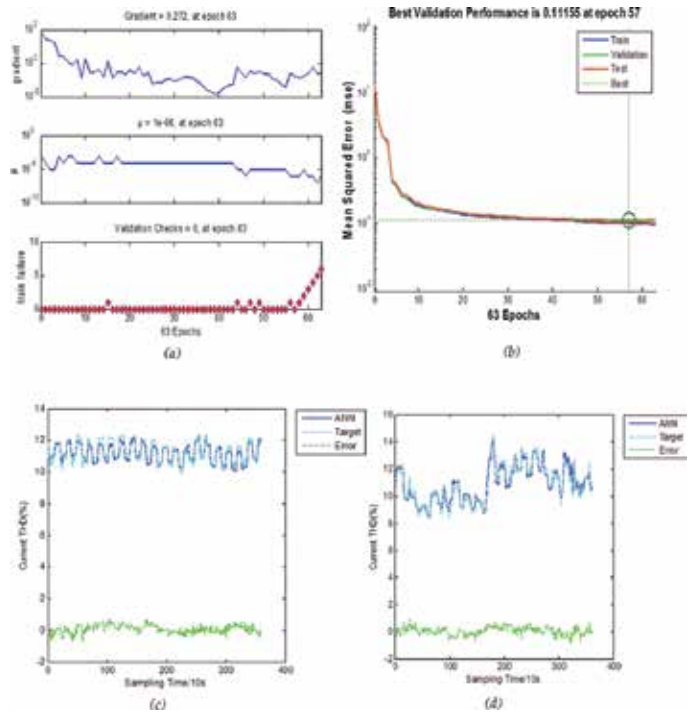

Figure 8. Field harmonic data and tracking of volt THD with ANN in Nigeria. (a)Training State of Current THD (b) Performance of ANN THD_I Tracking (c) Tracking THD_I with ANN-day 2 early morning (EM) (d) Tracking THD_I with ANN-Day2mid day (MD)

7. Conclusion

The results have facilitated the classification of tools into simple, semi-advanced and advanced types. It also buttressed further the need for periodic investigation and harmonic assessment in a plant at least on frequency of one quarter (Q1), two quarters (Q2), three quarter (Q3) or four quarter (Q4), especially with the installation of new non-linear loads. Based on the enumerated procedures the selection of needful tools can be accomplished.

Author details

Abdullahi Lanre Amoo*, Usman O. Aliyu and Ganiyu Ayinde Bakare

*Address all correspondence to: alabdullahi@atbu.edu.ng

Abubakar Tafawa Balewa University, Bauchi, Nigeria

References

[1] Biswas S, Chatterjee A, Goswami SK. An artificial bee colony-least square algorithm for solving harmonic estimation problems. Applied Soft Computing. 2013;**13**:2343-2355

[2] Amoo A, Said D, Yusuf A, Mohd Zin A. Harmonic power flow in Nigerian Power system with PV site. In: IEEE 7th International Power Engineering and Optimization Conference (PEOCO); 2013. pp. 319-323

[3] Amoo AL, Bappah AS, Aliyu UO. Virtual Platforms for Teaching Harmonic Load Flow to Technical and Engineering Students in Nigeria. In: Proceeding of IEEE, NIGERCON; November 14-16, 2013. Vol. 2. pp. 98-107

[4] Swiatek B, Rogoz M, Hanzelka Z. Power system harmonic estimation using neural networks. In: 9th International Conference on Electrical Power Quality and Utilisation, 2007. EPQU 2007. pp. 1-8

[5] Testa A, Langella R. Considerations on probabilistic harmonic voltages. In: Power Engineering Society General Meeting, 2003. IEEE, 2003. Vol. 2. pp. 1159

[6] Srivastava S, Gupta J, Gupta M. PSO & neural-network based signature recognition for harmonic source identification. In: IEEE Region 10 Conference TENCON; 2009. pp. 1-5

[7] Sexauer JM, Mohagheghi S. Voltage Quality Assessment in a Distribution System With Distributed Generation – A Probabilistic Load Flow Approach. IEEE Transactions on Power Delivery. Vol. 28; 2013. pp. 1652-1662

[8] Dugan RC, Key TS, Ball GJ. Distributed resources standards. Industry Applications Magazine. IEEE; 2006. Vol. 12. pp. 27-34

[9] Al-duaij EOS. Harmonics Effects in Power System. International Journal of Engineering Research and Applications. 2015;**5**:01-19

[10] Mayoral EH, López MAH, Hernández ER, Marrero HJC, Portela JRD, Oliva VIM. Fourier Analysis for Harmonic Signals in Electrical Power Systems. In: Fourier Transforms-High-tech Application and Current Trends. InTech; 2017

[11] Cespedes M, Sun J. Impedance modeling and analysis of grid-connected voltage-source converters. IEEE Transactions on Power Electronics. 2014;**29**:1254-1261

[12] Rygg A, Molinas M, Zhang C, Cai X. A modified sequence-domain impedance definition and its equivalence to the dq-domain impedance definition for the stability analysis of AC power electronic systems. IEEE Journal of Emerging and Selected Topics in Power Electronics. 2016;**4**:1383-1396

[13] Bairamkulov R, Ruderman A, Familiant YL. Time domain optimization of voltage and current THD for a three-phase cascaded H-Bridge inverter. In: IEEE International Power Electronics and Motion Control Conference (PEMC); 2016. pp. 227-232

[14] Wang J, Liang J, Gao F, Dong X, Wang C, Zhao B. A closed-loop time-domain analysis method for modular multilevel converter. IEEE Transactions on Power Electronics. 2017;**32**:7494-7508

[15] Guo X, Liu W, Zhang X, Sun X, Lu Z, Guerrero JM. Flexible control strategy for grid-connected inverter under unbalanced grid faults without PLL. IEEE Transactions on Power Electronics. 2015;**30**:1773-1778

[16] Wilsun X, Xian L, Yilu L. An investigation on the validity of power-direction method for harmonic source determination. IEEE Transactions on Power Delivery. 2003;**18**:214-219

[17] Li W, Kuo-Hua L. A study on randomly varying harmonic currents and total harmonic distortion of currents in power systems. In: International Conference on Future Power Systems; 2005. pp. 5

[18] Grady M. Understanding power system harmonics. Department of Electrical & Computer Engineering, University of Texas at Austin; 2012

[19] PPA and Capula Ed. Distribution Network Visibility (Report UK Power Networks. LCN Fund Tier 1 Close Down; 2013

[20] Kuhlmann V, Dewe M, Arnold C. Some aspects of precise synchronisation of data acquisition for power systems harmonic analysis

[21] Bullinaria J. Introduction to neural computation. Notas de aula. Disponível em:< http://www. cs. bham. ac. uk/~ jxb/inc. html>. Acesso em; 2010. Vol. 15

[22] Rojas R. Neural networks: a systematic introduction. Springer Science & Business Media; 2013

[23] Ibrahim WA, Morcos MM. Artificial intelligence and advanced mathematical tools for power quality applications: a survey. IEEE Transactions on Power Delivery. 2002;**17**: 668-673

[24] Riad AM, El-Bakry HM, Mastorakis N. Fast harmonic current/voltage prediction by using high speed time delay neural networks. In: Proceedings of the 3rd International Conference on Communications and information technology; 2009. pp. 245-272

Chapter 6

Power System Harmonics Estimation Using Adaptive Filters

Harish Kumar Sahoo and Umamani Subudhi

Additional information is available at the end of the chapter

http://dx.doi.org/10.5772/intechopen.74581

Abstract

Accurate estimation and tracking of power quality disturbances requires efficient adaptive model based techniques which should have elegant structures to be implemented in practical systems. Adaptive filters have been used as a popular estimator to track the time-varying power quality events, but the performance is limited due to higher order nonlinearity exists in system dynamics. Harmonics generated in the generation and distribution system are one of the critical power quality issues to be addressed properly. Least mean square (LMS) and recursive least square (RLS) based adaptive estimation models can be used to track the harmonic amplitudes and phases in practical power system applications. Due to time varying nature of harmonic parameters, modifications have to be incorporated in adaptive filters based modeling during estimation of the harmonic parameters and decaying DC components present in the distorted power signals. Volterra expansions can be combined with the adaptive filtering to improve the estimation accuracy and enhance the convergence rate of the estimation model.

Keywords: LMS, RLS, Volterra series, decaying DC, power quality

1. Introduction

Customers across the globe use large number of power electronic devices that are quite sensitive to power quality (PQ) disturbances in the power network. From the world-wide customer survey, it is found that PQ related issues like voltage dips, voltage swell, transient, harmonics, flicker [1, 2] are increasing every year and these events must be tracked accurately to protect the power networks. Among various PQ problems, harmonics in the network can interact adversely with the utility supply system. Harmonics are sinusoidal voltages or currents having frequencies that are integer multiples of the supply frequency. Any periodic

distorted waveform can be expressed as a sum of pure sine waves in which the frequency of each sinusoid is an integer multiple of the fundamental frequency of the distorted wave. Harmonic distortion is mostly caused by nonlinear characteristics of devices and loads used in a power transmission and distribution network. Adaptive filters are efficient parametric techniques to estimate the harmonic and other PQ parameters accurately. The estimated harmonic parameters can be used to design harmonic elimination filters. Popular harmonic estimation models are based on LMS, NLMS, and RLS family of adaptive filters and the parameters of model are updated in a recursive manner.

2. Effects of harmonic distortion

Due to the operation of power electronic devices, harmonic current is produced which give rise to additional harmonic power flow with decreased power factor of the network. Large harmonic current may cause overloading and extra power losses in the network elements. In extreme cases, it can lead to high thermal stresses and early aging of the network devices. Power system equipments such as transformers, cables, motors, capacitors [3] are network components that are mainly affected by harmonic distortion and described in the following sections.

2.1. Impact on transformer

Transformer losses are broadly classified into two types as no load losses (Hysteresis and Eddy current loss) and load losses. Among no load losses Eddy current loss varies with square of the frequency and load losses varies with square of the load current. With the presence of harmonic current containing higher frequencies, Eddy current flows in the windings, core and in other conducting bodies causes additional heating. Also because of presence of harmonics, RMS value of current increases such that load losses increases.

2.2. Impact on cables

Resistance of a cable depends on skin effect and proximity effect. Due to the presence of harmonics eddy current increases which leads to increase in the effective resistance as well as eddy current losses. Both the effects are dependent on power system frequencies, conductor size, the resistivity and permeability of the material. Due to the presence of harmonics in the cables, the conductor resistance increases and its operating temperature increases further which leads to early aging of the cables.

2.3. Impact on capacitor

In the presence of harmonics in the power system, impedance of capacitor decreases with increase in frequency. Due to voltage harmonic present in the power system dielectric losses in the capacitor increases at high operating temperature and reduces the reliability. In extreme situation operational life of capacitor reduces.

http://dx.doi.org/10.5772/intechopen.74581

2.4. Impact on motors

Harmonic voltage distortion present at the motor terminals produces harmonic fluxes within the motor such that motor rotates at a frequency different than the rotor synchronous frequency. Presence of harmonic causes additional losses, decreased efficiency, additional heating, vibration and high pitched noise.

Besides the above equipments, presence of harmonics causes interference in communication circuits, overheating of magnetic portions of electrical systems, voltage distortion during resonance. To reduce the effects of harmonics disturbances, harmonic filters must be designed. Before designing the filter, harmonic parameter should be estimated accurately using suitable signal processing method which provides a viable solution to power quality issues.

2.5. Causes and effects of decaying DC offset

Electrical signal may contain decaying dc offsets during transient state, performance of discrete Fourier transform (DFT) filter or analog to digital converter (ADC) is improves if DC offset is removed. When short circuit occur, dc offset may appear and normally are of exponential type. The time constant of the component depends on the X/R ratio of the circuit involved in the fault. Hence along with harmonics, decaying dc components has to be estimated and eliminated [3].

3. IEEE harmonic standards

The primary objective of standard is to provide regulation for all involved parties to work together to ensure compatibility between customer and service provider. For harmonic limits, standards are governed by IEEE and IEC as described below [1].

3.1. IEEE 519

IEEE 519-2009, Recommended Practices and Requirements for Harmonic Control in Electric Power Systems, established limits on harmonic currents and voltages at the point of common coupling (PCC) or point of metering.

The limits of IEEE 519 are intended to:

1. Assure that the electric utility can deliver relatively clean power to all of its customers
2. Assure that the electric utility can protect its electrical equipments from overheating, loss of life from excessive harmonic currents, and excessive voltage stress due to excessive harmonic voltage. Each point from IEEE 519 lists the limits for harmonic distortion at the point of common coupling (PCC) or metering point with the utility. The voltage distortion limits are 3% for individual harmonics and 5% THD.

All of the harmonic limits in IEEE 519 are based on customer load and location on the power system. The limits are not applied to particular equipment, although, with a high amount of nonlinear loads, it is likely that some harmonic suppression may be necessary.

3.2. IEEE 519 standard for current harmonics and voltage harmonics

Both end users and utility are responsible for harmonic distortion. According to this standard end users are responsible for limiting the harmonic current distortion and utility will be responsible for limiting harmonic voltage distortion. Distortion standards are based on short circuit capacity (ISC/IL)i.e. ratio of maximum short circuit current at PCC to maximum demand load current at PCC. Both current and voltage distortion limits for each customers are given in **Tables 1–3**.

3.3. IEC 61000-3-2 and IEC 61000-3-4 (formerly 1000–3-2 and 1000–3-4)

3.3.1. IEC 61000–3-2 (1995–2003)

It specifies limits for harmonic current emissions applicable to electrical and electronic equipment having an input current up to and including 16 A per phase, and intended to be connected to public low-voltage distribution systems.

ISC/IL	h < 11	11 ≤ h < 17	17 ≤ h < 23	23 ≤ h < 25	h ≥ 35	TDD (%)
<50	2.0	1.0	0.75	0.3	0.15	2.5
≥50	3.0	1.5	1.15	0.45	0.22	3.75

Table 1. Current distortion limits for harmonics.

ISC/IL	h < 11	11 ≤ h < 17	17 ≤ h < 23	23 ≤ h < 25	TDD (%)
<20	4.0	2.0	1.5	0.6	5
20–50	7.0	3.5	2.5	1.0	8
50–100	10	4.5	4.0	1.5	12
100–1000	12	5.5	5.0	2.0	15
>1000	15	7.0	6.0	2.5	20

Table 2. Current distortion limits for harmonics.

Bus voltage	Individual Vb (%)	THDV (%)
V < 69 kV	3.0	5.0
69 ≤ V < 161 kV	1.5	2.5
V ≥ 161 kV	1.0	1.5

Table 3. Voltage distortion limits for harmonics.

Harmonic order	Maximum permissible harmonic current	Harmonic order	Maximum permissible harmonic current
3	21.6	19	1.1
5	10.7	21	0.6
7	7.2	23	0.9
9	3.8	25	0.8
11	3.1	27	0.6
13	2	29	0.7
15	0.7	31	0.7
17	1.2	33	0.6

Table 4. Harmonic current limits according to IEC 61000–3-4.

3.3.2. IEC/TS 61000: 3-4 (1998: 2010)

It specifies to electrical and electronic equipment with a rated input current exceeding 16 A and up to 75A per phase and intended to be connected to public low-voltage ac distribution systems of the following types:

- Nominal voltage up to 240 V, single-phase, two or three wires
- Nominal voltage up to 600 V, three-phase, three or four wires
- Nominal frequency 50 or 60 Hz

Harmonic current limits based on this standard are shown in **Table 4**.

4. Brief literature for adaptive harmonic estimation

Design of robust and efficient harmonic estimation models for accurate estimation of signal parameters in presence of harmonics [4, 5] is a real challenge to power system engineers. Non parametric and parametric estimation models are frequently used to track the harmonic parameters. Non parametric methods are mostly transform based approaches like discrete Fourier transform (DFT) [6], short time Fourier transform (STFT). But these methods suffer from inaccuracies due to system noise and leakage effects. MSDFT proposed by Carugati et al. [7] eliminates the error due to spectral leakage and but still there is limitation during highly non stationary events. Alternately parametric approaches which assumes the signal satisfies a mathematical model with known functional can be used as robust techniques for harmonic estimation. Various parametric methods which include least mean square (LMS) [8], least square (LS) [9, 10], Kalman filters, (KF) [11] are frequently used in power quality monitoring. Among various adaptive filters, LMS has simple structure and offers good convergence behavior in case of stationary signal. But it provides poor estimation performance owing to its poor convergence rate when the signal statistics are time varying. In case of RLS and KF, initial

choice of covariance matrix is difficult for faster and stable convergence of the algorithm. To improve the error convergence property, Volterra expansion [12, 13] of the input samples is incorporated to develop robust adaptive filter in this chapter. LMS/F [14] filter is developed as a compromise between LMS and LMF [15] which is further extended by the use of Volterra series expansion to develop Volterra LMS/F filter. RLS filter also can be combined with Volterra series to develop Volterra RLS filter with faster convergence. The efficiency of all these filters can be tested for harmonic estimation using performance measures like estimation error, mean square error (MSE) etc.

5. Adaptive algorithms for harmonic estimation

Different adaptive algorithms for harmonic estimations are described in the following sections.

5.1. LMS algorithm for harmonic estimation

Least mean square (LMS) algorithm was originated by Window and Hoff (1960). LMS filter is simple to implement which involves processes like

a. A filtering process which involves computation of the output of a linear filter in response to an input signal and generates an estimation error by comparing this output with a desired response.

b. An adaptive process which involves the automatic adjustment of the parameters of the filter in accordance with the estimation error.

Steps to implement LMS algorithm:

- Initialize weight vector w
- Generate power signal
- Discretize the power signal with the desired sampling frequency meeting Nyquist criteria and estimate the signal using initial state vector
- Calculate the estimation error

Update the weight vector as-

$$\hat{w}(n) = \hat{w}(n-1) + \mu e(n-1)x(n-1) \tag{1}$$

where μ is the step size

- Go to step 4 if last iteration is not obtained
- Estimate amplitudes and phases of fundamental and harmonics using Eq. (24-27).

  The step size parameter μ convergence in mean square given by

http://dx.doi.org/10.5772/intechopen.74581

$$0 < \mu < \frac{1}{MS_{\max}} \tag{2}$$

where M is the length of the filter in terms of tap weights and S_{max} is the maximum value of the power spectral density of the tap inputs. This algorithm requires only 2 M + 1 complex multiplications and 2 M + 1 complex addition per iteration.

5.2. Recursive least square (RLS) for harmonic estimation

Recursive least square (RLS) is the recursive implementation of least square in which computation is started with prescribed initial conditions and use the information contained in new data samples to update the old estimates. The cost function to be minimized is given by:

$$\xi(n) = \sum_{i=1}^{n} \beta(n,i)|e(i)|^2 \tag{3}$$

where n is the variable length of the observable data; $\beta(n,i)$ is the weighting factor satisfying the property

$$0 < \beta(n,i) \leq 1, i = 1, 2.....n \tag{4}$$

The use of weighting factor is intended to ensure that data in the distance past are forgotten in order to afford the possibility of following statistical variation of the observable data when the filter operates in a non stationary environment. A special form of weighting is commonly used known as forgetting factor and is defined by:

$$\beta(n,i) = \lambda^{n-i} \qquad i = 1, 2....n \tag{5}$$

where λ is a positive constant close to but less than unity.

Steps to implement RLS algorithm:

- Initialize weight vector and inverse correlation matrix

$$W(0) = 0, P(0) = \delta^{-1}I \tag{6}$$

where δ is small positive constant for high SNR and large positive constant for low SNR.

- Generate the discretized form of power signal using the corresponding sampling frequency.
- Calculate the estimation error.
- Update the weight vector as

$$\hat{w}(n) = \hat{w}(n-1) + k(n)e(n) \tag{7}$$

where the relation between gain k with covariance parameter vector is

$$k(n) = \frac{\pi(n)}{\lambda + X^T(n)\pi(n)} \tag{8}$$

and

$$\pi(n) = P(n-1)X(n) \tag{9}$$

- Using matrix inversion lemma, the updated covariance matrix is given as

$$P(n) = \lambda^{-1}P(n-1) - \lambda^{-1}k(n)X^T(n)P(n-1) \tag{10}$$

- Amplitude and phases of fundamental and harmonic parameters as well as decaying dc components are estimated using Eq. (24)

6. Volterra series

Volterra series is an expansion applied to input vector for analysis of non-linear behavior of the system and the expanded patterns are the inputs to the adaptive estimation model as shown in **Figure 1**.

A continuous time-invariant system with x(t) as input and X(t) as output can be expanded through Volterra series as

$$X(t) = \left[x(t)\ \ x(t-1)\ldots x(t-M)\ x^2(t)\ldots x^2(t-M)\ \ldots\ldots\ x(t)x(t-1)\right] \tag{11}$$

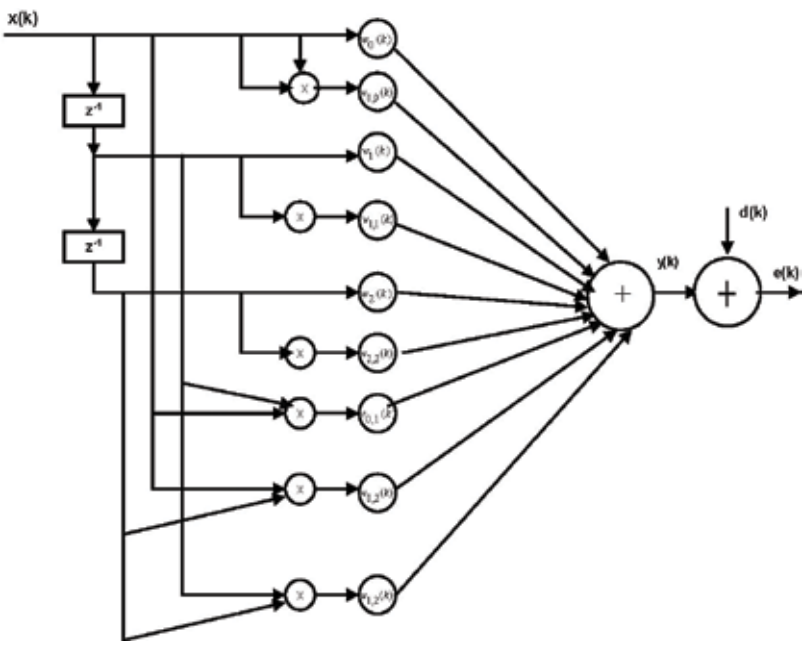

Figure 1. Structure of Volterra filter.

http://dx.doi.org/10.5772/intechopen.74581

Volterra structure can be combined with LMS, LMF, RLS to construct new kind of adaptive filters such as Volterra LMS, Volterra LMF and Volterra RLS etc.

6.1. Volterra LMS/F algorithm for harmonic estimation

LMS Algorithm is the simplest algorithm which is easy to implement. Since the convergence property degrades in case of non stationary signal, Walach & Widrow [15] applied the fourth order power optimization area. However the computational complexity of LMF is very high. A combined approach known as LMS/F algorithm proposed by Harris [17] considering the trade-off between convergence speed and steady state performance. Further reduction of convergence speed is achieved by using Volterra series expansion of input samples to develop a robust adaptive filter known as Volterra LMS/F filter [16].

Steps to implement VLMS/F algorithm:

- Initialize weight vector
- Generate expanded input vector using Volterra expansion
- Generate error signal vector using difference of desired and output signal vector

Updated weight vector can be evaluated as:

$$\hat{w}(n) = \hat{w}(n-1) + \mu \frac{e^3(n-1)}{e^2(n-1) + \alpha} x(n-1) \tag{12}$$

where μ is the step size and α is the threshold parameter. They are used to trade off between convergence and steady state performance.

6.2. Volterra RLS algorithm for harmonic estimation

To enhance the convergence speed of RLS filter, input signal vector is expanded to higher dimensions using Volterra series expansion. As a result a new filter came up known as Volterra RLS filter.

Steps to implement Volterra RLS Algorithm:

- Initialize weight vector and inverse correlation matrix
- Generate expanded input vector using Volterra expansion
- Generate error signal
- Inverse correlation matrix is updated as

$$P(n) = \lambda^{-1} P(n-1) - \lambda^{-1} k(n) X^T(n) P(n-1) \tag{13}$$

- Estimate the updated weight vector as:

$$\hat{w}(n) = \hat{w}(n-1) + k(n) e(n) \tag{14}$$

7. Harmonic estimation model

Assuming voltage or current waveforms of power signals with higher order harmonics corrupted by noise, the general form of the waveforms can be expressed as [16].

$$z(t) = \sum_{n=1}^{N} A_n \sin\left(\omega_n t + \phi_n\right) + a_{dc} e^{-\alpha_{dc} t} + v(t) \tag{15}$$

where $\omega_n = n2\pi f_0$ and f_0 is the fundamental frequency, N is the number of harmonics, $v(t)$ is the additive white Gaussian noise, $a_{dc}e^{-\alpha_{dc}t}$ is the decaying dc component.

The discrete version of Eq. (15) can be represented as:

$$z(k) = \sum_{n=1}^{N} A_n \sin\left(\omega n k T_s + \phi_n\right) + a_{dc} e^{-\alpha dc k TS} + v(kTs) \tag{16}$$

where T_s is the sampling period.

Decaying DC component can be approximated for smaller value of '$\alpha_{dc}kT_S$' as

$$a_{dc} e^{-\alpha_{dc} k T_S} \simeq a_{dc}(1 - \alpha_{dc} k T_S) \tag{17}$$

Using Eq. (17) in Eq. (16) $z(k)$ can be obtained as:

$$z(k) = \sum_{n=1}^{N} A_n \sin\left(w_n k T_s + \phi_n\right) + a_{dc} - a_{dc}\alpha_{dc} k T_s + v(kT_s) \tag{18}$$

For estimation of amplitudes and phases Eq. (18) can be rewritten as

$$z(k) = \sum_{n=1}^{N} \left[A_n \sin\left(\omega_n k T_s\right) \cos\phi_n + A_n \cos\left(\omega_n k T_s\right) \sin\phi_n\right] + a_{dc} - a_{dc}\alpha_{dc} k T_s + v(kT_s) \tag{19}$$

Eq. (19) can be expressed in parametric form as:

$$z(k) = X(k) w^T(k) \tag{20}$$

Thus input signal vector can be expressed as

$$x(k) = [\sin(\omega_1 kTs) \quad \cos(w_1 k\omega Ts) \ldots \quad \sin(\omega_N kTs) \quad \cos(\omega_N kTs) \quad 1 \quad -kT_s] \tag{21}$$

The vector of unknown parameter is expressed as:

$$w(k) = [w_1(k) \; w_2(k) \ldots w_{2N}(k) \; w_{2N+1}(k) \; w_{2N+2}(k)] \tag{22}$$

$$w(k) = \left[A_1 \cos\phi 1 \;\; A_1 \sin\phi 1 \ldots A_n \cos\phi_n \;\; A_n \sin\phi_n \;\; a_{dc} \;\; a_{dc}\alpha_{dc}\right] \tag{23}$$

Amplitude and phase estimation can be carried out with updated coefficients of filtering algorithms as given below.

$$\hat{A}_n = \sqrt{\hat{w}_{2N}^2 + \hat{w}_{2N-1}^2} \tag{24}$$

$$\hat{\phi}_n = \tan^{-1}\left(\frac{\hat{w}_{2N}}{\hat{w}_{2N-1}}\right) \tag{25}$$

$$a_{dc} = w_{2N+1} \tag{26}$$

$$\hat{\alpha}_{dc} = \tan^{-1}\left(\frac{\hat{w}_{2N+2}}{\hat{w}_{2N+1}}\right) \tag{27}$$

8. Simulation results

8.1. Case-1

For estimation of harmonics using VLMS/F algorithm, balanced voltage signals across any one phase can be expressed as

$$z(k) = 1\sin(k\omega Ts + \pi/6) + 0.5\sin(3k\omega Ts + \pi/3) + 0.3\sin(5k\omega Ts + \pi/4) + 0.2e^{-8kTS} \tag{28}$$

To test the performance of the proposed algorithm, comparison plots are presented from **Figures 2–7**. These figures include amplitude and phase estimation results of fundamental, third and fifth harmonic components. The results clearly indicate that VLMS/F filter has a faster tracking capability as compared to other algorithms. The decaying DC component is also included along with harmonics up to 5th order. Decaying DC amplitude estimation comparison plot is presented in **Figure 8**. It is observed that VLMS/F algorithm tracks the decaying DC component accurately than other algorithms. Absolute estimation comparison

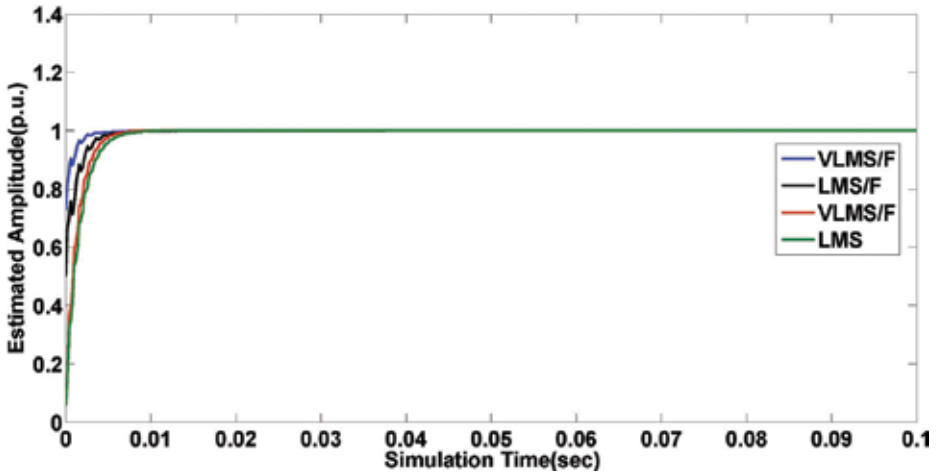

Figure 2. Comparison results of fundamental amplitude.

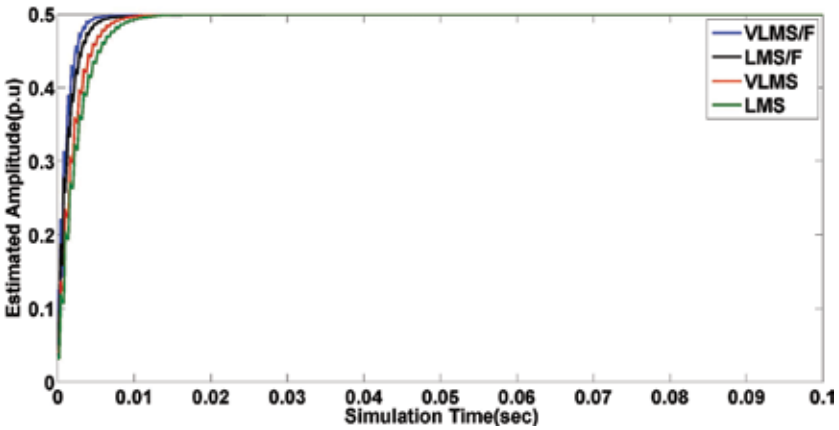

Figure 3. Comparison results of third harmonic amplitude.

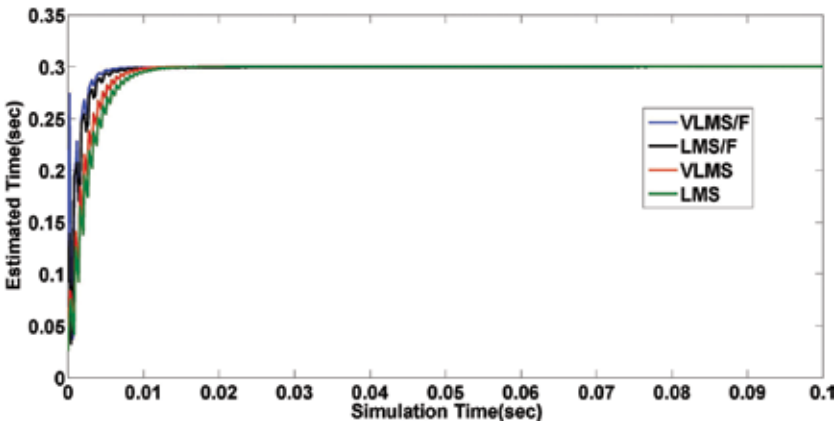

Figure 4. Comparison results of fifth harmonic amplitude.

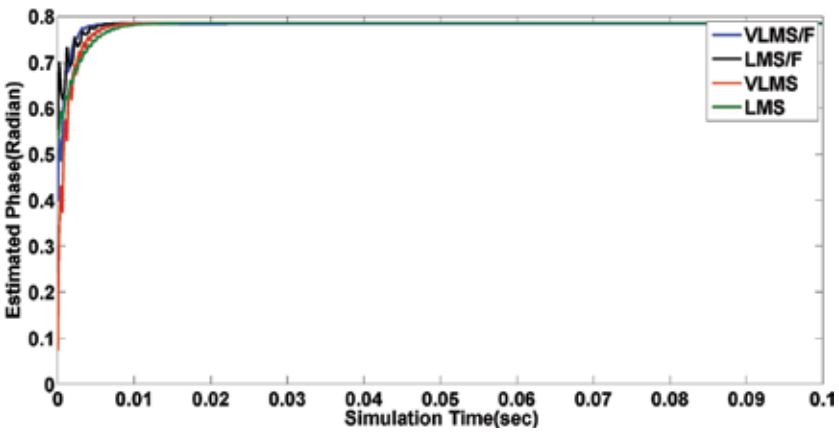

Figure 5. Comparison results of fundamental phase.

http://dx.doi.org/10.5772/intechopen.74581

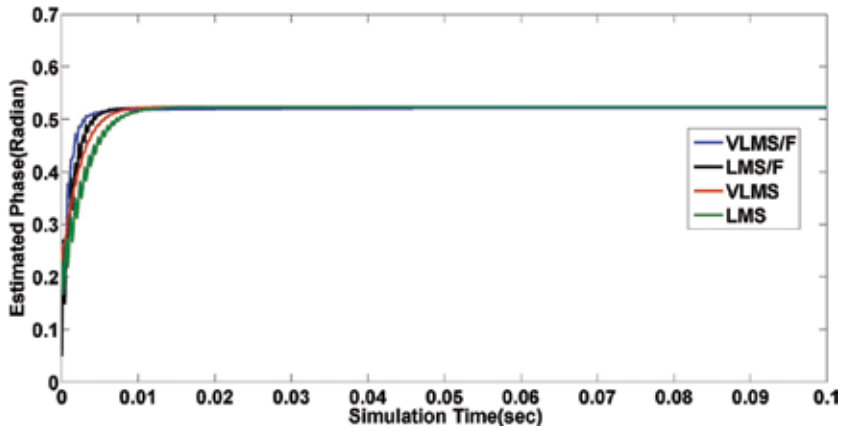

Figure 6. Comparison results of third harmonic phase.

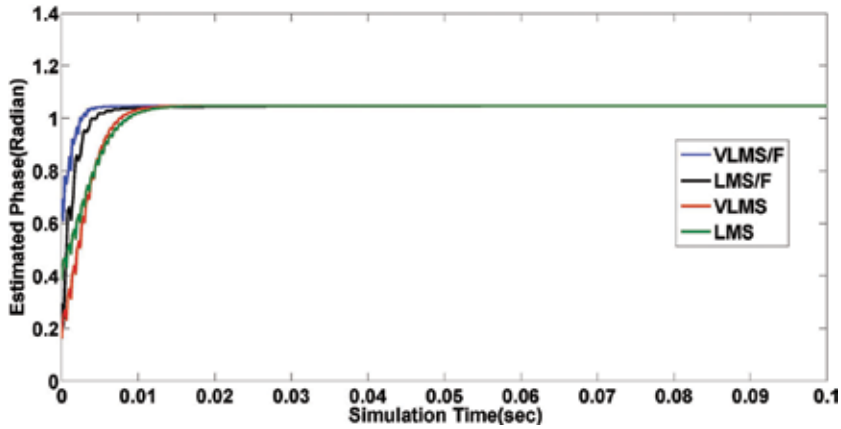

Figure 7. Comparison results of fifth harmonic phase.

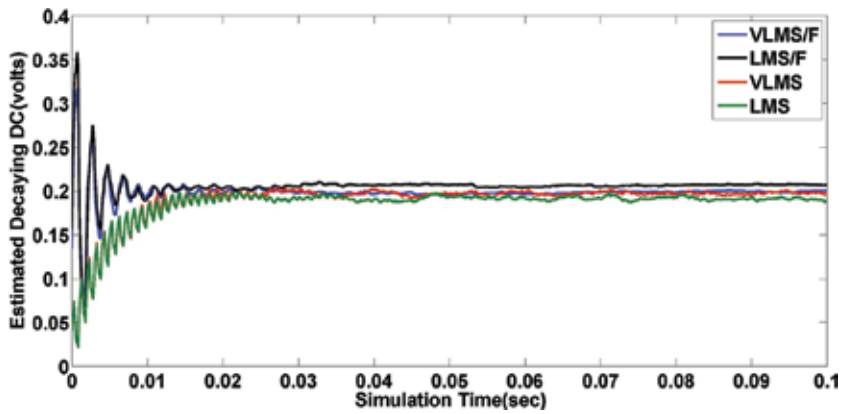

Figure 8. Comparison results of decaying DC amplitude.

Algorithms	Absolute estimation error						
	Fundamental amplitude	Third harmonic amplitude	Fifth harmonic amplitude	Fundamental phase	Third harmonic phase	Fifth harmonic phase	Decaying DC
LMS	0.0004383	0.002437	0.002505	0.001066	0.001251	0.00561	0.1218
Volterra LMS	0.0005238	0.002398	0.002328	0.001007	0.001181	0.005481	0.05339
LMS/F	0.16	0.004827	0.003253	0.0007725	0.0003231	0.006877	0.007843
VLMS/F	0.1599	0.004803	0.003209	0.0008388	0.0002715	0.006571	.07727

Table 5. Estimation error comparison results.

results are shown in **Table 5**. It is observed that performance of VLMS/F is better as compared to other algorithms.

8.2. Case-2

For estimation of harmonics using VRLS algorithm, balanced voltage signals across any one phase can be expressed is as

$$z(k) = 1.2\sin(k\omega Ts + \pi/6) + 0.8\sin(3k\omega Ts + \pi/3) + 0.3\sin(5k\omega Ts + \pi/4) \tag{29}$$

All the simulations are performed using MATLAB Simulink environment. For LMS and VLMS, step size is chosen as 0.001. For FFRLS and VRLS, 0.9995 is chosen as forgetting factor for simulation. Additive white Gaussian noise with 30 dB SNR and sampling frequency of 2 KHz are considered during estimation of harmonics. Estimated amplitude and phase comparison plots of fundamental, third and fifth harmonics are presented from **Figures 9–14**. From the harmonic estimation plots it is clear that LMS and VLMS have slower convergence as compared to FFRLS and VRLS.

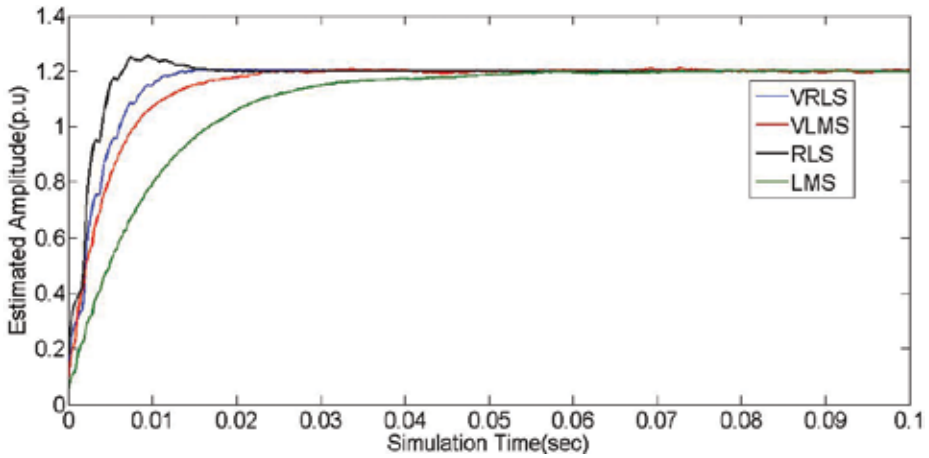

Figure 9. Comparison results of fundamental amplitude.

http://dx.doi.org/10.5772/intechopen.74581

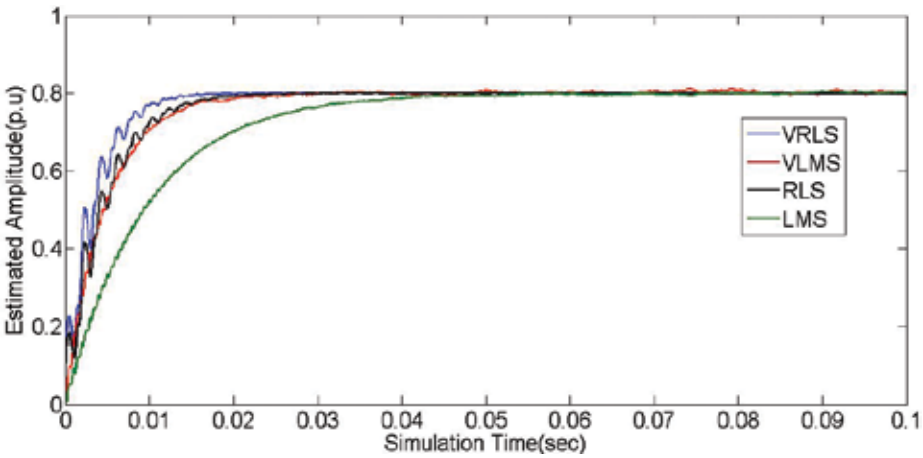

Figure 10. Comparison results of third harmonic amplitude.

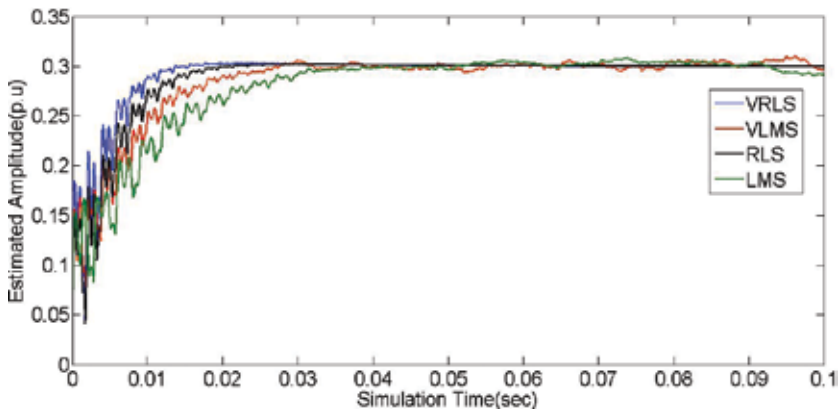

Figure 11. Comparison results of fifth harmonic amplitude.

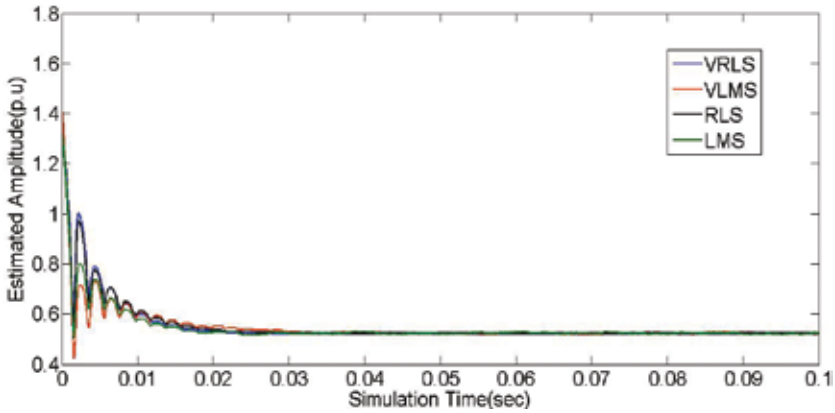

Figure 12. Comparison results of fundamental phase.

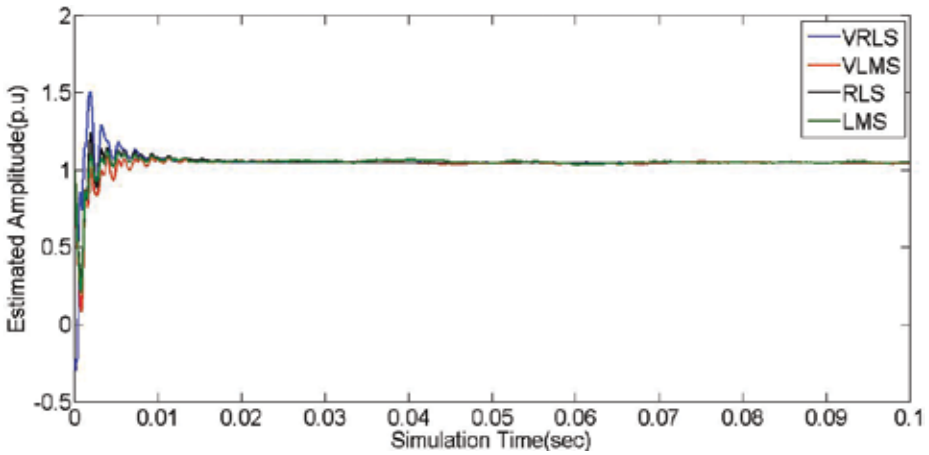

Figure 13. Comparison results of third harmonic phase.

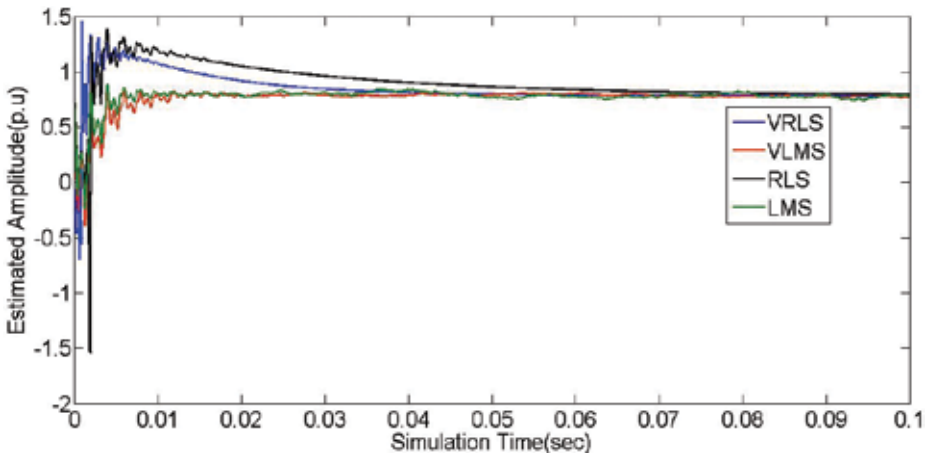

Figure 14. Comparison results of fifth harmonic phase.

8.3. Case-3

By using PQD signals from IEEE-1159-PQE databases distorted signal is generated for testing of VRLS algorithms and reconstructed signals are compared with the original signals. It is observed that VRLS tracks the distorted signal accurately as given in **Figure 15**.

8.4. Case-4

To validate the performance of VLMS/F algorithm, harmonic signal is generated in MATLAB/SIMULINK environment considering three phase rectifier as a load as shown in **Figure 16**.

Signal generated in each phase is compared with the estimated signal from the proposed algorithm. It is observed from **Figures 17–19** that VLMS/F tracks the distorted signal accurately.

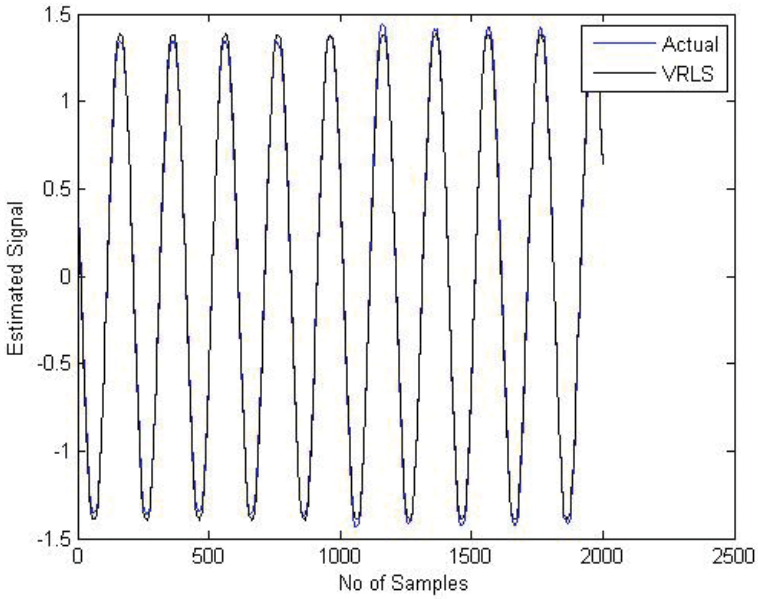

Figure 15. Estimated signal.

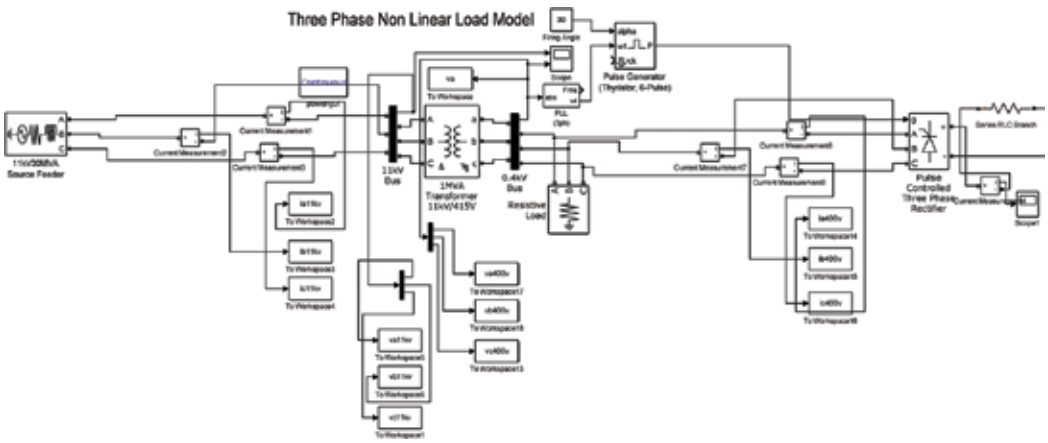

Figure 16. Three phase nonlinear load model.

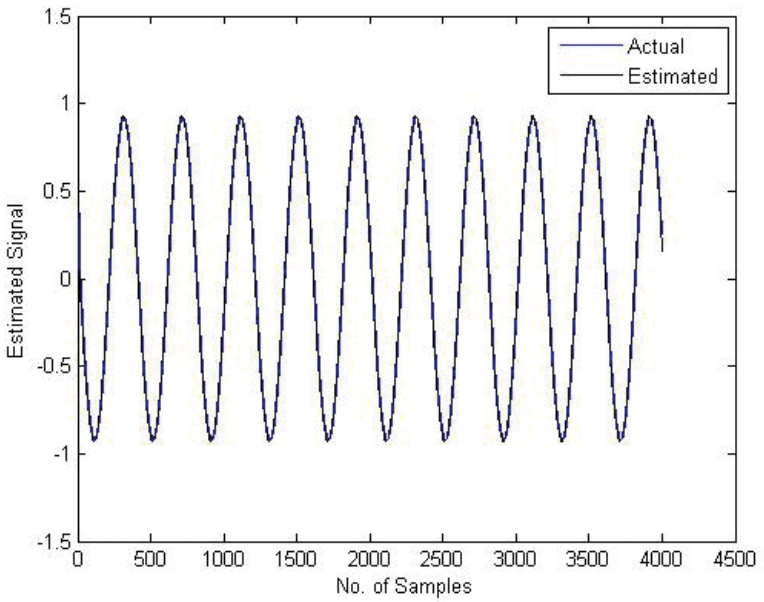

Figure 17. Estimated signal in phase a.

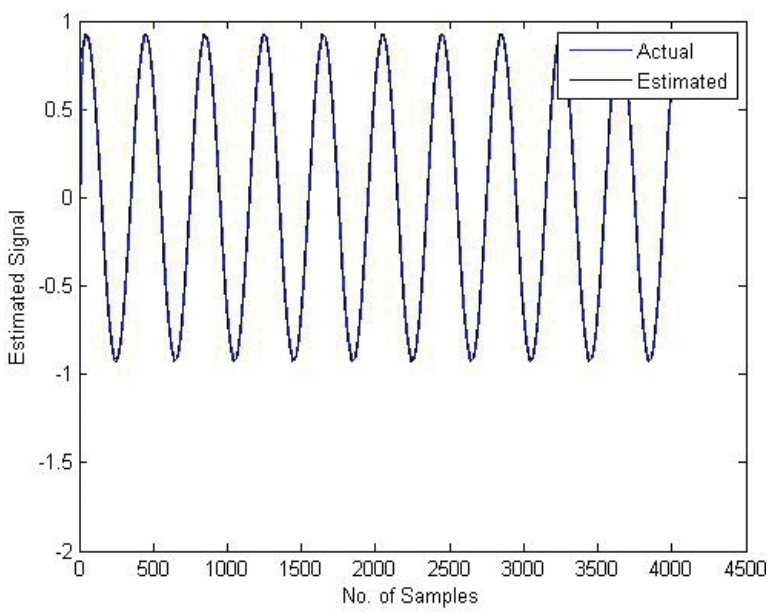

Figure 18. Estimated signal in phase b.

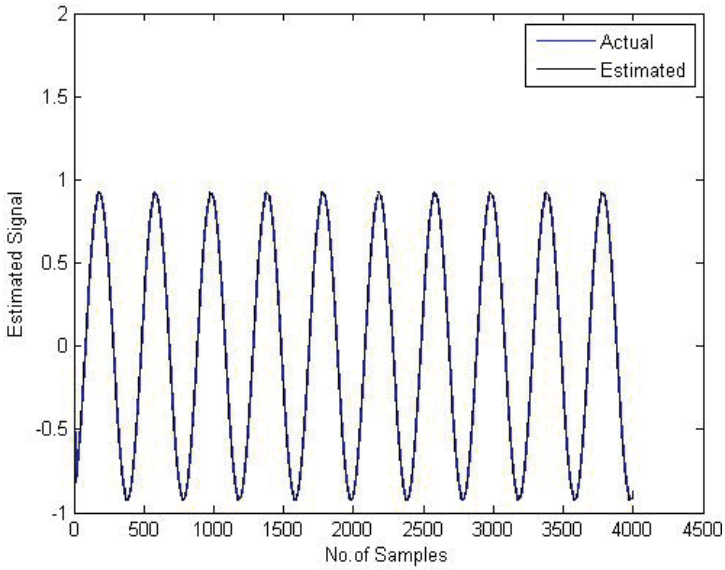

Figure 19. Estimated signal in phase c.

9. Conclusion

The chapter analyses different adaptive filtering models used to estimate harmonic amplitudes and phases in distorted power signals. Performances of Volterra series based adaptive filters are established through comparison results obtained through MATLAB simulations. It is quite apparent that VLMS/F filter gives better harmonic estimation accuracy as compared to LMS, VLMS and LMS/F. With a proper compromise between LMS and LMF, VLMS/F provides stable convergence of estimation error. Similarly Volterra RLS based harmonic estimation model provides faster and stable convergence with minimum estimation error.

Author details

Harish Kumar Sahoo[1]* and Umamani Subudhi[2]

*Address all correspondence to: harish_sahoo@yahoo.co.in

1 Department of Electronics and Tele Communication Engineering VSSUT, Burla, India

2 Department of Electrical and Electronics, IIIT Bhubaneswar, India

References

[1] Smith JC, Hensley G, Ray L. IEEE recommended practice for monitoring electric power quality. IEEE Studies. 1995:1159-1995

[2] Reid WE. Power quality issues-standards and guidelines. IEEE Transactions on Industry Applications. 1996;**32**(3):625-632. DOI: 10.1109/28.502175

[3] Electrical Power Systems Quality. 3rd ed. India: McGraw-Hill Education; 2012. p. 558. DOI: 9780071761550

[4] Bollen MH, Gu I. Signal Processing of Power Quality Disturbances. 30th ed. New York: John Wiley-IEEE; 2006

[5] Haykin SS. Adaptive Filter Theory. Englewood Cliffs, N.J: Prentice-Hall; 1986

[6] Begovic MM, Djuric PM, Dunlap S, Phadke AG. Frequency tracking in power networks in the presence of harmonics. IEEE Transactions on Power Delivery. 1993;**8**(2):480-486. DOI: 0885-8977/93

[7] Carugati I, Orallo CM, Donato PG, Maestri S, Strack JL, Carrica D. Three-phase harmonic and sequence components measurement method based on mSDFT and variable sampling period technique. IEEE Transactions on Instrumentation and Measurement. 2016;**65**(8): 1761-1772. DOI: 10.1109/TIM.2016.2552679

[8] Pradhan AK, Routray A, Basak A. Power system frequency estimation using least mean square technique. IEEE Transactions on Power Delivery. 2005;**20**(3):1812-1816. DOI: 10.1109/TPWRD.2004.843453

[9] Joorabian M, Mortazavi SS, Khayyami AA. Harmonic estimation in a power system using a novel hybrid least squares-Adaline algorithm. Electric Power Systems Research. 2009;**79** (1). DOI: 10.1016/j.epsr.2008.05.021

[10] Chudamani R, Vasudevan K, Ramalingam CS. Non-linear least-squares-based harmonic estimation algorithm for a shunt active power filter. IET Power Electronics. 2009;**2**(2):134-146. DOI: 10.1049/iet-pel:20080006

[11] Kennedy K, Lightbody G, Yacamini R. IEEE. In: Power System Harmonic Analysis Using the Kalman Filter. 2nd ed. 2003. pp. 752-757. DOI: 10.1109/PES.2003.1270401

[12] Clarkson PM, Dokic MV. Stability and convergence behaviour of second-order LMS Volterra filter. Electronics Letters. 1991;**27**(5):441-443. DOI: 10.1109/e1:19910279

[13] Singh TSD, Chatterjee A. A comparative study of adaptation algorithms for nonlinear system identification based on second order Volterra and bilinear polynomial filters. Measurement. 2011;**44**(10):1915-1923. DOI: 10.1016/j.measurement.2011.08.028

[14] Gui G, Peng W, Adachi F. Adaptive system identification using robust LMS/F algorithm. International Journal of Communication Systems,Wiley Online Library. 2014;**27**(11):2956-2963. DOI: 10.1002/dac.2517

[15] Walach E, Widrow B. The least mean fourth (LMF) adaptive algorithm and its family. IEEE transactions on Information Theory. 1984;**30**(2):275-283. DOI: 10.1109/TIT.1984.1056886

[16] Lim SJ, Haris JG. Combined LMS/F algorithm. Electronics Letters. 1997;**33**(6):467-468

[17] Subudhi, Umamani and Sahoo, Harish Kumar. Harmonics and decaying DC estimation using Volterra LMS/F algorithm. In: Power Electronics, Intelligent Control and Energy Systems (ICPEICES), IEEE International Conference on; 4–6 July 2016; DTU. Delhi,India: IEEE; 2016. p. 1-5. DOI: 10.1109/ICPEICES.2016.7853663

Chapter 7

Harmonic Reduction of a Single-Phase Multilevel Inverter Using Genetic Algorithm and Particle Swarm Optimization

Hui Hwang Goh, Chin Wan Ling, Kai Chen Goh,
Qing Shi Chua, Sy Yi Sim and
Mohd Ariff Mohd Aifaa

Additional information is available at the end of the chapter

http://dx.doi.org/10.5772/intechopen.74580

Abstract

Power inverter play an important role in power system especially with its capability on reducing system size and increase efficiently. The recent research trends of power electronic system are focusing on multilevel inverter topics in optimization on voltage output, reducing the total harmonics distortion, modulation technique, and switching configuration. The research emphasizes the optimization with a fundamental switching frequency method that is the optimized harmonic stepped waveform (OHSW) modulation method. The selective harmonic elimination (SHE) calculation has adapted with genetic algorithm (GA) and particle swarm optimization (PSO) in order to speed up the calculation. Both bioinspired algorithms are compared in terms of total harmonic distortion (THD) and selective harmonic elimination for both equal and unequal sources. The overall result showed that both algorithms have high accuracy in solving the nonlinear equation. However, the genetic algorithm showed better output quality in terms of selective harmonic elimination which overall no exceeding 0.4%. Particle swarm optimization shows strength in finding the best total harmonic distortion where in seven-level cascaded H-bridge multilevel inverter (m=0.8) shows 6.8% only as compared to genetic algorithm. Simulation for three-level, five-level, and seven-level for each multilevel inverter at different circumferences had been done in this research. The result draws out a conclusion where the possibility of having a filterless high-efficient inverter can be achieved.

Keywords: multilevel inverter, SPWM, OSHW, PSO, GA

1. Introduction

Inverters can be classified into two main types, that is, voltage source inverter (VSI) and current source inverter (CSI). Each type has its own unique characteristic, which has been listed in the literature [1–5]. From the literature, a brief conclusion of VSI which is more popular than CSI has been made [1]. VSI transformer-less inverter popular in renewable energy (RE) application due to overall size reduction. The most commonly used inverter is high-power two-level PWM inverter. However, high-power application ideally requires low switching losses.

Over the past decade, numberless of literature has proven multilevel inverter is a practical solution on resolving high switching losses problem exist in conventional inverter for high power application [6]. Research trends nowadays are more focusing on several multilevel inverter topologies for renewable energy source application. Multilevel inverter topologies generate multilevel voltage source output which synthesizes the staircase waveform from single or multiple low DC voltage source. The low-input voltage source reduces the stress encounter by the switches with the ability to produce high-output voltage source. Cascaded H-bridge multilevel inverter (CHB-MLI) and it modified topologies is highly grab researchers attention due to the flexibility toward renewable energy.

Multilevel inverter system can be separated into two sectors which are inverter topology system and switching strategy. Inverter topology system consists of the most part include switch, power sources, topology configuration, and filter system. Power sources are mostly RE such as solar panel and wind turbine. For topology configuration, there are three main types, which have been frequently cited in the literature, that is, diode-clamped multilevel inverter (DC-MLI), capacitor-clamped multilevel inverter (CC-MLI), and cascaded H-bridge multilevel inverter (CHB-MLI) [7–14]. Filter is applied to remove harmonics and to smoothen the inverter output quality.

Switching strategy aid in manipulate the harmonic profile for the inverter output waveform. Square wave output is a conventional type. This type evolves into a quasi-square wave, which gives a better profile as compared to square wave. The current trend is pulse width modulation (PWM), which has been widely applied in current VSI devices [15]. However, researchers explored other methods on overcoming the cons of PWM where different kinds of add-on methods have been applied in conjunction with PWM such as selective harmonic elimination (SHE). SHE consists of a complex nonlinear equation on resolving the best switching timing. Hence, various calculation approaches have been tested to optimize the overall performance. The calculation method includes Newton-Raphson, Fourier transform, and even bioinspired algorithm approach such as bee, ant, particle swarm, genetic, bat, and others [16–21]. The overview for this chapter is to introduce genetic algorithm and particle swarm optimization in resolving the SHE which eliminates the low order of undesired harmonics.

2. Multilevel inverter

One of the inverters discussed in this chapter is the cascaded H-bridge multilevel inverter. Simulation is conducted under the same parameters and the same modulation methods, which

http://dx.doi.org/10.5772/intechopen.74580

Parameters	Value
Modulation signal frequency	50 Hz
Carrier signal frequency	4000 Hz
Sampling time	$1 \times e^{-06}$ s
Total input voltage source(s)	240 V

Table 1. Simulation parameters.

are SPWM and OSHW. The simulation result will be evaluated based on the total harmonic distortion (THD) level of the inverter. SPWM is constructed with parameters shown in **Table 1**.

2.1. Cascaded H-bridge multilevel inverter

Two or more separate DC sources in a full bridge are placed in series to generate a staircase AC output waveform voltage. **Figure 1** shows a two-level CHB-MLI topology. CHB-MLI requires

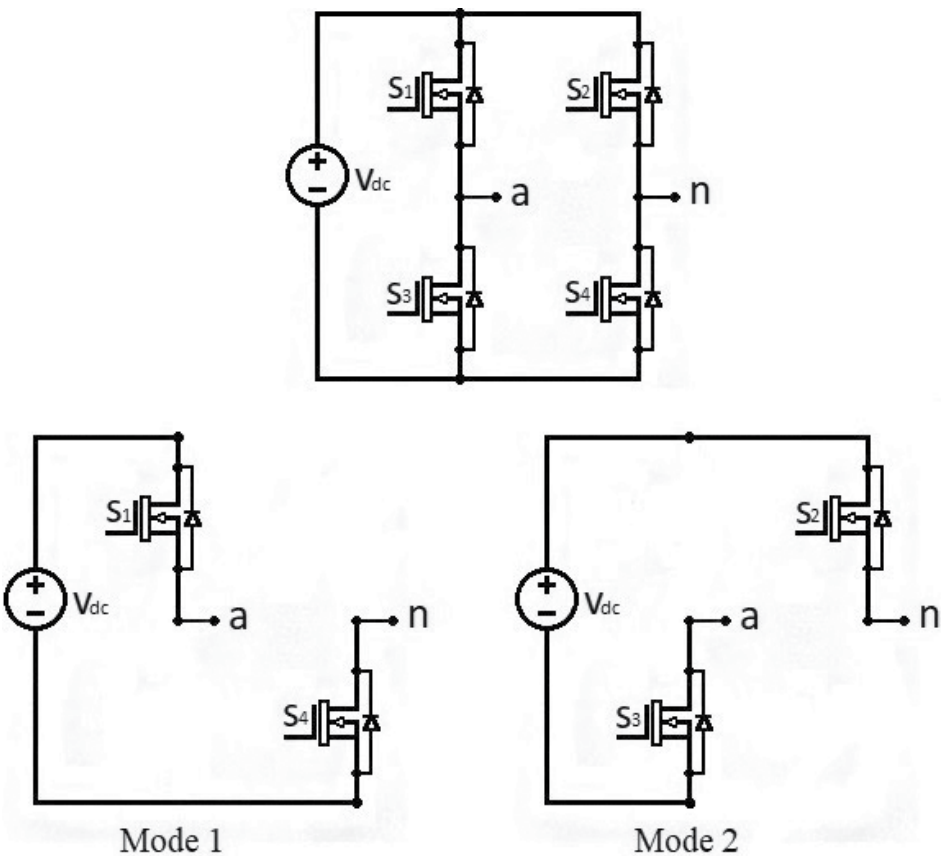

Figure 1. Two-level cascaded H-bridge multilevel inverter topology.

fewer components where each voltage level requires the same amount of components. However, the number of sources is higher since m voltage-level inverter $s = \frac{(m-1)}{2}$ sources are required. The number of sources s is also equal to the number of full-bridge modules.

The CHB-MLI switching configuration is similar to the other topology. When S1 and S4 are on and S2 and S3 are off, voltage V_{an} is equal to V_{dc} due to the current flow sequence. When S1 and S2 are on and S3 and S4 are off, the voltage output is 0. When S1 and S2 are off and S3 and S4 are on, the voltage output is 0. When S1 and S4 are off and S2 and S3 are on, the voltage output is $-V_{dc}$.

Every full-bridge module has four diodes and four switches s in turn giving the CHB-MLI $2(m-1) = 4s$ diodes and switches. When making a three-phase inverter with the topology, the number of needed components is multiplied by 3 for all components since there is no common DC bus to share.

CHB-MLI are suitable to be implemented in the photovoltaic cells, battery cells, or fuel cells [3, 16, 17]. The consideration of the number of levels for CHB-MLI is different from other. The calculation of CHB-MLI of the number of voltage levels includes the negative side of each voltage level, while other topologies do not.

The topology is implementing a combination of several H-bridges dependent on the number of levels required. Three-level cascaded H-bridge multilevel inverter is shown in **Figure 2**. The separate dc sources gain the possibility of a single-phase topology to be constructed. The numbers of levels involved are three-level, five-level, and seven-level, which are constructed throughout observing the effect on harmonic distortion.

2.2. Sinusoidal pulse width modulation

Sinusoidal pulse width modulation (SPWM) is applied with the capability of offering switching signal to the power electronic switch. The operation function is by comparing two principal component signals which are the modulation signal and the carrier signal. Modulation signal used is a sine wave signal due to the desired output wave. The carrier wave applied mostly is high-frequency triangle or Sawtooth repetition wave. This technique employs comparison between the modulation signal and the carrier signal to obtain a desired fundamental component of the voltage output waveform. **Figure 3** has shown phase disposition modulation, which uses one of the multicarrier PWM methods where the number of carriers depends on the multilevel inverter. The method is applied $(m-1)$ where m is referring to the number of sources. Both carriers are in the same phase, which gives rise to the name of phase disposition modulation.

The pulse generator operation is illustrated in **Figure 4**. The top-row black signal in the top figure is the triangle repetitive pulse, while the red signal in the top figure is the modulation wave. The bottom-row red signal in the bottom figures shows the pulse generated throughout the comparison. When the modulation signal is higher than the carrier signal, the output signal comparator would show 1. Then, when the modulation signal is less than the carrier signal, the output signal comparator would show 0. The generator switching pulse is then injected to a

http://dx.doi.org/10.5772/intechopen.74580

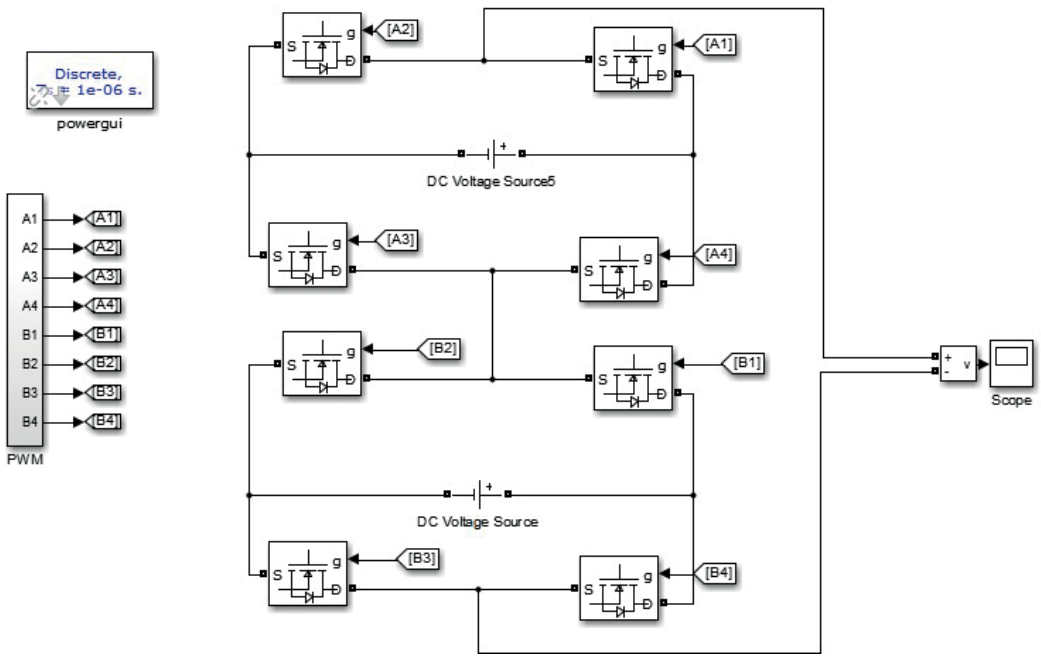

Figure 2. Three-level cascaded H-bridge multilevel inverter.

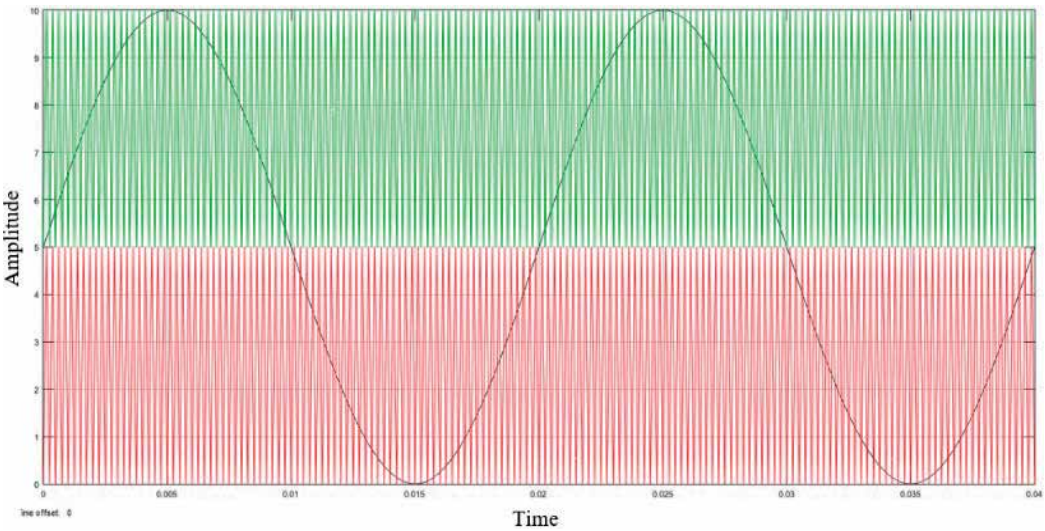

Figure 3. SPWM phase disposition modulation.

specific switch. The switching affects the output voltage where different switching sequences allow for different voltage-level configurations with different switching frequencies. Hence, the voltage levels are able to be switched according to the SPWM signal.

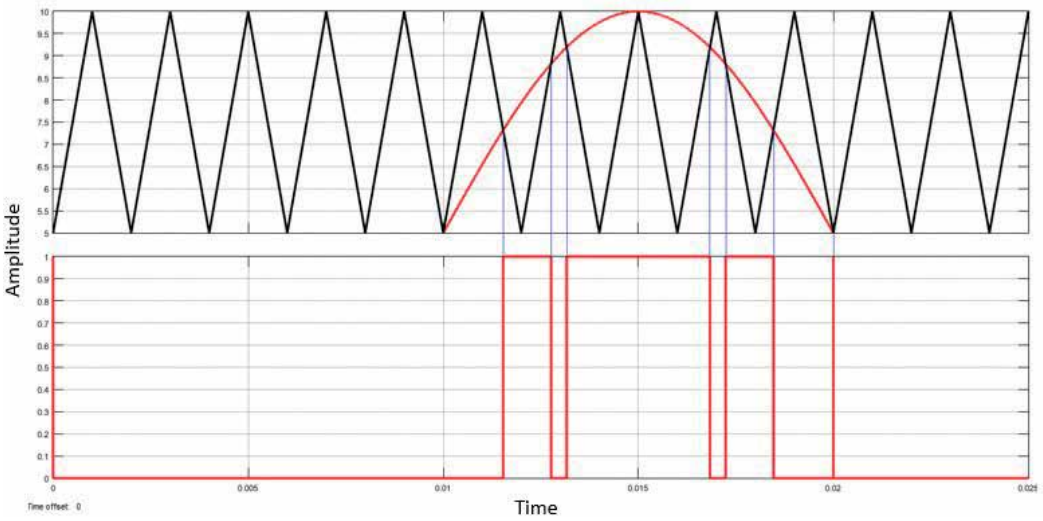

Figure 4. Comparison of modulation signal and carrier signal illustration.

2.3. Optimized harmonic stepped waveform

OHSW technique has the advantage to reduce harmonic distortion. The basic concept is applying selective harmonic elimination PWM and quarter-wave symmetric to eliminate low-order harmonics [18]. For the topology of OHSW cascaded H-bridge multilevel inverter to operate, switching angle is first calculated using MATLAB's main interface to obtain the best switching angle. The result obtained is applied to be the pulse generation block generated in Simulink environment. Other parameters such as modulation signal and carrier signal are added in the block.

From the MATLAB calculation for the selective harmonic elimination, the switching angle for each specific voltage-level change is recorded. The recorded data is simulated from 0 to 1 of the modulation index with a step of 0.5. The result obtained is converted into a graphical form for further analysis of the pattern.

2.4. Fourier series approach voltage output

The H-bridge multilevel inverter has an individual voltage supply for each full bridge. Hence, the total voltage output for the inverter is given as Eq. (1):

$$V_{out} = V_1 + V_2 + \cdots + V_n. \tag{1}$$

where n is the number of voltage source applied in the whole H-bridge multilevel inverter. **Figure 5** shows the generalized staircase waveform of a five-level multilevel inverter. From the **Figure 5**, it can be observed that the θ_1, θ_2, θ_3 and θ_4 showed the switching angle for the inverter. For each level, the voltage value is changed according to the switching angle time. Voltage at θ_1 switching timing is V_1, at θ_2 switching time is V_2, and so on. The voltage supplied

http://dx.doi.org/10.5772/intechopen.74580

Figure 5. Generalized staircase waveform of five-level multilevel inverter.

by the separate dc sources is different in the voltage level where the amplitude or voltage of each dc source can be different. There are two variables which may manipulate the harmonic distortion for the inverter. The first variable is the amplitude of the separate DC source where the voltage level of each DC source can be equal or unequal. The second variable is the switching step where the step can be short or long. Both variables will affect the result of the total harmonic distortion of the output voltage.

For the modulation index of an H-bridge multilevel inverter, the definition is similar to the modulation index for SPWM. The equation is drawn as given in Eq. (2) assuming that all the Vdc are equal:

$$m = \frac{V_{out}}{4nV_{dc}}. \tag{2}$$

where V_{out} is the amplitude output voltage, V_{dc} is the amplitude dc source of the H-bridge, and n is the number of dc source in H-bridge. For the condition of unequal voltage source, the V_{dc} value is replaced with the total voltage of all the DC sources in use as shown in Eq. (3):

$$m = \frac{V_{out}}{V_1 + V_2 + \cdots + V_n}. \tag{3}$$

The staircase waveform is analyzed to obtain a general equation. The quarter-wave symmetric waveform can be written in a Fourier series form shown in Eq. (4):

$$\begin{aligned} a_n &= \frac{4}{\pi}\int_0^{\frac{\pi}{2}} f(\omega t)\sin(n\omega t)\mathrm{d}(\omega \mathrm{t}),\ \textit{for odd } n \\ a_n &= 0,\ \textit{for even } n \\ b_n &= 0,\ \textit{for all } n. \end{aligned} \tag{4}$$

where

$$f(\omega t) = V_{out}(\omega t) \tag{5}$$

From Eqs. (4) and (5), the Fourier series can be concluded as Eq. (6):

$$f(\omega t) = \sum_{n=1}^{\infty} a_n \sin(\mathrm{n}\omega t). \tag{6}$$

Let x = ωt,

$$a_n = \frac{4}{\pi}\int_0^{\frac{\pi}{2}} f(x)\sin(nx)d(\mathrm{x}). \tag{7}$$

Then

$$\begin{aligned} a_n &= \frac{4}{\pi}\left[\int_{a_1}^{a_2} E_1\sin(\mathrm{nx})\mathrm{dx} + \int_{a_2}^{a_3} E_2\sin(\mathrm{nx})\mathrm{dx} + \cdots + \int_{a_k}^{\frac{\pi}{2}} E_k\sin(\mathrm{nx})\mathrm{dx} + \right] \\ &= \frac{4}{n\pi}\left[-E_1\cos(nx)|_{a_1}^{a_2} - E_2\cos(nx)|_{a_2}^{a_3} - \cdots - E_k\cos(nx)|_{a_k}^{\frac{\pi}{2}}\right] \\ &= \frac{4}{n\pi}\left[\begin{array}{l} -E_1\cos(nx_2) + E_1\cos(nx_1) - E_2\cos(nx_3) \\ +E_2\cos(nx_3) - \cdots - E_k\cos\left(\mathrm{n}\frac{\pi}{2}\right) + E_k\cos(nx_k) \end{array}\right] \\ &= \frac{4}{n\pi}[E_1\cos(nx_1) + (E_2 - E_1)\cos(nx_2) + \cdots + (E_k - E_{k-1})\cos(nx_k)]. \end{aligned} \tag{8}$$

Eq. (7) assumes that x is equal to ωt to simplify the calculation. Then, the resultant equation is Eq. (8). Eq. (8) shows separate DC source formulation where E_1 (E_2–E_1) and (E_{k}–$E_{\mathrm{k}-1}$) represents each H-bridge voltage source. There are two conditions in the simulation, that is, the equal dc source and the unequal DC source. The equation above applies for both conditions. However, for equal DC source, the equation is able to be simplified as show in Eq. (9).

Since DC source are equal

$$\begin{aligned} V_{1,2\ldots k} &= E_1 = (E_2 - E_1) = (E_k - E_{k-1}) \\ a_n &= \frac{4}{n\pi}[V\cos(nx_1) + V\cos(nx_2) + \cdots + V\cos(nx_k)] \\ a_n &= \frac{4V}{n\pi}[\cos(nx_1) + \cos(nx_2) + \cdots + \cos(nx_k)] \\ a_n &= \frac{4V}{n\pi}\sum_{s=1}^{k} V\cos(nx_s). \end{aligned} \tag{9}$$

http://dx.doi.org/10.5772/intechopen.74580

2.5. Selective harmonic elimination calculation

SHE is proposed to eliminate the unwanted harmonics. Harmonic distortion occurs due to the conversion of DC to AC. Harmonic distortion is able to be resolved by using harmonic filters such as low-pass filter to reduce the high-frequency harmonics. For medium and high voltage or power applications, the first approach and the number of switching angles are limited by switching loss and usually are used when the available voltage steps are limited.

SHE is manipulating the switching angle to reduce the harmonic distortion. In multilevel application, every single voltage level has multiple switching angles. The SHE method provides the best switching angle to decrease the harmonic frequency. The harmonic elimination is depending on the number of voltage step. In inverter with voltage output of three voltage steps, the possible harmonic elimination would be the third and fifth harmonic component only. The general staircase waveform Fourier series given in Eq. (10) is derivative of the above equation. The mathematical Fourier series formulation is shown as the possible method of eliminating the desire of low harmonic component and can be manipulated as selective harmonic elimination:

$$V_{out} = \sum_{n=1,3,5,\ldots}^{\infty} \frac{4V_{in}}{2\pi} \times \frac{1}{n}(\cos(n\theta_1) + \cos(n\theta_2) + \ldots + \cos(n\theta_k))\sin(n\omega t). \tag{10}$$

where V_{out} = voltage output (V), V_{in} = voltage input (V), n = harmonic component, k = number of switching angles.

The number of switching angles represents the harmonic component that is required to be eliminated. The fundamental component is the desired voltage, and the rest needs to be eliminated. Hence, the number of harmonics needed to be removed is *k-1*. From the expression of Eq. (10), each peak voltage for the nth harmonics is expressed in Eq. (11):

$$V_n = \frac{4V_{in}}{n\pi}[\cos(n\theta_1) + \cos(n\theta_2) + \ldots + \cos(n\theta_k)]. \tag{11}$$

Each peak voltage is calculated to obtain the switching angle. The equation showed that the voltage of each harmonic can be manipulated. The method to manipulate to remove the other undesired harmonic voltages is the basis of selective harmonic elimination (SHE) method. Eq. (12) showed the general SHE method calculation. H represents the number of harmonics step [22–26]:

$$\begin{aligned} H = 1: &\quad V_1 = \frac{4V_{in}}{\pi}[\cos(\theta_1) + \cos(\theta_2) + \ldots + \cos(\theta_n)] \\ H = 2: &\quad 0 = \cos(2\theta_1) + \cos(2\theta_2) + \ldots + \cos(2\theta_n) \\ H = 2n-1: &\quad 0 = \cos[(2n-1)\theta_1] + \cos[(2n-1)\theta_2] + \ldots + \cos[(2n-1)\theta_n]. \end{aligned} \tag{12}$$

3. Bioinspired algorithm

Selective harmonic elimination is a series of nonlinear equations that can be solved to obtain the switching angle for the inverter. Due to the multiple possible set of data, the calculation

involved is very complicated. In order to resolve the problem, the research makes comparison between particle swarm optimization algorithm and genetic algorithm.

3.1. Genetic algorithm

Genetic algorithm (GA) employs the natural biological evolution theory as the concept to solve constrained or unconstrained optimization problems [27, 28]. The algorithms are inspired by Darwin theory of "the survivor of the fittest" [29]. GA is a method where the first-generation individual left for the competition. For every round of competition, the survivor will become the new-generation individual to continue to be in the competition. The process will keep repeating where the survivor becomes the parent of the new generation to pass over the genetic. The survivor is also known as the fittest individual. The competition continues to leave the desired genetic behind until the best fitness individual is obtained [24].

The GA algorithm starts with the injection of the initial population. The existing instantaneous individual is evaluated by fitness function to determine the best answer. If the fitness in not reaching the desired level, the individual selection will undergo crossover, which mutates new offspring to be tested on its fitness, and the old generation will be disqualified. The process is repeated until the best fitness or optimum result is achieved.

There are several advantages of GA as compared to other optimization techniques. GA is more robust as compared to the conventional artificial intelligence. Besides that the GA is also not easy to break the error due to the slight input change or reasonable noise. This method also shows advantages of larger state space search optimization technique. The genetic algorithm parameter is set by the creation function in the optimization tool of MATLAB.

The genetic algorithm application method in MATLAB is done with a series of M-file code. The calculation to resolve the nonlinear equation is done by applying genetic algorithm. Calculation process is separated into two parts, that is, constraint and fitness. Constraint file functions as the limitation of the switching angle. The switching angle of the wave should not be more than 180°. The constraint also gives a faster guideline, which ensures that the switching angle of the each switch is in the feasible range. For example, the switching angle for θ_2 is greater than θ_1, θ_3 is greater than θ_2, and $\frac{\pi}{2}$ is greater than θ_3. This step is to make sure that the switching angle calculated is valid to be applied in the switching order which is $\theta_1 < \theta_2 < \cdots < \theta_k < \frac{\pi}{2}$.

The next part is fitness where the nonlinear equation is listed for calculation. In this part, the change variable is modulation index, where m affects the result of switching angle. Fitness function is added in this M-file which generates fitness indices to clarify the best fit modulation index. Fitness value (fval) is a measurement of the solution from the fitness function with respect to the original objective and the amount of infeasibility. The fitness function applied is shown in Eq. (13):

$$f = \theta_0^{\pi/2}\left\{\left(100\frac{V_{ref} - V_1}{V_1}\right)^4 + \sum_{i=1}^{n}\frac{1}{n}\left(50\frac{V_n}{V_1}\right)^2\right\}. \tag{13}$$

where n = 1, 3, 5, …, n.

Parameters	Values
Inertia weight maximum (ω_{max})	0.9
Inertia weight minimum (ω_{min})	0.4
Acceleration constants (c_1 and c_2)	2
Swarm size	100
Number of iterations range	10–1000
θ_{min}	0
θ_{max}	0.5π

Table 2. Particle swarm optimization algorithm parameter.

The modulation index (m) is set to the range of 0 to 1. The process takes a few seconds to finish depending on the complexity of the function. The switching angle computed according to the modulation index provide and the fitness value is determined. Fitness function section for a three-level inverter for unequal DC source includes harmonic elimination on the third harmonic order by applying Eqs. (12) and (13) as mentioned before.

Both the constraint and fitness m-files are applied in the genetic algorithm optimization tool. In this stage, the fitness function section where the fitness file is created needs to be included. The number of variables in the fitness function needs to be clarified. Besides that, the boundary needs to be set for each variable to narrow the prediction. The upper bound should be 0, while the lower bound should not exceed π/2. The last process applied is the nonlinear constraint function where the constraint m-file is applied at this point.

3.2. Particle swarm optimization algorithm

Particle swarm optimization (PSO) originates from the natural behavior of a flock of birds, a school of fish, or a swarm of bee. James Kennedy and Russell Eberhart are the PSO founders which use optimized nonlinear functions [30, 31] in this technique. By applying bioinspired algorithm, constraint or unconstraint optimization can be solved efficiently and faster. PSO terminology is based on the current moving speed and direction in progress of searching the best personal and group position and in the end is located to the optimal or almost optimal solution [32]. PSO starts with declaration of parameters. The PSO algorithm for the selective harmonic elimination parameter is set in **Table 2**. The process continues with the random generation of particles by initializing their position and velocity. Fitness of position and velocity are evaluated to obtain the best fitness, P_{best}, and global best, G_{best}. The process repeat is continuously updating the particles P_{best} and G_{best} until the optimum result is obtained.

4. Result and discussion

The simulation is repeated for three-, five-, and seven-level with equal and unequal DC source to test the topology performance and capability of the both algorithms in resolving such

problem. The example of simulation result is shown as follows, and the overall result is concluded.

4.1. Simulation of three-level CHB-MLI with OHSW method (equal sources)

The switching angle for each switch is calculated by applying SHE using genetic algorithm. Graph of switching angle versus modulation index is plotted and shown in **Figure 6**. The switching angle is set as a constraint where the angle theta_2 must be greater than theta_1. The result shows validated data for the switching angle, which only happened to be located in between the range of modulation index 0.05 and 0.85. In this range, the result fulfills the constraint set. Hence, the best fit switching angle is within this range. Modulation index of 0 gives an invalid result due to highly inaccurate switching angle. From modulation index 0.05 to 0.4, the difference between theta_1 and theta_2 is small which causes the fitness function value to be high. From 0.45 to 0.85, the difference between theta_1 and theta_2 is larger. Hence, the fitness value for this region is low. From 0.9 to 1, high fitness value is shown. Fitness value is affected in terms of validation of switching angle calculated.

To further narrow down the range, graph of fitness function versus modulation index is plotted as shown in **Figure 7**. Theoretically, the lower the fitness function value, the better the chance to obtain the optimized switching angle. Hence, the range of relevant switching angle is narrowed down to the range of 0.45 to 0.8 of the modulation index.

All sets of modulation index and switching angle were tested in the simulation environment, and the results are recorded in **Table 3**. The table shows information for modulation index, total harmonic distortion, and the third harmonic of the corresponding modulation index. The result of extremely low third harmonics is highlighted which shows the region achieving

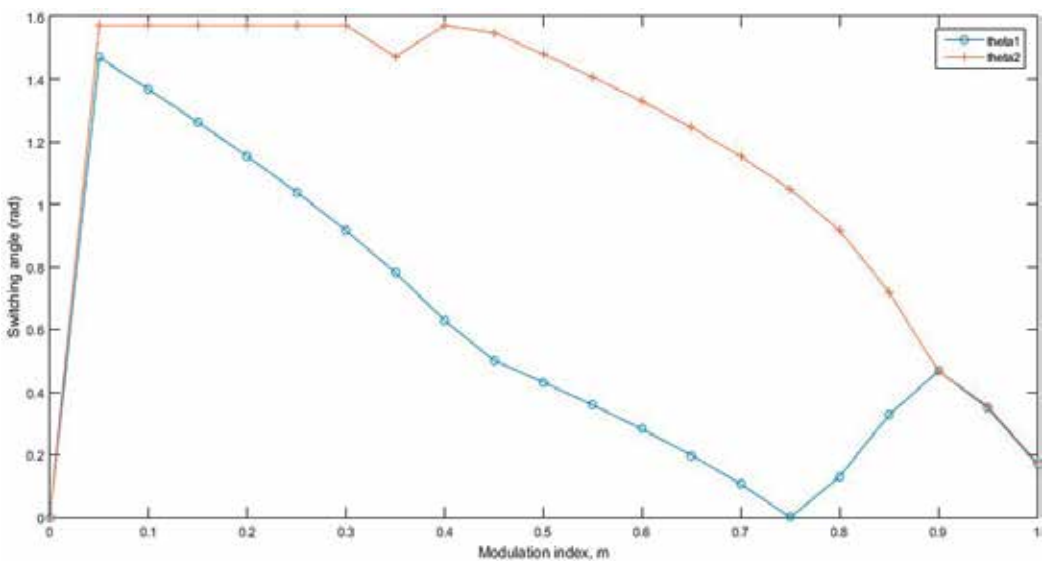

Figure 6. Three-level switching angle versus modulation index.

http://dx.doi.org/10.5772/intechopen.74580

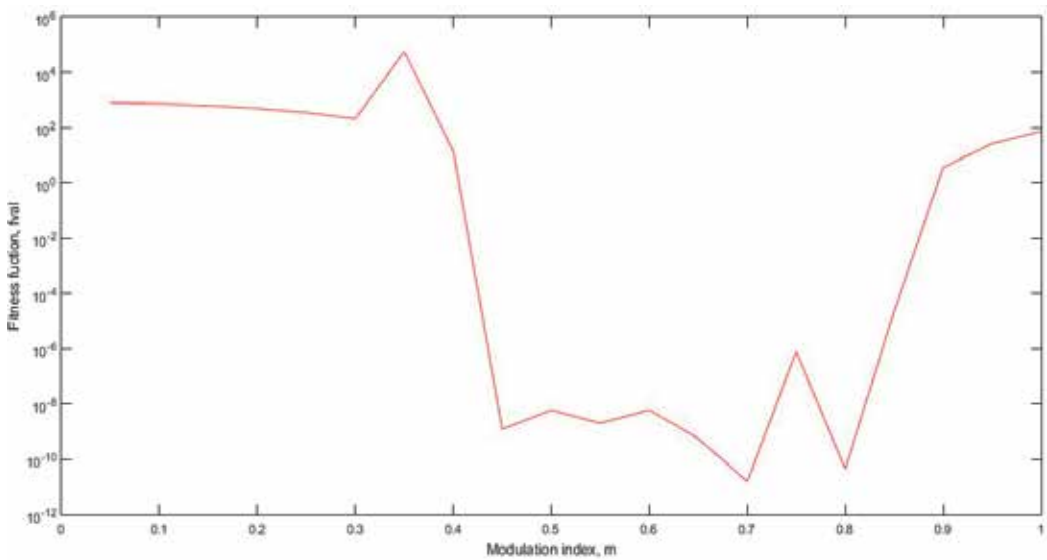

Figure 7. Graph of fitness function versus modulation index.

m	THD (%)	Third harmonic (%)
0.45	32.21	0.02
0.5	33.34	0.01
0.55	32.69	0.01
0.6	31.41	0.01
0.65	30.23	0
0.7	29.84	0
0.75	31.09	0
0.8	20.97	0
0.85	18.2	0.02

Table 3. Three-level total harmonic distortion with respective modulation index.

successful elimination of harmonics. Within the region, the lowest total harmonic distortion percentage is 18.2% with existing 0.02% of the third harmonic component present.

The result of the voltage output for m = 0.85 is shown in **Figure 8**. Output voltage is clearly a switched three-level voltage in a staircase sinusoidal waveform. The output undergoes FFT analysis, and the result is shown in **Figure 9**. The fundamental voltage component reaches 259.6 V_{rms} which shows the boosting character of cascaded H-bridge multilevel inverter character. The total harmonic distortion is 18.2% and clearly shows the third harmonics being reduced. The effect of selective harmonic elimination results in elimination of the third harmonics which is reduced to 0.02%.

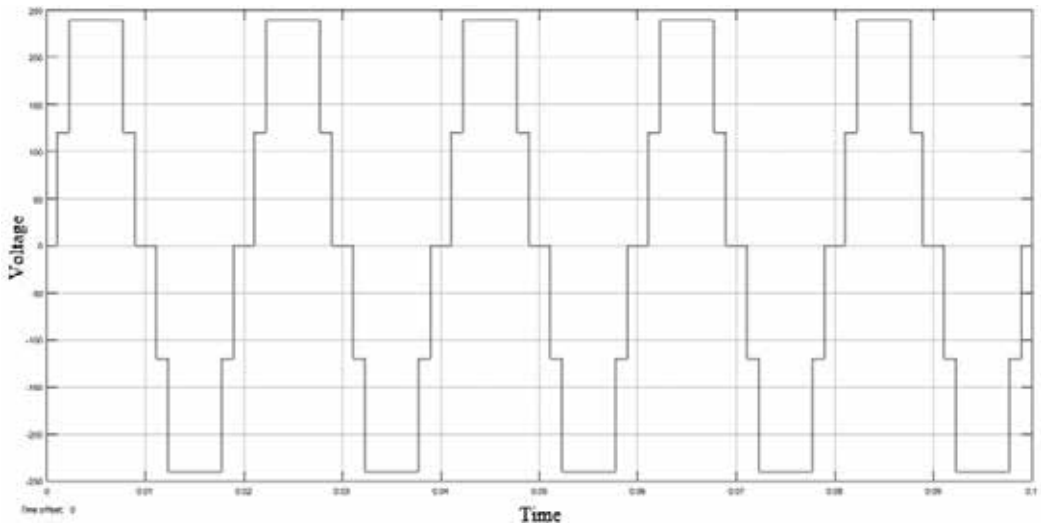

Figure 8. Three-level voltage output (m = 0.85).

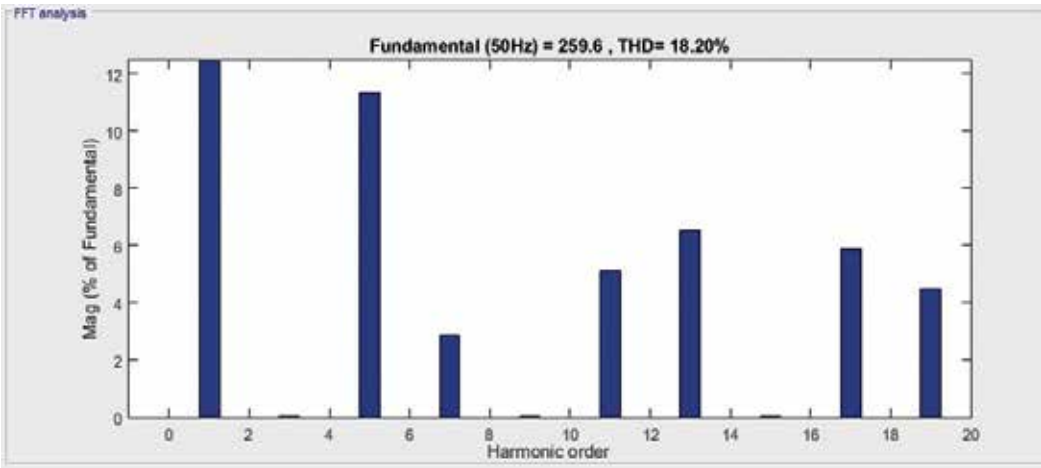

Figure 9. FFT analysis of three-level output (m = 0.85).

4.2. Overall result

The result simulation between SPWM and OHSW (GA) method is tabulated in **Table 4**. CHB-MLI applied optimized harmonic stepped waveform modulation method. The advantage for this method compared to SPWM is the switching frequency. SPWM in the first part of the simulation employed 4000 Hz carrier frequency which resulted in the pulse to occur at every step of the voltage. OHSW method operates at fundamental frequency. Switching frequency is mainly affecting the loss of energy and increases harmonic content. High switching frequency also results in short life span on power electronic switch. Hence, OSHW is superior to SPWM

CHB-MLI	Total harmonic distortion (%)	
	SPWM	OSHW(GA)
Three-level	26.96	18.2
Five-level	13.78	13.52
Seven-level	9.27	8.9

Table 4. Comparison between SPWM and OSHW method.

in terms of performance and durability. **Table 4** shows the THD comparison of SPWM and OSHW modulation on CHB-MLI. The result shows a huge reduction on THD for three-level but for five- and seven-level show minor reduction less than 1%. The result shown for CHB-MLI with OSHW method shows better performance as the selective harmonic elimination is applied. Genetic algorithm shows the capability of simplifying the Fourier series calculation and gets the most appropriate solution of switching angle.

The information obtained from the table show that THD percentage reduces as the number of the voltage level increases. This phenomena show that the increase of the voltage level is able to reduce the THD. This also inherits information that the decrement of THD is exponential to the number of levels. Hence, the increase of the voltage level to decrease THD is only limited to a certain number of voltage levels in terms of economical and performance aspect.

Standalone mode application mostly deals with the storage system. Hence, another set of simulation is done to test the capability of OSHW method with unequal DC source CHB-MLI. The result of the comparison of equal and unequal DC source CHB-MLI is tabulated in **Table 5**. The result shows that unequal DC source CHB-MLI performs better than equal DC source. All three-level, five-level and seven-level show lower THD percentage but the only minor differences. This result shows that OSHW modulation method is capable of reducing THD of both equal and unequal DC sources of cascaded H-bridge multilevel inverter. The result of low harmonic component elimination also shows the satisfactory level where the selected harmonics are reduced less than 1%.

Unequal DC source performs better than equal DC source CHB-ML. The problem is found to be related to modulation index step. Both GAs apply modulation step of 0.05 interval where a better solution possibly lies in the step with smaller interval. Besides that, the arrangement of

CHB-MLI (GA)	Total harmonic distortion (%)	
	Equal	Unequal
Three-level (m = 0.85)	18.2	18.06
Five-level (m = 0.80)	13.52	11.83
Seven-level (m = 0.80)	8.9	8.68

Table 5. Comparison between equal and unequal DC sources (genetic algorithm).

CHB-MLI (PSO)	Total harmonic distortion (%)	
	Equal	Unequal
Three-level (m = 0.85)	18.34	18.23
Five-level (m = 0.80)	12.17	12.63
Seven-level (m = 0.80)	9.4	6.80

Table 6. Comparison between equal and unequal DC sources (particle swarm optimization).

the voltage source is in increasing order which is also one of the factors, which smoothens the staircase waveform.

Another set of simulation applies the particle swarm optimization method with same fitness function and modulation step. The result is shown in **Table 6**. The result shows that SHE by PSO is less effective than GA. For three-level and seven-level CHB-MLI, GA produces lower THD output and then PSO type.

GA method has good prediction of switching angle for three-level CHB-MLI. But for five-level, the harmonic contained is higher than PSO method with the same level. For GA, the unequal DC source handling capability is there but not as good as compared to PSO. The result is obviously shown where PSO effectively reduces each selected harmonic.

5. Conclusion

Conventional inverter and SPWM switching method need high switching frequency. OHSW is introduced to overcome the problem. Besides that, SHE is also introduced to reduce low harmonic component. The result shows success in reducing the switching frequency with aid of GA and PSO as the nonlinear optimizer for switching angle. For seven-level CHB-MLI with OHSW by GA, 8.9% of THD, which is 0.37%, is lower compared to SPWM modulation method. The benefits for the low switching frequency are the increase of life span of the switching device and reduced power loss which is due to high switching frequency. The output waveform shows OHSW method switch on and off per cycle, which is far more less than the SPWM method. For comparison in three-level CHB-MLI (equal DC) total harmonic distortion, GA has a better output with 18.2% which is 0.14% lower than PSO. However, PSO shows more adaption for five-level CHB-MLI (equal DC) with 12.17%, which is 1.35% lower than GA. In seven-level CHB-MLI (equal DC) output voltage THD, GA is 8.9% which is 0.5% higher than PSO. However, unbalance voltage sources and GA-based CHB-MLI have better result for three-level and five-level. However, seven-level CHB-MLI showed that PSO has a better output with 6.8% of THD which is 1.88% lower than GA. However, the main intention of applying the bioinspired algorithm is to simplify the calculation of SHE in obtaining the most optimum result. The results in terms of selected low harmonic component elimination and GA is more efficient than PSO according to the result obtained where GA reduces all selected harmonics to below 0.4%, while PSO reduces to below 2.5%.

6. Future works

In this research, only single-phase CHB-MLI undergoes the optimization using OHSW. Hence, implementation of OHSW in three-phase multilevel inverter topology can be done for further detailed analysis. Three-phase system has additional switches and configuration which will be challenged on calculation complexity on the calculation of switching timing.

Besides that, implementation of different bioinspired algorithms in comparison mode will be a worthy research. The latest intelligent algorithm such as bat algorithm and bacterial foraging optimization can be applied for the switching timing calculation. As concluded from the research found, different algorithms can lead to different result accuracies. The latest intelligent algorithm is not yet being widely exposed in power electronic fields.

Furthermore, actual experimental work can be done in the future where the real work environment data can be obtained. This method is proposed to be suitably applied in the renewable energy harvest application where unstable sources frequently occur.

Author details

Hui Hwang Goh[1]*, Chin Wan Ling[1], Kai Chen Goh[2], Qing Shi Chua[1], Sy Yi Sim[1] and Mohd Ariff Mohd Aifaa[1]

*Address all correspondence to: jonathanhhgoh@gmail.com

1 Department of Electrical Engineering, Faculty of Electrical and Electronic Engineering, Universiti Tun Hussien Onn, Batu Pahat, Johor, Malaysia

2 Department of Construction Management, Faculty of Technology Management and Business, Universiti Tun Hussien Onn, Batu Pahat, Johor, Malaysia

References

[1] Azmi SA, Ahmed KH, Finney SJ, Williams BW. Comparative analysis between voltage and current source inverters in grid-connected application. In: Renewable Power Generation IET Conference; 2011. 101 p. DOI: 10.1049/cp.2011.0138 IET Digital Library

[2] Yunus HI, Bass RM. Comparison of VSI and CSI topologies for single-phase active power filters. In: Power Electronics Specialists Conference; IEEE; 1996;**2**:1892-1898 DOI: 10.1109/PESC.1996.548839

[3] Lakwal J, Deshpande DM, Suresh A, Mittal A. Cascaded multilevel inverter topologies for photovoltaic power generation systems. International Journal of ChemTech Research. 2013;**5**(2):1094-1100

[4] Ozdemir E, Ozdemir S, Tolbert LM. Fundamental-frequency-modulated six-level diode-clamped multilevel inverter for three-phase stand-alone photovoltaic system. IEEE Transactions on Industrial Electronics. 2009;**56**(11):4407-4415

[5] Yuan X, Barbi I. Fundamentals of a new diode clamping multilevel inverter. IEEE Transactions on power electronics. 2000;**15**(4):711-718

[6] Kim TJ, Kang DW, Lee YH, Hyun DS. The analysis of conduction and switching losses in multi-level inverter system. Power Electronics Specialists Conference. 2001;**3**:1363-1368

[7] Baker R, Bannister L. Electric power converter. US Patent 3 867 643. 1975

[8] Nabae A, Takahashi I, Akagi H. A new neutral-point-clamped PWM inverter. IEEE Transactions on Industry Applications. 1981;**5**:518-523

[9] Meynard TA, Henry F. Multi-level conversion: High voltage choppers and voltage-source inverters. Power Electronics Specialists Conference. 1992;**23**:397-403

[10] Peng FZ. A generalized multilevel inverter topology with self voltage balancing. Industry Applications Conference. 2000;**3**:2024-2031

[11] Hill WA, Harbourt CD. Performance of medium voltage multi-level inverters. Industry Applications Conference. 1999;**34**:1186-1192

[12] Manjrekar MD, Steimer PK, Lipo TA. Hybrid multilevel power conversion system: A competitive solution for high-power applications. IEEE Transactions on Industry Applications. 2000;**36**(3):834-841

[13] Lai Y-S, Shyu F-S. Topology for hybrid multilevel inverter. IEE Proceedings-Electric Power Applications. 2002;**149**(6):449-458

[14] Song BM, Kim J, Lai JS, Seong KC, Kim HJ, Park SS. A multilevel soft-switching inverter with inductor coupling. IEEE Transactions on Industry Applications. 2001;**37**(2):628-636

[15] Kanimozhi M, Geetha P. A new boost switched capacitor multilevel inverter using different multi carrier PWM techniques. Circuit, Power and Computing Technologies (ICCPCT). 2014:432-437

[16] Khamooshi R, Sh Moghani J. Comprehensive harmonic optimization in cascaded h-bridge multilevel inverters using variable DC sources. In: Power Electronics, Drive Systems and Technologies Conference (PEDSTC 2014), Tehran; 2014. pp. 249-254. DOI: 10.1109/PEDSTC.2014.6799380

[17] Ganesan K, Barathi K, Chandrasekar P, Balaji D. Selective harmonic elimination of cascaded multilevel inverter using bat algorithm. In: Procedia Technology; 2015;**21**:651-657. ISSN 2212-0173

[18] Aghdam MGH, Fathi SH, Gharehpetian GB. Comparison of OMTHD and OHSW harmonic optimization techniques in multi-level voltage-source inverter with non-equal DC sources. IEEE Power Electronics. 2007;**7**:587-591

[19] Kumar J, Das B, Agarwal P. Selective harmonic elimination technique for a multilevel inverter. Fifteenth National Power Systems Conference (NPSC), IIT Bombay. 2008;**1**(3):608-613

[20] Kavousi A, Vahidi B, Salehi R, Bakhshizadeh MK, Farokhnia N, Fathi SH. Application of the bee algorithm for selective harmonic elimination strategy in multilevel inverters. IEEE Transactions on Power Electronics. 2012;**27**(4):1689-1696

[21] Parkash A, Shimi SL, Chatterji S. Harmonics reduction in Cascade H-bridge multilevel inverters using GA and PSO. International Journal of Engineering Trends and Technology. 2014;**12**

[22] Abd-El-Wahed WF, Mousa AA, El-Shorbagy MA. Integrating particle swarm optimization with genetic algorithms for solving nonlinear optimization problems. Journal of Computational and Applied Mathematics. 2011;**235**(5):1446-1453

[23] Debnath S, Ray RN. THD optimization in 13 level photovoltaic inverter using genetic algorithm. International Journal of Engineering Research and Applications. 2012;**2**(3): 385-389

[24] Hosseini SH, Sadigh AK, Barakati SM, Kangarlu MF. Comparison of SPWM technique and selective harmonic elimination using genetic algorithm. Electrical and Electronics Engineering; 2009. pp. I-278-I-282. DOI: 10.1109/ELECO.2009.5355372

[25] Perumal M, Nanjudapan D. Performance enhancement of embedded system based multilevel inverter using genetic algorithm. Journal of Electrical Engineering. 2011;**62**(4): 190-198

[26] Ozpineci B, Tolbert LM, Chiasson JN. Harmonic optimization of multilevel converters using genetic algorithms. Power Electronics Specialists Conference. 2004;**5**:3911-3916

[27] Vas P, editors. Artificial-intelligence-based electrical machines and drives: Application of fuzzy, neural, fuzzy-neural, and genetic-algorithm-based techniques. 45th ed. Oxford: Oxford University Press; 1999

[28] Yang H, Zhou W, Lu L, Fang Z. Optimal sizing method for stand-alone hybrid solar-wind system with LPSP technology by using genetic algorithm. Solar Energy. 2008;**82**(4):354-367

[29] Adedeji AA. Genetic (evolutionary) algorithm: Introduction and its use as an engineering design tool. In: Department of Civil Engineering, University of Ilorin, editors. Ilorin, Nigeria: Olad Publishers And Printing Enterprisers; 1st Ed. 2007. pp. 1-62. ISBN: 978-8115-86-1

[30] Song MP, Gu GC. Research on particle swarm optimization: A review. In machine learning and cybernetics. In: Machine Learning and Cybernetics, editors. Proceedings of 2004 International Conference, 4; 2004;**4**:2236-2241. DOI: 10.1109/ICMLC.2004.1382171

[31] Eberhart R, Kennedy J. A new optimizer using particle swarm theory. IEEE Micro Machine and Human Science. 1995;**60**:39-43

[32] Shi Y. Particle swarm optimization: Developments, applications and resources. IEEE Evolutionary Computation. 2001;**1**:81-86

Chapter 8

Harmonic Mitigation for VSI Using DP-Based PI Controller

Ragini Meshram, Monika Madhusoodan and Sushama Wagh

Additional information is available at the end of the chapter

http://dx.doi.org/10.5772/intechopen.74587

Abstract

The chapter focuses on the strengths of dynamic phasor (DP) based model over conventional time domain model and the controller designed using it for selected harmonic mitigation. To validate the effectiveness of the controller designed using DP-based model, the single-phase voltage source inverter (VSI) with various loads has been considered including effects of intermittent nature of renewable energy sources e.g. photovoltaic module. The DP technique offers distinct advantages in modelling, simulation, and control with respect to the time domain models. With the assets of DP modelling technique based on the measurement of harmonic coefficients, the PI controller is designed which eliminates selected voltage and current harmonics in VSI and results are compared with the repetitive control technique. It has been proved through simulations that as compared to conventional technique, the proposed DP-based PI controller eliminates multiple selected frequencies effectively.

Keywords: dynamic phasor (DP), harmonics, photovoltaic (PV) inverter, repetitive control (RC), voltage source inverter (VSI)

1. Introduction

In modern power system, the growth of photovoltaic (PV) due to increase in efficiency, clean sources of energy and decrease in cost of solar technology promotes substantial power integration. According to their functionality and operating requirements, it is classified in standalone and grid connected [1]. In standalone system, remote area is supplied by dc or ac power with converters and energy storage devices, on the other hand, in grid connected system the generated

power is supplied to the utility services without any energy storage equipments. Distributed generation (DG) systems making use of renewable energy sources are being designed and connected to grid. In distribution feeder, the high penetration of PV generators has considerable impact on the system behaviour. For better insight into these impacts development and fine tuning of existing power system and power converters in the simulation environment is essential. For fast computation of large distribution systems, the dynamical models for various components and various stages are essential. The chapter concentrates on development of the dynamic phasor (DP)-based model of pulse width modulated (PWM) converters that are capturing the transients of interest. The topology of PV system considered, consist of, three power stage circuit stages, such as dc/dc boost converter for maximum power point tracking (MPPT), low voltage single phase dc/ac inverter and filter inductance with grid.

In grid-connected PV inverter systems, the important power quality issue is current distortion [2–4]. According to IEEE Standard 1547–2003 and IEC standard 61,727, the total harmonic distortion (THD) for the grid current is lower than 5% to avoid unfavourable effects on the other equipments that are connected to grid. In addition, for odd harmonics from 3rd to 9th, the limitation is 4% and even harmonics are limited to 25% of the odd harmonic limits [5]. These acceptable current distortion levels are defined for grid-connected PV inverter systems in rated operational mode. Since, solar radiations are not steady in PV inverter systems, the output current of PV is less than its rated value.

Many filter topologies are used in literature for reduction of harmonics, the higher order power filter named as LLCL filter, which inserts a small inductor in the branch of the capacitor in the traditional LCL filter to create a series resonant circuit at the switching frequency [4, 6]. It can attenuate current ripple component of switching frequency much better than LCL filter [7], also decrease in total inductance which raise the characteristic resonance frequency for better operation of inverter system control [8–11].

For analysis of harmonics in PWM systems and the harmonics generated by switching, the DP-based model is best available tool as explained in [18]. The DP-based model is developed from generalised averaging technique and is capable of converting periodic varying state variables into dc state variables which is a widely employed method for modelling of oscillatory systems [12–13]. Contrary to different types of existing numerical methods available in literature, the DP-based technique [14, 15] focuses on the frequencies of interest and provides accurate simulations for larger time steps [16].

The chapter highlights the important advantages of DP-based models to capture the harmonic content in the signals. The harmonics of the DP model is represented by Fourier coefficients which are determined by harmonic balance equation which contains useful information according to the selected harmonics. This information can be used for better controller design as well as deeper analysis on system performance according to oscillating dynamics and its interaction within and with system. A DP-based model can also be formed using sequence components of alternators and its voltage controller can be designed as mentioned in [17].

Control strategies that are applied to the power electronics converter could support the power conditioning functionality of the current and grid-connected inverters. With respect to the

current control, proportional resonant (PR) controller is the most popular controller for single-phase PV inverters. It is well known that the odd harmonics (3rd, 5th and 7th) are dominant in the output current of single-phase grid-connected inverters. Since PR controller cannot reject all harmonics appearing in the grid current, the PR controlled inverters may not be able to feed high quality currents into the grid. In order to eliminate the current harmonics distortion effectively, repetitive controller (RC) can be used with phase compensator to track and eliminate all the harmonics in the system.

The reduction in THD indicates the accuracy with which the periodic signal is tracked at the steady state. For achieving precise tracking of periodic signal, one of the most preferred approaches is the RC [19–21]. The fundamental operating principle of the RC is based on internal model principle [22], where it observes the systems' periodic signals for one-cycle period and a corresponding compensating signal is generated in next cycle period to ensure precise tracking of the signal [23]. From the frequency point of view, the RC performs finer error cancellation for periodic signals by presenting a large magnitude of loop gain at the fundamental frequency and its integral multiples. This can be identified as a form of period-based integral control [24–28].

2. Background preliminaries

2.1. Concept of repetitive control

The main objective of RC is to asymptotically track the reference signal while rejecting disturbances. Any periodic signal with period T can be generated by a positive feedback system with the specified initial function as shown in **Figure 1(a)**. According to Internal Model Principle [29], it is necessary to include model of **Figure 1(a)** into closed loop system in order to achieve perfect tracking or external disturbance rejection. In case of inverter control, when reference signal is the periodic signal, a pair of conjugate imaginary poles should be included at the frequency w in the closed loop which can be provided by $1/(s^2 + w^2)$, as used in proportional resonant controller scheme. The inverter output voltage is full of harmonics and it is essential to reduce the level of concern harmonics to obtain low THD. One of the solutions is to include bundle of pairs of conjugate imaginary poles at different frequencies. Another solution could be so-called RC [30–32], which adopts infinite dimensional internal model to provide series of conjugate poles at all concerned harmonic frequencies. The stability and robustness of RC

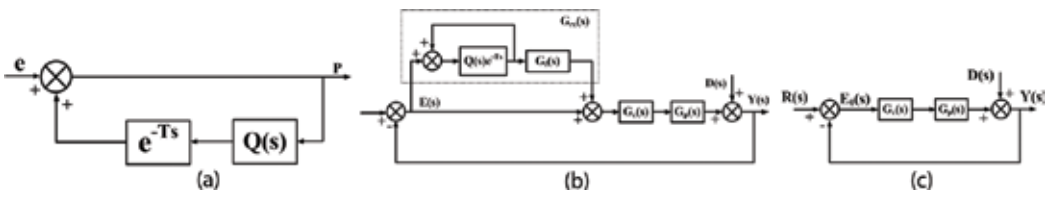

Figure 1. Repetitive control system (a) periodic signal generator (b) general structure of plug-in repetitive control (c) closed-loop control without RC.

system is improved by introducing a low pass filter Q(s) in series with time delay element. Any low pass filter satisfying $\|Q(s)\|_\infty < 1$ can be used in minimum phase systems, but there are bandwidth restrictions on Q(s) for non-minimal phase plant [30].

The design and synthesis methods for modified RC system vary with different configurations as mentioned in [25–28, 31]. The plug-in RC system depicted in **Figure 1(b)** is most commonly used structure. The design problem is mainly to choose and optimise the dynamic compensator G_f (s) and the low pass filter Q(s). The choice of controller parameters involves a trade-off between steady-state accuracy, robustness, and transient response of the system. The closed-loop control of single-phase VSI without RC is shown in **Figure 1(c)**, where R(s) is the reference signal, D(s) is the disturbance, G_p(s) is the plant and G_c(s) is the closed-loop controller. The closed-loop transfer function H(s) of the control system without RC is represented in (1) and the tracking error E_0(s) of the signal due to periodic input R(s) and disturbance D(s) is given by

$$H(s) = \frac{G_c(s)G_p(s)}{1 + G_c(s)G_p(s)} \quad E_0(s) = \frac{R(s) - D(s)}{1 + G_s(s)G_p(s)} \tag{1}$$

To assure the effectiveness of RC for accurate tracking, the system tracking error E(s) with RC is written in terms of tracking error E_0(s) of the original system without RC and is expressed as

$$E(s) = E_0(s)\frac{1 - Q(s)e^{-Ts}}{1 - \left[1 - G_f(s)H(s)\right]Q(s)e^{-Ts}} \tag{2}$$

To assure stability, the dynamic compensator must be chosen such that

$$\|[1 - \mathrm{G_f(s)H(s)}]\mathrm{Q(s)}\|\infty < 1, \qquad \mathrm{s} = j\omega, \qquad \text{for all } \omega \tag{3}$$

Eq. (2) can be expressed as the sum of a geometric progression

$$\begin{aligned} E(s) = E_0(s)\left[1 - Q(s)e^{-Ts}\right]\Big\{1 + \left[1 - G_f(s)H(s)\right]Q(s)e^{-Ts} \\ + \left[1 - G_f(s)H(s)\right]^2 Q^2(s)e^{-2Ts} + \cdots\Big\} \end{aligned} \tag{4}$$

where e^{-T_s} implies a one-cycle delay of fundamental period. Eq. (4) indicates that the first cycle error $e_0(t) = L^{-1}[E_0(s)]$ for $t \in [0, T]$ is unaffected by RC. If

$$1 - G_f(s)H(s) = 0 \text{ or } G_f(s)H(s) = 1 \tag{5}$$

then the error can be simplified to $\mathrm{E(s)} = \mathrm{E_0(s)}\left[1 - \mathrm{Q(s)e^{-T_s}}\right]$, which is the error of second cycle. If Q(s) can be achieved by

$$1 - Q(jk\omega)e^{-jk\omega T} = 0 \quad \text{for } k = 0, 1, 2, \ldots \tag{6}$$

where $w = 2\pi/T$, then the steady-state tracking will converge to zero at each of the harmonics. However, because of physical nonideality of the system, the design requirements (5), (6)

cannot be practically satisfied for all of the harmonics, rather it is more appropriate to adopt the conditions

$$1 - G_f(s)H(s) \simeq 0 \qquad G_f(s)H(s) \simeq 1 \quad \text{and} \qquad 1 - Q(jk\omega)e^{-jk\omega T} \simeq 0 \tag{7}$$

thus, the task of designing the RC is to meet the harmonic elimination requirements of (7) while satisfying stability conditions (1) and (3).

2.2. The dynamic phasor-based model

The voltages and currents in power electronic converters and electrical drives are typically periodic in steady state, and mostly nonsinusoidal. The dynamics of interest for analysis and control are often those of deviations from periodic behaviour, for instance as manifested in deviations of the envelope of a quasi-sinusoidal waveform from its steady-state value. For analysis of the steady state, generally used methods are phasor, harmonic, and describing function [12, 13, 18]. With analytical approach reviewed, the main aim of this research is systematic development of phasor dynamics, from which the dynamic behaviour of the original waveform or its envelope can efficiently be deduced.

2.2.1. Definition and concepts used in DP model

The DP modelling technique is based on the generalised averaging method wherein the complex time domain signal is represented in the interval (t-T, t) with the Fourier series representation. The time varying Fourier coefficients are termed as DPs, which is essentially a frequency-domain method where various harmonics developed over time can be decomposed. In power system steady-state analysis, these Fourier coefficients X_k (t) are also called as phasors. During transients, the system is not in a pure periodic state but nearly periodic state. The idea is now to extend this approach to nearly periodic signals [13] and to approximate x(τ) in the interval $t \in$ (t−T, t] with a Fourier series representation given as

$$x(\tau) = \sum_{k=-\infty}^{\infty} X_k(t)\, e^{jk\omega_s \tau} \tag{8}$$

In this representation, as the signal x(τ) is nearly periodic and since the interval under consideration slides as a function of time, the Fourier coefficients X_k (t) are time varying. This expression can also interpreted as an orthogonal signal expansion of the function x(t) with orthonormal basis $e^{jk\omega_s t}$. The k^{th} phasor (Fourier coefficient) of X is defined as:

$$X_k(t) = \frac{1}{T} \int_{t-T}^{t} x(\tau)\, e^{-jk\omega_s \tau} d\tau = \langle x \rangle_k(t) \tag{9}$$

where $w_s = 2\pi/T_s$. Note that the phasors are defined over a moving time-window and hence, time dependent. Additionally, if X is periodic with time T_s, then X_k (t) is constant. In the DP

approach, only a few coefficients provide a good approximation of the original waveform. Some important properties of DPs are-

i. The relation between the derivatives of x(τ) and the derivatives of X_k (t) is given by

$$\frac{d}{dt}\langle x\rangle_k = \left\langle \frac{d}{dt}x \right\rangle_k - jk\omega_s\langle x\rangle_k \tag{10}$$

ii. The product of two time-domain variables equals a discrete time convolution of the two DP sets of the variables, which is given by

$$\langle xy\rangle_k = \sum_{l=-\infty}^{\infty} \langle x\rangle_{k-l}\langle y\rangle_l \tag{11}$$

iii. For a complex valued signal x, the relationship between X_k and X_{-k} is given as $X_{-k} = X_k^*$

2.3. Advantages and limitations of dynamic phasors

The DP approach offers a numbers of advantages over conventional methods.

1. The oscillating waveforms of ac circuits become constant or slowly-varying in the DP domain and different frequency components can be handled separately with convenience.

2. It approximates a periodically switched system with a continuous system, thereby converting periodic varying state variables into dc state variables.

3. At steady state the DP X_k becomes constant.

4. As the variations of DP X_k are much slower than the instantaneous quantities x(t), they can be used to compute the fast electromagnetic transients with larger step sizes, so that it makes simulation potentially faster than conventional time domain EMTP-like simulation.

5. The selection of DP index-k gives a wider bandwidth in the frequency domain than traditional slow quasi-stationary models used in transient stability programs.

6. The selection and variation of k also gives the possibility of showing coupling between various quantities and addressing particular problems at different frequencies.

The only disadvantage of the DP approach is that the number of variables and equations are higher than in the original equations.

3. DP-based modelling

3.1. Single-phase inverter with R-load

The typical structure of a single-phase inverter is presented in **Figure 2** which includes H-bridge with switching function S_i that is fed by LVDC link voltage (V_{dcL}) and LC circuit is

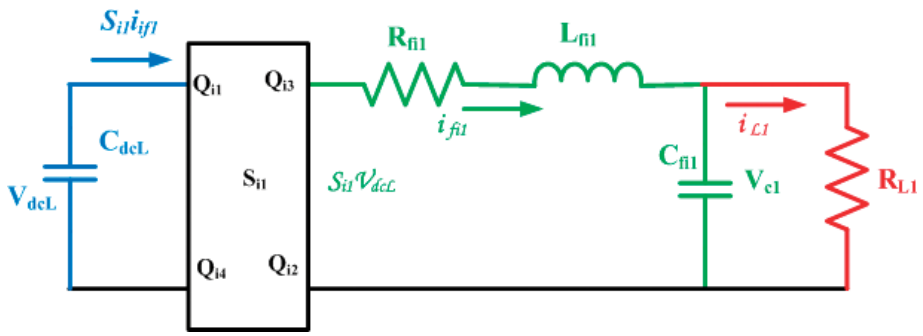

Figure 2. Single-phase inverter with LC output filter.

connected between inverter output and load resistance (R_L) for filtering purposes. LC filter consists of filter inductor L_{fi}, filter resistance R_{fi}, and filter capacitor C_{fi}.

3.1.1. System modelling of inverter with R-load

The dynamic model of inverter can be represented as:

$$L_{fi}\frac{d}{dt}i_{fi} = S_i V_{dcL} - R_{fi}i_{fi} - V_{cfi} \tag{12}$$

$$C_{fi}\frac{d}{dt}V_{cfi} = i_{fi} - \frac{V_{cfi}}{R_L} \tag{13}$$

where, S_i (t) is a switching function that denotes the switching status as:

$$S_i(t) = \begin{cases} 1 & t \in [kT_s, (k+d_k)T_s] \\ 0 & t \in [(k+d_k)T_s, (k+1)T_s] \end{cases} \tag{14}$$

In this case, the switch is controlled using fixed frequency switching, i.e. time axis is divided into intervals [kT_s, (k + 1)T_s], where $T_s > 0$ is the switch period and k ∈ N. The duty cycle $d_k \in [0, 1]$ is chosen at the beginning of each switch. The duty cycle determines the fraction of time the switch is active (1 & 0 represents the on-mode and off-mode respectively) and thus controls the system dynamics. The aim of controller is to regulate inverter output voltage (V_{cfi}) at desired value of voltage, which is a pure sinusoidal signal with angular frequency w and amplitude V_P.

3.1.2. DP model of inverter with R-load

The DP-based dynamic model for inverter topology shown in **Figure 2** has been developed based on theory explained in Section 2.2. In order to obtain an accurate approximation, the foremost step is to fix Fourier coefficients for the DP model as specified in **Table 1**.

Converting (12) and (13) into DP form, the state variables, inductor current and capacitor voltage are modified to

State variables	DP index k	Discontinuous variables	DP index k
i_{fi}, V_{cfi}	1, 3, 5	S_i	1, 3, 5

Table 1. Fourier coefficients of the system.

$$L_{fi}\frac{d}{dt}\langle i_{fi}\rangle_k = \langle S_i V_{dcL}\rangle_k - R_{fi}\langle i_{fi}\rangle_k - \langle V_{cfi}\rangle_k - jk\omega L_{fi}\langle i_{fi}\rangle_k \tag{15}$$

$$C_{fi}\frac{d}{dt}\langle V_{cfi}\rangle_k = \langle i_{fi}\rangle_k - \frac{\langle V_{cfi}\rangle_k}{R_L} - jk\omega C_{fi}\langle V_{cfi}\rangle_k \tag{16}$$

Eqs. (15)–(16) represented in real and imaginary coefficients as

$$L_{fi}\frac{d}{dt}\langle i_{fi}\rangle_k^R = \mathrm{Re}\left\{\sum_{l=-\infty}^{\infty}\langle S_i\rangle_{k-l}\langle V_{dcL}\rangle_l\right\} - R_{fi}\langle i_{fi}\rangle_k^R - \langle V_{cfi}\rangle_k^R + k\omega L_{fi}\langle i_{fi}\rangle_k^I \tag{17}$$

$$L_{fi}\frac{d}{dt}\langle i_{fi}\rangle_k^I = \mathrm{Re}\left\{\sum_{l=-\infty}^{\infty}\langle S_i\rangle_{k-l}\langle V_{dcL}\rangle_l\right\} - R_{fi}\langle i_{fi}\rangle_k^I - \langle V_{cfi}\rangle_k^I - k\omega L_{fi}\langle i_{fi}\rangle_k^R \tag{18}$$

$$C_{fi}\frac{d}{dt}\langle V_{cfi}\rangle_k^R = \langle i_{fi}\rangle_k^R - \frac{\langle V_{cfi}\rangle_k^R}{R_L} + k\omega C_{fi}\langle V_{cfi}\rangle_k^I \tag{19}$$

$$C_{fi}\frac{d}{dt}\langle V_{cfi}\rangle_k^I = \langle i_{fi}\rangle_k^I - \frac{\langle V_{cfi}\rangle_k^I}{R_L} - k\omega C_{fi}\langle V_{cfi}\rangle_k^R \tag{20}$$

(i) Modelling of switching function S_i

Let the duty cycle d_i and switching period T are the variables associated with a switch and H-bridge of inverter consists of 4 switches Q_{i1}−Q_{i4} (with reference to **Figure 2**). Representing state 1 in S_i (t) for Q_{i1} and Q_{i2} ON while state −1 for Q_{i3} and Q_{i4} ON, the switching function (S_i (t)) and its DP form $\left(\langle S_i\rangle_k\right)$ is defined in (21).

$$S_i(t) = \begin{cases} 1, & 0 < t < d_i T \\ -1, & d_i T < t < T \end{cases} \langle S_i\rangle_0 = d_i \;\; \langle S_i\rangle_k^R = \frac{\sin 2\pi k d_i}{k\pi} \;\; \langle S_i\rangle_k^I = \frac{\cos 2\pi k d_i - 1}{k\pi} \tag{21}$$

Substituting (21) into (17)–(20), and organising dynamical equations into state-space representation will result in $\frac{d}{dt}X = AX + Bu$, where

$$X = \left[\langle i_{fi}\rangle_1^R \;\; \langle i_{fi}\rangle_1^I \;\; \langle i_{fi}\rangle_3^R \;\; \langle i_{fi}\rangle_3^I \;\; \langle i_{fi}\rangle_5^R \;\; \langle i_{fi}\rangle_5^I \;\; \langle V_{cfi}\rangle_1^R \;\; \langle V_{cfi}\rangle_1^I \;\; \langle V_{cfi}\rangle_3^R \;\; \langle V_{cfi}\rangle_3^I \;\; \langle V_{cfi}\rangle_5^R \;\; \langle V_{cfi}\rangle_5^I\right] \tag{22}$$

$$A = \begin{bmatrix} -\frac{R_{fi}}{L_{fi}}[I]_{6\times6} & -\frac{1}{L_{fi}}[I]_{6\times6} \\ \frac{1}{C_{fi}}[I]_{6\times6} & -\frac{1}{C_{fi}R_L}[I]_{6\times6} \end{bmatrix} + diag\left(\omega[J]_{2\times2}, 3\omega[J]_{2\times2}, 5\omega[J]_{2\times2}, \omega[J]_{2\times2}, 3\omega[J]_{2\times2}, 5\omega[J]_{2\times2}\right) \tag{23}$$

$$B = \left[\frac{\sin 2\pi d_i}{\pi L_{fi}} \quad \frac{\cos 2\pi d_i - 1}{\pi L_{fi}} \quad \frac{\sin 6\pi d_i}{3\pi L_{fi}} \quad \frac{\cos 6\pi d_i - 1}{3\pi L_{fi}} \quad \frac{\sin 10\pi d_i}{5\pi L_{fi}} \quad \frac{\cos 10\pi d_i - 1}{5\pi L_{fi}} \quad 0 \quad 0 \quad 0 \quad 0 \quad 0 \quad 0 \right]^T \tag{24}$$

$$u = \left[\langle V_{dcL} \rangle_0 \right] \quad J = \begin{bmatrix} 0 & 1 \\ -1 & 0 \end{bmatrix} \tag{25}$$

The state Eqs. (22)–(25) implies that the dynamics of single-phase inverter represented using index-1, 3 and 5 of output filter inductor current (i_{fi}) and index-1, 3 and 5 of output filter capacitor voltage (V_{cfi}) as state variables. If more indices-k were used, then the model would be more accurate, however, the resulting model would be too complex to provide insightful information for controller design.

3.2. Single-phase inverter with RL-load

The typical structure of a single-phase inverter is same as presented in **Figure 2** except the load part, where R is replaced by combination of R_L and inductance L_L as a RL load. State variables for this case are output filter inductor current (i_{fi}), output filter capacitor voltage (V_{cfi}), and load current (i_L).

The dynamic model of inverter with RL load can be represented as:

$$L_{fi} \frac{d}{dt} i_{fi} = S_i V_{dcL} - R_{fi} i_{fi} - V_{cfi} \tag{26}$$

$$C_{fi} \frac{d}{dt} V_{cfi} = i_{fi} - i_L \tag{27}$$

$$L_L \frac{d}{dt} i_L = V_{cfi} - R_L i_L \tag{28}$$

The DP form of (26)–(28) for the state variables inductor current, capacitor voltage and load current are:

$$L_{fi} \frac{d}{dt} \langle i_{fi} \rangle_k = \langle S_i V_{dcL} \rangle_k - R_{fi} \langle i_{fi} \rangle_k - \langle V_{cfi} \rangle_k - jk\omega L_{fi} \langle i_{fi} \rangle_k \tag{29}$$

$$C_{fi} \frac{d}{dt} \langle V_{cfi} \rangle_k = \langle i_{fi} \rangle_k - \langle i_L \rangle_k - jk\omega C_{fi} \langle V_{cfi} \rangle_k \tag{30}$$

$$L_L \frac{d}{dt} \langle i_L \rangle_k = \langle V_{cfi} \rangle_k - R_L \langle i_L \rangle_k - jk\omega L_L \langle i_L \rangle_k \tag{31}$$

Using the switching function model derived in Section 3.1 the detailed DP model can be summarised as:

$$L_{fi} \frac{d}{dt} \langle i_{fi} \rangle_k^R = \mathrm{Re}\left\{ \sum_{l=-\infty}^{\infty} \langle S_i \rangle_{k-l} \langle V_{dcL} \rangle_l \right\} - R_{fi} \langle i_{fi} \rangle_k^R - \langle V_{cfi} \rangle_k^R + k\omega L_{fi} \langle i_{fi} \rangle_k^I \tag{32}$$

$$L_{fi} \frac{d}{dt} \langle i_{fi} \rangle_k^I = \mathrm{Re}\left\{ \sum_{l=-\infty}^{\infty} \langle S_i \rangle_{k-l} \langle V_{dcL} \rangle_l \right\} - R_{fi} \langle i_{fi} \rangle_k^I - \langle V_{cfi} \rangle_k^I - k\omega L_{fi} \langle i_{fi} \rangle_k^R \tag{33}$$

$$C_{fi}\frac{d}{dt}\langle V_{cfi}\rangle_k^R = \langle i_{fi}\rangle_k^R - \langle i_L\rangle_k^R + k\omega C_{fi}\langle V_{cfi}\rangle_k^I \tag{34}$$

$$C_{fi}\frac{d}{dt}\langle V_{cfi}\rangle_k^I = \langle i_{fi}\rangle_k^I - \langle i_L\rangle_k^I - k\omega C_{fi}\langle V_{cfi}\rangle_k^R \tag{35}$$

$$L_L\frac{d}{dt}\langle i_L\rangle_k^R = \langle V_{cfi}\rangle_k^R - R_L\langle i_L\rangle_k^R + k\omega L_L\langle i_L\rangle_k^I \tag{36}$$

$$L_L\frac{d}{dt}\langle i_L\rangle_k^I = \langle V_{cfi}\rangle_k^I - R_L\langle i_L\rangle_k^I - k\omega L_L\langle i_L\rangle_k^R \tag{37}$$

The state space representation $\frac{d}{dt}X = AX + Bu$ can be obtained by substituting (21) into (32)–(37), where

$$X = \left[\langle i_{fi}\rangle_1^R \;\; \langle i_{fi}\rangle_1^I \;\; \langle i_{fi}\rangle_3^R \;\; \langle i_{fi}\rangle_3^I \;\; \langle i_{fi}\rangle_5^R \;\; \langle i_{fi}\rangle_5^I \;\; \langle V_{cfi}\rangle_1^R \;\; \langle V_{cfi}\rangle_1^I \;\; \langle V_{cfi}\rangle_3^R \;\; \langle V_{cfi}\rangle_3^I \;\; \langle V_{cfi}\rangle_5^R \;\; \langle V_{cfi}\rangle_5^I \langle i_L\rangle_1^R \;\; \langle i_L\rangle_1^I \;\; \langle i_L\rangle_3^R \;\; \langle i_L\rangle_3^I \;\; \langle i_L\rangle_5^R \;\; \langle i_L\rangle_5^I\right] \tag{38}$$

$$A = \begin{bmatrix} -\frac{R_{fi}}{L_{fi}}[I]_{6\times6} & -\frac{1}{L_{fi}}[I]_{6\times6} & [0]_{6\times6} \\ \frac{1}{C_{fi}}[I]_{6\times6} & [0]_{6\times6} & -\frac{1}{C_{fi}R_L}[I]_{6\times6} \\ [0]_{6\times6} & \frac{1}{L_L}[I]_{6\times6} & -\frac{R_L}{L_L}[I]_{6\times6} \end{bmatrix} + diag\left(\omega[J]_{2\times2}, 3\omega[J]_{2\times2}, 5\omega[J]_{2\times2}, \omega[J]_{2\times2}, 3\omega[J]_{2\times2}, 5\omega[J]_{2\times2}, \omega[J]_{2\times2}, 3\omega[J]_{2\times2}, 5\omega[J]_{2\times2}\right) \tag{39}$$

$$B = \left[\frac{\sin 2\pi kd_i}{\pi L_{fi}} \;\; \frac{\cos 2\pi kd_i - 1}{\pi L_{fi}} \;\; \frac{\sin 6\pi kd_i}{3\pi L_{fi}} \;\; \frac{\cos 6\pi kd_i - 1}{3\pi L_{fi}} \;\; \frac{\sin 10\pi kd_i}{5\pi L_{fi}} \;\; \frac{\cos 10\pi kd_i - 1}{5\pi L_{fi}} \;\; 0 \;\; 0 \;\; 0 \;\; 0 \;\; 0 \;\; 0 \;\; 0 \;\; 0 \;\; 0 \;\; 0 \;\; 0 \;\; 0\right]^T \tag{40}$$

$$u = \left[\langle V_{dcL}\rangle_0\right] \;\; J = \begin{bmatrix} 0 & 1 \\ -1 & 0 \end{bmatrix} \tag{41}$$

3.3. Single-phase grid-connected inverter for PV system

The configuration of system consist of three stages, the boost converter stage which is used for tracking of maximum power of photovoltaic array, the inverter stage which generates the behaviour of a sine square wave and the filtering step through L arrangement with grid is represented in **Figure 3**. The input voltage V_{PV} is from photovoltaic array and the system employs signals at different frequencies:

i. The boost converter with switch μ having switching frequency (f_c), which is of kHz.

ii. The switching function (S) constitutes inverter switching frequency (f_i) in range of kHz.

iii. The main systems frequency (f) of 50 Hz.

3.3.1. System modelling of grid-connected PV inverter

In **Figure 3**, V_{PV} is the input voltage to the system from photovoltaic renewable source where i_L is a input current to boost converter, V_C is the output voltage of the boost converter and also the input voltage to the inverter, μ is the control signal of the boost converter. In inverter output side i_{Lf} is the current passing through the filter inductor while V_{AC} = Esin(2πft) is the grid voltage and switching function for all inverter switches (S_1 to S_4) is S.

For the topology considered in **Figure 3**, different operating states can be obtained depending on the position of switches, μ and S. The dynamical model of single-phase grid-connected PV system is obtained in (42)–(44).

$$L\frac{d}{dt}i_L = V_{PV} - (1-\mu)V_C \tag{42}$$

$$C\frac{d}{dt}V_C = (1-\mu)i_L - Si_{Lf} \tag{43}$$

$$L_f\frac{d}{dt}i_{Lf} = SV_C - V_{AC} \tag{44}$$

3.3.2. DP model of grid-connected PV inverter

Similar procedure is followed for the model development of PV inverter system which is shown in **Figure 3**. The considered Fourier coefficients for the system are specified in **Table 2**. Converting (42)–(44) into DP domain, the revised model is represented in (45)–(47).

$$L\frac{d}{dt}\langle i_L\rangle_k = \langle V_{PV}\rangle_k - \langle V_C\rangle_k + \langle \mu V_C\rangle_k - jk\omega L\langle i_L\rangle_k \tag{45}$$

$$C\frac{d}{dt}\langle V_C\rangle_k = \langle i_L\rangle_k - \langle \mu i_L\rangle_k - \langle Si_{Lf}\rangle_k - jk\omega C\langle V_C\rangle_k \tag{46}$$

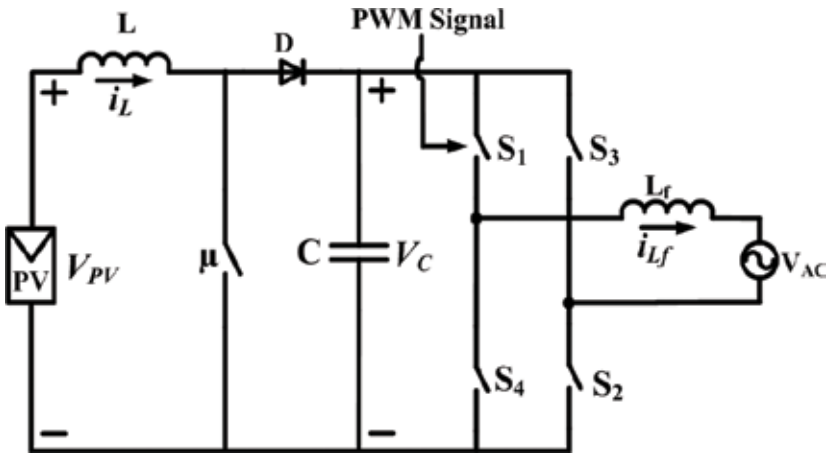

Figure 3. Single-phase grid-connected PV inverters power circuit topology.

State variables	DP index k	Discontinuous variables	DP index k
i_L, V_C	0, 2, 4	μ	0, 2, 4
i_{Lf}	1, 3, 5	S	1, 3, 5

Table 2. Fourier coefficients of the system.

$$L_f \frac{d}{dt}\langle i_{Lf}\rangle_k = \langle SV_C\rangle_k - \langle V_{AC}\rangle_k - jk\omega L_f \langle i_{Lf}\rangle_k \tag{47}$$

(i) Modelling of the boost converter switching function μ.

Let, the duty cycle d and switching period T_s be the variables associated with a boost converter switch and state 1 and 0 represents ON and OFF mode of the switch respectively. The switching function (μ) and its DP form $\left(\langle\mu\rangle_k\right)$ is provided in (48).

$$\mu(t) = \begin{cases} 1, & 0 < t < dT_s \\ -1, & dT_s < t < T_s \end{cases} \quad \langle\mu\rangle_0 = d \quad \langle\mu\rangle_k^R = \frac{\sin 2\pi kd}{k\pi} \quad \langle\mu\rangle_k^I = \frac{\cos 2\pi kd - 1}{k\pi} \tag{48}$$

(ii) Modelling of the inverter switching function S.

Let, the duty cycle d_i and switching period T be the variables associated with a inverter switch and H-bridge inverter consisting of 4 switches S_1 to S_4 (as shown in **Figure 3**). Using state 1 to represent S_1 and S_2 ON while state −1 for S_3 and S_4 ON, the switching function (S(t)) and its DP notation $\left(\langle S\rangle_k\right)$ can be defined as (49).

$$S(t) = \begin{cases} 1, & 0 < t < d_iT \\ -1, & d_iT < t < T \end{cases} \quad \langle S\rangle_0 = d_i \quad \langle S\rangle_k^R = \frac{\sin 2\pi kd_i}{k\pi} \quad \langle S\rangle_k^I = \frac{\cos 2\pi kd_i - 1}{k\pi} \tag{49}$$

Expanding (45)–(47) for every coefficient of **Table 2**, a system dynamics can be obtained as:

$$L\frac{d}{dt}\langle i_L\rangle_k^R = \langle V_{PV}\rangle_k^R - \langle V_C\rangle_k^R + \mathrm{Re}\left\{\sum_{l=-\infty}^{\infty}\langle\mu\rangle_{k-l}\langle V_C\rangle_l\right\} + k\omega L\langle i_L\rangle_k^I \tag{50}$$

$$L\frac{d}{dt}\langle i_L\rangle_k^I = \langle V_{PV}\rangle_k^I - \langle V_C\rangle_k^I + \mathrm{Re}\left\{\sum_{l=-\infty}^{\infty}\langle\mu\rangle_{k-l}\langle V_C\rangle_l\right\} - k\omega L\langle i_L\rangle_k^R \tag{51}$$

$$C\frac{d}{dt}\langle V_C\rangle_k^R = \langle i_L\rangle_k^R - \mathrm{Re}\left\{\sum_{l=-\infty}^{\infty}\langle\mu\rangle_{k-l}\langle i_L\rangle_l\right\} - \mathrm{Re}\left\{\sum_{l=-\infty}^{\infty}\langle S\rangle_{k-l}\langle i_{Lf}\rangle_l\right\} + k\omega C\langle V_C\rangle_k^I \tag{52}$$

$$C\frac{d}{dt}\langle V_C\rangle_k^I = \langle i_L\rangle_k^I - \mathrm{Re}\left\{\sum_{l=-\infty}^{\infty}\langle\mu\rangle_{k-l}\langle i_L\rangle_l\right\} - \mathrm{Re}\left\{\sum_{l=-\infty}^{\infty}\langle S\rangle_{k-l}\langle i_{Lf}\rangle_l\right\} - k\omega C\langle V_C\rangle_k^R \tag{53}$$

$$L_f\frac{d}{dt}\langle i_{Lf}\rangle_k^R = \mathrm{Re}\left\{\sum_{l=-\infty}^{\infty}\langle S\rangle_{k-l}\langle V_C\rangle_l\right\} - \langle V_{AC}\rangle_k^R + k\omega L_f\langle i_{Lf}\rangle_k^I \tag{54}$$

$$L_f\frac{d}{dt}\langle i_{Lf}\rangle_k^I = \mathrm{Re}\left\{\sum_{l=-\infty}^{\infty}\langle S\rangle_{k-l}\langle V_C\rangle_l\right\} - \langle V_{AC}\rangle_k^I - k\omega L_f\langle i_{Lf}\rangle_k^R \tag{55}$$

Corresponding to the boost converter switching frequency, for both current (i_L) and voltage (V_C) signals, the DPs are chosen as the direct current (k = 0) and the second harmonic (k = 2). On the other hand, for inverter, the DP form of the filter current (i_{Lf}) is chosen as fundamental and the third harmonic frequencies (k = 1, 3). In addition, if switching harmonics needs to be accommodated in the model, the DP index should be extended to $k = m_{fc}$ for boost converter and $k = m_{fi}$ for inverter.

4. DP-based PI controller design

4.1. Development of PI controller using DP model

To design a PI controller using DP-based small signal model, for maintaining constant desired voltage at the output of the inverter, a nested controller is proposed as shown in **Figure 4** with inner current and outer voltage control loops.

Controller design and stability analysis for inverter requires the deviation of small-signal control-to-output transfer function, which is the dynamic response for small perturbation in control signal. In state-space model of single-phase inverter, when there is a small perturbation in d_i, all the state variables will deviate from their steady states. Assume that the input voltage $\langle V_{dcL}\rangle_0$ is constant, the capitalised variables represents steady state values, lower case variables are the actual states and Δ variables represents small-signal states. The deviation of state variables are defined as:

$$\Delta\langle i_{fi}\rangle_1^R = \langle i_{fi}\rangle_1^R - I_{fi}1R \quad \Delta\langle i_{fi}\rangle_5^R = \langle i_{fi}\rangle_5^R - I_{fi}5R \quad \Delta\langle V_{cfi}\rangle_3^R = \langle V_{cfi}\rangle_3^R - V_{cfi}3R$$

$$\Delta\langle i_{fi}\rangle_1^I = \langle i_{fi}\rangle_1^I - I_{fi}1I \quad \Delta\langle i_{fi}\rangle_5^I = \langle i_{fi}\rangle_5^I - I_{fi}5I \quad \Delta\langle V_{cfi}\rangle_3^I = \langle V_{cfi}\rangle_3^I - V_{cfi}3I$$

$$\Delta\langle i_{fi}\rangle_3^R = \langle i_{fi}\rangle_3^R - I_{fi}3R \quad \Delta\langle V_{cfi}\rangle_1^R = \langle V_{cfi}\rangle_1^I - V_{cfi}1R \quad \Delta\langle V_{cfi}\rangle_5^R = \langle V_{cfi}\rangle_5^R - V_{cfi}5R$$

$$\Delta\langle i_{fi}\rangle_3^I = \langle i_{fi}\rangle_3^I - I_{fi}3I \quad \Delta\langle V_{cfi}\rangle_1^I = \langle V_{cfi}\rangle_1^I - V_{fi}1I \quad \Delta\langle V_{cfi}\rangle_5^I = \langle V_{cfi}\rangle_5^I - V_{cfi}5I$$

$$\Delta d_i = d_i - D_i$$

The small signal model of the single-phase inverter is given as: $\frac{d}{dt}[\Delta X_{inv}] = [A_{inv}][\Delta X_{inv}] + [B_{inv}][\Delta d_i]$ where,

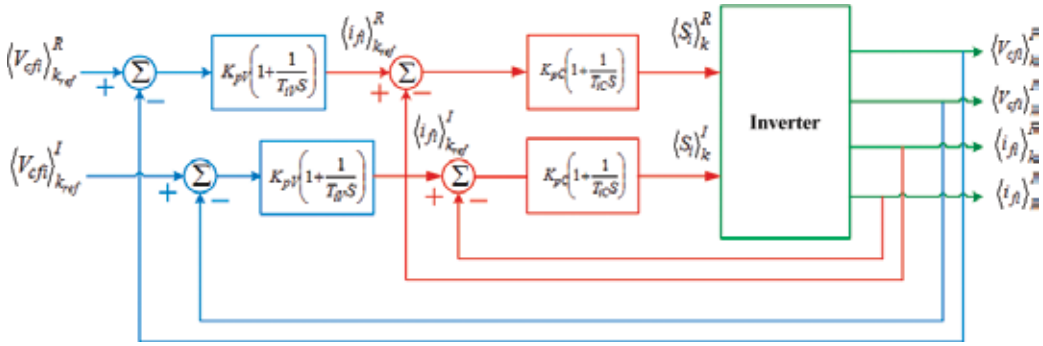

Figure 4. PI control scheme for DP model of single-phase inverter.

$$[\Delta X_{inv}] = \left[\Delta\langle i_{fi}\rangle_1^R \;\; \Delta\langle i_{fi}\rangle_1^I \;\; \Delta\langle i_{fi}\rangle_3^R \;\; \Delta\langle i_{fi}\rangle_3^I \;\; \Delta\langle i_{fi}\rangle_5^R \;\; \Delta\langle i_{fi}\rangle_5^I \;\; \Delta\langle V_{cfi}\rangle_1^R \;\; \Delta\langle V_{cfi}\rangle_1^I \;\; \Delta\langle V_{cfi}\rangle_3^R \;\; \Delta\langle V_{cfi}\rangle_3^I \;\; \Delta\langle V_{cfi}\rangle_5^R \;\; \Delta\langle V_{cfi}\rangle_5^I\right] \tag{56}$$

$$[A_{inv}] = \begin{bmatrix} -\dfrac{R_{fi}}{L_{fi}}[I]_{6\times6} & -\dfrac{1}{L_{fi}}[I]_{6\times6} \\ \dfrac{1}{C_{fi}}[I]_{6\times6} & -\dfrac{1}{C_{fi}R_L}[I]_{6\times6} \end{bmatrix} + diag\left(\omega[J]_{2\times2}, 3\omega[J]_{2\times2}, 5\omega[J]_{2\times2}, \omega[J]_{2\times2}, 3\omega[J]_{2\times2}, 5\omega[J]_{2\times2}\right) \tag{57}$$

$$[B_{inv}] = \left[\frac{\sin 2\pi D_i}{\pi L_{fi}} \;\; \frac{\cos 2\pi D_i - 1}{\pi L_{fi}} \;\; \frac{\sin 6\pi D_i}{3\pi L_{fi}} \;\; \frac{\cos 6\pi D_i - 1}{3\pi L_{fi}} \;\; \frac{\sin 10\pi D_i}{5\pi L_{fi}} \;\; \frac{\cos 10\pi k D_i - 1}{5\pi L_{fi}} \;\; 0 \;\; 0 \;\; 0 \;\; 0 \;\; 0 \;\; 0\right]^T \tag{58}$$

Eqs. (56)–(58) can be used to calculate the control-to-output transfer function of single-phase inverter.

The real and imaginary references for the voltage loop are generated by phase-locked-loop (PLL) with the desired ac voltage. The outer voltage loop generates the current references for inner current loop whereas the inner current loop generates desired duty ratio.

4.1.1. Design of the inner current loop controllers

The inner current loop dynamics is described as

$$\begin{cases} L_{fi}\dfrac{d}{dt}\Delta\langle i_{fi}\rangle_k^R = -R_{fi}\Delta\langle i_{fi}\rangle_k^R + k\omega L_{fi}\Delta\langle i_{fi}\rangle_k^I + \dfrac{\cos(2k\pi D_i)}{k}\Delta d_i \\ L_{fi}\dfrac{d}{dt}\Delta\langle i_{fi}\rangle_k^I = -R_{fi}\Delta\langle i_{fi}\rangle_k^I - k\omega L_{fi}\Delta\langle i_{fi}\rangle_k^R - \dfrac{\sin(2k\pi D_i)}{k}\Delta d_i \end{cases} \tag{59}$$

In (59), $\Delta\langle i_{fi}\rangle_k^I$ and $\Delta\langle i_{fi}\rangle_k^R$ are considered as perturbation which are further eliminated by the decoupling structure.

Describing transfer function for both $\Delta\langle i_{fi}\rangle_k^R$ and $\Delta\langle i_{fi}\rangle_k^I$

$$H_C(s) = \frac{\cos(2k\pi D_i)}{kR_{fi}}\frac{1}{(L_{fi}/R_{fi})s+1} = K_C\frac{1}{T_C s+1} \tag{60}$$

the current control loop is built using a PI controller H_{PIC} (s) and the closed loop transfer function is H_{0C} (s) as given in (61)

$$H_{PIC}(s) = K_{pC}\left(1+\frac{1}{T_{iC}s}\right)\;\; H_{0C}(s) = \frac{H_{PIC}(s).H_C(s)}{1+H_{PIC}(s).H_C(s)} = \frac{T_{iC}s+1}{\frac{T_C T_{iC}}{K_C K_{pC}}s^2 + T_{iC}\left(\frac{1}{K_C K_{pC}}+1\right)s+1} \tag{61}$$

To compute T_{iC} in terms of T_{0C} and hence, K_{pC} for given fixed damping coefficient ξ_C, imposing a closed-loop transfer function of the form (61) leads to (62).

$$H_{0C}(s) = \frac{T_{iC}s+1}{T_{0C}^2 s^2 + 2\xi_C T_{0C}s + 1},\;\; T_{iC} = 2\xi_C T_{0C} - \frac{T_{0C}^2}{T_C}\;\; K_{pC} = \frac{T_C T_{iC}}{K_C T_{0C}^2} \tag{62}$$

4.1.2. Design of the outer voltage loop controllers

The dynamics of outer voltage loop is described as

$$\begin{cases} C_{fi}\Delta\langle V_{cfi}\rangle_k^R = \Delta\langle i_{fi}\rangle_k^R - \dfrac{\Delta\langle V_{cfi}\rangle_k^R}{R_L} + k\omega C_{fi}\Delta\langle V_{cfi}\rangle_k^I \\ C_{fi}\Delta\langle V_{cfi}\rangle_k^I = \Delta\langle i_{fi}\rangle_k^I - \dfrac{\Delta\langle V_{cfi}\rangle_k^I}{R_L} - k\omega C_{fi}\Delta\langle V_{cfi}\rangle_k^R \end{cases} \tag{63}$$

The transfer function from current component to voltage is

$$H_V(s) = \frac{1}{R_{fi}}\frac{1}{C_{fi}R_L s + 1} = K_V\frac{1}{T_V s + 1} \tag{64}$$

The voltage control loop is built using PI controller H_{PIV} (s) and the voltage closed loop transfer function H_{0V}(s) is given in (65)

$$H_{PIV}(s) = K_{pV}\left(1 + \frac{1}{T_{iV}s}\right), \quad H_{0V}(s) = \frac{H_{PIV}(s)\cdot H_V(s)}{1 + H_{PIV}(s)\cdot H_V(s)} = \frac{T_{iV}s + 1}{\frac{T_V T_{iV}}{K_V K_{pV}}s^2 + T_{iV}\left(\frac{1}{K_V K_{pV}} + 1\right)s + 1} \tag{65}$$

By imposing closed loop transfer function of the form (65) for fixed damping coefficients ξ_V, the time constant T_{iV} can be investigated in terms of T_{0V} and hence, K_{pV} is calculated as (66)

$$H_{0V}(s) = \frac{T_{iV}s + 1}{T_{0V}^2 s^2 + 2\xi_V T_{0V}s + 1}, \quad T_{iV} = 2\xi_V T_{0V} - \frac{T_{0V}^2}{T_V} \quad K_{pV} = \frac{T_V T_{iV}}{K_V T_{0V}^2} \tag{66}$$

It should be noted that the outer voltage control loop time constant is larger than inner current control loop.

5. Performance evaluation of harmonic mitigation for VSI

Using simulation parameters as shown in **Table 3**, the models for single-phase inverter and grid-connected PV inverters are developed in MATLAB/Simulink and effectiveness of controller is validated for the single-phase inverter with R-load.

Single-phase inverter with R and RL load			**Grid-connected PV inverter**		
R_{fi} = 0.07 W	L_{fi} = 1.07 mH	C_{fi} = 30*m*F	L = 15 mH	L_f = 20 mH	C = 20*m*F
R_L = 35 W	L_L = 69.6 mH		V_{PV} = 200 V	V_{AC} = 230V_{rms}	

Table 3. Simulation parameters for harmonic mitigation of VSI.

5.1. Single-phase inverter with R and RL load

5.1.1. Response of VSI using conventional time domain model

Using input voltage to the inverter as 400 V with constant modulation of 0.8, the response obtained by conventional time domain model without controller is shown in **Figure 5** and **Figure 6** for only R and RL load respectively. It can be seen from **Figures 5** and **6(a)** and **(b)**,

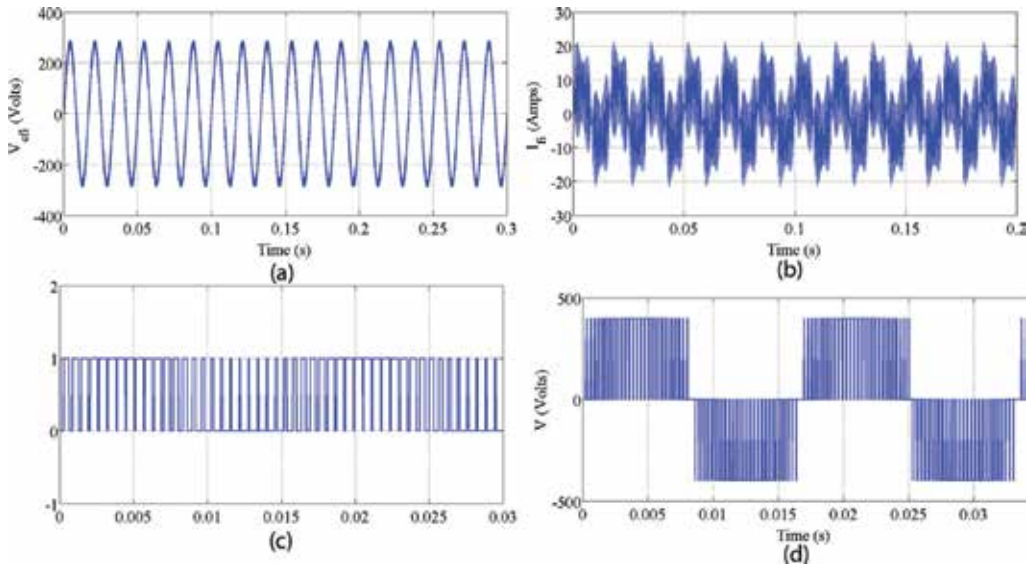

Figure 5. Performance analysis of single-phase inverter with R-load but without controller. (a) Output filter voltage of inverter (V_{cfi}) (b) output filter current of inverter (I_{fi}). (c) Switching signal (d) discontinuous output voltage.

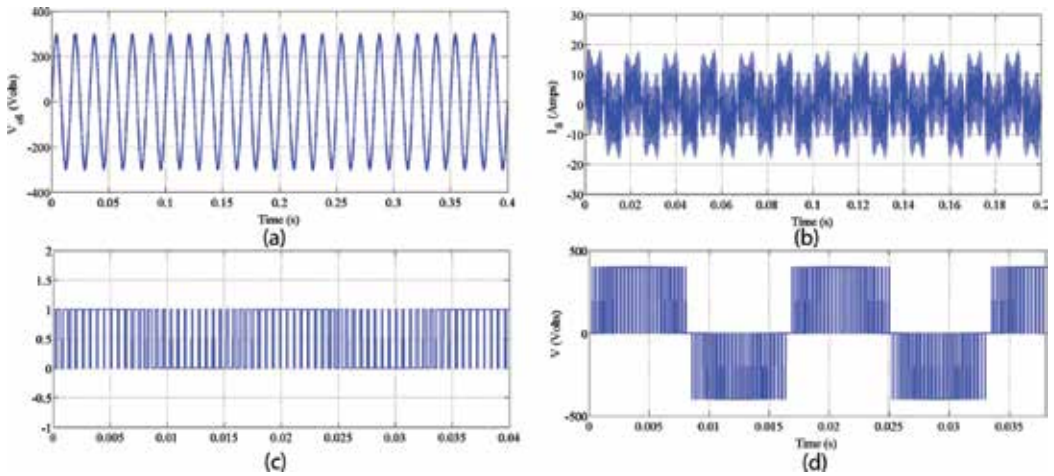

Figure 6. Performance analysis of single-phase inverter with RL-load but without controller. (a) Output filter voltage of inverter (V_{cfi}) (b) output filter current of inverter (I_{fi}). (c) Switching signal (d) discontinuous output voltage.

irrespective of type of load R or RL, the inverter output filter current is more distorted as compared to output filter voltage which indicates the necessity of proper controller to eliminate unwanted harmonics in voltage or current. **Figures 5** and **6(c)** and **(d)** shows switching signal and discontinuous output voltage of inverter respectively.

5.1.2. Response of VSI using DP model

In this section, open loop analysis of simulation results using DP model are built within the SimPowerSystem of the MATLAB/Simulink library with the change in load resistance from 35 Ω to 25 Ω at 0.2 sec. DP coefficient dynamics of state variables of inverter are presented in **Figures 7** and **8**. With DP index k = 1, 3, 5 inverter filter output voltage and current is shown in **Figures 7** and **8(a)** and **(b)** for R and RL load respectively.

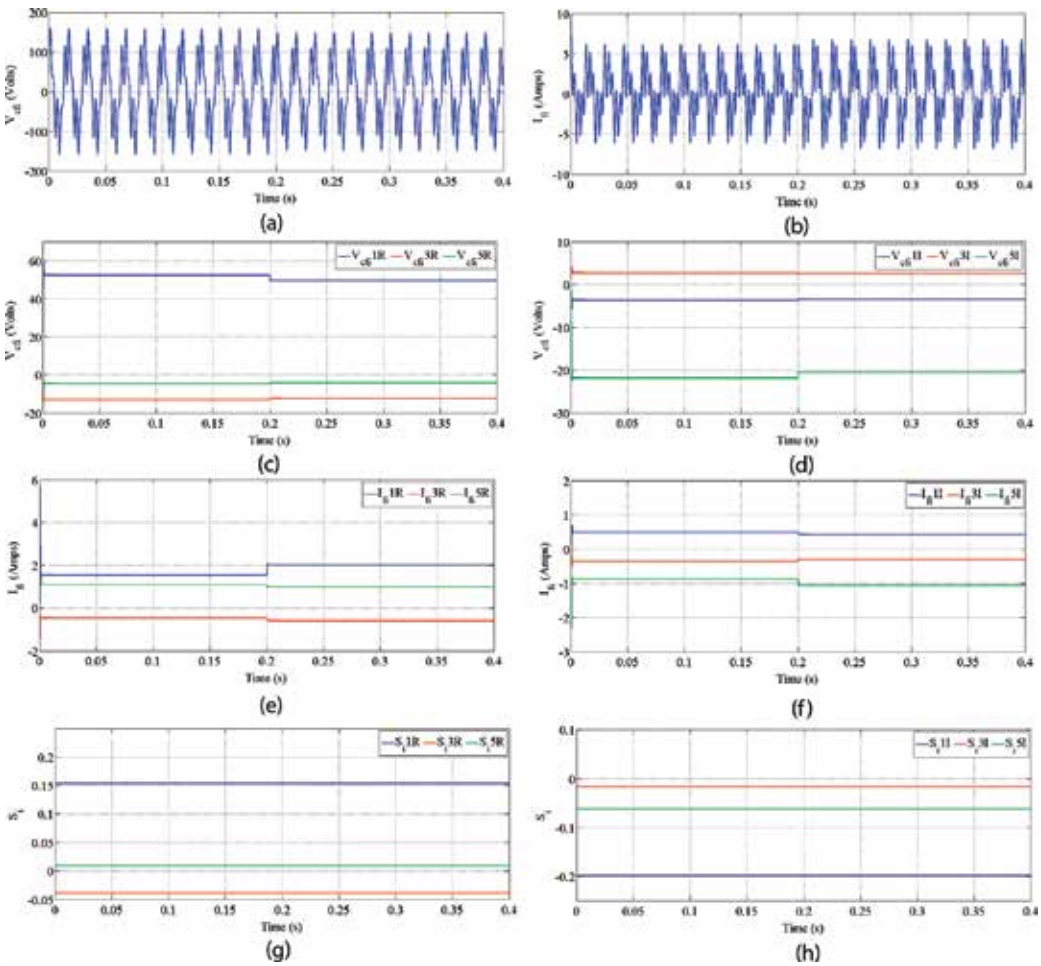

Figure 7. Response of single-phase inverter with R-load using DP-based model without controller(a) output filter voltage (V_{cfi}) (b) output filter current (I_{fi}) (c) re-coefficients of DP V_{cfi} (d) Im-coefficients of DP V_{cfi} (e) re-coefficients of DP I_{fi} (f) Im-coefficients of DP I_{fi} (g) re-coefficients of DP S_i (h) Im-coefficients of DP S_i.

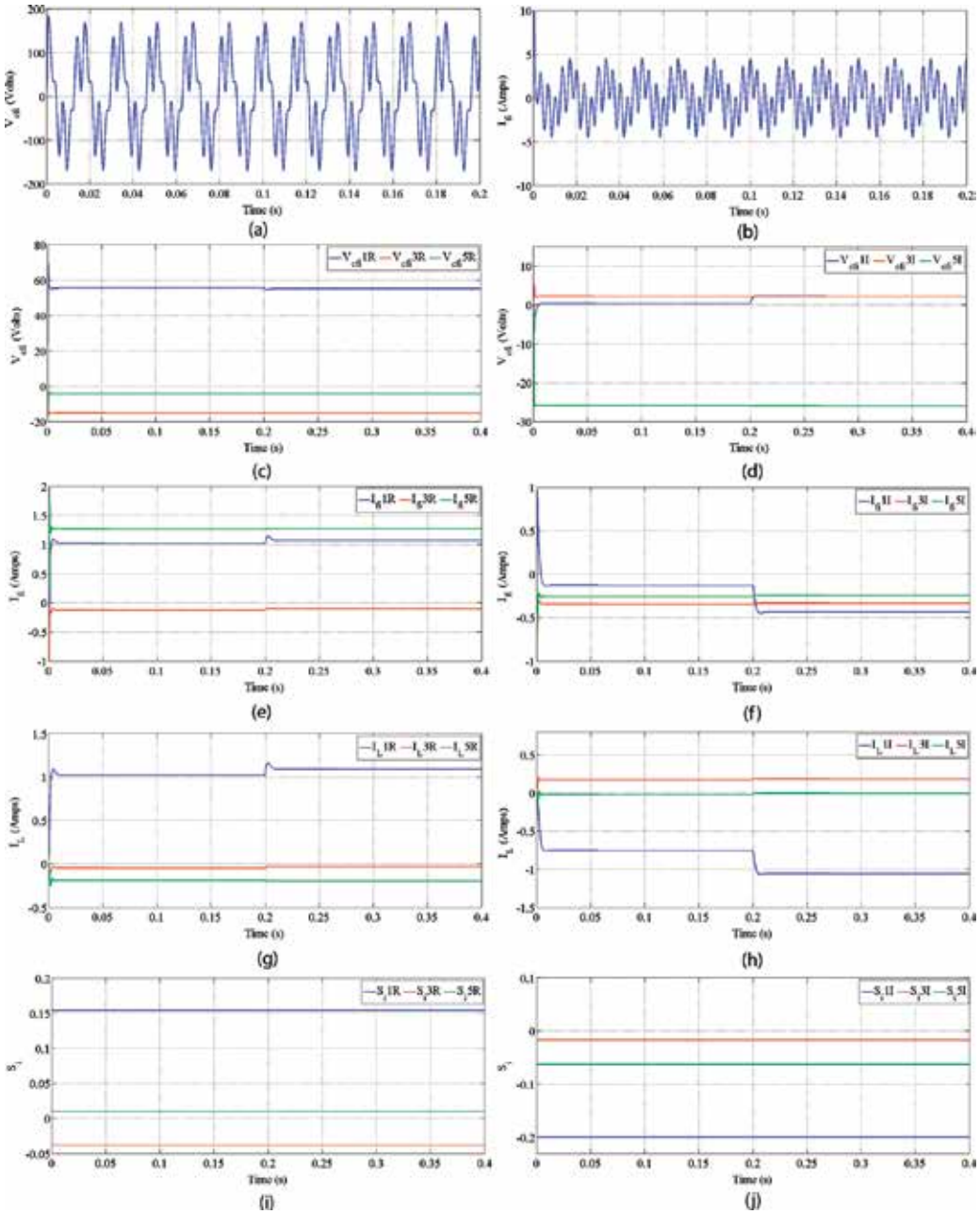

Figure 8. Response of single-phase inverter with RL-load using DP-based model without controller. (a) Output filter voltage (V_{cfi}) (b) output filter current (I_{fi}) (c) re-coefficients of DP V_{cfi} (d) Im-coefficients of DP V_{cfi} (e) re-coefficients of DP I_{fi} (f) Im-coefficients of DP I_{fi} (g) re-coefficients of DP i_L (h) Im-coefficients of DP i_L (i) re-coefficients of DP S_i (j) Im-coefficients of DP S_i.

The corresponding real and imaginary parts of harmonic coefficients are separately shown in **Figures 7** and **8(c)** and **(d)** for inverter filter voltage and **Figures 7** and **8(e)** and **(f)** for load current for R and RL load respectively. The switching function is also separated in harmonic coefficients that are shown in **Figures 7** and **8(g)** and **(h)**.

It should be noted that as compared to conventional time domain model, DP-based model provides better insight in the features of output current and voltage waveforms. Using this valuable precise details, the controller could be designed to target selected harmonics.

5.2. Response comparison of single-phase grid-connected inverter for PV system using time domain and DP-based model

The single-phase grid-connected PV model is simulated in MATLAB/Simulink using input PV voltage as 200 V. The system consists of three stages that is boost stage, inverter stage, and filter stage. The variable of interest for harmonic analysis is the filter current in inverter stage and **Figure 9** shows the inverter filter current with harmonics. Same single-phase grid-connected PV system response is observed using DP-based model using higher index by plotting harmonic coefficients separately for output filter current as shown in **Figure 10**.

5.3. Performance analysis of VSI with controller

Again it should be noted that DP-based model provides more accurate information about harmonic content as compared to time domain model. In both models, it is clearly seen that the controller is highly recommended for mitigation of dominant harmonic components. As a result, a conventional RC is designed and used with time domain model. On the other hand, a proposed DP-based PI controller is also designed to show its effectiveness as compared to RC in harmonic mitigation. The aim of the repetitive controller is to track the sinusoidal reference voltage of $230V_{rms}$ and eliminate all harmonics present in output voltage of inverter system. In **Figure 11(a)**, the tracking of output voltage signal (V_{cfi}) to the desired reference signal with

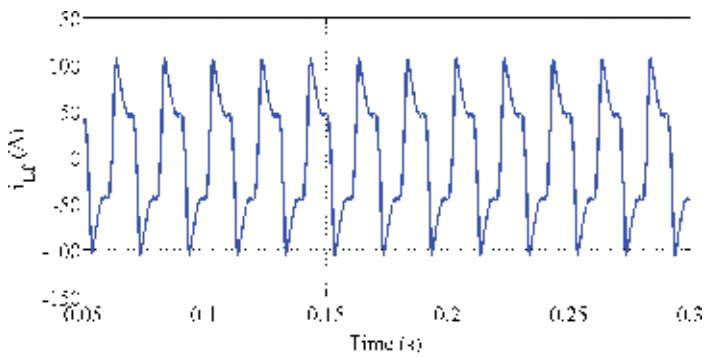

Figure 9. Response of inductor filter current (i_{Lf}) of grid-connected PV inverter.

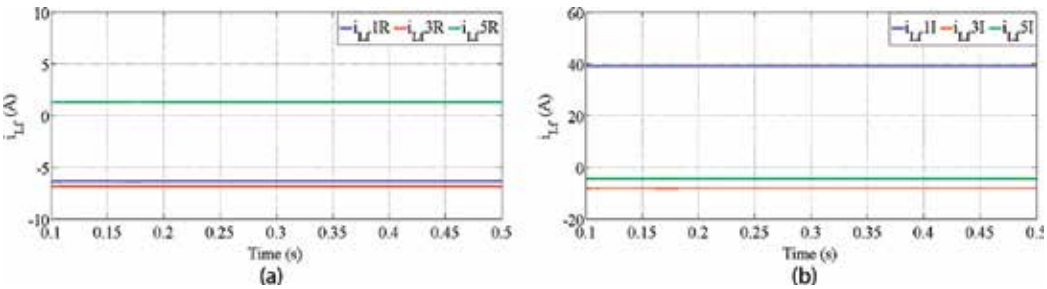

Figure 10. Response of inductor filter current (i_{Lf}) of grid-connected PV inverter using DP-based model. (a) Re-coefficients of DP i_{Lf} and (b) Im-coefficients of DP i_{Lf}.

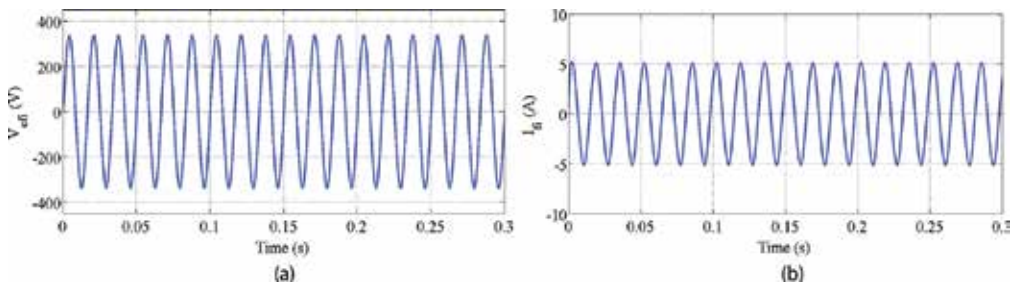

Figure 11. Performance analysis of single phase inverter with repetitive controller. (a) Inverter output filter voltage (V_{cfi}) and (b) inverter output filter current (I_{fi}).

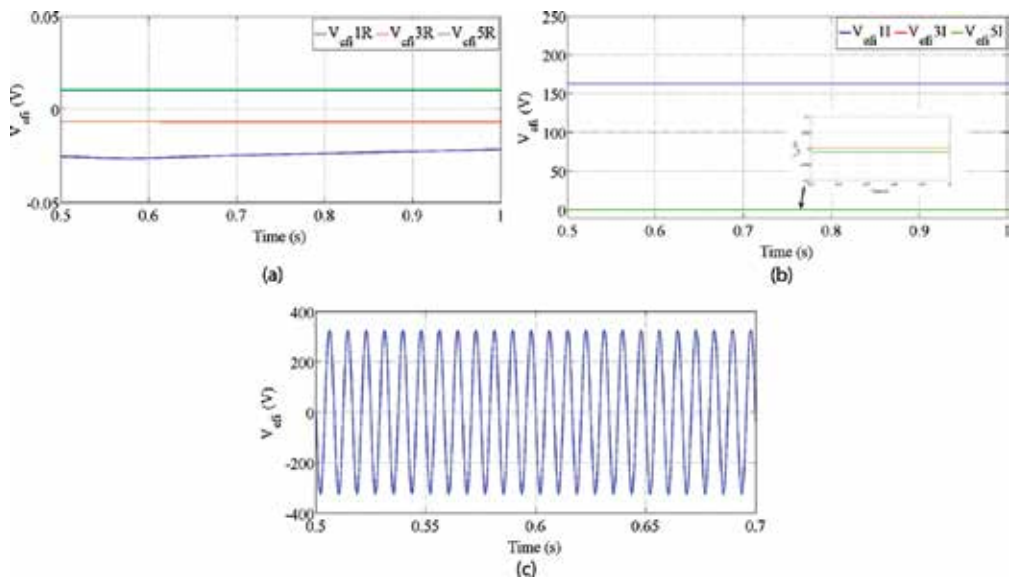

Figure 12. Performance analysis of DP single-phase inverter model with PI controller. (a) Re-coefficients of DP V_{cfi} (b) Im-coefficients of DP V_{cfi} (c) controlled filter output voltage (V_{cfi}).

load resistance of 100 Ω is observed and shows the elimination of harmonics present in **Figure 5(a)**. The corresponding current harmonics are also eliminated with this controller as shown in **Figure 11(b)** which were present in **Figure 5(b)**. A DP-based PI controller is designed with nested form as shown in **Figure 4** with outer voltage loop and the inner current loop. The controlled DP coefficients of inverter filter output voltage are shown in **Figure 12(a)** and **(b)** and the actual filter output voltage (V_{cfi}) is shown in **Figure 12(c)**. Though, PI gains can be calculated by numerous techniques like loop shaping, pole placement, root locus, prediction-based method etc., in the proposed controller the gains are computed as explained in Section 4, specifically designed to eliminate 3rd and 5th harmonic coefficients.

Comparing response of VSI with RC- and DP-based PI controller **Figures 11** and **12**, it can be observed that proposed controller has achieved required quality of output voltage by eliminating selected harmonics. It was possible to target individual harmonic components because of higher index DP model which gave detailed precise information about the elements responsible for deviation from desired quality output. It should be noted that, irrespective of harmonics, the DP-based controller helps in providing better voltage regulation for various disturbances such as intermittent nature of renewable input sources and load variations [32].

6. Conclusions

In this chapter, the DP technique is used to model single-phase inverter with R-load, RL-load and grid-tied PV inverters with multiple frequencies. The overall design aims to obtain acceptable signal approximations with the selected DP coefficients. The harmonics coefficients (DP index-k) for each model are chosen after analysing the main harmonic from the original systems. These DP-based equations have been introduced to compute total, fundamental and distorting dc/ac voltage and currents. In view of this, the chapter has proposed two major contributions: strengths of DP-based model over time domain model and effectiveness of DP-based PI controller over RC. The simulation results comparing various circuit topologies in time domain and DP-based model has shown that the DP-based model provides more detailed information about harmonic contents in the output variables. Using this pinpoint knowledge of selected harmonics of concern, a DP-based controller with higher index can be designed to precisely target the required response which is otherwise not possible in general time domain model. As a result, the DP-based PI controller has shown expected quality improvements as compared to well-known RC controller in voltage regulation and selected harmonic elimination in both steady-state and transient state. It could be also useful in designing best possible operations by minimising losses in system.

Acknowledgements

The authors would like to acknowledge Dr. N. M. Singh, Department of Electrical Engineering, VJTI, Mumbai and Dr. A. M. Stanković, Department of Electrical and Computer Engineering, Tufts University, USA for their continuous guidance throughout this research.

A. Appendix

Procedure to be adopted for three-phase case study:

The switching function of the switch S_{jk} is defined as

$$S_{jk} = \begin{cases} 1, & switch\ S_{jk}\ is\ closed \\ 0, & switch\ S_{jk}\ is\ open \end{cases} \tag{67}$$

where j represents the phase i.e. j ∈ {a, b, c} and variable k ∈ {p, n} is used to distinguish the upper and lower component of phase leg. The switching constraints for upper switch S_{jp} and the lower switch S_{jn} is $S_{jP} + S_{jn} = 1$.

The phase switching function defines if the output terminal of the phase leg (point j) is connected to the positive potential or to the negative potential of the dc link voltage by the single-pole double-throw switch S_j. The phase switching function (S_j) is defined as follows

$$S_j = \begin{cases} 1, & S_j\ is\ connected\ to\ point\ p \\ -1, & S_j\ is\ connected\ to\ point\ n \end{cases} \tag{68}$$

Assuming the case of three-phase inverter with R-load, the notations will be followed as given in Section 3.1. The dynamic equations are as:

$$L_{fi}\frac{d}{dt}\begin{bmatrix} i_{fi_{ab}} \\ i_{fi_{bc}} \\ i_{fi_{ca}} \end{bmatrix} = \begin{bmatrix} S_{i_{ab}} \\ S_{i_{bc}} \\ S_{i_{ca}} \end{bmatrix} V_{dcL} - R_{fi}\begin{bmatrix} i_{fi_{ab}} \\ i_{fi_{bc}} \\ i_{fi_{ca}} \end{bmatrix} - \begin{bmatrix} V_{cfi_{ab}} \\ V_{cfi_{bc}} \\ V_{cfi_{ca}} \end{bmatrix} \tag{69}$$

$$C_{fi}\frac{d}{dt}\begin{bmatrix} V_{cfi_{ab}} \\ V_{cfi_{bc}} \\ V_{cfi_{ca}} \end{bmatrix} = \begin{bmatrix} i_{fi_{ab}} \\ i_{fi_{bc}} \\ i_{fi_{ca}} \end{bmatrix} - \frac{1}{R_L}\begin{bmatrix} V_{cfi_{ab}} \\ V_{cfi_{bc}} \\ V_{cfi_{ca}} \end{bmatrix} \tag{70}$$

where $i_{fi_{ab}} = i_{fi_a} - i_{fi_b}$, $i_{fi_{bc}} = i_{fi_b} - i_{fi_c}$, $i_{fi_{ca}} = i_{fi_c} - i_{fi_a}$, $S_{i_{ab}} = S_{i_a} - S_{i_{bc}}$, $S_{i_{bc}} = S_{i_b} - S_{i_c}$, $S_{i_{ca}} = S_{i_c} - S_{i_a}$, $V_{cfi_{ab}} = V_{cfi_a} - V_{cfi_b}$, $V_{cfi_{bc}} = V_{cfi_b} - V_{cfi_c}$ and $V_{cfi_{ca}} = V_{cfi_c} - V_{cfi_a}$.

In Sine Pulse Width Modulation (SPWM) technique, Sij can be replaced by its fundamental component d_{ij}

$$d_{ij} = \frac{1}{2}\left(1 + \frac{v_m}{v_{tri}}\right) = \frac{m}{2}\cos\left(\omega t - \phi_j\right) + \frac{1}{2} \tag{71}$$

where j = a, b, c, $\phi_a = \phi_0$, $\phi_b = \phi_0 + 2\pi/3$, $\phi_c = \phi_0 - 2\pi/3$, ϕ_0 is initial phase angle and m is amplitude modulation ratio.

The state variables in of (69) and (70) can be approximated in DP form as sum of the their DC components and index-k components

$$i_{fi_{ab}} \approx \left\langle i_{fi_{ab}} \right\rangle_{-k} e^{-jk\omega t} + \left\langle i_{fi_{ab}} \right\rangle_{0} + \left\langle i_{fi_{ab}} \right\rangle_{k} e^{jk\omega t} \tag{72}$$

$$i_{fi_{bc}} \approx \left\langle i_{fi_{bc}} \right\rangle_{-k} e^{-jk\omega t} + \left\langle i_{fi_{bc}} \right\rangle_{0} + \left\langle i_{fi_{bc}} \right\rangle_{k} e^{jk\omega t} \tag{73}$$

$$i_{fi_{ca}} \approx \left\langle i_{fi_{ca}} \right\rangle_{-k} e^{-jk\omega t} + \left\langle i_{fi_{ca}} \right\rangle_{0} + \left\langle i_{fi_{ca}} \right\rangle_{k} e^{jk\omega t} \tag{74}$$

$$V_{cfi_{ab}} \approx \left\langle V_{cfi_{ab}} \right\rangle_{-k} e^{-jk\omega t} + \left\langle V_{cfi_{ab}} \right\rangle_{0} + \left\langle V_{cfi_{ab}} \right\rangle_{k} e^{jk\omega t} \tag{75}$$

$$V_{cfi_{bc}} \approx \left\langle V_{cfi_{bc}} \right\rangle_{-k} e^{-jk\omega t} + \left\langle V_{cfi_{bc}} \right\rangle_{0} + \left\langle V_{cfi_{bc}} \right\rangle_{k} e^{jk\omega t} \tag{76}$$

$$V_{cfi_{ca}} \approx \left\langle V_{cfi_{ca}} \right\rangle_{-k} e^{-jk\omega t} + \left\langle V_{cfi_{ca}} \right\rangle_{0} + \left\langle V_{cfi_{ca}} \right\rangle_{k} e^{jk\omega t} \tag{77}$$

The input dc voltage can be considered as a constant V_{dcL}, thus it has

$$\langle V_{dcL} \rangle_{\pm k} = 0 \quad \langle V_{dcL} \rangle_{0} = V_{dcL} \tag{78}$$

$$L_{fi} \frac{d}{dt} \begin{bmatrix} \left\langle i_{fi_{ab}} \right\rangle_{k} \\ \left\langle i_{fi_{bc}} \right\rangle_{k} \\ \left\langle i_{fi_{ca}} \right\rangle_{k} \end{bmatrix} = \begin{bmatrix} \left\langle S_{i_{ab}} V_{dcL} \right\rangle_{k} \\ \left\langle S_{i_{bc}} V_{dcL} \right\rangle_{k} \\ \left\langle S_{i_{ca}} V_{dcL} \right\rangle_{k} \end{bmatrix} - R_{fi} \begin{bmatrix} \left\langle i_{fi_{ab}} \right\rangle_{k} \\ \left\langle i_{fi_{bc}} \right\rangle_{k} \\ \left\langle i_{fi_{ca}} \right\rangle_{k} \end{bmatrix} - \begin{bmatrix} \left\langle V_{cfi_{ab}} \right\rangle_{k} \\ \left\langle V_{cfi_{bc}} \right\rangle_{k} \\ \left\langle V_{cfi_{ca}} \right\rangle_{k} \end{bmatrix} - jk\omega L_{fi} \begin{bmatrix} \left\langle i_{fi_{ab}} \right\rangle_{k} \\ \left\langle i_{fi_{bc}} \right\rangle_{k} \\ \left\langle i_{fi_{ca}} \right\rangle_{k} \end{bmatrix} \tag{79}$$

$$L_{fi} \frac{d}{dt} \begin{bmatrix} \left\langle i_{fi_{ab}} \right\rangle_{0} \\ \left\langle i_{fi_{bc}} \right\rangle_{0} \\ \left\langle i_{fi_{ca}} \right\rangle_{0} \end{bmatrix} = \begin{bmatrix} \left\langle S_{i_{ab}} V_{dcL} \right\rangle_{0} \\ \left\langle S_{i_{bc}} V_{dcL} \right\rangle_{0} \\ \left\langle S_{i_{ca}} V_{dcL} \right\rangle_{0} \end{bmatrix} - R_{fi} \begin{bmatrix} \left\langle i_{fi_{ab}} \right\rangle_{0} \\ \left\langle i_{fi_{bc}} \right\rangle_{0} \\ \left\langle i_{fi_{ca}} \right\rangle_{0} \end{bmatrix} - \begin{bmatrix} \left\langle V_{cfi_{ab}} \right\rangle_{0} \\ \left\langle V_{cfi_{bc}} \right\rangle_{0} \\ \left\langle V_{cfi_{ca}} \right\rangle_{0} \end{bmatrix} \tag{80}$$

$$C_{fi} \frac{d}{dt} \begin{bmatrix} \left\langle V_{cfi_{ab}} \right\rangle_{k} \\ \left\langle V_{cfi_{bc}} \right\rangle_{k} \\ \left\langle V_{cfi_{ca}} \right\rangle_{k} \end{bmatrix} = \begin{bmatrix} \left\langle i_{fi_{ab}} \right\rangle_{k} \\ \left\langle i_{fi_{bc}} \right\rangle_{k} \\ \left\langle i_{fi_{ca}} \right\rangle_{k} \end{bmatrix} - \frac{1}{R_L} \begin{bmatrix} \left\langle V_{cfi_{ab}} \right\rangle_{k} \\ \left\langle V_{cfi_{bc}} \right\rangle_{k} \\ \left\langle V_{cfi_{ca}} \right\rangle_{k} \end{bmatrix} - jk\omega C_{fi} \begin{bmatrix} \left\langle V_{cfi_{ab}} \right\rangle_{k} \\ \left\langle V_{cfi_{bc}} \right\rangle_{k} \\ \left\langle V_{cfi_{ca}} \right\rangle_{k} \end{bmatrix} \tag{81}$$

$$C_{fi} \frac{d}{dt} \begin{bmatrix} \left\langle V_{cfi_{ab}} \right\rangle_{0} \\ \left\langle V_{cfi_{bc}} \right\rangle_{0} \\ \left\langle V_{cfi_{ca}} \right\rangle_{0} \end{bmatrix} = \begin{bmatrix} \left\langle i_{fi_{ab}} \right\rangle_{0} \\ \left\langle i_{fi_{bc}} \right\rangle_{0} \\ \left\langle i_{fi_{ca}} \right\rangle_{0} \end{bmatrix} - \frac{1}{R_L} \begin{bmatrix} \left\langle V_{cfi_{ab}} \right\rangle_{0} \\ \left\langle V_{cfi_{bc}} \right\rangle_{0} \\ \left\langle V_{cfi_{ca}} \right\rangle_{0} \end{bmatrix} \tag{82}$$

$$\begin{cases} \langle S_{ij} \rangle_{0} = d_{ij} \\ \langle S_{ij} \rangle_{k} = \dfrac{M + jN}{2\pi} \end{cases} \tag{83}$$

where $M = \sin\left(2\pi d_{ij} - \phi_j\right)$ and $N = \cos\left(2\pi d_{ij} - \phi_j\right) - 1$.

Author details

Ragini Meshram*, Monika Madhusoodan and Sushama Wagh

*Address all correspondence to: raginimeshram18@gmail.com

Electrical Engineering Department, VJTI, Mumbai, India

References

[1] Baekhoej KS, Pedersen JK, Blaabjerg F. A review of single-phase grid-connected inverters for photovoltaic modules. IEEE Transactions on Industry Applications. 2005;**41**(5):1292-1306

[2] Xu Jinming, Qiang Qian, Binfeng Zhang, Huizhen Wang, and Shaojun Xie. An adaptive algorithm for grid-connected inverter to suppress current harmonics and instabilities due to grid impedance and distortion. In: Applied Power Electronics Conference and Exposition (APEC), 2017 IEEE;2017. IEEE. pp. 2638-2643

[3] Aleksandr R, Simoes MG, Al-Durra A, Muyeen SM. LCL filter design and performance analysis for grid-interconnected systems. IEEE Transactions on Industry Applications. 2014;**50**(2):1225-1232

[4] Wu W, He Y, Blaabjerg F. An LLCL power filter for single-phase grid-tied inverter. IEEE Transactions on Power Electronics. 2012;**27**(2):782-789

[5] Yang Y, Zhou K, Blaabjerg F. Current harmonics from single-phase grid-connected inverters examination and suppression. IEEE Journal of Emerging and Selected Topics in Power Electronics. 2016;**4**(1):221-233

[6] Grahame HD, McGrath BP. Opportunities for harmonic cancellation with carrier-based PWM for a two-level and multilevel cascaded inverters. IEEE Transactions on Industry Applications. 2001;**37**(2):574-582

[7] Erika T, Holmes DG. Grid current regulation of a three-phase voltage source inverter with an LCL input filter. IEEE Transactions on Power Electronics. 2003;**18**(3):888-895

[8] Miguel C, Miret J, Matas J, Vicuna LG d, Guerrero JM. Control design guidelines for single-phase grid-connected photovoltaic inverters with damped resonant harmonic compensators. IEEE Transactions on Industrial Electronics. 2009;**56**(11):4492-4501

[9] Abhijit K, John V. Mitigation of lower order harmonics in a grid-connected single-phase PV inverter. IEEE Transactions on Power Electronics. 2013;**28**(11):5024-5037

[10] Marco L, Teodorescu R, Blaabjerg F. Multiple harmonics control for three-phase grid converter systems with the use of PI-RES current controller in a rotating frame. IEEE Transactions on Power Electronics. 2006;**21**(3):836-841

[11] Cardoso MF, Spaduto RR, Freitas LCG d, Tavares CE, Macedo JR, Rezende PHO. Harmonic distortion analysis in a low voltage grid-connected photovoltaic system. IEEE Latin America Transactions. 2015;**13**(1):136-142

[12] Sanders Seth R, Mark Noworolski J, Liu XZ, Verghese GC. Generalized averaging method for power conversion circuits. IEEE Transactions on Power Electronics. 1991;**6**(2):251-259

[13] Stefan A, Mariéthoz S, Morari M. Dynamic phasor model predictive control of switched mode power converters. IEEE Transactions on Control Systems Technology. 2015;**23**(1): 349-356

[14] Seddik B, Munteanu I, Bratcu AI. Power electronic converters modeling and control. Advanced Textbooks in Control and Signal Processing. 2014;**454**:454

[15] Alberto C-M, Pérez-Cisneros MA, Domínguez-Navarro JA, Osuna-Enciso V, Zúñiga-Grajeda V, Gurubel-Tun KJ. Dynamic phasors modeling for a single phase two stage inverter. Electric Power Systems Research. 2016;**140**:854-865

[16] Parimi M, Monika M, Rane M, Wagh S, Stankovic A. Dynamic phasor-based small-signal stability analysis and control of solid state transformer. IEEE 6th International Conference on Power Systems (ICPS). IEEE. pp. 1-6;2016

[17] Zhixin M, Piyasinghe L, Khazaei J, Fan L. Dynamic phasor-based modeling of unbalanced radial distribution systems. IEEE Transactions on Power Systems. 2015;**30**(6):3102-3109

[18] Stefan A, Jönsson U. Harmonic analysis of pulse-width modulated systems. Automatica. 2009;**45**(4):851-862

[19] Souvik D, Sahoo SK, Panda SK. Single-phase inverter control techniques for interfacing renewable energy sources with microgrid part I: Parallel-connected inverter topology with active and reactive power flow control along with grid current shaping. IEEE Transactions on Power Electronics. 2011;**26**(3):717-731

[20] Fatih E. Plug-in repetitive control of single-phase grid-connected inverter for AC module applications. IET Power Electronics. 2017;**10**(1):47-58

[21] Hitoshi H, Sayama K, Ohishi K, Shimizu T. Current control system based on repetitive control and disturbance observer for single-phase five-level inverter. In: Industrial Electronics Society, IECON. IEEE. pp. 004370-004375;2015

[22] Paolo M, Marafao FP. Repetitive-based control for selective harmonic compensation in active power filters. IEEE Transactions on Industrial Electronics. 2004;**51**(5):1018-1024

[23] Zhou Xuesong, Daichun Song, Youjie Ma, and Deshu Cheng. Grid-connected control and simulation of single-phase two-level photovoltaic power generation system based on repetitive control. International Conference on Measuring Technology and Mechatronics Automation (ICMTMA). Vol. 2. IEEE; 2010. pp. 366-369

[24] Keliang Z, Yang Y, Blaabjerg F. Frequency adaptive repetitive control of grid-tied single-phase PV inverters. Energy Conversion Congress and Exposition (ECCE), 2015 IEEE; 2015. pp. 1689-1693

[25] Weiss G. Repetitive control systems: Old and new ideas. In: Systems and Control in the twenty-First Century. Boston, MA: Birkhäuser; 1997. pp. 389-404

[26] Sufen C, Lai YM, Tan S-C, Tse CK. Analysis and design of repetitive controller for harmonic elimination in PWM voltage source inverter systems. IET Power Electronics. 2008; **1**(4):497-506

[27] Gerardo E, Martinez PR, Leyva-Ramos J. Analog circuits to implement repetitive controllers with feedforward for harmonic compensation. IEEE Transactions on Industrial Electronics. 2007;**54**(1):567-573

[28] Keliang Z, Wang D, Low K-S. Periodic errors elimination in CVCF PWM DC/AC converter systems: Repetitive control approach. IEEE Proceedings-Control Theory and Applications. 2000;**147**(6):694-700

[29] Francis Bruce A, Wonham WM. The internal model principle for linear multivariable regulators. Applied Mathematics and Optimization. 1975;**2**(2):170-194

[30] Li C, Dongchun Z, Xianyi Z. Theory and applications of the repetitive control. SICE 2004 Annual Conference. 2004;**1**:27-34. IEEE

[31] Wu-Sung Y, Tsai M-C. Analysis and estimation of tracking errors of plug-in type repetitive control systems. IEEE Transactions on Automatic Control. 2005;**50**(8):1190-1195

[32] Meshram RV, Bhagwat M, Khade S, Wagh SR, Stankovi'c AM, Singh NM. Port-controlled Phasor Hamiltonian modeling and IDA-PBC control of solid-state transformer. IEEE Transactions on Control Systems Technology. Nov 2017

Edited by Moulay Tahar Lamchich

Harmonic analysis is a diverse field including such branches as signal processing, medical imaging, power electrical systems, wireless telecommunications, etc. This book is primarily written with the objective of providing recent developments and new techniques in harmonic analysis. In the recent years, a number of methods of quality control of signals under different perturbations, and especially the harmonics, have emerged. Some of these techniques are described in this book. This book is the result of contributions from many researchers and is a collection of eight research works, which are focused around the harmonic analysis theme but with different applications. The topics mainly concern the areas of medical imaging, biopotential systems, renewable energy conversion systems, wireless telecommunications, power converters, as well as the different techniques for estimating, analyzing, reducing, and eliminating harmonics.

Published in London, UK

IntechOpen

ISBN 978-1-83881-317-8